Investigations Into Dual-Grating Dielectric Laser-Driven Accelerators

UNIVERSITY OF LIVERPOOL

Thesis submitted in accordance with the requirements of the University of Liverpool for the degree of Doctor in Philosophy

By

Yelong Wei

（Student ID: 201061445）

June 2018

Abstract

Dielectric laser-driven accelerators (DLAs) utilizing the large electric fields from commercial laser systems to accelerate particles with high gradients - in the range of GV/m - have the potential to dramatically reduce the size and cost of future particle accelerators. Dual-gratings are one of the candidates for DLAs. They can be mass-produced using currently-available nanofabrication techniques, due to their simpler structural geometry compared to other types of DLA. So far, dual-grating structures have experimentally demonstrated accelerating gradients of 300 MV/m, 690 MV/m, and 1.8 GV/m for relativistic electron acceleration and gradients of 220 MV/m and 370 MV/m for non-relativistic electron acceleration. These demonstrations pave the way for implementing an on-chip particle accelerator in the future.

This thesis presents detailed studies of dual-grating DLAs, including geometry optimizations, beam quality and energy efficiency studies, wakefield and particle-in-cell (PIC) simulations, as well as the fabrication and experimental preparations beyond the current state-of-the-art DLAs. In order to identify the optimum geometry, various numerical studies are carried out using the CST and VSim simulation codes, to maximize the accelerating factor and the accelerating efficiency for dual-grating structures, and results from both codes are compared. The beam parameters of the future Compact Linear Accelerator for Research and Applications (CLARA) facility are then used to load an electron bunch into an optimized 100-period dual-grating structure, where it interacts with a realistic laser pulse. The emittance, energy spread, and loaded accelerating gradient for modulated electrons are then analysed in detail. Results from simulations show that an accelerating gradient of up to 1.15 GV/m, with an extremely small emittance growth, 3.6%, can be expected. Two new kinds of schemes are also investigated in this thesis to improve the electron energy efficiency for dual-grating DLAs. One is to introduce a Bragg reflector, which can boost the accelerating field to generate a 70% higher energy gain compared to bare dual-grating structures, from PIC simulations. As a second scheme, pulse-front-tilted operation for the laser beam is proposed, to extend the interaction length and thereby increase the greater energy gain by more than 138% compared to normal laser illumination, from PIC simulations. When both schemes are combined together for dual-grating DLAs, the energy gain generated is increased by 254% compared to normal laser illumination on bare dual-gratings.

This thesis also presents numerical studies for a THz-driven dual-grating structure to accelerate electrons, including geometry optimizations and detailed studies of wakefield and THz-bunch interaction. Such scaled structures can be fabricated using conventional machining techniques, which makes future demonstrations easier than for DLAs.

Finally, the fabrication techniques for laser-driven dual-grating structures are studied, with researchers in Paul Scherrer Institut (PSI). A dual-grating structure with a channel depth of 7.6 μm and excellent alignment has been successfully fabricated using a monolithic method. The preliminary experimental studies carried out using the electron beam from the Swiss FEL facility are also presented in this thesis, and the future challenges for dual-grating DLAs are discussed.

Acknowledgements

First and foremost I would like to express my sincere gratitude to my advisor and supervisor, Prof. Dr. Carsten Welsch, head of physics department, for his strong support during my PhD study. In 2014, he offered me an opportunity to become a Marie Curie Fellow within the EU-funded LA3NET network and pursue my PhD with University of Liverpool. During this period, I received lots of PhD training including attending many international workshop and conference to present my work and discuss with other collaborators, which improves my soft skills in the research area. In addition, he always encourages me to work hard on completing my PhD project. I really appreciate all his contributions of time, ideas, and funding to make my PhD experience productive and stimulating.

I would like to express my thanks to my second supervisor, Dr. Steven Jamison, for his tremendous academic support during my PhD study. I really learned a lot every time when I discussed with him on my projects. His guidance and comments helped me in all the time of research and paper writing.

Besides my supervisors, I would like to thank all the QUASAR group members for their kind help and accompany. Thanks to Dr. Mark Ibison for his carefully proof reading all the original manuscripts and PhD thesis. Thanks to Dr. Javier Resta-Lopez for his strong support on my reference letters which are used for my job applications. Thanks to all the other QUASARs for their kind help on my Schengen visa issues I suffered in 2017. Finally I managed to solve this issue and got the visa to visit Paul Scherrer Institute (PSI), Switzerland for the collaborative experimental studies.

My sincere thanks also go to Dr. Guoxing Xia, Dr. Kieran Hanahoe, Yangmei Li and Jonathan Smith for their help in the programming. They provided me with an opportunity to join the simulation studies on the beam-driven plasma wakefield accelerator. Without their precious support it would not be possible for me to conduct such a research.

I am very grateful to researchers in PSI, Switzerland, Dr Rasmus Ischebeck, Dr. Micha Dehler, as well as the entire beam diagnostics group members for their support and assistance in designing and performing the beam experiments, Dr. Soichiro Tsujino and Dr. Mahta Monshipouri for their effort on the fabrication studies for dual-grating microstructures.

I would like to thank all the Chinese colleagues in the Daresbury laboratory, Dr. Xiaojun Gu, Dr. Xiaohu Guo, Dr. Jianping Meng, Dr. Jian Fang, Dr. Wei Wang, Dr. Kai Liu, Dr.

Zijian Li, Dr. Hao Zhang, Dr. Rui Pan, Dr. Sihui Wang, Dr. Yong Ma, Dr. Jie Wang, Dr. Yuchen Yang, Weidan Ni, Yangmei Li. I really enjoyed the funny discussions with you guys in the lunch time and the parties you organized. Time flies and our friendship last forever.

I would like to thank all the mates in the Daresbury table tennis club, Norbert Collomb, Dr. Sue Smith, Dr. Xiaojun Gu, Dr. Xiaohu Guo, Dr. Sebastian Metz, Brenda Owen, Phil Lingwood, Maurice Willis, Helena Dennett, Alan Brown, Jo Carter, Weidan Ni. I really enjoyed every game and practise with you, being a precious memory in my heart forever.

I would like to thank all the friends in the Liverpool Chinese Gospel Church, Tianbing Huang, Yawen Zheng, Dr. Yannan Jin, Dr. Jin Zhou, Nan Zhi, Zhouxiang Fei, Cheng Shen, Xiaohuai Hao, Xinyang Li, Jingwen Li, Dan Wang, Xiaoxue Huang, Yanli Hu, Qi Chen. I really experienced a good time with you in Liverpool.

I would like to thank all the friends I made in the UK in the past few years.

Finally, I would like to thank my parents, family and my wife (Dr. Yanfen Xiao) for their support and understanding throughout this journey.

Table of Contents

List of Figures

List of Tables

Acronyms

AD	Angular Dispersion
AE	Accelerating Efficiency
AF	Accelerating Factor
ASTA	Advanced Superconducting Test Accelerator
CLARA	Compact Linear Accelerator for Research and Applications
CPA	Chirped Pulse Amplification
CST	Computer Simulation Technology
DBR	Distributed Bragg Reflector
DE	Decelerating Efficiency
DF	Decelerating Factor
DLA	Dielectric Laser-driven Accelerators
DTA	Dielectric THz-driven Accelerators
EMC	Electromagnetic Compatibility
EMI	Electromagnetic Interference
FDTD	Finite Difference Time Domain
FEL	Free Electron Laser
FEM	Finite Element Method
FWHM	Full Width at Half Maximum
Linac	Linear Accelerator
LML	Lower Mesh Limit

LPW	Lines Per Wavelength
LPWA	Laser Plasma Wakefield Accelerator
MAL	Matched Absorbing Layer
MAP	Micro-Accelerator Platform
MLRL	Mesh Line Ratio Limit
MMA	Methyl Methacrylate
OTR	Optical Transition Radiation
PCB	Printed Circuit Boards
PFT	Pulse-Front-Tilted
PIC	Particle In Cell
PML	Perfectly Matched Layer
PMMA	Poly Methyl Methacrylate
PSI	Paul Scherrer Institute
RF	Radio Frequency
RIE	Reactive Ion Etching
RMS	Root Mean Square
SEM	Scanning Electron Microscope
SLAC	Stanford Linear Accelerator Center
SSTF	Simultaneous Spatial and Temporal Focusing
TE	Transverse-Electric
TM	Transverse-Magnetic

1. Introduction

The purpose of this chapter is to introduce the background and motivation of dual-grating dielectric laser-driven accelerators (DLAs). Section 1.1 of this chapter reviews conventional Radio-Frequency (RF) accelerating structures and the limitations on their accelerating gradient. With the development of laser technology, laser-driven particle acceleration schemes with accelerating gradients higher than 1 GV/m are considered to be one of the most promising candidates to reduce the size and cost of future particle accelerators. One such scheme is the laser plasma wakefield accelerator (LPWA) which has been demonstrated to generate acceleration gradients higher than 100 GV/m. Section 1.2 presents the working principle, applications and challenges for laser plasma wakefield accelerators. Section 1.3 introduces DLAs 'on a chip', including high quality particle sources and different dielectric laser-driven accelerating structures. The experimental studies and potential applications of DLAs are also described in Section 1.3. Section 1.4 describes the motivation of this thesis and outlines the structural layout of this thesis.

1.1 Conventional Radio-frequency Accelerators

Charged particles can be accelerated by either static or oscillating electromagnetic fields. In electrostatic accelerators [1]–[3], charged particles are accelerated by a static electric field. But such accelerators are limited to about 30 MV by the voltage hold-off across ceramic insulators used to generate the high voltages. It is followed by a particle accelerator operating with oscillating fields with a phase velocity equal to the particle's velocity and an electric field component parallel to the particle's velocity. Compared to electrostatic accelerators, the maximum achievable energy in such an acceleration scheme is not limited by high-voltage breakdown.

Oscillating field particle accelerators can be either circular or linear. In circular accelerators (cyclotrons, betatrons and synchrotrons), charged particles are accelerated in a circular orbit and emit synchrotron radiation. For electrons, which have a much smaller mass than protons, their energy loss is much larger than that of protons because the radiation loss scales with $1/m_0^4$ [4], [5], which limits the maximum achievable final energy for such accelerators. In linear accelerators on the other hand, charged particles are accelerated in a straight line with negligible radiation losses [4], [5]. The largest linear accelerator, which is

located at the Stanford Linear Accelerator Centre (SLAC), is about 3.2 kilometres long and can accelerate electrons and positrons up to 50 GeV [6].

Linear accelerators usually work with normal (metal) or superconducting (niobium) radio-frequency (RF) structures. The normal conducting RF structures operate at gradients of 20~50 MV/m and a maximum gradient of up to 100 MV/m has been demonstrated [7], [8]. High gradients of up to 50 MV/m [9] have been achieved for superconducting cavities. Accelerating gradients for RF-cavity-based accelerating structures such as these are severely limited by RF-induced metal surface breakdown [10]–[12]. Figure 1 shows a X-band accelerating structure which has been demonstrated to generate an accelerating gradient of 100 MV/m and Figure 2 shows a superconducting 1.3 GHz 9-cell cavity for the TESLA Test Facility, which demonstrated an accelerating gradient of 25 MV/m at a quality factor $Q_0 \geq 5\times10^9$. However, the major challenge for the conventional accelerator is its size: long accelerating structures are necessary to produce high-energy electron bunches. For example, in order to generate a 100 GeV electron beam, an accelerating structure of 1-10 kilometers is required, which can cost billions of pounds [13], [14].

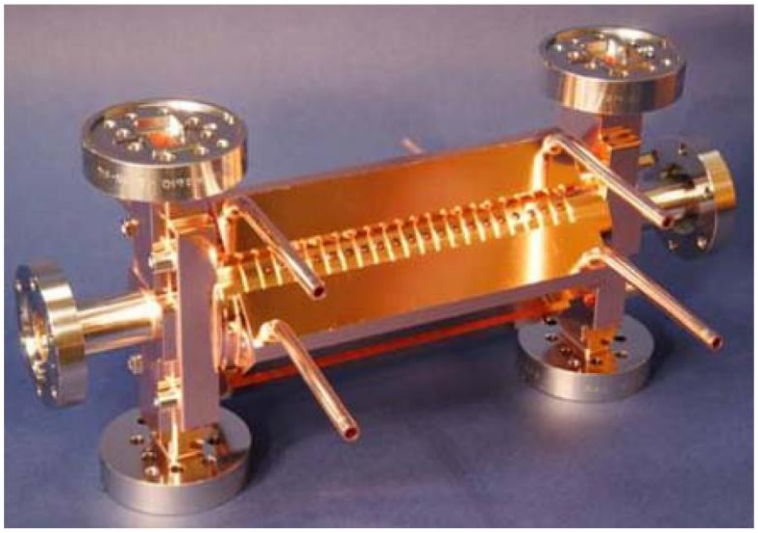

Figure 1. High gradient X-band accelerating structure with a gradient of 100 MV/m [7], [8].

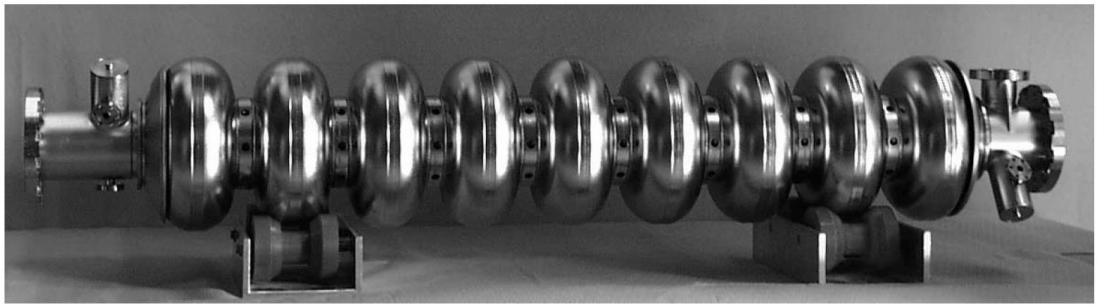

Figure 2. Superconducting 1.3 GHz 9-cell cavity for the TESLA Test Facility [15].

1.2 Laser Plasma Wakefield Accelerators

In order to miniaturize future particle accelerators, advanced acceleration technologies are being studied. One such technology is laser plasma wakefield accelerators (LPWAs) which demonstrated accelerating gradients higher than 100 GV/m [16]. Such LPWAs were originally proposed by Tajima and Dawson [17] in 1979. When an intense laser beam is used to interact with a plasma, as shown in Figure 3, the rising edge of the laser pulse envelope pushes away the background plasma electrons through the laser ponderomotive force. The ions are much heavier than the electrons and so do not respond to the ponderomotive force. Once the laser pulse has passed, the electrons are dragged back towards their original positions by the space charge field. In this situation, a plasma oscillation is formed. As the laser pulse moves forward through the plasma this oscillation sets up a plasma wave travelling with a phase velocity equal to the group velocity of the laser pulse. Once established, the plasma wave can then grow until wave-breaking occurs [18], [19]. This happens when, at very large plasma wave amplitude, the wave motion becomes so nonlinear that wave energy is transferred directly into particle energy. For LPWAs, the minimum laser intensity needed to drive a suitable plasma wave is of the order of > 10^{18} W/cm^2 [20]. Such intense laser pulses could not be produced until 1985 due to the damage threshold for laser amplifying crystals, when Strickland and Mourou [21] successfully realized the chirped pulse amplification (CPA) laser technique, resulting in the production of laser pulses with intensities of 10^{18}-10^{20} W/cm^2. The implementation of CPA triggered significant experimental progress for laser plasma wakefield accelerators.

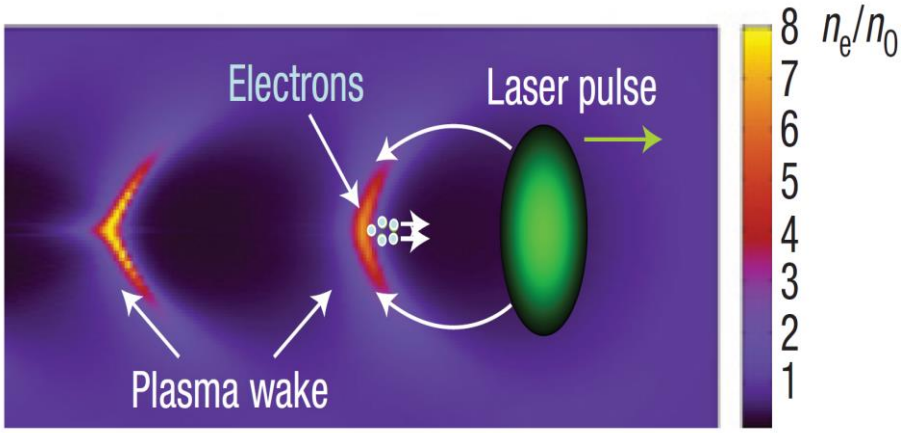

Figure 3. A schematic diagram for a LPWA [22], [23], where n_e and n_0 represent electron density and plasma density, respectively.

LPWA experiments [19], [24]–[27] prior to 2004 have demonstrated accelerating gradients > 100 GV/m, accelerated electron energies > 100 MeV, and accelerated bunch

charge > 1 nC. However, the quality of the accelerated electron bunch was lower than desired. This situation was dramatically changed in 2004 when three groups from the UK, USA, and France reported the production of high beam quality for LPWAs. Specifically, Mangles *et al.* [28] observed a 70 MeV monoenergetic electron beam with a small energy spread of < 3%, Geddes *et al.* [29] demonstrated the production of electron beams with an energy spread of 2%, 3 mrad divergence and increased energy (more than 10^9 electrons above 80 MeV) by using a preformed plasma density channel to guide a relativistically intense laser, resulting in a longer propagation distance; and Faure *et al.* [30] realized extremely well-collimated beams with 10 mrad divergence and 0.5 ± 0.2 nC charge at 170 MeV. These experimental studies show that it is possible to generate beams of relativistic electrons characterized by a significant charge of ≥ 100 pC, at a high mean energy of ≥ 100 MeV, with small energy spread (approximately a few percent) and low divergence (approximately a few milliradians), through careful control of the laser and plasma parameters, an improvement of diagnostic techniques, an extension of the laser propagation distance through the plasma, and the matching of the acceleration length to the dephasing length. Recently, LPWAs have successfully demonstrated the generation of GeV electrons in a cm-scale gas-filled capillary-discharge waveguide using a 40 TW Ti: Sapphire laser [31], and electron bunches with a spectrum prominently peaked at 2 GeV with only a few percent energy spread and unprecedented sub-milliradian divergence, by applying new petawatt laser technology [32]. These results open the way for a future compact TeV electron-positron collider, which can be seen in Figure 4. However, such LPWAs require a massive laser system with enormous costs, and suffer the instability of plasma generation and the low repetition rate of high-power laser pulses.

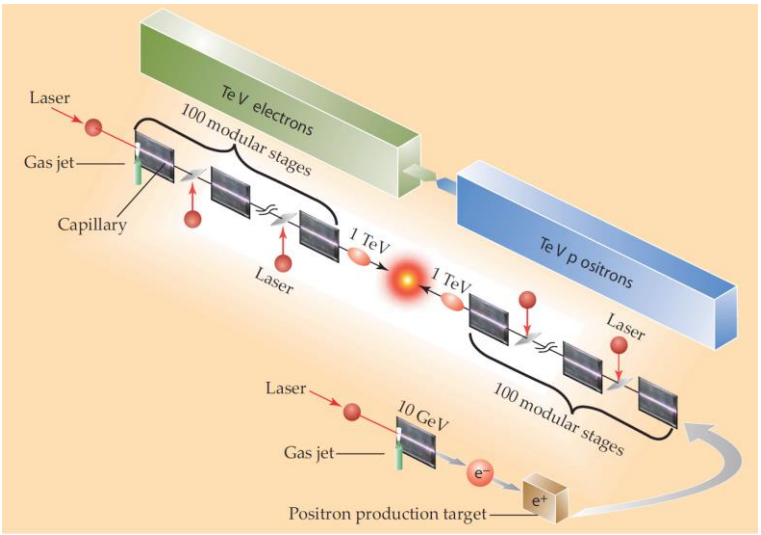

Figure 4. Schematic diagram of a TeV electron–positron collider based on LPWA [33].

1.3 Dielectric Laser-driven Accelerators

Besides LPWAs, the approach to accelerate charged particles using a laser is the abrupt termination of an incident field at a boundary [34]. Experimental demonstrations have been made for acceleration of electrons by laser pulses at single-boundary structures, evading the Lawson-Woodward theorem [35], [36]. Such structures may prove useful as a diagnostic of femtosecond (and shorter) electron-photon interactions [37]–[39], however they present practical difficulties in staging as a high-gradient laser-driven linear accelerator. Then several early proposals employing open structures were based on reflective (all-metallic) gratings, employing a wavelength-scaling of existing linear accelerator designs [40]–[42]. The acceleration mechanism employed in those demonstrations was the inverse Smith-Purcell effect [43]. However, these metallic gratings suffer a low damage threshold, which is not suitable for high gradient accelerators.

An alternative way to realize compact, low cost particle accelerators is to use optical scale dielectric structures, which can withstand electric fields roughly 2 orders of magnitude higher than metals at optical frequencies. Some dielectric materials have a high field damage threshold in the range of ~ 10 GV/m, and together with large electric fields from ultra-short laser pulses, they enable a new acceleration scheme of dielectric laser-driven accelerators (DLAs) which support accelerating gradients up to several GV/m. There are many advantages for such DLAs: first of all, these robust dielectric structures can be mass-fabricated using existing nanofabrication technologies, allowing much more stable acceleration of electrons than plasma-based accelerators. Secondly, a solid-state laser system can be used to drive the electrons in such dielectric structures with a much lower energy and higher repetition rate than LPWAs. These advantages greatly promote the development of DLAs. However, near-infrared laser wavelength is usually in the range of hundreds of nanometers to several micrometers, thereby resulting in short wavelength operation for DLAs. Many DLA stages are therefore needed to accelerate electrons from tens of keV to relativistic regime. Due to the short NIR wavelength, phase matching between the electromagnetic field and electrons, space charge effects, and limited bunch charge present challenging hurdles for DLAs. This is completely different from conventional RF-cavity-based accelerators which utilize DC or RF gun to accelerate electrons emitted from photocathodes from non-relativistic energy to relativistic regime. Conventional DC guns reach their performance limit at 10 MV/m due to field emission breakdown [44], while RF guns operate below 120 MV/m due to plasma breakdown limitations [45].

As illustrated in Figure 5, the basic conceptual layout for an integrated optical accelerator, based entirely upon DLAs and compatible optical elements, can be divided into three main components: a particle source, a tapered non-relativistic accelerating structure, and a relativistic accelerating structure. These components will be described in the following sections. The power distribution scheme can be envisioned as an input coupler which brings a pulse from an external fiber laser onto the integrated chip, distributes it into multiple structures via guided wave power splitters, and then recombines the spent laser pulse and extracts it from the chip via an output coupler [46], after which the laser power is either dumped, or for optimal efficiency, recycled.

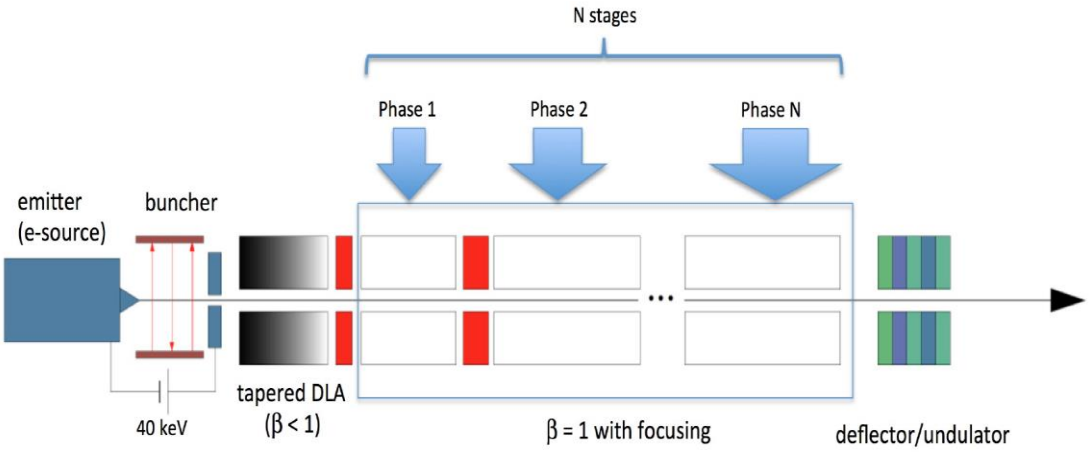

Figure 5. Conceptual schematic of an integrated optical accelerator based on DLAs including source, buncher, tapered non-relativistic accelerating section and relativistic accelerating section with periodic focusing elements (shown in red) [14]. A deflector/undulator section is added to disperse the beam for X-ray or XUV generation.

1.3.1 Particle Sources

One aspect of DLAs that is significantly different from RF accelerating structures is that the transverse aperture for DLAs is of the order of ~1 μm [47], [48] in order to generate GV/m gradients. Thus, the injection of an external beam into DLAs requires an ultrashort bunch length, a sub-micron spot size and an ultralow transverse emittance of the order of 1 nm-rad. This is well below the standard operating conditions for copper photocathodes used in most particle accelerator facilities.

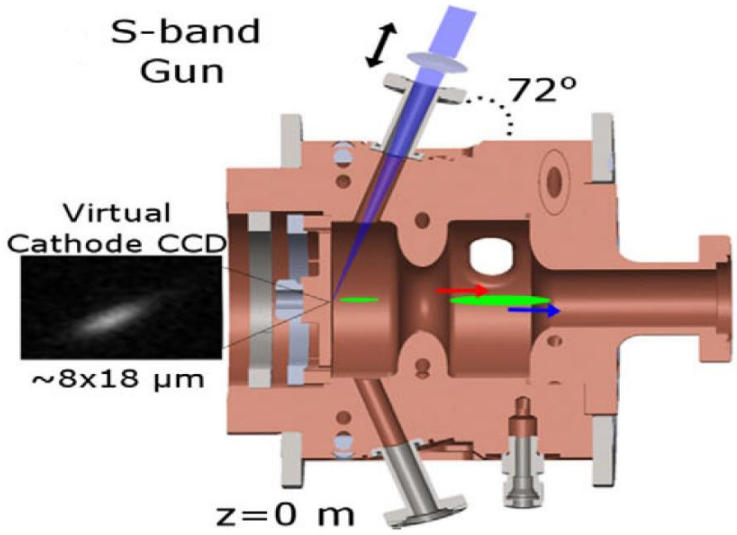

Figure 6. The layout of a conventional RF flat photocathode to generate ultrashort bunch lengths, ultralow transverse emittances and ultralow charges [49].

An attractive method to produce short bunch lengths is through a conventional RF flat photocathode, as shown in Figure 6, which has been demonstrated to produce electron beams with an ultralow normalized emittance (< 50 nm) and ultralow charge (0.1-1 pC) by shaping and focusing the laser pulses to small transverse sizes [50] on the photocathode. Such electron beams can be compressed using velocity bunching to a longitudinal waist of <10 fs and a transverse emittance of 5 nm [49], which would be well-matched to DLA structures driven by a 2 μm laser (6.7 fs) with micron scale transverse apertures. Simulations have shown that such sources could be implemented with an accelerator lattice including skew quadrupole magnets in order to produce 'ribbon' electron beams with a high transverse emittance ratio. Such electron beams can be used for injection into dual-grating DLAs.

An alternative particle source can be generated through direct-current (DC) thermal emission from a Scanning Electron Microscope (SEM). Such electron sources have been successfully employed in many DLA experiments [51]–[53]. A desirable feature of these electron sources is their low electron energy spread (< 10 eV), and sub-100 nm beam waist that can be positioned with nm-accuracy. However, the low emission rate leads to very small electron-laser interaction probability in the DLAs; hence detection of accelerated electrons would be accomplished by integrating over many laser pulses.

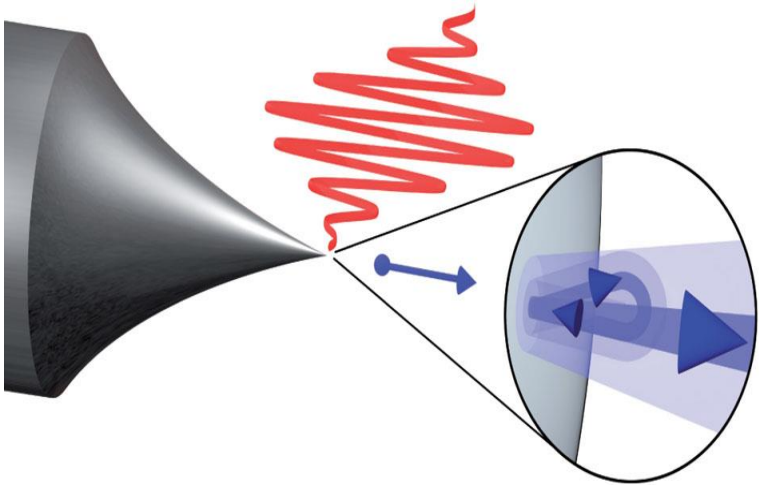

Figure 7. Overview of a laser-triggered electron source from a sharp tungsten tip, where electrons are indicated in a blue colour and a few-cycle laser electric field in red, respectively [54].

Particle sources could also be the emission from laser-triggered metal nanotips. As shown in Figure 7, a linearly-polarized laser beam which consists of few-cycle laser pulses is focused on the apex of a tungsten tip with a radius of ~10-20 nm. In this situation, the electric field at the tip's apex is around five times higher than in the laser focus alone, corresponding to a 25-fold increase in intensity. Due to this field enhancement, electron emission is limited to a single well-defined site with a diameter of ~10nm, on the tip's apex. As this is much smaller than the focal diameter of the laser beam, the laser intensity can be well-approximated as constant over the electron emission area. Thus electrons are emitted from a single nanometre-sized area exposed to a well-defined laser intensity. Such tungsten tips have been demonstrated to emit femtosecond electron bunches with sub-nanometre transverse emittances [55]–[58]. It is found that these sources can be well-suited to experimental studies on DLAs.

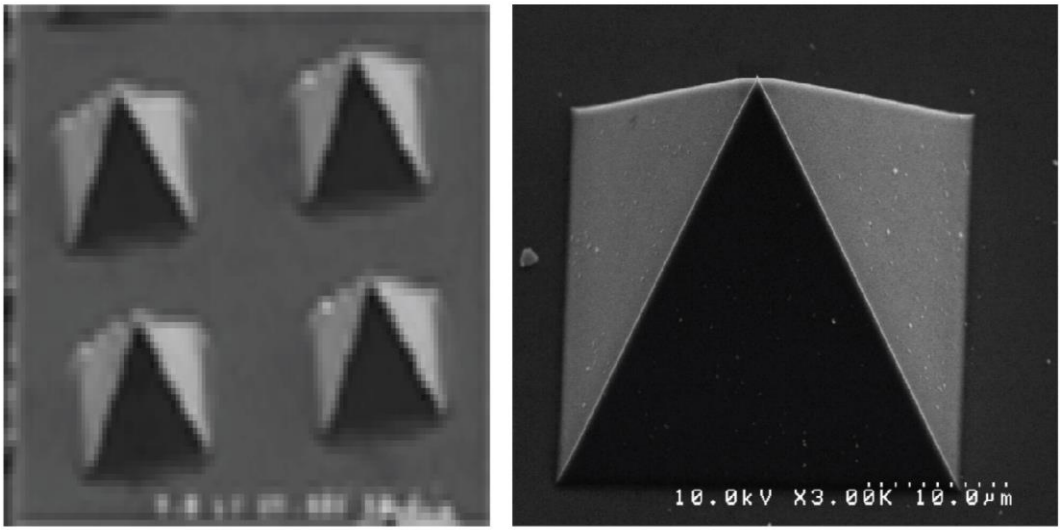

Figure 8. SEM images of diamond tips field emitter array under different magnifications [59].

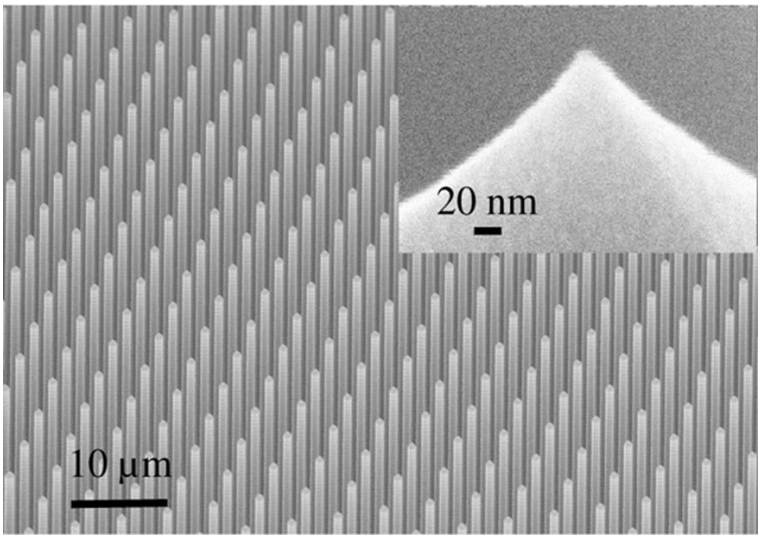

Figure 9. SEM images of silicon tips field emitter array under different magnifications [60].

Nano diamond and silicon tips are a new type of electron source which is under consideration. Figure 8 and Figure 9 are SEM images of these nanotips. Diamond tip arrays have demonstrated low transverse emittance beams under field emission [59]. New research is still needed, however, to characterise the emittance of photoemitted electrons from diamond tips before they can be used as an electron injector for DLAs, while silicon tip arrays have demonstrated electron beams with small emittance and spot size under photoemission. In order to characterise various nanotip sources, an emittance diagnostic has also been developed [61]. Using electrostatic focussing, the transverse distribution of emitted electrons is imaged at a downstream screen.

In conclusion, a particle source with an ultrashort bunch length, a sub-micron spot size and an ultralow transverse emittance of the order of 1 nm-rad is a critical component for DLAs. Further research efforts are still required to investigate the integration of nano-tip emitters with accelerating structures on the same wafer, which could pave the way to realizing an optical particle accelerator on a chip.

1.3.2 Dielectric Accelerating Microstructures

To date, many dielectric laser-driven accelerating structures have been proposed, with some specific designs being three dimensional (3D) woodpile structures [62]–[67], two dimensional (2D) photonic band-gap structures [68]–[71], one dimensional (1D) photonic band-gap structures [72]–[78], and grating-based structures [47], [48], [51]–[53], [79]–[82]. These DLA structures operate by laser-induced excitation of an electromagnetic field mode with a nonzero electric field component parallel to the velocity of electrons traversing the mode. The phase velocity of the excited mode and the electron velocity have to be

synchronized for interaction over a long distance. These DLA structures will be described in detail in the following sections.

(1) 3D Woodpile Structures

Woodpile structures are based on a well-established 3D photonic crystal lattice designed to provide a complete photonic band gap in a structure with a straightforward fabrication process. The lattice consists of layers of dielectric rods in vacuum, with the rods in each layer rotated 90^0 relative to the layer below and offset by half a lattice period from the layer two below, as shown in Figure 10 (a). An accelerating waveguide can be formed by removing all dielectric material in a region which is rectangular in the transverse dimensions, and extends infinitely in the beam propagation direction. Similar to photonic band-gap structures, such a waveguide can be used to confine a speed-of-light accelerating TM mode while allowing non-accelerating modes to leak out of the waveguide. In addition, in order to avoid deflecting fields in the accelerating mode as shown in Figure 10 (b), the structure is made vertically symmetric by inverting the upper half of the lattice so that it is a vertical reflection of the lower half.

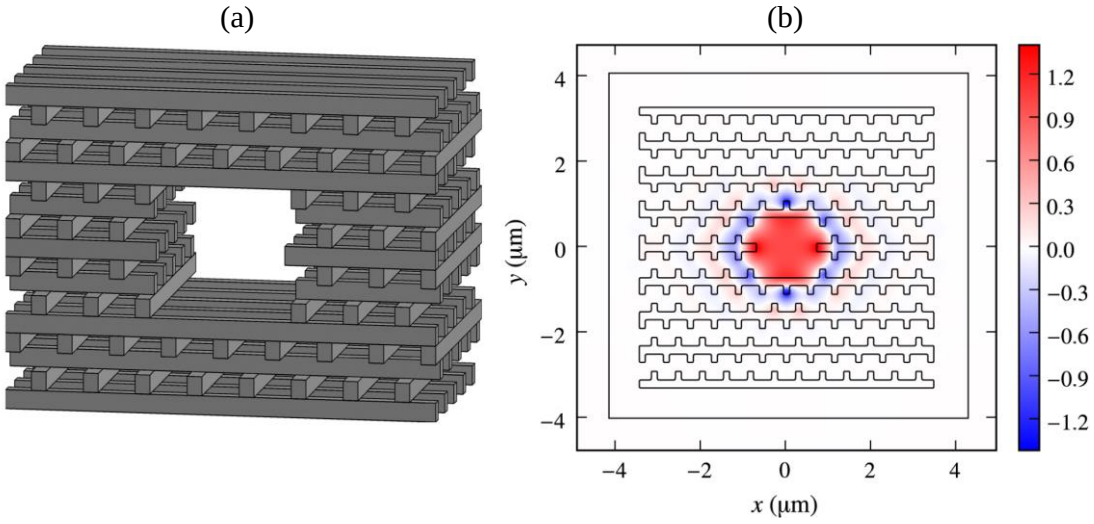

Figure 10. (a) The geometry of a woodpile accelerating structure, and (b) the accelerating field seen by a speed-of-light particle, averaged over a lattice period, normalized to the accelerating field on axis, shown with structure contours for a transverse slice at z = 0 [63].

Researchers from SLAC have demonstrated numerically an efficient silicon-guide-based side coupler which can couple near 100% laser power into a 3D photonic crystal waveguide for acceleration of relativistic charged particles. Such a coupler launches a full travelling-wave propagation of the accelerating mode, which maintains its propagation quality over long waveguide structures, and provides better tolerance of the structure fabrication uncertainty and material breakdown than standing-wave coupling. Simulations also show that an unloaded gradient of about 300 MV/m can be expected for silicon woodpile

structures. Such woodpile structures have been fabricated by researchers from SLAC; however, further experimental studies are still required to realize acceleration of particles in these woodpile structures.

(2) 2D Photonic Band-gap Structures

The 2D Photonic band-gap structures has frequency band gaps that are two dimensional in wave-number space. They usually have a periodicity in the transverse dimensions for confinement, and are uniform in the longitudinal dimension. A cylindrical defect can be introduced to the lattice in the form of a large hole in its centre, in which a transverse magnetic (TM) mode is confined to accelerate charged particles. In such a structure, the radius of the lattice holes, the lattice periodicity, the radius of the defect hole, and the permittivity of the material affect the band gap properties. These parameters can be carefully controlled to ensure the TM mode confined in the defect has a phase velocity matching the velocity of accelerated electrons. A prototype hollow-core photonic band-gap structure designed for speed-of-light TM modes has been successfully fabricated with a 12 μm central defect [70], as shown in Figure 11.

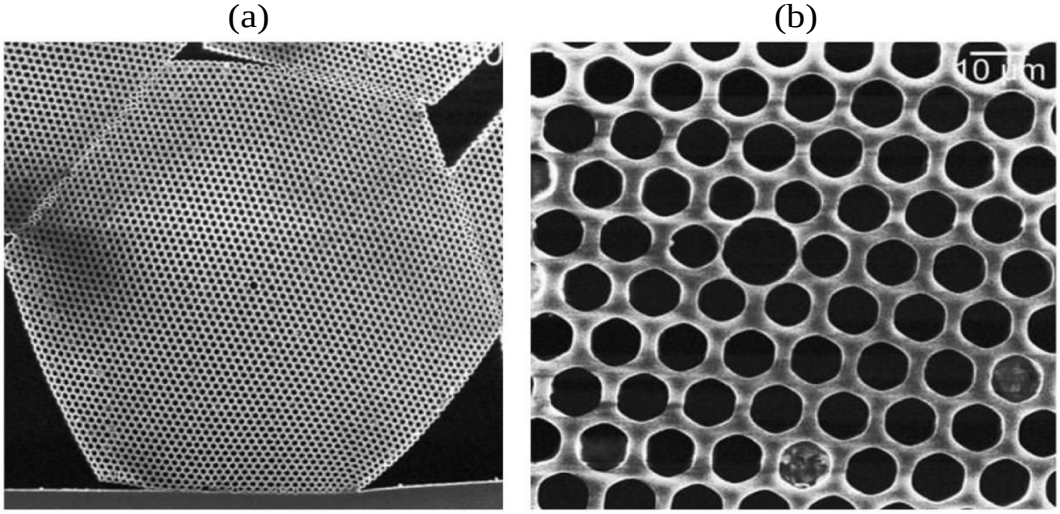

Figure 11. Photographs showing (a) 700 μm-wide cross section of a hollow-core photonic band-gap structure drawn from borosilicate glass, and (b) magnified view of the 12 μm central defect [70].

The radius of the lattice holes, the lattice periodicity, the radius of the defect hole, and the permittivity of the material should be carefully designed in such a way that this confined mode is separated in frequency from other non-accelerating modes which are not confined within the defect hole. Furthermore, such a confined TM mode should have a phase velocity equal to the velocity of injected electrons. Figure 12 shows the longitudinal and radial electric field intensities for the confined mode in the defect hole of the photonic band-gap structure. However, due to the small radius of the defect hole which is limited by the size of

the driven laser wavelength, it is a major challenge to transmit particles of significant charge. Experimental studies for such photonic band-gap structures are still ongoing, although researchers at the SLAC have attempted to excite the TM mode and accelerate electrons in these structures [83].

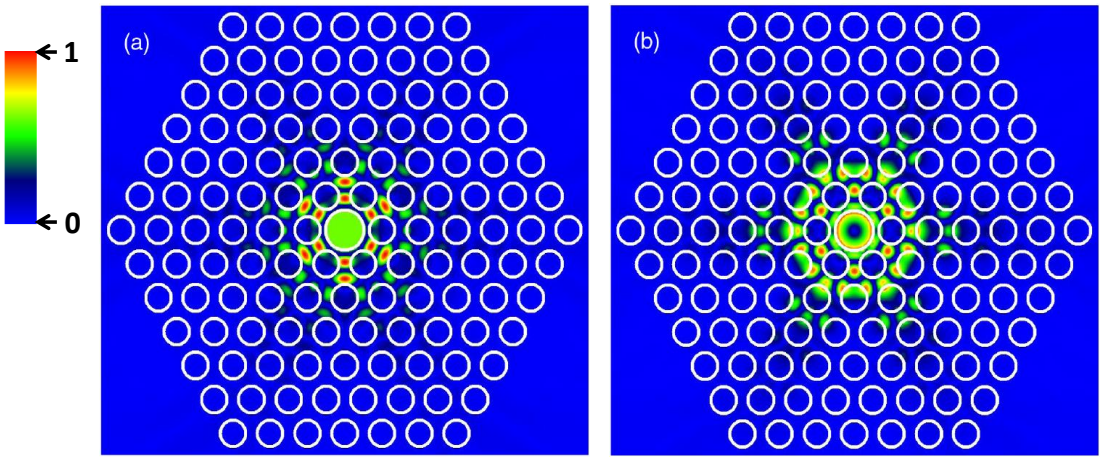

Figure 12. (a) Longitudinal and (b) radial electric field intensities calculated with the multipole method for the defect mode in a photonic band-gap structure [70].

(3) 1D Photonic Band-gap Structures

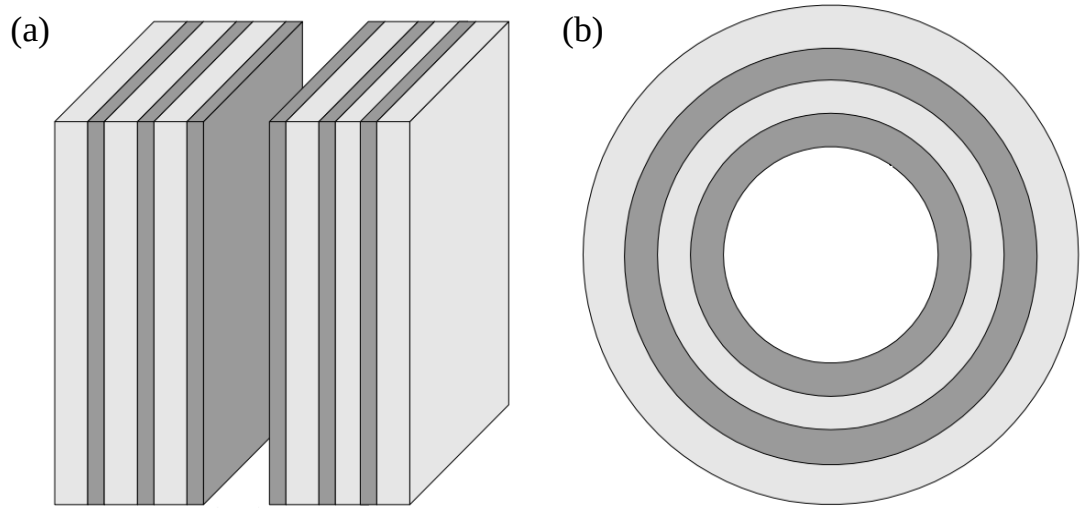

Figure 13. Planar (a) and cylindrical (b) Bragg fiber accelerating structures [72]–[74].

Bragg reflection waveguides are 1D periodic photonic band-gap structures, and they are designed to guide light in a low refractive index medium surrounded by alternating layers of high refractive index. As shown in Figure 13, two kinds of configuration are proposed: one is the planar fiber structure and the other is the cylindrical fiber structure. The theory of Bragg reflection waveguides was developed by Yeh and Yariv [84], [85], and recently there has been a growing interest in using such hollow cylindrical structures as low-loss optical fibers in long distance telecommunications.

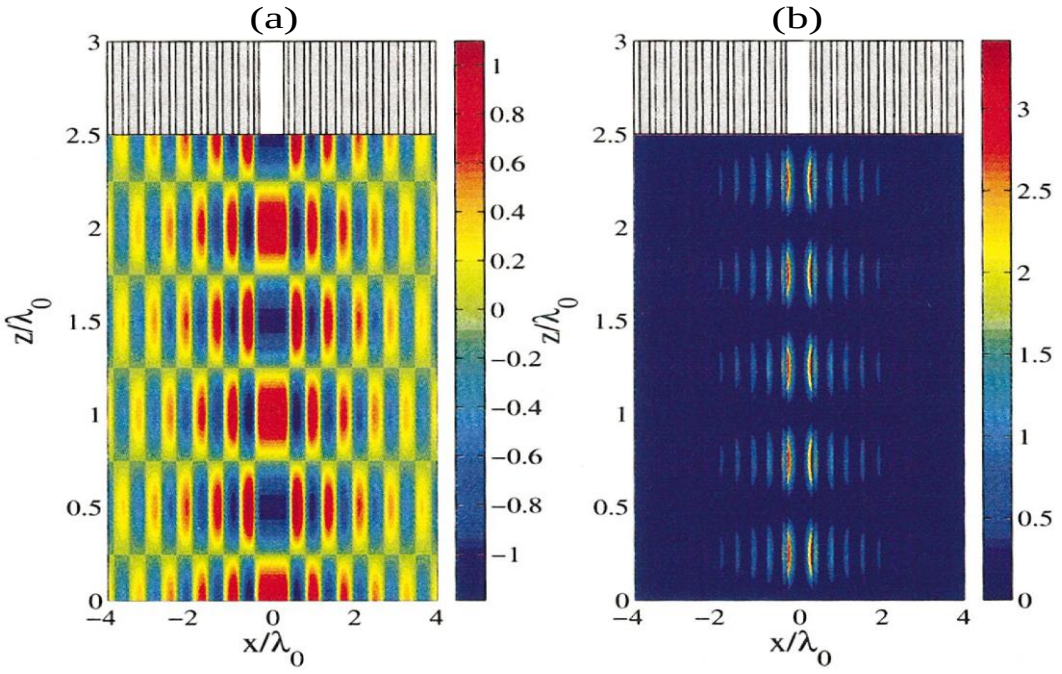

Figure 14. Normalized longitudinal electric field (a) and the Poynting vector (b), normalized by $|E_0|^2/\eta_0$, where η_0 is the vacuum impedance [74], [86]. The electron and laser beam propagate along the *z*-axis, with the vacuum channel centered at $x = 0$.

A Bragg fiber structure consisting of a series of dielectric layers may form an excellent optical acceleration structure. The confinement of the accelerating fields can be achieved, for both planar and cylindrical configurations, by adjusting the widths of each dielectric layer and the number of layers. Figure 14 illustrates the normalized longitudinal electric field and the Poynting vector, which is normalized by $|E_0|^2/\eta_0$ at time t = 0. Such a field can be designed for a given phase velocity which is synchronous with the velocity of the electrons travelling along the *z*-axis in the vacuum channel. It is demonstrated that such a structure made of silica and zirconia may support gradients of the order of 1 GV/m, with an interaction impedance of a few hundreds of ohms and with an energy velocity of less than 0.5c [74]. Here, the interaction impedance is a measure of the accelerating gradient experienced by the electrons for a given amount of power injected into the system, and it is defined by $Z_{\text{int}} = \frac{|\lambda_0 E_0|^2}{P}$, where P denotes the flowing power in the z direction, λ_0 and E_0 are the wavelength and amplitude of the accelerating mode, respectively. In addition, a Bragg fiber structure can also work as a wakefield accelerator [87] in which a short, relativistic electron beam with moderate charge is used to drive the wakefields in the structure. In the case of a relatively small number of layers, the total electromagnetic power emitted is proportional to the square of the number of electrons in the bunch and inversely proportional to the number of bunches; for a cylindrical structure, this power is also

inversely proportional to the square of the internal radius of the structure, and in a planar structure to the width of the vacuum core [74].

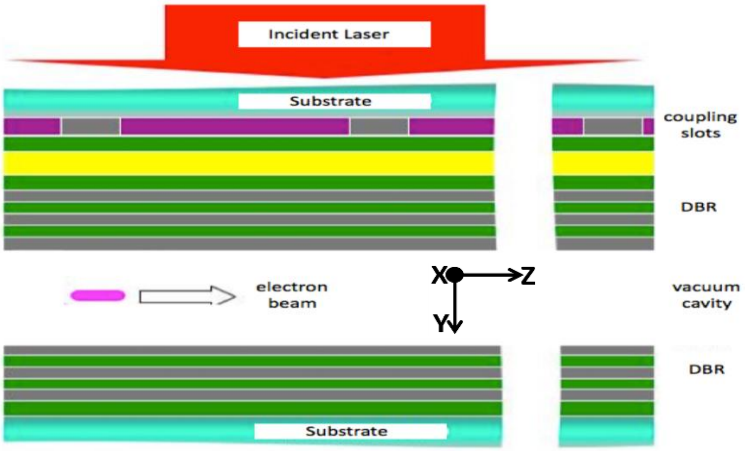

Figure 15. A schematic design of a cross-section of the MAP [75]–[78].

The Micro-Accelerator Platform (MAP) is a minor modification of a Bragg fiber structure. As shown in Figure 15, the difference is that a phase mask, consisting of coupling slots with longitudinal periodicity, is introduced to match the periodicity of the standing wave resonance. These coupling slots are surrounded by a second dielectric material with a lower index of refraction. As the incident laser traverses the coupling slots, the electric field which travels through the slots with a lower refraction index evolves in phase faster than the electric field which travels through the adjacent material with a higher refraction index. After travelling through the matching layers and the top Distributed Bragg Reflectors (DBRs), a standing wave pattern will be generated as shown in Figure 16, with a large longitudinal electric field parallel to the velocity of electrons which are travelling in the vacuum channel gap. In this situation, the MAP is similar to a resonant cavity accelerator and such a standing wave pattern is referring to the resonant or accelerating mode of the MAP.

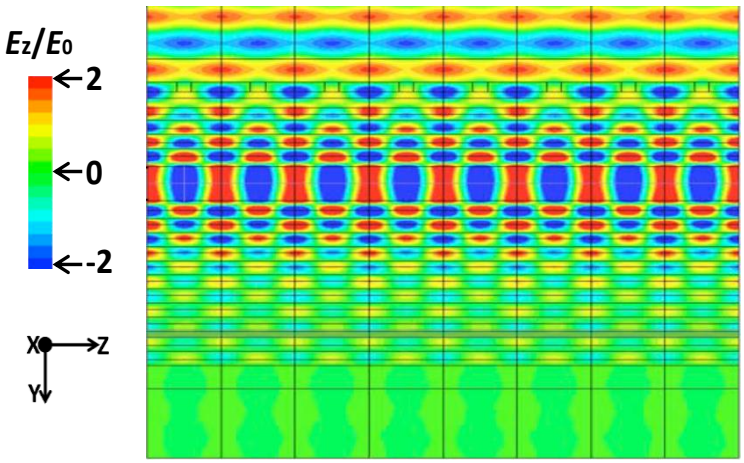

Figure 16. The longitudinal electric field component E_z of the standing wave resonance for a MAP [76]. The incident laser with a field of E_0 is propagating from the top of the image to the bottom.

As shown in Figure 15, a DBR for a MAP consists of two dielectric materials in alternating layers. By setting each layer thickness to one quarter of the wavelength of the standing wave mode being confined, each dielectric interface reflects back that mode in such a way that the cumulative effect of the DBR is to serve as a mirror for a mode at the designed wavelength. The reflection coefficient of the DBR increases for a larger difference between the refractive indices of these two materials. Thus, high contrast materials are desirable to effectively confine the standing wave mode in the vacuum channel gap. Furthermore, the reflection coefficient also increases as the number of alternating layers increases. In addition, it should be noted that the number of layers in the top DBR (the set of alternating dielectric layers above the vacuum channel gap) is less than that in the bottom DBR (the set of alternating dielectric layers below the vacuum channel gap). On the one hand, the top DBR needs to be transmissive enough to let the incident laser wave travel through, but reflective enough to confine the standing wave mode in the vacuum channel gap beneath it. On the other hand, a bottom DBR with a larger number of layers is desirable so as to effectively confine the standing wave mode in the vacuum channel gap.

(4) Grating-based Structures

These 3D, 2D, and 1D photonic band gap accelerators are designed to satisfy the speed-of-light velocity condition for the travelling wave being an accelerating mode. However, due to the natural group-velocity dispersion of the structure, the speed of the pulse envelope is seriously compromised and is lower than c which is speed of light. This results in a rapid slippage of the pulse envelope over a finite waveguide distance that is not much longer than the laser pulse length itself. In order to eliminate this pulse-slippage problem, grating-based structures based on the periodic electric field reversal was proposed by Plettner *et al*. [79]. They can be single-gratings, or dual-gratings consisting of two single-gratings facing each other. Such grating-based structures have a simpler geometry than other types of DLA, which reduces the complexity and expense of the fabrication process. Figure 17 illustrates the dual-grating structure and shows the cross-section of the geometry. When the plane wave of a linearly polarized laser beam travels through the structure, the speed of the wave in the vacuum is higher than that in the dielectric grating pillar. This creates a phase difference of π for the wave front in the vacuum channel where electrons are travelling and are periodically modulated along the longitudinal z-axis. To produce the desired phase difference of π, the grating pillar height H should be set to $H = \frac{\lambda_0}{2(n_r - 1)}$, where n_r is the refractive index of the grating material.

The fundamental difference between such grating-based structures and other DLAs is that the acceleration from this structure is not due to trapped accelerating modes. In accordance with the Lawson-Woodward theorem [35], [36], it is the non-propagating near field that provides the synchronous accelerating field and not the incoming free-space wave. The laser pulses generate a series of grating diffraction modes inside the vacuum channel, and phase synchronicity [88] has to be achieved between the spatial harmonics and the particle beam through matching the grating period to the laser wavelength. As indicated in Figure 17, extended overlap of an electron bunch in the structure with the few-cycle laser pulse envelope can be readily accomplished by tilting the pulse fronts. For relativistic particles, a 45^0 pulse-front tilt of the incoming plane wave is required. For non-relativistic particles, the tilt angle is related to the velocities of particles [89] and can be adjusted to ensure the extended overlap.

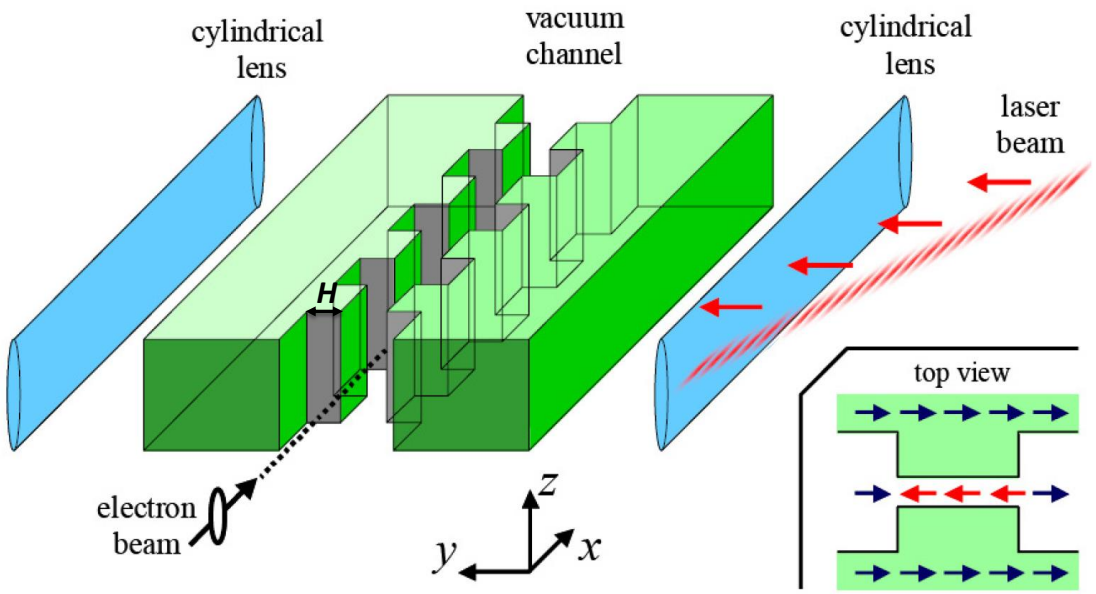

Figure 17. Schematic of a dual-grating structure which is illuminated by a single laser beam [79].

1.3.3 Experiments on DLAs

(1) Dielectric Laser Acceleration of Relativistic Electrons

These proposed DLA structures have been theoretically and numerically demonstrated to generate high accelerating gradients of up to GV/m. However, no successful experimental demonstrations have been observed except with grating-based structures. In 2013, a milestone experiment demonstrating dielectric laser acceleration of relativistic electrons in a fused-quartz dual-grating structure was reported by SLAC [47]. In this experiment, an accelerating gradient of up to 300 MeV/m was observed in a fused silica dual-grating structure. A Ti:Sapphire laser system operating at a wavelength of λ = 800 nm, pulse energy

up to 319 μJ and pulse duration of 2 ps was used as the pumping power and highly relativistic 60 MeV electron bunches were used as the particle source. The interaction length of laser and electrons was estimated at 563 ± 104 grating periods (one grating period was equal to 800 nm). The cross section of a DLA structure and the relevant experimental set up are illustrated in Figure 18.

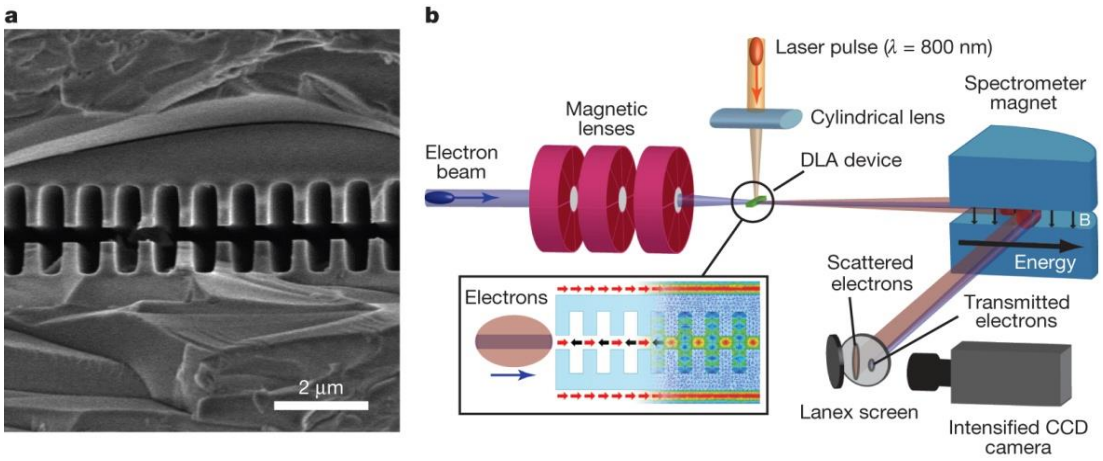

Figure 18. (a) SEM image of a dual-grating DLA structure, and (b) experimental setup [47].

In this experiment, the dual-grating structure has a vacuum channel gap of only 400 nm, which makes beam loading a very challenging task. Particle tracking simulation shows that only 2.2% of the 60 MeV beam can pass through the vacuum channel and be modulated by the laser field. Those electrons travelling through the structure substrate and grating pillars suffer significant energy loss due to collisional straggling [90] in the dielectric material, so they were excluded from Figure 19. This shows only the energy distribution for modulated electrons, with the laser on and off. It can be seen that the laser field efficiently modifies the bunch energy distribution, which is in good agreement with simulation results. In addition, the electron bunch has a RMS length of 129 ± 9 μm, which is much longer than the laser wavelength of 800 nm. Electrons therefore sampled all phases of the laser field, causing some electrons to gain energy from acceleration while some were decelerated.

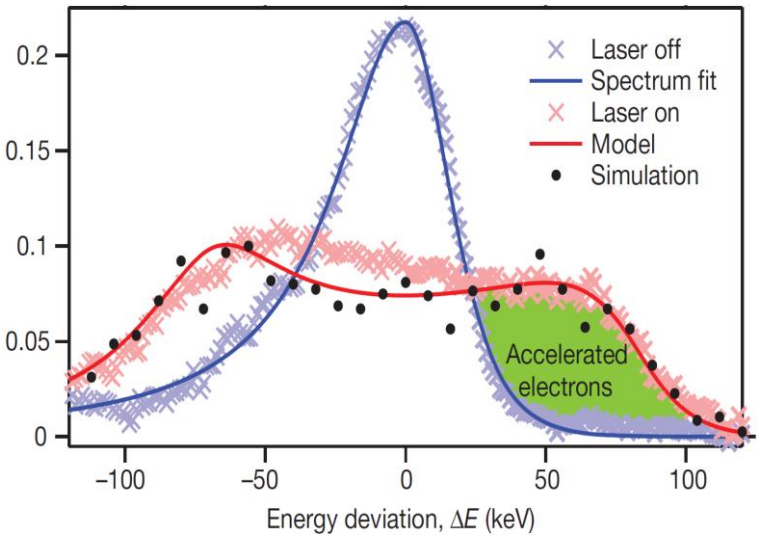

Figure 19. Experimental and simulation results of bunch energy distribution with the laser on and off [47].

It is then followed by another experiment carried out by SLAC in 2016 [48]. A dual-grating structure with the same geometry was also used for this experiment. A Ti:Sapphire laser system operating at a wavelength of λ = 800 nm and pulse duration of 64^{+11}_{-7} fs was used to illuminate a dual-grating structure. The only difference from the earlier experiment is that a femtosecond laser system was used in order to generate an accelerating gradient higher than 300 MV/m. Figure 20 shows the measured and simulated energy distribution for those electrons transmitted through the vacuum channel of the dual-grating structure. The measured maximum energy gain is 24 ± 1.1 keV, corresponding to an accelerating gradient of G = 690 ± 110 MV/m which is a record gradient for DLA experiments to date.

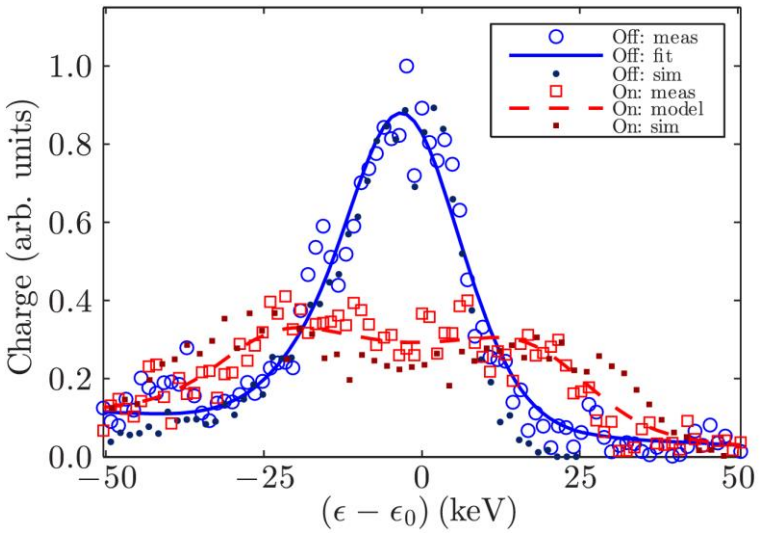

Figure 20. Measured, fitted, and simulated electron beam energy distribution, with the laser off and on [48]. Electrons which traversed the structure substrate and grating pillars were observed to suffer a mean energy loss of 300 keV, and are not shown.

(2) Dielectric Laser Acceleration of Non-relativistic Electrons

In order to realize a particle accelerator 'on a chip', synchonized acceleration between the non-relativistic electrons emitted from the injector and the exciting laser pulses should be achieved. This requires that the transit time of the electrons across a period of the grating structure must be equal to the laser period. Based on this, three experiments have so far been performed for acceleration of non-relativistic electrons in grating-based structures. In 2013, a milestone experiment successfully demonstrated acceleration of non-relativistic electrons in the vicinity of a fused-quartz single-grating structure [51]. In this experiment, a laser beam with a centre wavelength of 787 nm and a pulse duration of 110 fs was used to illuminate a single-grating structure located on top of a mesa, as shown in Figure 21. The grating period of 750 nm was chosen so that the third spatial harmonics travelled synchronously with 28 keV electrons due to a trade-off between the available accelerating gradient and fabrication limitations on the grating period ($\lambda_p > 0.6$ μm). A maximum accelerating gradient of 25 MV/m was observed, which was already comparable with state-of-the-art conventional RF cavity-based accelerators. The parameter dependencies were investigated in detail and had excellent agreement with numerical simulations.

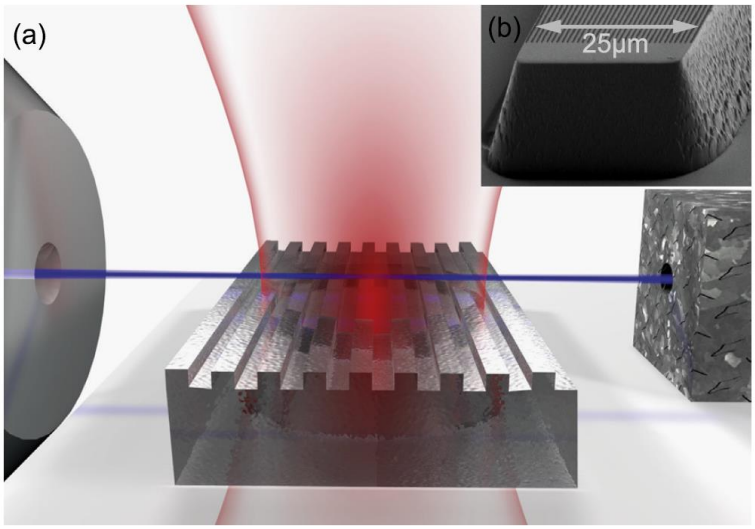

Figure 21. (a) Schematic of experimental setup for acceleration of 28 keV electrons at a fused-quartz single-grating structure, where the electron beam and laser are represented in blue and red colors, respectively; (b) SEM image of a single-grating structure which is located on the top of a mesa with a width of 25 μm [91].

After this, similar successful demonstrations were reported for the acceleration of sub-100 keV electrons by researchers from Stanford University [52], [53]. As shown in Figure 22, a 5 nJ, 130 fs mode-locked Ti-sapphire laser with 907 nm wavelength was used to acclerate 96.3 keV electrons in a silicon single-grating structure with a period of 490 nm. In this situation, the phase synchronicity was achieved between the first spatial harmonics and the electrons. Due to higher accelerating efficiency for the first spatial harmonics, an

accelerating gradient of 218 MV/m [52], higher than the previous 25 MV/m, was obtained. The single-grating structure was then replaced by a dual-pillar structure for acceleration of 96.3 keV and 86.5 keV electrons using the same laser system, which can be seen in Figure 23. Because the dual-pillar structures have a higher accelerating efficiency than the single-grating structures, an accelerating gradient of 370 MV/m [53] was observed, even higher than the 218 MV/m seen earlier. Such a dual-pillar structure can be integrated with a Bragg reflector, which will be studied in Chapter 6.

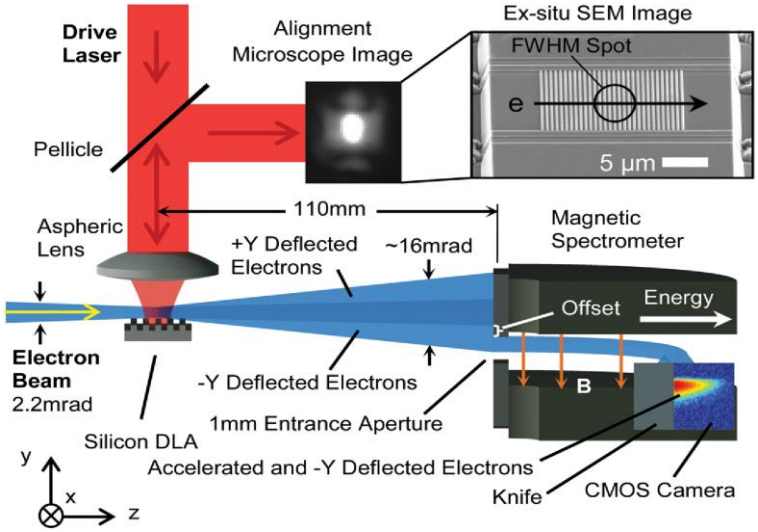

Figure 22. Schematic of experimental setup for acceleration of 96.3 keV electrons at a silicon single-grating structure [52].

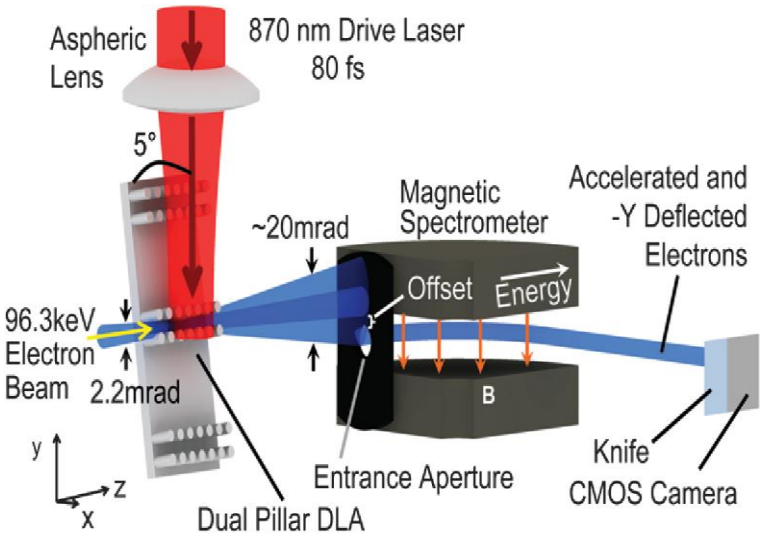

Figure 23. Schematic of experimental setup for acceleration of sub-100 keV electrons at a silicon dual-pillar structure [53].

With the mature lithographic techniques and availability of compact and efficient fiber laser technology, the successful demonstrations of relativistic and non-relativistic electron

acceleration discussed above may pave the way towards an all-optical compact particle accelerator ‘on a chip’.

(3) Damage Threshold Measurement

One major advantage of DLAs is their ability to support accelerating fields 2 orders of magnitude higher than those achieved in conventional RF cavity-based accelerators. The key to sustaining such high accelerating gradients is the much higher damage threshold of dielectric materials compared with metals. The appropriate dielectric material should therefore be chosen to maximize the achievable accelerating gradient. Experimental studies [92]–[94] have been carried out to investigate the damage threshold for different dielectric materials. As shown in Figure 24, researchers at SLAC demonstrated that the quartz material has a damage threshold of 4 J/cm^2 for a 1 ps pulsed laser. Lenzner *et al*. [95] found that the damage threshold for a 1 ps pulsed laser is about twice as large as for a 100 fs pulsed laser, which is also supported by Breuer’s measurement [92]. This indicates that the damage threshold for quartz material is 2 J/cm^2 for 100 fs laser pulses, implying that a peak electric field of the order of 10 GV/m can be sustained in the quartz surface. Quartz material is therefore usually chosen for DLA structures, as has been demonstrated in many DLAs experiments [47], [48], [51]. Figure 24 also shows that silicon has a much lower damage threhold (0.18 J/cm^2) than quartz, corresponding to a peak field of about 3 GV/m. However, silicon may be still chosen to create a resonant-like cavity for many DLA structures, due to its having a higher refractive index [53], [82] than quartz. In addition, silicon can be specifically designed to take advantage of the mass-production techniques of the computer chip industry and so offers a far less expensive way to build a partcle accelerator ‘on a chip’.

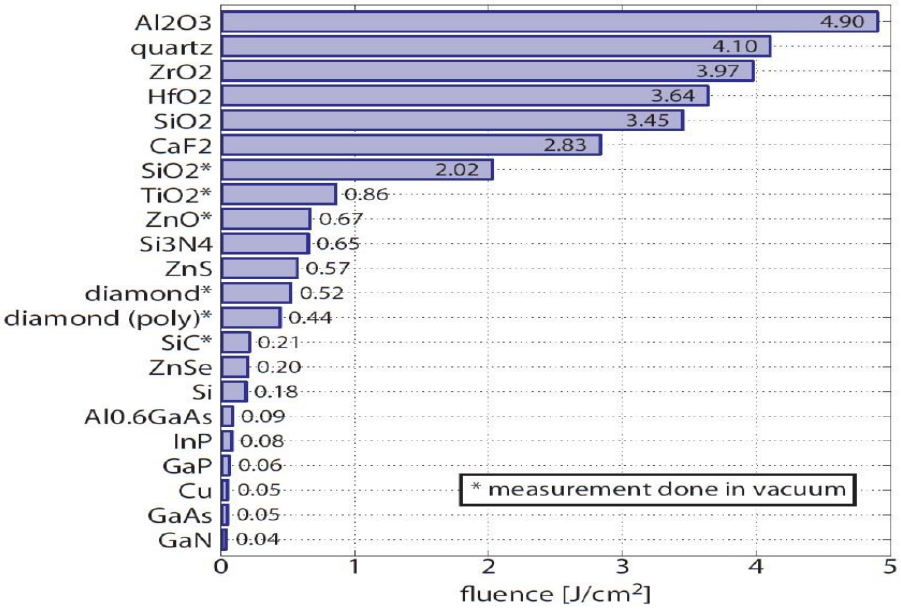

Figure 24. The laser damage threshold of a variety of optical materials, including copper for comparison [94]. Each of these measurements was conducted with a 1 ps, 800 nm, 600 Hz Ti:Sapphire laser.

1.3.4 Potential Applications

DLAs leverage well-established industrial fabrication capabilities and the commercial availability of fibre lasers to reduce cost effectively, while offering significantly higher accelerating gradients and hence a smaller footprint. Such DLAs have many potential applications beyond energy frontier science, including medical therapy, x-ray light sources and high-energy linear colliders.

(1) Medical Therapy

Medically, electron irradiation is used only for skin or superficial treatment due to the energy deposition along the path from the surface, while protons can be used to irradiate tumours deep inside the body. Typical radiotherapy devices operate at electron energies of 6-20 MeV. The generation of such an electron beam usually requires a RF accelerator with a metre-long accelerating structure. The accelerating length is determined by the accelerating gradient, which is limited to 10-20 MeV/m. Furthermore, a metre-long delivery system is used to localize and position the electron beam onto the tumour. The irradiation volume and dose should be tightly controlled, and exposure is typically from multiple directions to avoid damage to normal organs and structures in the body. In order to improve the treatment quality, a series of technological improvements, from intensity-modulated radiation therapy to image-guided radiation therapy, have been developed [96]. However, existing medical electron radiation therapy still suffers from damage to healthy tissue and high operating costs.

With a DLA and an expected accelerating gradient of several GV/m, an accelerating length in the range of millimetres to centimetres can be expected to generate multi-MeV electron beams. In this case one may envision a multi-MeV electron beam generation device of the size of a pen tip. Such a compact source with micron-scale beams could also remove the complicated beam delivery system. Therefore, a whole accelerator system on a millimetre to centimetre scale would enable a DLA-based fibre endoscope [97] for the purpose of tumour irradiation, as illustrated schematically in Figure 25. Such a DLA-based endoscope offers clinicians new forms of minimally-invasive cancer treatment with increased flexibility of use. It could be placed within a tumour site using standard endoscopic methods, allowing it to deliver the same radiation dose as provided by existing medical electron radiation therapy without damage to surrounding tissue. Due to the small exposed volume, an electron current in the range of nA is sufficient to deliver a single massive dose

over an exposure time of the order of 1s, which enables efficient intraoperative electron radiation therapy. The manufacturing and operating costs of such radiation therapy are anticipated to be much lower than those for conventional medical electron radiation therapy.

A DLA-based endoscope therefore has the potential to provide more effective and affordable radiation treatment with fewer side effects and better patient quality of life than current practice. Radiation energy and dose can be electronically controlled by the laser source, which enables the surgeon to treat a wide range of tumour morphologies. Such treatment is ideally suited to the precise and remote control afforded by robotic surgery systems.

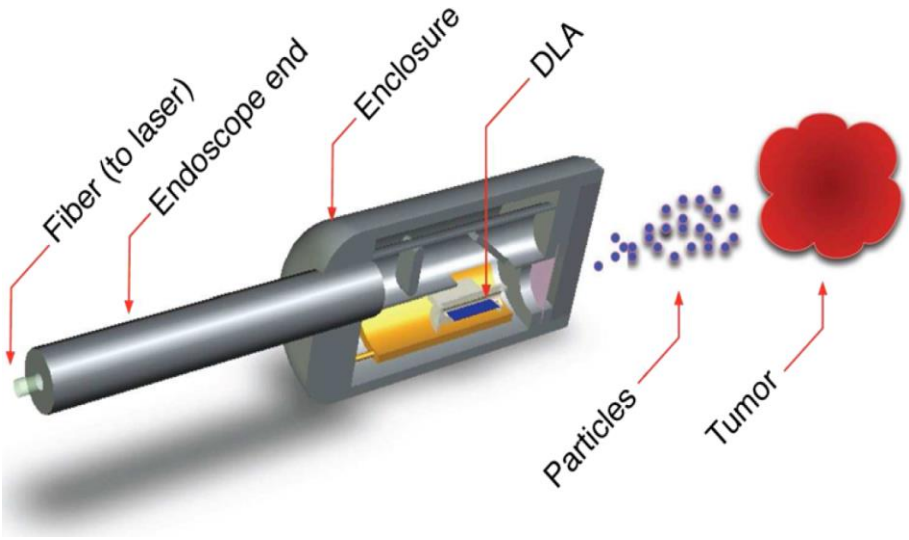

Figure 25. Schematic of a DLA-based endoscope for the purpose of tumour irradiation [97].

(2) X-ray Light Sources

A dielectric laser-driven microstructure can be used to deflect the electron beam to generate x-ray radiation [98]–[102]. As shown in Figure 26, the period of the vacuum channel grooves, denoted by λ_p, is chosen such that its projection onto the electron beam propagation axis equals the laser wavelength, $\lambda_p = \lambda \cos \alpha$. Due to the tilt of the periodic grooves, the electrons travelling along the vacuum channel centre experience a nonzero deflection field from the laser electromagnetic wave. Such a deflecting field should be synchronous with the electron beam. Through appropriate geometry optimizations, a maximum deflecting field can be generated in the channel centre.

Many stages of dielectric deflecting structures can form an undulator, as shown in Figure 27, which can be specifically designed to generate soft and hard x-ray radiation [98], [99]. This allows for an undulator period which is much bigger than the laser wavelength. Numerical studies have demonstrated the generation of 0.01 nm radiation from an undulator

period of 300 μm, with deflecting fields exceeding 1.3 GV/m, equivalent to a magnetic field of ~4 T [99] on highly relativistic (2 GeV) electrons. In addition, such an undulator can be integrated with other DLA components onto an integrated chip, through well-established lithography techniques.

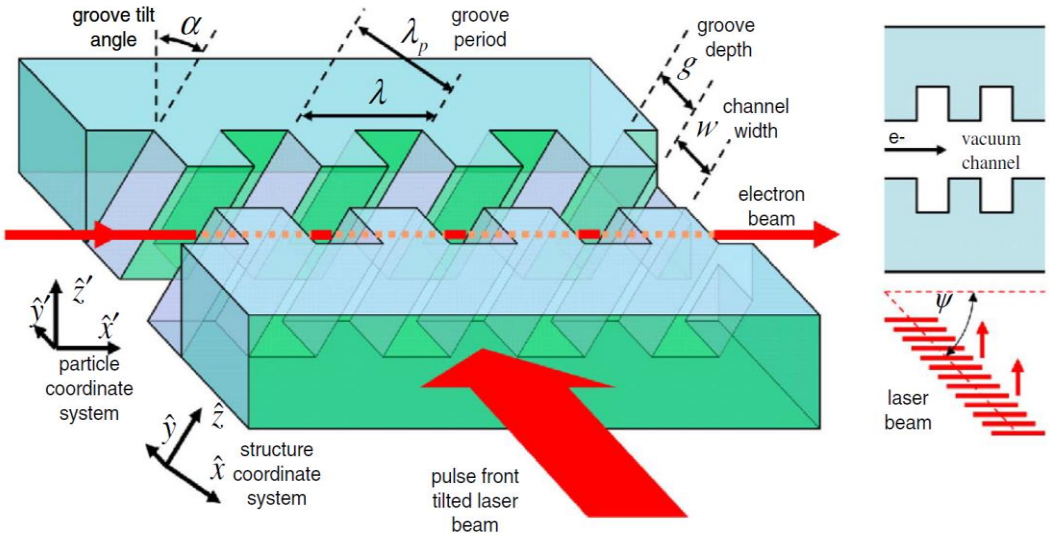

Figure 26. Schematic of a deflecting structure with a groove tilt angle α [99].

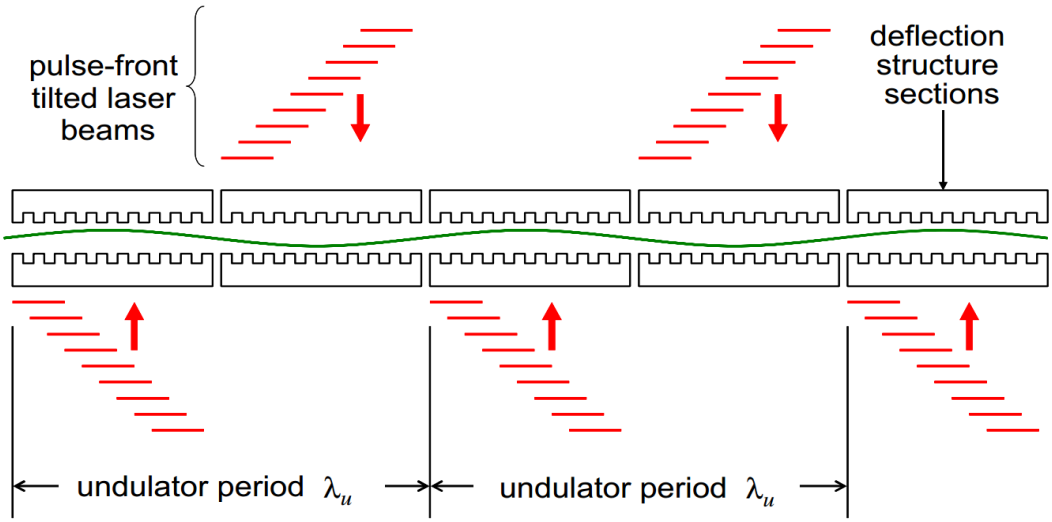

Figure 27. Schematic of an undulator consisting of many stages of laser-driven deflecting structures [98].

(3) High-energy Linear Collider

DLAs are a strong potential candidate for a future electron-positron collider due to their high accelerating gradients in the GV/m range. To reach 10 TeV centre-of-mass energies, a linear accelerator (linac) over 100 km in length is required, which would cost tens of billions of dollars to build. However, a DLA linac of length of 10 km operating at an accelerating gradient of 1 GV/m could reach the same energy. Considering well-established nanofabrication technology, the manufacturing cost would be much lower than that of a

conventional TeV collider. As for the required luminosity of 10^{36} $cm^{-2}s^{-1}$ for such a collider, the DLA linac can operate at low bunch charge but at a high repetition rate to avoid bremsstrahlung energy spread at the interaction point [97].

The wall-plug efficiency is another key factor for development of a linear collider. An efficient integrated power coupler is needed to deliver the laser power into various DLA components. From the DLA calculations in Ref. [103], laser power to electron coupling efficiencies of 40% can be achieved. Given that a laser wall-plug efficiency above 30% has been obtained using current solid-state thulium-doped fiber laser technology, an electrical wall-plug efficiency for a DLA-based linac exceeding 10% is possible, which is desirable for a future DLA-based collider [46], [104].

1.4 About The Thesis

Dual-grating DLAs have been studied numerically and experimentally, demonstrating the acceleration of electrons with high gradients of up to several GV/m. However, few studies have been conducted into the particle beam quality that can be obtained from a DLA, despite its being one of the most essential parameters for any accelerator. The work described in this thesis mainly focuses on detailed numerical studies of dual-grating DLAs, including geometry optimizations, beam quality and energy efficiency studies, wakefield and particle-in-cell (PIC) simulations, as well as the fabrication and experimental preparations beyond the current state-of-the-art DLAs.

From a theoretical point of view, this thesis presents insight on the beam quality for acceleration of electrons in an optimized dual-grating DLA in terms of the emittance, energy spread, and loaded accelerating gradient. Two kinds of scheme, the addition of a Bragg reflector and the use of pulse-front-tilted (PFT) laser illumination, are then studied to improve the energy efficiency for dual-grating DLAs. From an experimental point of view, the current fabrication and experimental preparations pave the wave for future demonstrations on these dual-grating structures, although it is still underway due to a different time schedule.

Chapter 2 describes the theory of a grating-based DLA, and also lists some basic definitions used for the simulation studies in the following chapter.

Chapter 3 presents the optimization studies on dual-grating structures, including analytical geometry studies for relativistic and non-relativistic electrons and a detailed beam quality study in terms of the emittance, energy spread, and loaded accelerating gradient. In addition, the wakefield effect is also studied in detail.

Chapter 4 studies how to improve the energy efficiency for a dual-grating DLA. A Bragg reflector is added into a dual-grating structure in order to boost the accelerating field, thereby increasing the energy gain for a DLA. A pulse-front-tilted laser is then used to illuminate a dual-grating structure, thereby extending the interaction length between electrons and laser pulses and boosting the electron energy gain. Both schemes are investigated in detail, including analytical studies and PIC simulations.

Chapter 5 investigates a THz-driven dual-grating structure including geometry optimizations, wakefield studies and THz-bunch interaction in detail. These studies pave the way to the wakefield experimental studies using Swiss Free Electron Laser (FEL) facility.

Chapter 6 presents the preliminary fabrication studies on dual-grating structures using existing nanofabrication technology. This is followed by some experimental preparations for wakefield studies on a THz-driven dual-pillar structure, using an electron beam from the SwissFEL facility. These studies are carried out with the collaboration of researchers from the Paul Scherrer Institute (PSI), Switzerland.

Chapter 7 summarizes the thesis and outlines the proposed future experimental studies.

2. Theory of Particle Acceleration in Grating-based Structures

This chapter describes the theory for a grating-based DLA structure driven by a plane wave. Starting with Maxwell's equations, the properties of the evanescent fields close to a single-grating structure are derived. It is found that the single-grating structure is not suitable for acceleration of relativistic particles due to its exponential decay for accelerating fields. Symmetric double grating structures, which are called 'dual-grating structures' in this thesis, are therefore proposed for acceleration of particles. The electric and magnetic fields for dual-grating structures which are illuminated by a single laser beam are then presented. Such dual-grating structures can be used to accelerate both non-relativistic and relativistic particles. It is followed by definitions of some basic equations including accelerating and deflecting gradients, accelerating and deflecting factors, accelerating and deflecting efficiencies, emittance and energy spread. These basic definitions will be used in the following chapters of the thesis.

2.1 Particle Acceleration in Single-grating Structures

Evanescent electromagnetic fields close to a single grating structure excited by a plane wave have been explored by Palmer [105], Pai and Awada [106], and Breuer *et al*. [107]. Based on their methods, we can describe the electric and magnetic fields for a dual-grating structure which is illuminated by an incident plane wave. As shown in Figure 28, the diffraction of the incident plane wave excites a Fourier series of all spatial harmonics above the grating surface with the order number n = 0, 1, 2,….

The electromagnetic field of the nth mode $\boldsymbol{A}(\boldsymbol{r},t) = (\boldsymbol{E}(\boldsymbol{r},t), \boldsymbol{B}(\boldsymbol{r},t))$, with the electric field $\boldsymbol{E}$ and magnetic field $\boldsymbol{B}$, can be written as

$$\boldsymbol{A}(\boldsymbol{r},t) = \boldsymbol{A}_{\mathrm{n}} e^{i(k_{\perp}^{n} y + \boldsymbol{k}_{\parallel}^{n} \boldsymbol{r} - \omega t + \phi)}, \tag{1}$$

where $\mathbf{k}_{\parallel}^{n} = n\boldsymbol{k}_{\parallel}$, $k_{\parallel} = \frac{2\pi}{\lambda_{\mathrm{p}}}$, λ_{p} is the grating period, ω is the angular frequency of an incident plane wave and ϕ is a phase term.

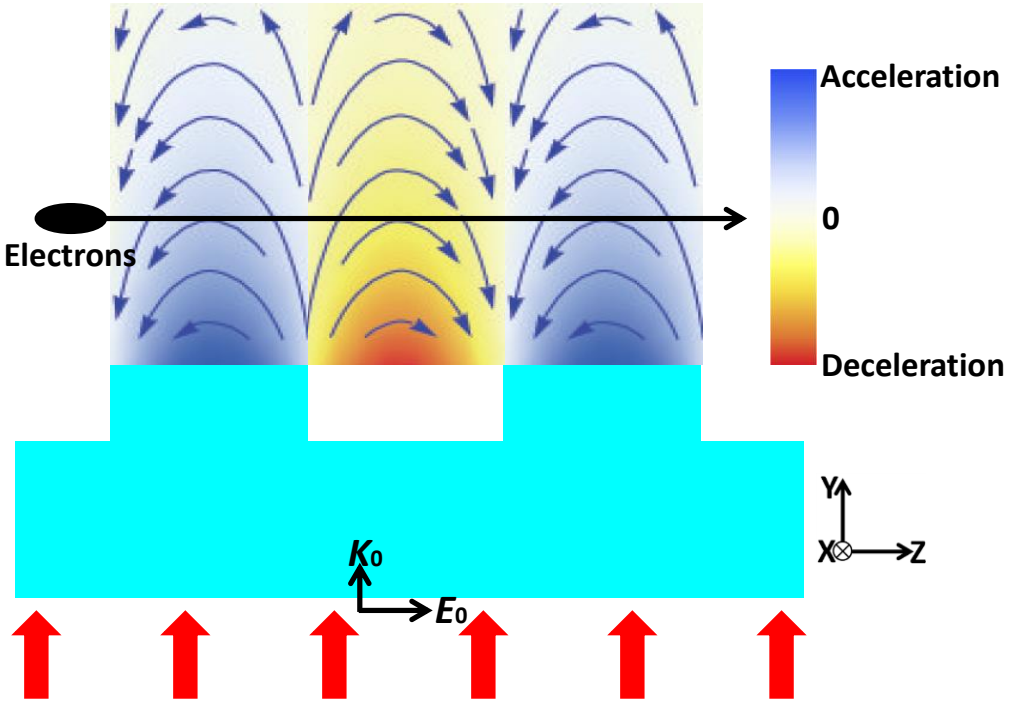

Figure 28. Conceptual pictures of the single-grating microstructure which is illuminated by a polarized laser beam from below. The polarization is along the z-axis.

A charged particle is assumed travelling along the z-axis close to the grating surface, with trajectory $\boldsymbol{r}(t) = \boldsymbol{v}t$, and velocity $v = |\boldsymbol{v}| = \beta c$, where c is the speed of light. In order to realize continuous acceleration, the phase velocity of the accelerating mode has to equal the particle velocity, yielding the synchronicity condition

$$\left|\boldsymbol{k}_{\parallel}^{n}\right| = \frac{\omega}{\beta c} = \frac{k_0}{\beta} \tag{2}$$

where k_0 is the wave vector of the incident plane wave in vacuum, $k_0 = 2\pi/\lambda_0$, λ_0 is the wavelength of the incident plane wave. By substituting $\left|\mathbf{k}_{\parallel}^{n}\right| = nk_{\parallel} = n\frac{2\pi}{\lambda_\mathrm{p}}$ into Equation (2), we get

$$nk_{\parallel} = n\frac{2\pi}{\lambda_\mathrm{p}} = \frac{k_0}{\beta}. \tag{3}$$

Thus, the synchronicity condition can be simply written as

$$\lambda_\mathrm{p} = n\beta\lambda_0. \tag{4}$$

This synchronicity condition can work not only for single-grating microstructures but also for dual-grating microstructures.

Only the synchronous modes are considered in the following analysis in which Equation (2) is satisfied. The fields in the vacuum channel gap have to satisfy the wave equation $\left(\nabla^2 - \frac{1}{c^2}\partial_t^2\right)\mathbf{A}(\mathbf{r},t) = 0$, which generates

$$(k_\perp^n)^2 + \left(k_\parallel^n\right)^2 - \frac{\omega^2}{c^2} = 0. \tag{5}$$

Therefore, by substituting Equation (2) into Equation (5) we get

$$k_\perp^n = k_0\left(1 - \frac{1}{\beta^2}\right)^{0.5} = i\frac{k_0}{\beta\gamma}, \tag{6}$$

where $\gamma = (1-\beta^2)^{-0.5}$. Because $\beta \leq 1$ and $\gamma \geq 0$, $k_\perp^n$ has an imaginary value. This means that the accelerating fields fall off exponentially perpendicular to the particle trajectory. In other words, only evanescent fields contribute to the acceleration, which is in agreement with the Lawson-Woodward theorem. Particles therefore have to pass the grating surface within a distance of the order of the transverse decay length

$$\delta = \frac{i}{k_\perp^n} = \frac{\beta\gamma\lambda_0}{2\pi}, \tag{7}$$

After getting $k_\parallel^n$ and $k_\perp^n$, the electromagnetic fields of the synchronous mode can be calculated using

$$\boldsymbol{k} = k_0\begin{pmatrix} 0 \\ i/(\beta\gamma) \\ 1/\beta \end{pmatrix}, \tag{8}$$

$$\nabla \times \boldsymbol{E} = -\frac{\partial \boldsymbol{B}}{\partial t}, \tag{9}$$

$$\nabla \times \boldsymbol{B} = \frac{1}{c^2}\frac{\partial \boldsymbol{E}}{\partial t}. \tag{10}$$

We obtain that

$$\boldsymbol{E} = \begin{pmatrix} E_x \\ -cB_x/\beta \\ icB_x/(\beta\gamma) \end{pmatrix}, \tag{11}$$

$$\boldsymbol{B} = \begin{pmatrix} B_x \\ E_x/(\beta c) \\ -iE_x/(\beta\gamma c) \end{pmatrix}. \tag{12}$$

It should be noted that here there are two independent solutions corresponding to the transverse electric (TE) and the transverse magnetic (TM) modes. The E_x and B_x for different modes have to be calculated individually.

When a charged particle travels along the *z*-axis close to the grating surface, with velocity

$$\boldsymbol{v} = \begin{pmatrix} 0 \\ 0 \\ \beta c \end{pmatrix}, \tag{13}$$

then using Equations (9) and (10), we can compute the Lorentz force from $\boldsymbol{F} = q(\boldsymbol{E} + \boldsymbol{v} \times \boldsymbol{B})$, to get

$$\boldsymbol{F} = q \begin{pmatrix} 0 \\ -cB_x/(\beta\gamma^2) \\ icB_x/(\beta\gamma) \end{pmatrix}, \tag{14}$$

where q is the charge of a single particle. For an incident plane wave with TE modes, we get $B_x = 0$ and hence $F = 0$ according to Equation (14). In this situation, TE modes are not suitable for acceleration of particles at the single-grating surface. In the following analysis, our discussion therefore only focuses on the TM modes with $E_x = 0$. The field profile for *n*th order spatial harmonics can be analytically described as:

$$B_x = B_0 e^{i(k_\perp^n y + k_\parallel^n z - \omega t + \phi)}, \tag{15}$$

$$E_y = \frac{-cB_0}{\beta} e^{i(k_\perp^n y + k_\parallel^n z - \omega t + \phi)}, \tag{16}$$

$$E_z = \frac{icB_0}{\beta\gamma} e^{i(k_\perp^n y + k_\parallel^n z - \omega t + \phi)}, \tag{17}$$

where B_0 is the amplitude of the transverse magnetic field.

Figure 28 shows the concept of synchronous particle acceleration exploiting the first spatial harmonic close to the grating surface, which is excited by an incident laser beam perpendicular to the particle trajectory. It is found that the particles experience a longitudinal force accompanied by a transverse component that causes deflection of the particles. When particles are accelerated synchronously by the spatial harmonics, the particles are temporally bunched. However, the accelerating and deflecting forces are out of phase, which implies that longitudinal temporal focusing leads to a defocusing of the particle bunch. This issue can be addressed by alternating phase focusing [13], [108]–[110] in which the electrons are injected at different positions relative to the synchronous field, thereby ensuring stable acceleration. An alternative method has been proposed by Naranjo *et al.* [111] in which particles are accelerated by interaction with synchronous spatial harmonics and are focused by strong ponderomotive interaction with asynchronous spatial harmonics.

The exponential dependence of the accelerating force as a function of the particle's distance from the surface can result in a distortion of the particle bunch. It has however been

shown that by using symmetric illumination on two parallel grating surfaces a symmetric force pattern [80], [81], [88], [100] is created, and the deflecting forces cancel each other on the axis of the accelerator. The distance between the two surfaces has to be of the order of decay length δ in order to efficiently accelerate particles in the vacuum channel centre. In addition, Equation (14) also reveals that a single-grating structure cannot be used for acceleration of relativistic particles with $\beta = 1$, due to $\gamma \neq 0$. When $\beta = 1$ and $\gamma = 0$, according to Equation (5) we get $k_{\parallel}^{n} = k_0$ and hence

$$\frac{d^2\boldsymbol{A}}{dy^2} = 0. \tag{18}$$

This can be solved by

$$\boldsymbol{A}(\boldsymbol{r}) = \boldsymbol{A}(x, z)(1 + \kappa y). \tag{19}$$

where κ is a constant for mathematical calculations. In this case, the mode cannot exist at the surface of a single-grating microstructure because a constant or linearly increasing electromagnetic field extending to infinity is unphysical. However, such a linear solution exists physically when a second dielectric boundary is added into the simulation, implying a constant longitudinal accelerating field [88]. Such an accelerating mode can be used to continuously accelerate relativistic particles with $\beta \approx 1$.

2.2 Particle Acceleration in Dual-grating Structures

Following the descriptions for particle acceleration at a single-grating microstructure, this section describes the theory for particle acceleration at a dual-grating microstructure. The dual-grating microstructure usually consists of two parallel single-grating microstructures facing each other. The fields between two grating surfaces are a superposition of evanescent waves travelling in opposite directions due to either reflection off of the second surface or a second incident plane wave. It creates a hyperbolic cosine transverse profile for the synchronous accelerating mode in the vacuum channel, which does not decay exponentially with increasing distance from the grating surface, as shown in Figure 29. In this situation, the dual-grating microstructures are suitable for acceleration of relativistic particles with $\beta \approx 1$.

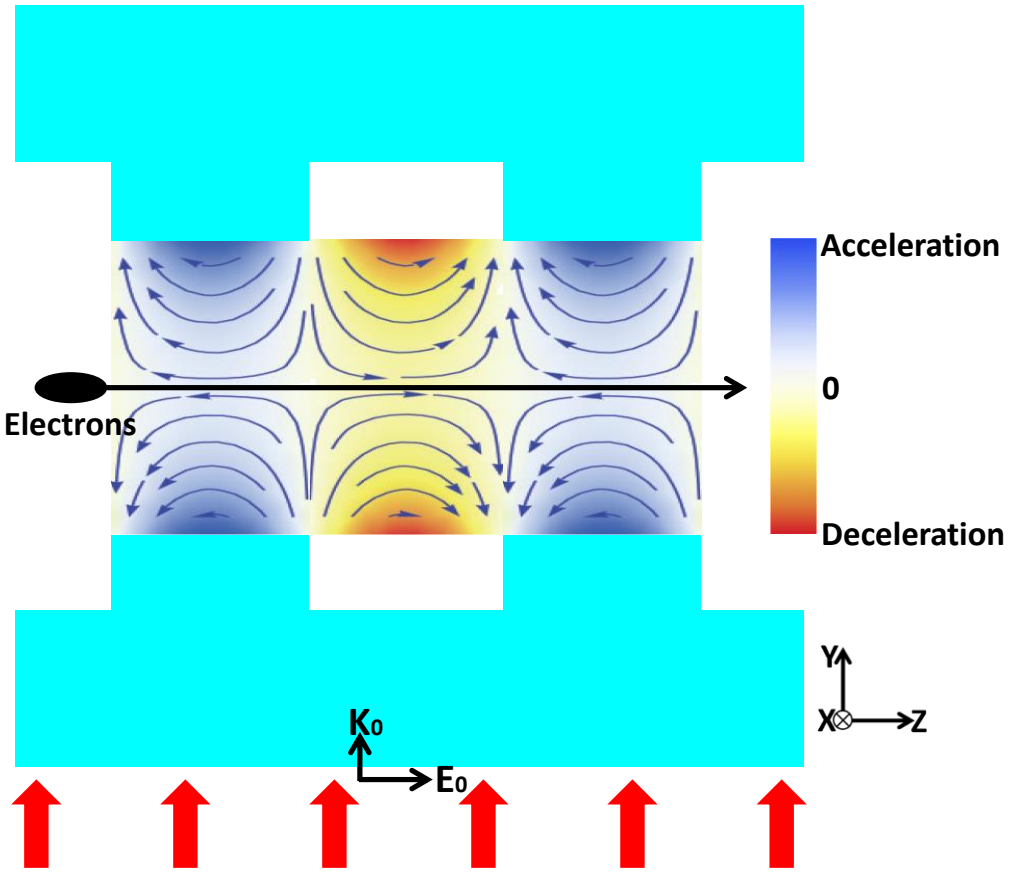

Figure 29. Conceptual picture of a dual-grating microstructure which is illuminated by a polarized laser beam from below. The polarization is along the *z*-axis.

For a linear polarized TM mode, the transverse magnetic field of the *n*th order spatial harmonics can be written as

$$B_x = \left(D_{1,n}e^{-k_y y} + D_{2,n}e^{+k_y y}\right)e^{i(k_\parallel^n z-\omega t+\phi)}$$

$$= \left(\left(D_{1,n} + D_{2,n}\right)\cosh\left(k_y y\right) + \left(D_{2,n} - D_{1,n}\right)\sinh\left(k_y y\right)\right)e^{i(k_\parallel^n z-\omega t+\phi)}, \quad (20)$$

where $D_{1,n}$ and $D_{2,n}$ are the coefficients of the transmitted and reflected propagating modes, k_y is the transverse wave number, $k_y = 2\pi/(\beta\gamma\lambda_0)$, $\beta = v/c$ for electron velocity, $\gamma = (1-\beta^2)^{-0.5}$, ω_0 and λ_0 are the angular frequency and wavelength of an incident plane wave, $k_\parallel^n$ is the longitudinal wave number, and $k_\parallel^n = nk_\parallel = n\frac{2\pi}{\lambda_p} = \frac{k_0}{\beta}$. Then according to Maxwell's equation $\nabla \times \boldsymbol{B} = -\mu\epsilon i\omega \boldsymbol{E}$, we can easily find the expressions for E_y and E_z:

$$E_y = \frac{-c}{\beta}\left(D_{1,n}e^{-k_y y} + D_{2,n}e^{+k_y y}\right)e^{i(k_\parallel^n z-\omega t+\phi)}, \quad (21)$$

$$E_z = \frac{ic}{\beta\gamma}\left(D_{1,n}e^{-k_y y} - D_{2,n}e^{+k_y y}\right)e^{i(k_\parallel^n z-\omega t+\phi)}. \quad (22)$$

so the Lorentz force calculated from $\boldsymbol{F} = e(\boldsymbol{E} + v \times \boldsymbol{B})$ is described by

$$\boldsymbol{F} = \begin{bmatrix} 0 \\ \frac{-qc}{\beta\gamma^2}\left(D_{1,n}e^{-k_y y} + D_{2,n}e^{+k_y y}\right)e^{i(k_\parallel^n z-\omega t+\phi)} \\ \frac{iqc}{\beta\gamma}\left(D_{1,n}e^{-k_y y} - D_{2,n}e^{+k_y y}\right)e^{i(k_\parallel^n z-\omega t+\phi)} \end{bmatrix}. \tag{23}$$

This can be simplified as follows

$$\boldsymbol{F} = \begin{bmatrix} 0 \\ \frac{-qc}{\beta\gamma^2}\left(D_{\mathrm{s}}\cosh(k_y y) + D_{\mathrm{c}}\sinh(k_y y)\right)\cos(k_z z - \omega_0 t + \varphi) \\ \frac{qc}{\beta\gamma}\left(D_{\mathrm{s}}\sinh(k_y y) + D_{\mathrm{c}}\cosh(k_y y)\right)\sin(k_z z - \omega_0 t + \varphi) \end{bmatrix} = \begin{bmatrix} 0 \\ F_y \\ F_z \end{bmatrix}. \tag{24}$$

where $D_{\mathrm{s}} = D_{1,\mathrm{n}} + D_{2,\mathrm{n}}$ and $D_{\mathrm{c}} = D_{2,\mathrm{n}} - D_{1,\mathrm{n}}$, q is the charge of a single particle, c is the speed of light, F_y is the deflecting force, and F_z is the accelerating force. When $D_{\mathrm{s}} = 0$ and $D_{\mathrm{c}} \neq 0$, a uniform accelerating mode as shown in Figure 30, with vanishing deflecting force on axis, will exist in the channel, which is our desired case for the following optimization. When $D_{\mathrm{s}} \neq 0$ and $D_{\mathrm{c}} = 0$, the accelerating force vanishes on axis, which is not suitable for acceleration of electrons. It is found that there is always a weak, but non-zero deflecting force accompanying the accelerating force for particle acceleration in dual-grating microstructures. This deflecting force can be mitigated when the microstructure is symmetrically illuminated [88].

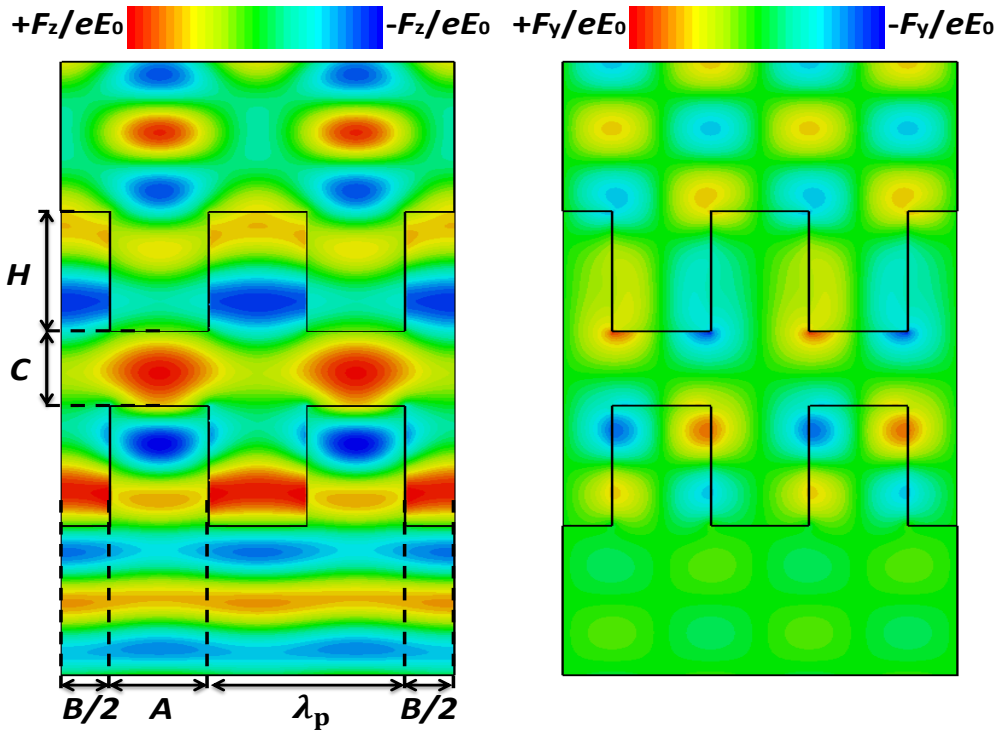

Figure 30. Longitudinal accelerating force F_z (left) and a weak deflecting force F_y (right) in a dual-grating structure illuminated by an input laser field E_0 along the y-axis [112].

2.3 Basic Definitions

(1) Accelerating and Deflecting Gradients

When the electromagnetic fields in the microstructures are computed by finite difference time domain (FDTD) [113] simulation, we can calculate the accelerating gradient, which is the average longitudinal electric field $E_z[z(t),t]$experienced by a single electron in one period of the microstructure:

$$G_0 = \frac{1}{\lambda_\mathrm{p}}\int_0^{\lambda_\mathrm{p}} E_z[z(t),t]dz = \frac{1}{q\lambda_p}\int_0^{\lambda_p} F_z[z(t),t]dz, \tag{25}$$

where λ_p is the grating period, q and $F_z[z(t),t]$ have the same definitions as Equation (24). Similarly, the deflecting gradient can be defined by

$$D_0 = \frac{1}{\lambda_\mathrm{p}}\int_0^{\lambda_\mathrm{p}} (E_y[z(t),t] + vB_x[z(t),t])dz = \frac{1}{q\lambda_p}\int_0^{\lambda_p} F_y[z(t),t]dz. \tag{26}$$

(2) Accelerating and Deflecting Factors and Efficiencies

When a plane wave with an input field of E_0 travels through a dual-grating structure, the maximum electric field E_m in the structure should not exceed the material damage field. The accelerating factor *AF* and the deflecting factor *DF* are defined as the ratios of the accelerating gradient G_0 and deflecting gradient D_0 respectively to the maximum electric field E_m in the structure:

$$AF = G_0/E_m, \tag{27}$$

$$DF = D_0/E_m. \tag{28}$$

Similarly, the accelerating efficiency *AE* and deflecting efficiency *DE* are defined as the ratios of the accelerating gradient G_0 and deflecting gradient D_0 respectively to the input electric field E_0 in the structure:

$$AE = G_0/E_0, \tag{29}$$

$$DE = D_0/E_0. \tag{30}$$

(3) Energy Efficiency

When the dual-grating structures are illuminated by a uniform plane wave, the electrons experience a uniform gradient G_0 within the entire interaction length L_int, thereby resulting in an energy gain $\Delta E = G_0 L_\mathrm{int}$. When a Gaussian laser beam with a temporal profile $s(t,\tau_0)$, and a spatial profile $g(z,w_\mathrm{z})$ is used to illuminate a dual-grating structure with a length *LZ*, the electrons' energy gain is calculated to be

$$\Delta E = \int_{-0.5LZ}^{0.5LZ} qG_{\mathrm{p}} s(t,\tau_0) g(z,w_z)\, dz, \tag{31}$$

where τ_0 is the laser full-width at half-maximum (FWHM) duration, w_{z} is the laser transverse RMS waist radius, q is the charge on a single electron, and G_{p} is the accelerating gradient. Since the structure is not powered uniformly, the accelerating gradient G_{p} is the peak gradient. Here, z = 0 is defined as corresponding to the longitudinal center of a dual-grating structure and the center of the laser transverse profile. Equation (31) shows that the energy gain depends on the laser FWHM duration τ_0, waist radius w_{z}, structure length LZ, and peak gradient G_{p}. The ratio of the energy gain ΔE and the product of the incident laser field E_0 and q is defined as the energy efficiency (EE), which can be used to evaluate the accelerating performance for a dual-grating structure:

$$EE = \Delta E/(qE_0). \tag{32}$$

(4) Emittance and Energy Spread

Emittance and energy spread are properties of a particle beam used in accelerator physics to characterise beam quality. Emittance represents the area of the transverse phase space occupied by a bunch of particles, which is generally an ellipse as shown in Figure 31. In a particle accelerator, damping or synchrotron radiation losses can reduce the emittance of a bunch of particles. However, in many cases it is a good approximation to neglect non-conservative forces on particles in an accelerator. Liouville's theorem [114]–[116] is of specific importance in this respect and it is used extensively to describe the properties of a bunch of particles. This theorem states that under the influence of conservative forces the emittance of a bunch of particles is conserved as the particles move through an accelerator.

There are two transverse phase spaces for each spatial direction. The phase space variables for particles are *x*, *px*, *y*, *py*, with time as the independent variable. These coordinates correspond to the position and momentum components of the particles. Often the coordinates are taken to be the errors in position and momentum with respect to an ideal particle. For example, an ideal particle would have no transverse momentum component, *px* = 0. Its position would lie along the ideal trajectory through the machine and be denoted as *x* = 0. Longitudinally, the energy or momentum of a particle is taken to be the difference from the ideal momentum or energy. It is desirable for the longitudinal motion along the beam axis to be decoupled from the transverse motion in any particle accelerator. In this situation, the transverse 4-D phase space can be studied separately. Transverse phase space can be decomposed into two orthogonal dimensions and so into two 2-D transverse sub-phase spaces. Phase space area conservation is valid for each of the decomposed phase spaces. For the 2-D phase spaces the coordinates are represented as *x* (or *y*) in units of length for the

position and *x*' (or *y*') in units of radians for the angular divergence. The beam emittance multiplied by π is equal to the area occupied by the beam in the phase spaces.

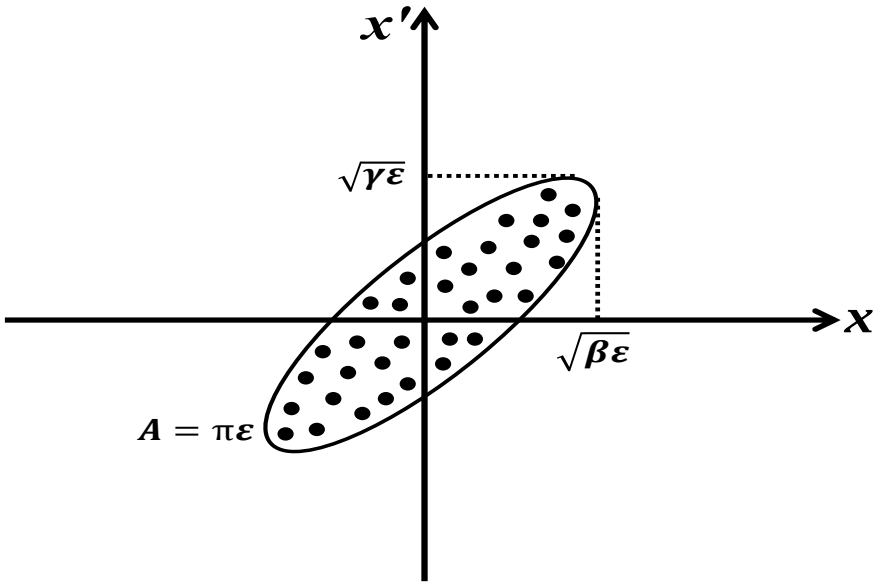

Figure 31. Emittance ellipse and Twiss parameters, where *A* is the area of the ellipse.

In particle accelerators with very precisely-known beamline optics, the lattice functions (or Twiss parameters α_x, β_x, γ_x), in combination with beam profile measurements, are used to calculate beam emittance in the *x* spatial direction. Figure 31 shows the beam emittance and relevant Twiss parameters in a phase space plot. Beam motion can be described in transverse phase space by the emittance ellipse defined in Equation (33). The Twiss parameters relate emittance to beam parameters as shown in Equations (34)-(36) where the brackets denote averages. If the accelerator is composed of linear elements such as dipoles and quadrupoles, the emittance defined in Equation (33) is invariant.

$$\gamma_x x^2 + 2\alpha_x x x' + \beta_x x'^2 = \varepsilon_x, \tag{33}$$

$$\langle x^2 \rangle = \beta_x \varepsilon_x, \tag{34}$$

$$\langle x'^2 \rangle = \gamma_x \varepsilon_x, \tag{35}$$

$$\alpha_x{}^2 = \beta_x \gamma_x - 1. \tag{36}$$

In some particle accelerators a particle beam with irregular beam size is produced, and it is preferred to calculate its emittance statistically, based on the distribution of particles in phase space. Such a statistical emittance was introduced by Chasman [117] and later refined by Lapostolle [118]. The transverse emittance ε_x can be calculated using Equations (37) to (42), and the other transverse emittance ε_y can be determined in the same way. The brackets

denote the weighted average over all particles and the parameter I is proportional to the intensity of the beam.

$$\varepsilon_x = \sqrt{\langle x^2 \rangle \langle x'^2 \rangle - \langle xx' \rangle^2}, \tag{37}$$

$$\langle x^2 \rangle = \frac{\sum_{all}(x-\langle x \rangle)^2 I(x)}{\sum_{all} I(x)}, \tag{38}$$

$$\langle x'^2 \rangle = \frac{\sum_{all}\left(x-\langle x' \rangle\right)^2 I(x)}{\sum_{all} I(x)}, \tag{39}$$

$$\langle xx' \rangle = \frac{\sum_{all}(x-\langle x \rangle)(x-\langle x' \rangle) I(x)}{\sum_{all} I(x)}, \tag{40}$$

$$\langle x \rangle = \frac{\sum_{all} x I(x)}{\sum_{all} I(x)}, \tag{41}$$

$$\langle x' \rangle = \frac{\sum_{all} x' I(x)}{\sum_{all} I(x)}. \tag{42}$$

As far as we know, emittance as defined above is only constant in beamlines without acceleration. In the case of acceleration, we need to define a normalized emittance as follows

$$\varepsilon_N = \beta\gamma\varepsilon. \tag{43}$$

where β and γ are relativistic parameters not to be confused with the Twiss parameters. The normalized emittance remains constant under acceleration, and will be used for our analysis in the following chapters of this thesis.

In the longitudinal plane, particles are accelerated by the electric fields and also undergo synchrotron oscillations. In this case, we can use energy as a longitudinal variable, together with its canonical conjugate, time. Frequently, the relative energy variation σ and relative time τ with respect to a reference particle are used to characterize the beam:

$$\sigma = \frac{E-E_0}{E_0}, \tag{44}$$

$$\tau = \frac{t-t_0}{t_0}, \tag{45}$$

According to Liouville's theorem, in the presence of Hamiltonian forces, the area occupied by the beam in longitudinal phase space is also conserved. For a finite bunch length, the relative energy variation, which is also called energy spread, is often used for evaluating the property of a beam in longitudinal phase space.

2.4 Chapter Summary

This chapter has presented the theory of particle acceleration in single-grating and dual-grating microstructures. It was found that single-grating microstructures are not suitable for acceleration of relativistic particles, due to the exponential dependence of the accelerating force as a function of the particle's distance from the surface. A dual-grating consisting of two parallel single-grating microstructures facing each other was then proposed for acceleration of relativistic particles. The fields in the vacuum channel of dual-grating microstructures are superpositions of evanescent waves travelling in opposite directions due either to reflection off the second surface or to a second incident plane wave. This creates a hyperbolic cosine transverse profile for the synchronous accelerating mode in the vacuum channel, which does not decay exponentially with increasing distance from the grating surface. In this case, dual-grating microstructures are suitable for acceleration of relativistic and non-relativistic particles. The calculated electric and magnetic fields have also been presented for such dual-grating microstructures.

In addition, some basic definitions have been described in this chapter including accelerating and deflecting gradients, accelerating and deflecting factors, accelerating and deflecting efficiencies, energy efficiency, emittance and energy spread. These basic definitions are used frequently in the following chapters of this thesis.

3. Optimizations and Beam Quality Studies for Laser-driven Dual-grating Structures

This chapter presents detailed geometry optimizations, wakefield and beam quality studies on the dual-grating structures. The optimization of these structures with respect to maximization of the accelerating factor and efficiency for both non-relativistic and relativistic electrons is discussed. Simulations are carried out using the commercial CST and VSim simulation codes and results from both codes are compared.

The first two sections discuss the motivation and working principle for dual-grating structures driven by a single laser beam. Compared to previously-reported dual-grating structures, our structures have a larger grating period due to their illumination by a longer wavelength laser of 2.0 μm,, which indicates a larger accelerating channel; hence more electrons can be loaded.

The chapter then moves on to describe in Section 3.3 different modelling tools based on FDTD methods. The codes CST and VSim are used to study analytically the acceleration of relativistic and non-relativistic electrons in dual-grating structures. The optimization of these structures with respect to maximising the accelerating factor and accelerating efficiency for different spatial harmonics is discussed. Simulation results from both codes are shown in comparison. Very good agreement is found between the simulation results obtained, giving confidence in their validity.

The chapter proceeds to study the wakefield effect, which can lead to energy loss and deflection of the beam through a transverse momentum kick. Analytical studies into both the longitudinal and the transverse wakefield are presented in Section 3.4.

Finally, laser-bunch interaction and beam quality optimizations are discussed in Sections 3.5 and 3.6. In my simulations I use the beam parameters of the future Compact Linear Accelerator for Research and Applications (CLARA) [119] to load an electron bunch into an optimized 100-period dual-grating structure, where it interacts with a realistic laser pulse. The emittance, energy spread and loaded accelerating gradient for modulated electrons are then analyzed in detail. In addition, the effect of laser parameters and electron density on the final beam quality is also analyzed in detail. These numerical simulations pave the way for the future realization of a micro accelerator based on DLAs.

3.1 Motivation

Dual-grating structures have been studied numerically and experimentally, demonstrating the acceleration of electrons with high gradients of up to several GV/m [47], [48], [51]–[53], [79]–[82]. However, few studies have been conducted into the particle beam quality that can be obtained from a DLA, despite its being one of the most essential parameters for any accelerator. This chapter reports on geometry optimizations and beam quality studies for dual-grating DLAs. It investigates numerically the beam quality for modulated electrons travelling in the vacuum channel of a quartz dual-grating structure in terms of the emittance, energy spread and loaded accelerating gradient. Simulations are performed using beam properties of the future CLARA [119] which is planned as a X-ray FEL test facility, to be located at the Daresbury laboratory, UK. The wakefield effect, which can result in energy loss for extremely short and small bunches, is also studied in detail for dual-grating DLAs. This will have to be taken into account for a realistic DLA in the future. In addition, the dual-grating structures used in this chapter have a grating period of $\lambda_p = 2.0$ μm, which is larger than that of previous DLAs demonstrations [47], [48]. This enables a larger vacuum channel gap of C = 1.0 μm, which allows more electrons to be loaded.

3.2 Dual-grating Geometry and Working Mechanism

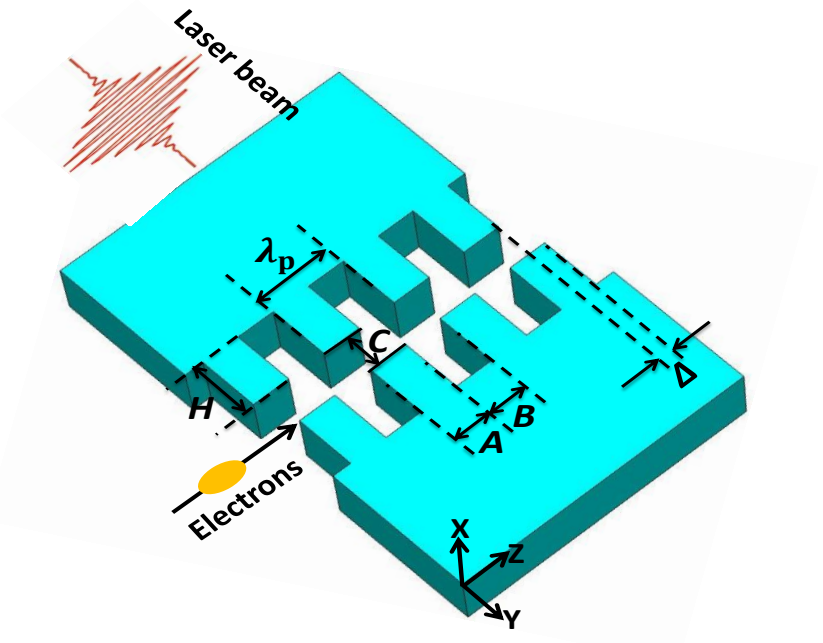

Figure 32. Schematic of a laser-driven dual-grating structure. λ_p, A, B, C, H, and Δ represent grating period, pillar width, pillar trench, vacuum channel gap, pillar height and longitudinal shift, respectively. The condition $A + B = \lambda_p$ is selected for all simulations to ensure synchronicity.

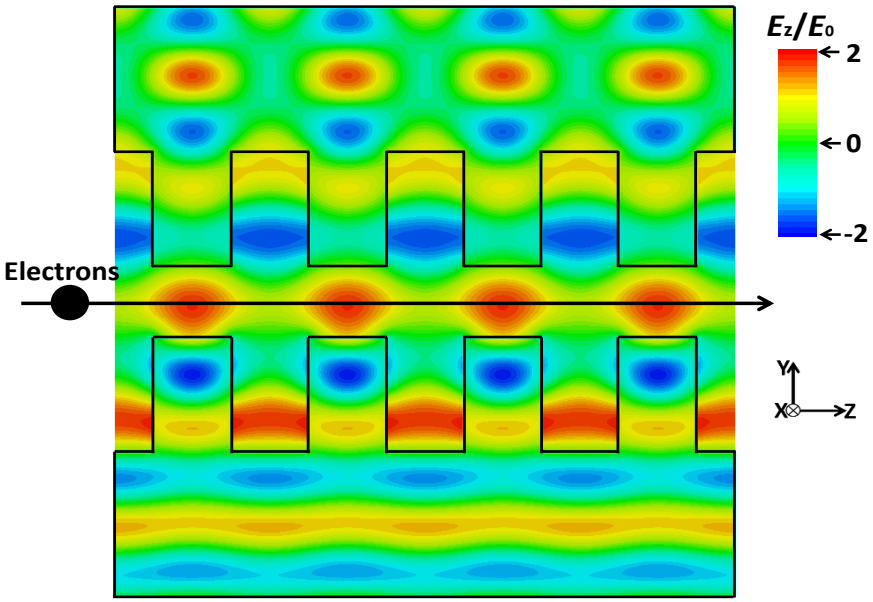

Figure 33. Longitudinal electric field distribution in a dual-grating structure illuminated by an input field E_0 along the *y*-axis.

The dual-grating structures were originally proposed by Plettner *et al*. [79]. The cross sectional geometry and dimensions for dual-grating structures are shown in Figure 32. *A* represents the dielectric pillar width, and *B* represents the dielectric pillar trench. The lattice length $A + B$ is equal to the operating laser wavelength λ_0. Δ describes the misalignment level of the structure. The vacuum channel gap *C* and pillar height *H* are determined through optimization studies. Electrons move in the vacuum channel (along the *z* axis), while laser pulses are fed perpendicular to the direction of electron movement from a single side, along the *y* axis.

Figure 33 illustrates the working principle of the dual-grating accelerating structure. As the plane wave of a linearly polarized laser beam travels through the structure, the speed of the wave in the dielectric grating pillar is lower than that in the adjacent vacuum space. This produces the desired π-phase-delay and a periodic standing-wave-like electric field distribution inside the vacuum channel, where electrons are travelling and are periodically modulated along the longitudinal *z*-axis. To create the desired phase difference of π, the grating pillar height *H* should be set to $H = \frac{\lambda_0}{2(n_r - 1)}$, where n_r is the refractive index of the grating material.

The fundamental difference between dual-grating structures and other waveguide DLAs [62]–[78] is that the acceleration is not due to trapped accelerating modes. It is the non-propagating near field that provides the synchronous accelerating field for dual-grating structures. In addition, electrons are travelling along the vacuum channel perpendicular to the laser in dual-grating structures, while the electrons move in the same direction as the

laser propagation for waveguide DLAs. As described in Chapter 2, as the laser pulses illuminate the dual-grating structures, a series of grating diffraction modes are generated inside the vacuum channel. Phase synchronicity [88] has to be achieved between the spatial harmonics and the particle beam, through matching the grating period λ_p to the laser wavelength λ_0.

In the following simulation studies, a wavelength of 2000 nm emitted from an erbium-fiber laser system is used. Quartz [120], with a refractive index n_r = 1.5, is chosen as the grating material due to its high level of transparency in the optics frequency range, high field damage threshold and high thermal conductivity.

3.3 FDTD Simulation

The dual-grating structure is invariant along the *x*-direction and the region of interest is assumed to have no net charge density. The incident electromagnetic wave is also invariant along the x-direction and hence the field solution is 2D. The 2D geometry of such a dual-grating structure, and the choice of a plane wave at the input face, are ideally suited for evaluation with well-established FDTD numerical methods [113]. In the FDTD method, the grid spacing Δs is chosen to be much smaller that the wavelength λ_0 so that the evolution of the field components for Maxwell's equations can be found in discrete time Δt and space steps Δs. The numerical analysis based on the FDTD method only requires a single grating period and can use periodic boundary conditions at the sides of the region of interest and absorbing boundary conditions at the input and exit planes. For a 2D geometry two independent transverse-electric (TE) and transverse-magnetic (TM) field solutions exist. As described in Chapter 2, TE modes are not suitable for acceleration of particles in the dual-grating structure. An incident plane wave with electric field component polarized along the electron beam axis, belongs to the TM field solution. This incident wave can be TEM mode. Such wave is therefore of particular interest to us.

3.3.1 Modelling Tools

Computer Simulation Technology (CST) [121] is a high-frequency electromagnetic software that has been frequently used to understand the properties of dual-grating structures. It uses both a finite element method (FEM) solver and adaptive meshing to generate solutions to Maxwell's Equations in a variety of structures with different boundary conditions. CST includes a full 3D electromagnetic simulation tool and various static solvers

and is widely used in electromagnetic design and analysis. CST simulation suite is comprised of 7 packages to meet the various demands of users, as follows:

(1) CST Microwave studio: it is used mainly for the fast and accurate 3D simulation of high frequency devices such as filters, couplers, planar and multi-layer structures.
(2) CST EM studio: it is used mainly for the design and analysis of static and low frequency electromagnetic applications such as motors, sensors, actuators, et al.
(3) CST Particle studio: it is used mainly in the analysis of charged particle dynamics subject to static and dynamic fields. Applications include electron guns, cathode ray tubes, magnetrons, and wake fields.
(4) CST Cable studio: it is used mainly for the simulation of signal integrity and electromagnetic compatibility (EMC) / electromagnetic interference (EMI) analysis of cable harnesses.
(5) CST PCB studio: it is used mainly for the simulation of signal integrity and EMC/EMI on printed circuit boards (PCB).
(6) CST Mphysics studio: it is used mainly for thermal and mechanical stress analysis.
(7) CST Design studio: it is a versatile tool that facilitates 3D electromagnetic/circuit co-simulation and synthesis.

In the following studies, CST microwave studio and particle studio are used for simulation of our DLAs. CST microwave studio includes various solvers such as the eigenmode solver, time domain solver, frequency domain solver, integral equation solver, multilayer solver, asymptotic solver. It supports hexahedral and tetrahedral mesh settings along with a fully automated meshing procedure specific to the desired frequency range, dielectrics and metallic edges, etc. An adaptive meshing process can refine the mesh settings in the calculation region according to the desired accuracy of the solutions by repeating the simulations. CST particle studio includes particle tracking solver and PIC solver. PIC solver calculates the particle movement in the total electromagnetic field due to the mutual coupling of the external field with the space charge field due to the particles. The algorithm of a PIC simulation is shown in Figure 34. At the starting point of the cycle, the program calculates the charge density and current density on the grid (uniform charged cloud) from the given initial particle quantities such as position and velocity of the particles after performing some weighting. At the second step of the cycle, the program calculates the electromagnetic field from Maxwell's equations. At the third step of the cycle, the program interpolates the fields from the grid and particles by waiting again to get the force on the particles. The last step is to solve the equations of motion to get the new particle quantities.

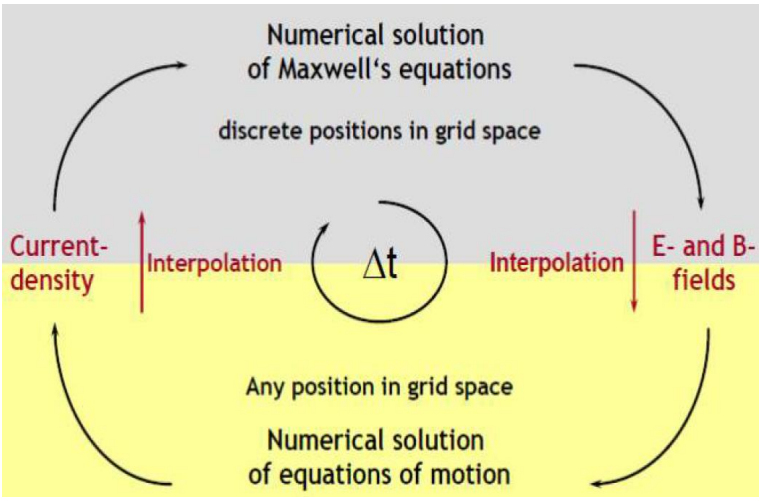

Figure 34. CST PIC algorithm [121].

CST Microwave studio with time domain solver is usually used to compute the electromagnetic fields in dual-grating structures. It should be noted here that the time domain solver for CST is based on the finite integration technique [122] which is similar but not the same as FDTD method. Open boundary conditions (equal to a fully absorbing boundary) are used at both laser input and output faces along the *y* direction. Periodic boundary conditions are used on both the surfaces in the *z* direction, to represent the periodic characteristics of this structure. The electromagnetic fields are uniform along the *x* direction, so magnetic boundary conditions are used at both outer surfaces in the *x* direction. There are two symmetry planes for a four-period dual-grating structure: magnetic ($H_t = 0$) at the YZ plane, and electric ($E_t = 0$) at the XY plane. Furthermore, a hexahedral mesh type is used, as it matches the geometry of the structures. For a dual-grating structure, the mesh size is chosen to be much smaller than the operating laser wavelength, to increase accuracy. The mesh density is determined by three parameters: lines per wavelength (LPW), lower mesh limit (LML), and mesh line ratio limit (MLRL). LPW determines the minimum number of mesh lines to be used across, for the minimum wavelength set by the simulation. The default value for LPW is 10, and LPW higher than 10 will increase the accuracy of the result as well as the calculation time. LML, which defines a maximum distance $L_{\max}$ between two mesh lines, is given as follows:

$$L_{\max} = D_{\min}/\sqrt{3}\mathrm{LML}, \tag{46}$$

where $D_{\min}$ represents the smallest face diagonal of the bounding box of the calculation domain. MLRL stands for the minimum ratio between two mesh lines (the absolute smallest mesh step). The calculation time depends not only on the absolute number of mesh cells, but also on the distance between mesh lines, since the smallest time step is determined by the smallest distance in a mesh.

The electromagnetic fields generated in the Microwave studio are then loaded into the same dual-grating structure to interact with the injected particles in the vacuum channel, through Particle studio with PIC solver. The energy gain and accelerating gradient can be calculated by analysing the phase space of the particles.

VSim [123] is a PIC code combined with a self-consistent electromagnetic field solver based on the FDTD numerical method. It allows more freedom to create the desired simulation by using the Python language. It can also compute electromagnetic fields between 1, 2, or 3 dimensions. It can be used for simulations in the time domain as well as for particle dynamics. Similar to CST Microwave studio, VSim can take a user-specified dielectric design with boundary conditions and compute the electromagnetic fields involved. For a dual-grating structure illuminated by a laser pulse with a Gaussian envelope, the periodic boundary conditions are applied along the electron channel in the z direction, magnetic boundary conditions are used in the x direction, and perfectly matched layers (PMLs) are employed along the laser propagation direction (*y*-axis) to absorb the transmitted light. It then tracks and characterizes loaded particles travelling through these fields, as well as the self-fields generated by those particles in the vacuum channel of the dual-grating structure. To solve for the fields as a function of time, VSim takes into account initial conditions of the electromagnetic fields, particle positions and velocities, and the user-defined mesh parameters. The algorithm is the same as that of CST PIC solver which can be seen in Figure 34. In each cell of the mesh, the magnetic field on the boundary of the cell is used to update the electric field at the centre of each cell over one half time-step, according to Faraday's law. During the next half time-step, the electric field at the centre of the cell is used to update the magnetic field on the boundary according to Ampere's law. The particle positions and velocities are then updated using the Biot-Savart law. The new particle positions/velocities are then used to update the electric and magnetic fields. VSim therefore is well-suited for modelling DLA structures and performing intensive PIC simulations to obtain all the relevant physical characteristics of DLA structures.

In addition, the mesh setup at convergence for CST and VSim are found to be different. CST automatically generates the mesh sizes by setting up mesh density parameters (LPW, LM and MLRL). As described previously, LPW, LM and MLRL are set to 80, 80, and 50 for convergence. For VSim, we found that *dx* (the mesh size along *x* direction) and *dy* (the mesh size along *y* direction) is set to period/200 and period/100 in order for convenience. These mesh setup will be used for the following simulations.

In the following simulations, CST and VSim code have been used to perform the optimization studies, and results from both codes are shown for comparison.

3.3.2 Optimizations for Acceleration of Non-relativistic Electrons

When dual-grating structures are used to accelerate non-relativistic electrons, the grating period λ_p, the laser wavelength λ_0 and the electron velocity $\beta = v/c$ have to be matched, yielding the synchronicity condition [88]:

$$\lambda_p = n\beta\lambda_0, \tag{47}$$

where n is the number of laser cycles per electron passing one grating period, v is the speed of the electron and c is speed of light.

In the following simulations, a uniform plane wave with a wavelength of λ_0 = 2.0 μm is used to excite the dual-grating structure from a single side, as shown in Figure 35. Such a wavelength can be emitted from the fiber laser system in PSI. Quartz, with a refractive index n_r = 1.50, is chosen as the grating material due to its beneficial properties in terms of transparency and field damage threshold. As shown in Figure 35, different grating periods λ_p can be chosen to excite spatial harmonics synchronous with 25 keV electrons with $\beta = 0.3$ in the vacuum channel of the dual-grating structure, providing several principal options for accelerating the electrons [124]. This will be studied in the following.

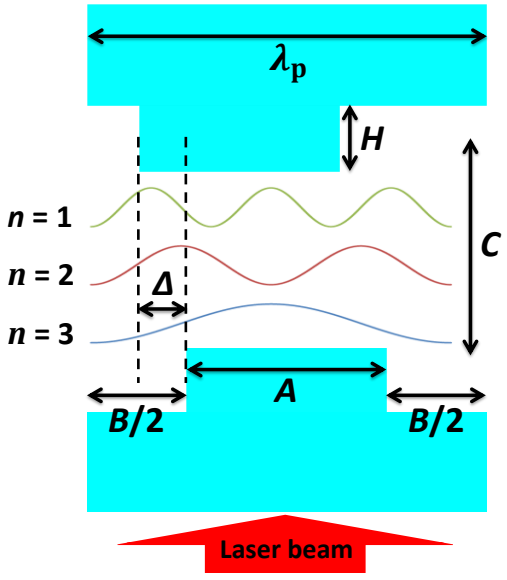

Figure 35. Illustration of the first, second and third spatial harmonics for the case of a single-period dual-grating structure illuminated by a single laser beam. λ_p, *A*, *B*, *C*, *H*, and *Δ* represent the same geometry as in Figure 32.

(1) First Spatial Harmonics

Firstly, a grating period of $\lambda_{p1} = 0.3\lambda_0$ = 0.6 μm is chosen. In this case the first spatial harmonics are synchronous with the 25 keV electrons in the vacuum channel of the dual-grating structure.

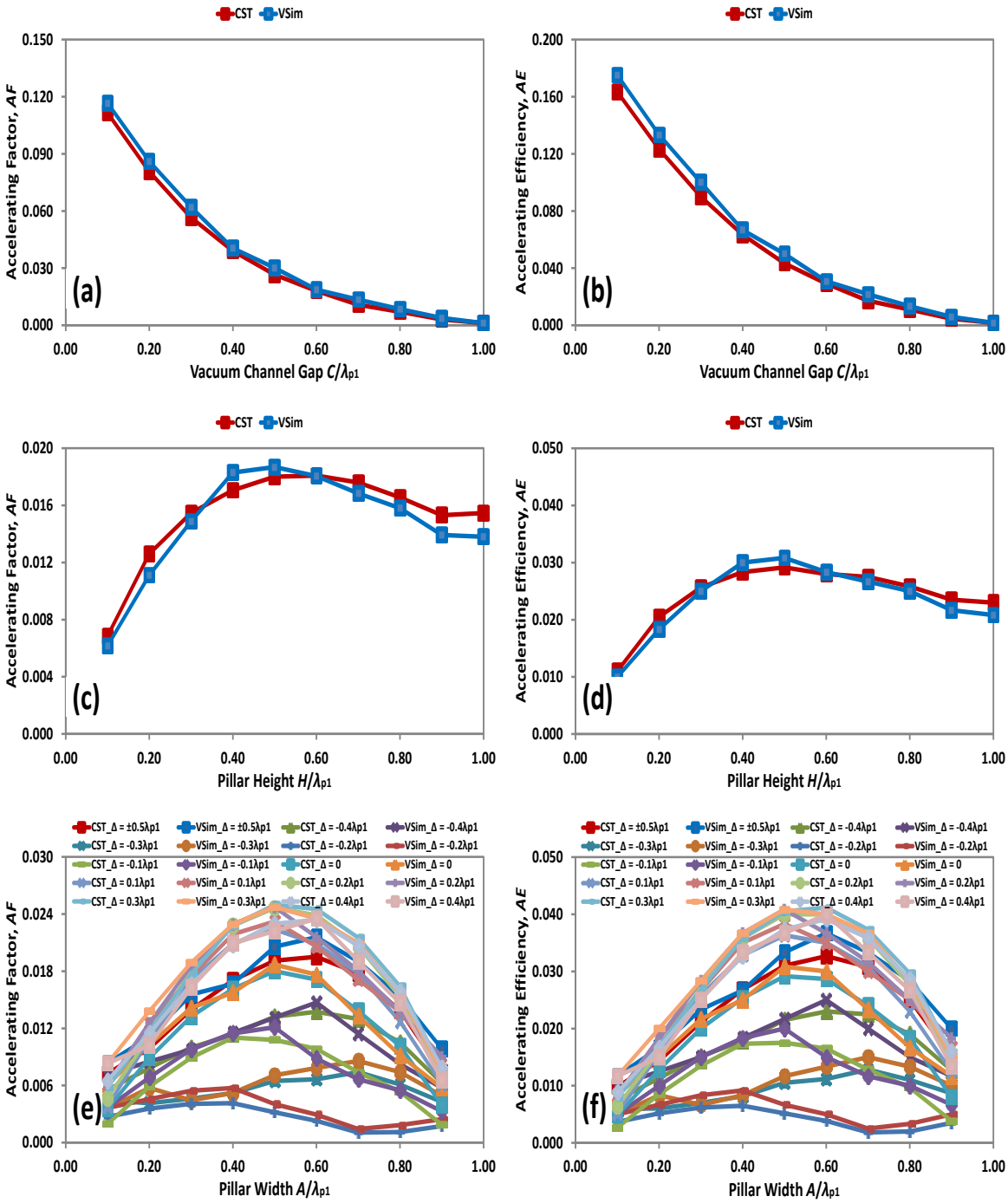

Figure 36. Optimization for a single-period dual-grating structure with first spatial harmonics, showing calculated accelerating factor *AF* ((a), (c), (e)) and accelerating efficiency *AE* ((b), (d), (f)) as functions of vacuum channel gap C ($H = 0.5\lambda_{p1}$, $A = 0.5\lambda_{p1}$ and $\Delta = 0$ m), pillar height H ($C = 0.6\lambda_{p1}$, $A = 0.5\lambda_{p1}$ and $\Delta = 0$ m), and pillar width A with variable longitudinal misalignment level Δ ($C = 0.6\lambda_{p1}$, $H = 0.5\lambda_{p1}$).

In order to find the optimum geometries for such a dual-grating structure, C, H, A, Δ are varied to maximize accelerating factor and accelerating efficiency. Reported studies [79]–[82], [124] have shown that the accelerating gradient G usually decreases for a larger vacuum channel gap C for the first spatial harmonics. This is in good agreement with Figure 36 (a) and (b) which show the effect of increasing the vacuum channel gap on the *AF* and *AE*, respectively. A channel gap of $C = 0.6\lambda_{p1} = 0.36$ μm is chosen as an acceptable parameter,

representing a trade-off between the accelerating gradient and available phase space in which high acceleration occurs. Figure 36 (c) and (d) show that the maximum *AF* and *AE* can be obtained at $H = 0.5\lambda_{p1}$ for structures with a fixed $C = 0.6\lambda_{p1}$. After fixing $C = 0.6\lambda_{p1}$ and $H = 0.5\lambda_{p1}$, we then find the optimal pillar width *A* and longitudinal misalignment level Δ. The pillar width *A* is swept from $0.1\lambda_{p1}$ to $0.9\lambda_{p1}$, combined with variable misalignment Δ from $-0.5\lambda_{p1}$ to $0.5\lambda_{p1}$ to obtain the optimum geometries. As shown in Figure 36 (e) and (f), the global maximum accelerating factor (CST: *AF* = 0.025, VSim: *AE* = 0.025) and accelerating efficiency (CST: *AE* = 0.040, VSim: *AE* = 0.041) can be easily found for a structure with $C = 0.6\lambda_{p1}$, $H = 0.5\lambda_{p1}$, $A = 0.5\lambda_{p1}$, $\Delta = 0.3\lambda_{p1}$.

The damage threshold for quartz is about 2.0 J/cm^2 for laser pulses of 100 fs [93]–[95], which is equivalent to an electric field E_{th} = 10.0 GV/m. This means that the maximum achievable gradient for first spatial harmonics in such a dual-grating structure is 0.025 × 10.0 = 0.25 GV/m. In this case, an incident laser peak field of 6.25 GV/m can be used for illumination of such an optimum dual-grating structure based on the calculated accelerating efficiency *AE* = 0.04.

Both the CST and the VSim codes have been used for modelling and optimization of these dual-grating structures. It can be seen from Figure 36 that the simulation results of both simulation codes are in very good agreement, giving confidence in the validity of the results. Finally, all the optimum geometries and simulation results are summarized in Table 1.

Table 1: Optimum parameters for the first spatial harmonics as calculated by CST and VSim for $C = 0.60\lambda_{p1}$ = 0.36 μm.

	CST	VSim
Grating period λ_{p1} (μm)	0.6	0.6
Vacuum channel gap C/λ_{p1}	0.6	0.6
Pillar height H/λ_{p1}	0.5	0.5
Pillar width A/λ_{p1}	0.5	0.5
Longitudinal misalignment Δ/λ_{p1}	0.3	0.3
Accelerating factor, *AF*	0.025	0.025
Accelerating efficiency, *AE*	0.040	0.041

(2) Second Spatial Harmonics

Secondly, a grating period $\lambda_{p2} = 0.6\lambda_0 = 1.2$ μm is considered, allowing acceleration of 25 keV electrons by the second spatial harmonics in the dual-grating structures.

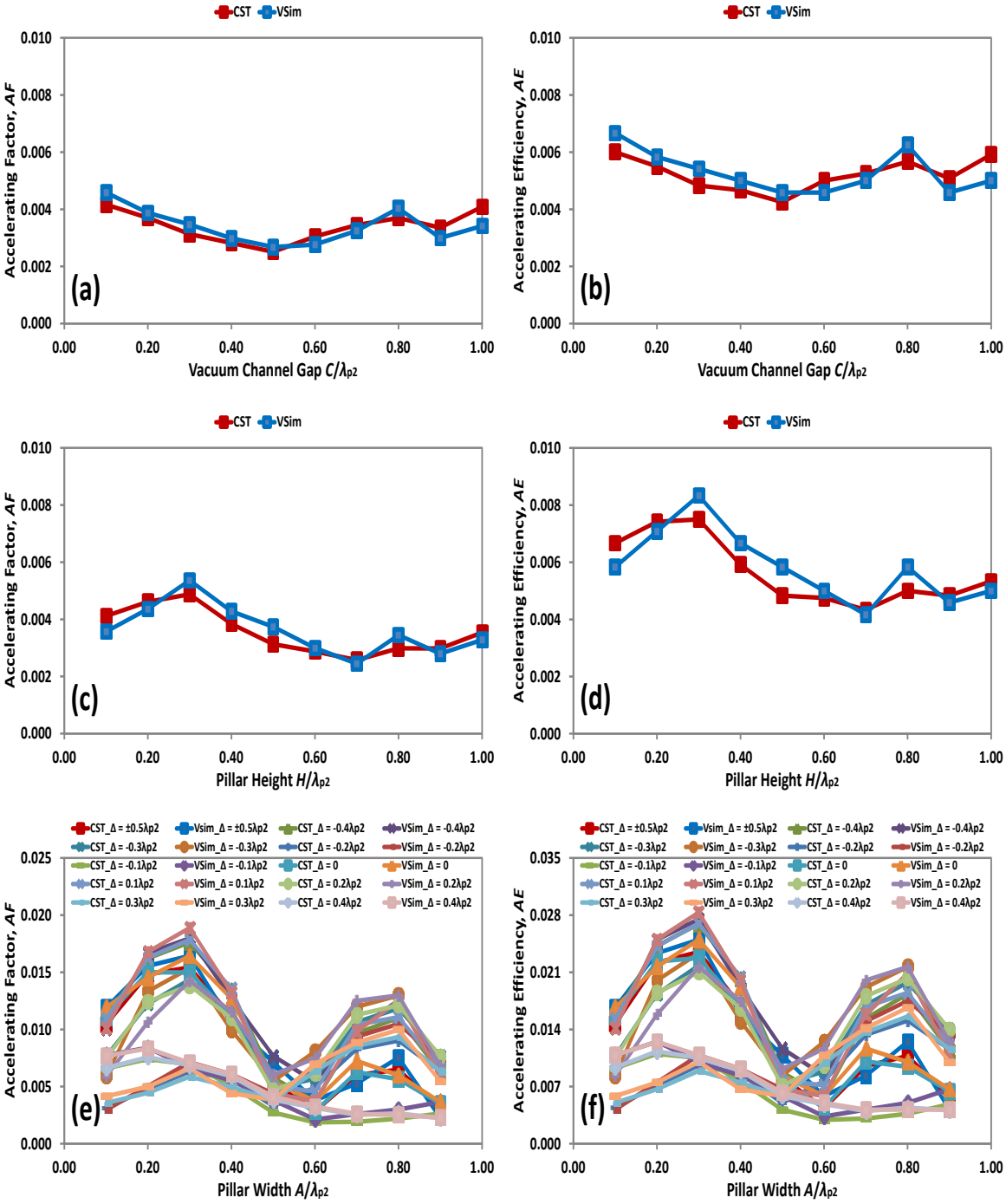

Figure 37. Optimization for a single-period dual-grating structure with second spatial harmonics, showing calculated accelerating factor *AF* ((a), (c), (e)) and accelerating efficiency *AE* ((b), (d), (f)) as functions of vacuum channel gap C ($H = 0.5\lambda_{p2}$, $A = 0.5\lambda_{p2}$ and $\Delta = 0$ m), pillar height H ($C = 0.3\lambda_{p2}$, $A = 0.5\lambda_{p2}$ and $\Delta = 0$ m), and pillar width A with variable longitudinal misalignment level Δ ($C = 0.3\lambda_{p2}$, $H = 0.3\lambda_{p2}$).

In order to compare with structures for first and third spatial harmonics, the same vacuum channel gap $C = 0.3\lambda_{p2} = 0.36$ μm is chosen. H, A, Δ are then varied to maximize

accelerating factor and accelerating efficiency with the aim of finding the optimum geometry. As shown in Figure 37 (c) and (d), the maximum *AF* and *AE* are achieved at $H = 0.3\lambda_{p2}$ for structures with a fixed $C = 0.3\lambda_{p2}$. After fixing $C = 0.3\lambda_{p2}$ and $H = 0.3\lambda_{p2}$, we use the same method to find the optimal pillar width *A* and longitudinal misalignment level Δ. The pillar width *A* is then swept from $0.1\lambda_{p1}$ to $0.9\lambda_{p1}$ combined with variable misalignment Δ from $-0.5\lambda_{p2}$ to $0.5\lambda_{p2}$, to obtain the optimum geometries. Figure 37 (e) and (f) show the global maximum accelerating factor (CST: $AF = 0.018$, VSim: $AF = 0.019$) and accelerating efficiency (CST: $AE = 0.027$, VSim: $AE = 0.028$) respectively for a structure with $C = 0.3\lambda_{p2}$, $H = 0.3\lambda_{p2}$, $A = 0.3\lambda_{p2}$, $\Delta = 0.1\lambda_{p2}$.

When the same material, quartz, is used for such a dual-grating structure, it has a breakdown field of $E_{th} = 10.0$ GV/m, so that the maximum achievable gradient for second spatial harmonics is about $0.020 \times 10.0 = 0.20$ GV/m. In this case, an incident laser peak field of 6.7 GV/m should be used to generate the maximum gradient, based on the calculated accelerating efficiency $AE = 0.03$.

In addition, it can be seen from Figure 37 (a) and (b) that the accelerating factor and accelerating efficiency do not decrease with a larger vacuum channel gap. This can be explained by the different properties of second spatial harmonics as compared to first and third spatial harmonics. Finally, simulation results from both CST and VSim codes are in good agreement with each other; all the optimum geometries and simulation results are summarized in Table 2.

Table 2. Optimum parameters for the second spatial harmonics as calculated by CST and VSim for $C = 0.30\lambda_{p2} = 0.36$ μm.

	CST	VSim
Grating period λ_{p2} (μm)	1.2	1.2
Vacuum channel gap C/λ_{p2}	0.3	0.3
Pillar height H/λ_{p2}	0.3	0.3
Pillar width A/λ_{p2}	0.3	0.3
Longitudinal misalignment Δ/λ_{p2}	0.1	0.1
Accelerating factor, *AF*	0.018	0.019
Accelerating efficiency, *AE*	0.027	0.028

(3) Third Spatial Harmonics

Thirdly, a grating period of $\lambda_{p3} = 0.9\lambda_0 = 1.8$ μm is analysed, allowing the use of the third spatial harmonic for acceleration of 25 keV electrons in the dual-grating structures.

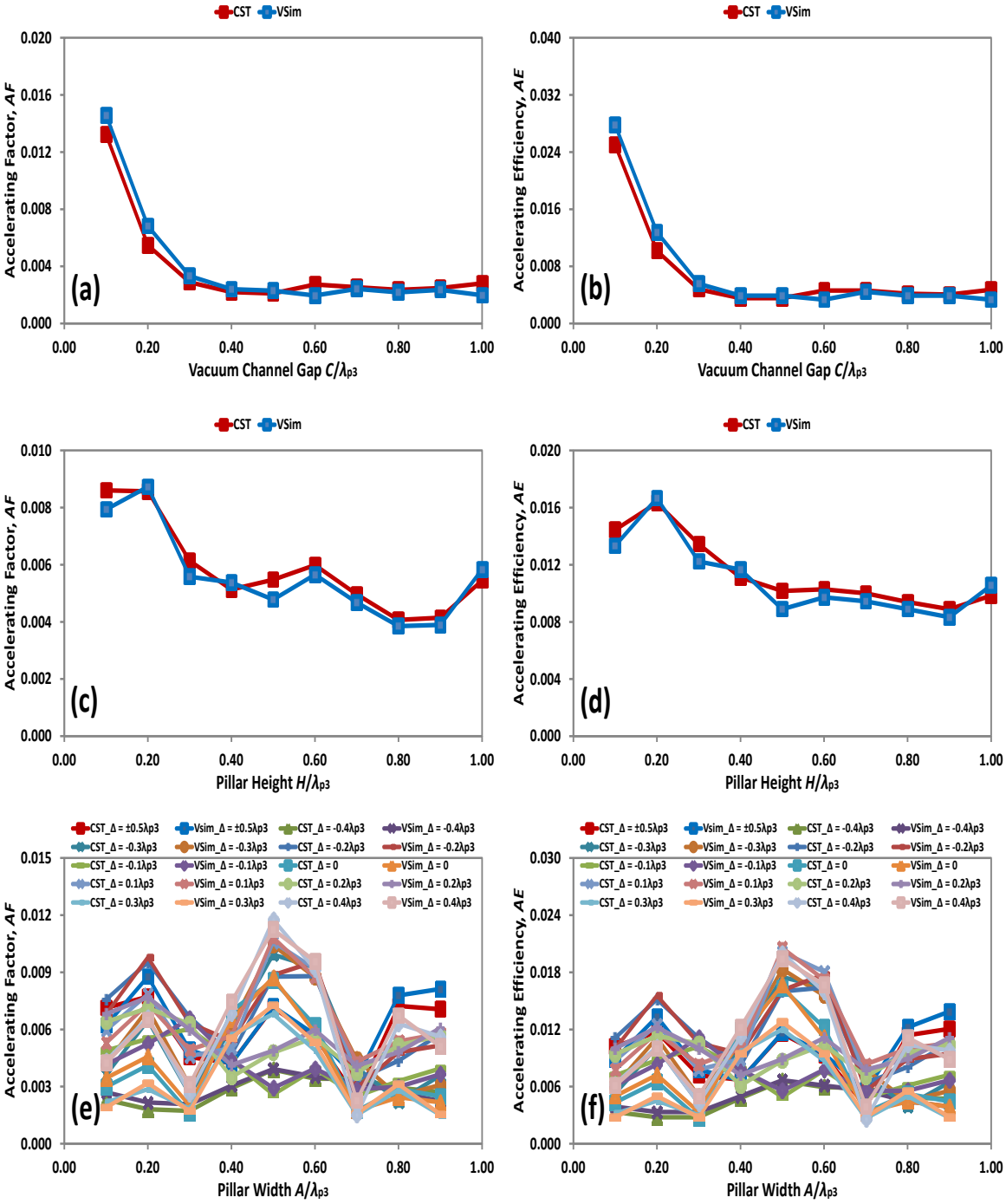

Figure 38. Optimization for a single-period dual-grating structure with third spatial harmonics, showing calculated accelerating factor *AF* ((a), (c), (e)) and accelerating efficiency *AE* ((b), (d), (f)) as functions of vacuum channel gap *C* ($H = 0.5\lambda_{p3}$, $A = 0.5\lambda_{p3}$ and $\Delta = 0$ m), pillar height *H* ($C = 0.2\lambda_{p3}$, $A = 0.5\lambda_{p3}$ and $\Delta = 0$ m), and pillar width *A* with variable longitudinal misalignment level Δ ($C = 0.2\lambda_{p3}$, $H = 0.2\lambda_{p3}$).

The same vacuum channel gap $C = 0.2\lambda_{p3} = 0.36$ μm is chosen for the geometry optimizations. Based on the same optimization procedures, the global maximum accelerating

factor (CST: AF = 0.012, VSim: AF = 0.011) and accelerating efficiency (CST: AE = 0.020, VSim: AE = 0.019) can be found respectively for a structure with $C = 0.2\lambda_{p3}$, $H = 0.2\lambda_{p3}$, $A = 0.5\lambda_{p3}$, $\Delta = 0.4\lambda_{p3}$, as seen in Figure 38. Furthermore, as both CST and VSim codes present similar simulation results, the numerical results may be benchmarked even in the absence of experimental studies. All the optimum parameters are summarized in Table 3.

Given the use of the same material, quartz, for such a dual-grating structure, the breakdown field equals to E_{th} = 10.0 GV/m. In this situation, the maximum achievable gradient for third spatial harmonics is about 0.010 × 10.0 = 0.10 GV/m. In order to generate such a maximum gradient, an incident laser peak field of 5.0 GV/m should be used according to the calculated accelerating efficiency AE = 0.02.

By comparing different spatial harmonics, it is clear that the first spatial harmonics is the most efficient to accelerate non-relativistic electrons in the terms of accelerating factor and accelerating efficiency. If fabrication limitations on grating period ($\lambda_p > 0.6$ μm) are discounted, first spatial harmonics are preferred to accelerate 25 keV (β = 0.3) electrons. In this case an accelerating gradient of up to 250 MV/m can be expected. When fabrication limitations have to be considered for a grating period $\lambda_p > 0.6$ μm, the optimum identified is a compromise between acceleration performance and fabrication limitations, in acceleration using the second spatial harmonics ($\lambda_{p2} = 0.6\lambda_0$) to accelerate 25 keV ($\beta$ = 0.3) electrons. In this case an accelerating gradient of up to 200 MV/m can be generated.

Table 3. Optimum parameters for the third spatial harmonics as calculated by CST and VSim for $C = 0.20\lambda_{p3}$ = 0.36 μm.

	CST	VSim
Grating period λ_{p3} (μm)	1.8	1.8
Vacuum channel gap C/λ_{p3}	0.2	0.2
Pillar height H/λ_{p3}	0.2	0.2
Pillar width A/λ_{p3}	0.5	0.5
Longitudinal misalignment Δ/λ_{p3}	0.4	0.4
Accelerating factor, AF	0.012	0.011
Accelerating efficiency, AE	0.020	0.019

3.3.3 Optimizations for Acceleration of Relativistic Electrons

After optimization on the acceleration of non-relativistic electrons, I start to investigate the acceleration of relativistic electrons in dual-grating structures. Both CST and VSim codes, based on the FDTD method, are used to compute the electric and magnetic fields generated in the structure. A uniform plane wave with a wavelength of λ_0 = 2.0 μm illuminates the bottom side of the single-period dual-grating structure, as shown in Figure 35. A grating period of λ_p = 2.0 μm is chosen so that phase synchronicity [88] can be achieved between the first spatial harmonics (n = 1) and relativistic electrons (β = 1). Quartz with a refractive index n_r = 1.5 is chosen as the grating material.

The first design criterion is to generate a periodic π phase shift for wave front in the channel centre to remain synchronous with relativistic electrons. This can be achieved by initially setting pillar height $H = \frac{\lambda_p}{2(n_r-1)} = \lambda_p$. It can be seen in Figure 39 (a) that the accelerating factor gradually decreases when the vacuum channel gap C increases. Figure 39 (b) shows that the deflecting factor drops with C for $C \leq 0.6\lambda_p$, but it turns to increase when $C > 0.7\lambda_p$. A channel gap of $C = 0.5\lambda_p$ is chosen as an acceptable parameter due to a trade-off between the accelerating gradient with weak deflecting force and available phase space in which high acceleration occurs. Figure 39 (c) shows that the maximum AF can be obtained at $H = 0.8\lambda_p$ for the structures with a fixed $C = 0.5\lambda_p$ while the peak DF occurs at $H = 0.7\lambda_p$ as shown in Figure 39 (d). Fixing the grating, $C = 0.5\lambda_p$ and $H = 0.8\lambda_p$, we then set out to find the optimal pillar width A and longitudinal misalignment level Δ. The simulations sweep the pillar width A from $0.1\lambda_p$ to $0.9\lambda_p$ combining with variable misalignment Δ from $-0.5\lambda_p$ to $0.5\lambda_p$ to obtain the optimum geometries. As shown in Figure 39 (e), a global maximum accelerating factor (CST: AF = 0.170, VSim: AF = 0.173) can be easily found for a structure with $C = 0.5\lambda_p$, $H = 0.8\lambda_p$, $A = 0.7\lambda_p$, Δ = 0 m. It is interesting to note that the structures usually perform best when perfectly aligned (Δ = 0 m), which can be seen in Figure 39 (e) and (f). This agrees well with results from England *et al.* [97] in which they found that the weakest transverse deflecting force appeared for gratings with perfect alignment. All the optimum parameters are summarized in Table 4.

The damage threshold for quartz is about 2 J/cm^2 for laser pulses of 100 fs [93]–[95], which is equivalent to an electric field of E_{th} = 10.0 GV/m, so the maximum achievable gradient for such an optimum structure is 0.170 × 10.0 = 1.70 GV/m.

In addition, the simulation results from both CST and VSim codes agree well with each other, verifying the numerical methods for modelling and optimization of dual-grating structures.

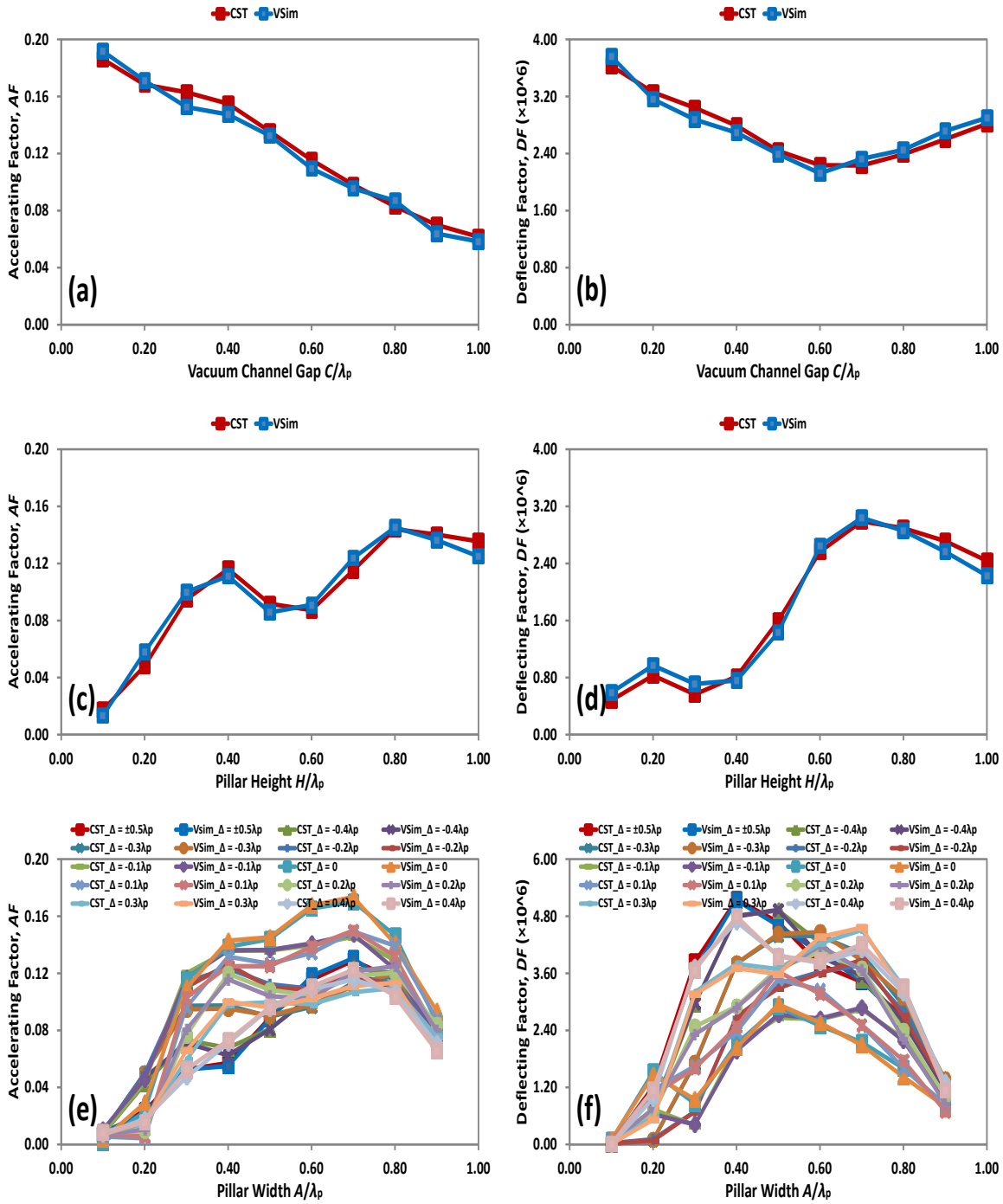

Figure 39. Optimization for a single-period dual-grating structure to accelerate relativistic electrons, with calculated accelerating factor *AF* ((a), (c), (e)) and deflecting factor *DF* ((b), (d), (f)) as functions of vacuum channel gap C ($H = \lambda_p$, $A = 0.5\lambda_p$ and $\Delta = 0$ m), pillar height H ($C = 0.5\lambda_p$, $A = 0.5\lambda_p$ and $\Delta = 0$ m), and pillar width A with variable longitudinal misalignment level Δ ($C = 0.5\lambda_p$, $H = 0.8\lambda_p$).

Table 4. Optimum parameters for acceleration of relativistic electrons as calculated by CST and VSim for $C = 0.50\lambda_p = 1.0$ μm.

	CST	VSim
Grating period λ_p (μm)	2.0	2.0
Vacuum channel gap C/λ_p	0.5	0.5
Pillar height H/λ_p	0.8	0.8
Pillar width A/λ_p	0.7	0.7
Longitudinal misalignment Δ/λ_p	0.0	0.0
Accelerating factor, AF	0.170	0.173

3.3.4 Proposed Design of a Multi-stage DLA

In this section, a multi-stage DLA [89] is studied analytically, accelerating electrons from non-relativistic energy to relativistic regime using the same laser wavelength (λ_0 = 2000 nm) and grating material (quartz with a refractive index n_r = 1.50), as seen in Figure 40: a first-stage non-relativistic DLA from 25 keV (β = 0.3) to 1 MeV (β = 0.94), and a second-stage relativistic DLA from 1 MeV to 1 GeV. In subsections 3.3.2 and 3.3.3, optimization studies have been carried out for the acceleration of non-relativistic (25 keV, β = 0.3) and highly relativistic electrons in a dual-grating structure. It was found that the first spatial harmonics have the best accelerating performance to interact with 25 keV electrons as compared to the second and third spatial harmonics.

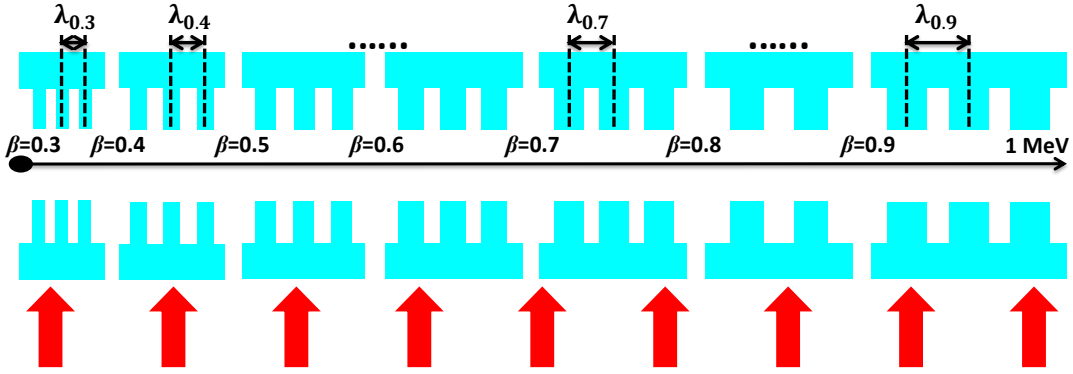

Figure 40. Sketch of a multi-staged dual-grating DLA to accelerate electrons from non-relativistic energy to relativistic regime, where red arrows represent the laser beam from the bottom side.

Firstly, I evaluate the length for the first-stage non-relativistic DLA, which starts at an injection energy of 25 keV and accelerates to 1 MeV exploiting different spatial harmonics. Through similar optimization procedures, the optimum accelerating efficiency for different spatial harmonics can be achieved to accelerate non-relativistic electrons from 25 keV to 1 MeV in dual-grating structures with a fixed vacuum channel gap of 360 nm = 0.18λ_0, as seen in Figure 41. It is found that the accelerating efficiency *AE* gradually increases with electron energy due to wave matching between the wave vector of the incident laser k_0 and of the synchronous spatial harmonics $k = k_0/\beta$. It should be noted that the grating period λ_p gradually increases with higher electron speed β in order to maintain the synchronicity condition $\lambda_p = n\beta\lambda_0$ in the simulations.

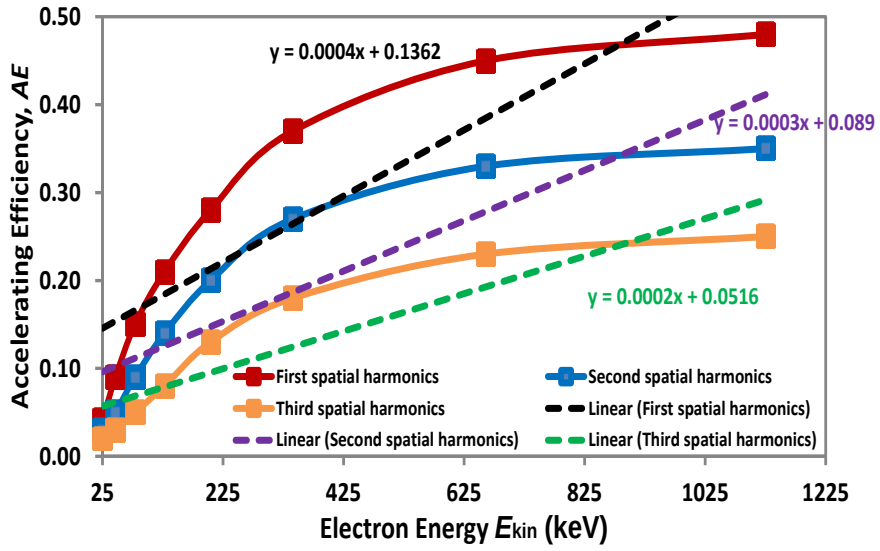

Figure 41. Optimum accelerating efficiency *AE* as a function of electron speed β from 25 keV (β = 0.3) to 1.0 MeV (β = 0.94) for the first, second and third spatial harmonics, respectively.

In order to analyse Figure 41, three linear fits are used to approximate the relationship between the accelerating efficiency and electron energy from 25 keV to 1.0 MeV: $G/E_0 = 4 \times 10^{-7}E_{\text{kin}} + 0.1362$ for the first spatial harmonics, $G/E_0 = 3 \times 10^{-7}E_{\text{kin}} + 0.0890$ for the second spatial harmonics, $G/E_0 = 2 \times 10^{-7}E_{\text{kin}} + 0.0516$ for the third spatial harmonics, where G is the accelerating gradient, E_0 is the incident laser field, and E_{kin} is the kinetic energy for electrons with units of eV. Combing these equations with the definition of the acceleration gradient $qG = \frac{\mathrm{d}E_{\text{kin}}}{\mathrm{d}z}$ yields the solutions $E_{\text{kin}} = \left(E_{\text{kin}}^{\text{i}} + 0.03405 \times 10^7\right)\mathrm{e}^{qE_0z\times 4\times 10^{-7}\mathrm{eV}^{-1}} - 0.03405 \times 10^7$ for the first spatial harmonics, $E_{\text{kin}} = \left(E_{\text{kin}}^{\text{i}} + 0.02967 \times 10^7\right)\mathrm{e}^{qE_0z\times 3\times 10^{-7}\mathrm{eV}^{-1}} - 0.02967 \times 10^7$ for the second spatial harmonics, and $E_{\text{kin}} = \left(E_{\text{kin}}^{\text{i}} + 0.02580 \times 10^7\right)\mathrm{e}^{qE_0z\times 2\times 10^{-7}\mathrm{eV}^{-1}} - 0.02580 \times 10^7$ for the third spatial

harmonics, where $E_{kin}^{i} = 25$ keV is kinetic energy of the electrons at injection and q is the charge of a single particle. After substituting E_{kin} = 1.0 MeV into these solutions, the accelerating lengths for different spatial harmonics can be calculated. Table 5 shows the analytical-calculated lengths of these DLA structures from 25 keV to 1 MeV for all three spatial harmonics.

It can be seen in Table 5 that the first spatial harmonics are most efficient for accelerating electrons from 25 keV to 1 MeV, compared to the second and third spatial harmonics. The corresponding DLA lengths for first, second and third spatial harmonics are 3.25 mm, 4.65 and 7.46 mm, respectively, when the incident laser electric field is 1.0 GV/m. However, it is noted that acceleration exploiting the first spatial harmonic may not be feasible for non-relativistic electrons due to fabrication limitations on the grating period. When using the third spatial harmonics for acceleration, the accelerating efficiency is much lower than the first and second spatial harmonics. Therefore, the second spatial harmonics with an initial grating period of 930 nm is a good compromise between accelerating efficiency and fabrication limitation. Please note that the length of focusing structures is not included in our calculations although they are especially needed inside the non-relativistic DLA.

Table 5. Calculated length of a DLA for different spatial harmonics which accelerates from 25 keV to 1 MeV.

	E_0 = 1.0 GV/m	E_0 = 2.0 GV/m
First spatial harmonics	3.25 mm	1.62 mm
Second spatial harmonics	4.65 mm	2.32 mm
Third spatial harmonics	7.46 mm	3.73 mm

In the second-stage relativistic DLA, the electrons are accelerated from 1 MeV to highly relativistic energies. The acceleration gradient G is calculated to be about $0.5E_0$ for dual-grating structures with a fixed vacuum channel gap of 360 nm = $0.18\lambda_0$ which is illuminated by a single laser beam. Hence, I can find the calculated length for a relativistic DLA from 1 MeV to highly relativistic regime, as seen in Table 6. It is found that the calculated length scales linearly with the final energy of the relativistic electrons and inversely with the incident laser field.

Table 6. Calculated length of a relativistic DLA for different final energies of the electron beam.

Final electron energy	E_0 = 1.0 GV/m	E_0 = 2.0 GV/m
100 MeV	0.2 m	0.1 m
1 GeV	2.0 m	1.0 m
10 GeV	20.0 m	10.0 m

3.4 Wakefield Study

Due to the micron-scale beam apertures in the dual-grating structures, wakefields are of particular interest in order to fully characterize and optimize these structures. Wakefields are electromagnetic radiations caused by the interaction between a charged particle beam and its surrounding environment, which for a DLA is dielectric. Under beam loaded conditions, wakefields are generally left behind the bunch charge, especially for the relativistic beams considered here. They can act on the bunch itself because of the finite bunch length, or on a nearby trailing bunch, thereby effecting the accelerating performance in terms of stored current. As the beam traverses the vacuum channel of dual-grating structures, the excited wakefields can be an issue since the energy loss is inversely proportional to the channel gap dimension. Many instability phenomena may occur because of these wakefields, produced by the beam and acting back on itself. The wakefields produced by the beam may affect the energy gain and deflect the beam through a transverse momentum kick.

In order to perform wakefield simulations, CST Particle studio with wakefield solver is used, from the CST suite. An electron bunch with 4 fC charge and 30 fs length is loaded to travel through the channel in *z* direction of an optimized 100-period structure with a grating period of 2.0 μm, for wakefield simulations. It should be noted here that a 100-period dual-grating structure is used for our simulations due to limitations of our computing hardware. In the subsequent simulations for laser-bunch interaction, an electron bunch from CLARA [119] with 0.1 pC charge is used. Through particle tracking simulations, it is found that only 4% of such a CLARA bunch travels through the vacuum channel of an optimized structure with a gap of 1.0 μm. The bunch charge is therefore chosen to be 4 fC in this case. As the bunch travels along the channel centre, it generates electromagnetic fields which propagate in the vacuum channel. The wakefields are reflected back by dielectric gratings and interact with the bunch itself, which may lead to energy loss or deflection of electrons in the bunch.

The wake potential [125] in a structure is obtained by integration of the electromagnetic forces acting on a test charge at a distance behind a heading charge. To calculate the wake potential, the heading charge is replaced by a bunch of particles, of finite length, and the distance to the test charge is measured from the bunch centre. Therefore, the wake function is the wake potential of a delta-function distribution, and can be considered as a Green's function for the wake potential of a finite particle distribution in the same structure. Ideally, I want to perform this integration over the full length of the structure, which is not feasible due to the large computational space required. Therefore, I perform the simulation for a finite length of the structure and calculate the wake potential per period. Figure 42 (a) shows the longitudinal (*z*-component) wakefield distribution on the *z*-axis for an optimized 100-period structure. It can be seen in Figure 42 (a) that the head bunch experiences a maximum longitudinal decelerating wakefield of 1.12 MV/m while the tail bunch sees an accelerating field of 1.12 MV/m. After travelling out of a structure with a length of 200 μm, the maximum energy gain and energy loss are 224 eV, which can be considered negligible for the 50 MeV electron bunch. In this situation, the longitudinal wakefield has no effect on the energy spectrum for a 50 MeV electron bunch. This is verified by the PIC simulations in the following subsection 3.5.4. In addition, the transverse wakefield, which deflects electrons, is also negligible as shown in Figure 42 (b) due to the small transverse size and symmetrical Gaussian profile in the *y* direction.

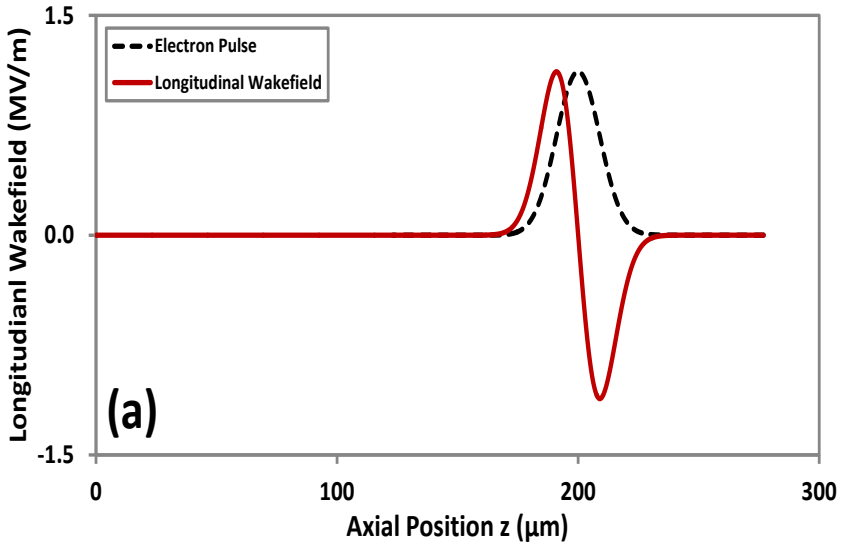

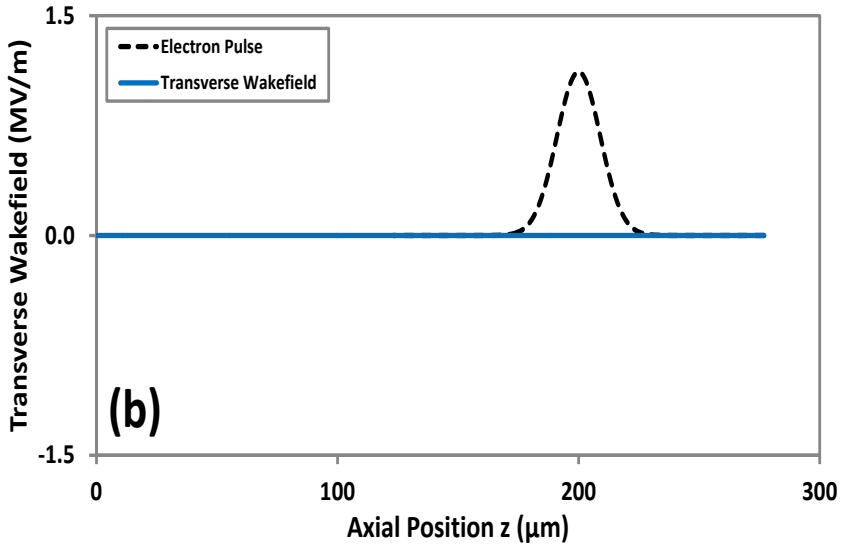

Figure 42: Simulated longitudinal (a) and transverse (b) wakefield distribution on *z*-axis. The electron bunch travels along the *z*-axis.

3.5 Laser-bunch Interaction

In this section, I use the beam parameters of the future CLARA to load an electron bunch into an optimized dual-grating structure where it interacts with a realistic laser pulse. The emittance, energy spread, and loaded accelerating gradient for modulated electrons are then analyzed in detail.

3.5.1 Optimum Structure Geometry

From optimizations in subsection 3.3.3, a dual-grating structure with $C = 0.5\lambda_p$, $H = 0.8\lambda_p$, $A = 0.7\lambda_p$ and $\Delta = 0$ m was found to be desirable as an optimum choice for acceleration of relativistic electrons. Such an optimized dual-grating structure with 100 periods as illustrated in Figure 44 is chosen for subsequent beam quality studies, and the geometry parameters are summarized in Table 7. It should be noted that a 100-period optimum structure with a length $LZ = 200$ μm is chosen for our PIC simulations due to limitations in our computing hardware.

Table 7. Geometry details of an optimized 100-period dual-grating structure.

Geometry	
Number of periods	100
Grating period λ_p	2.0 μm
Vacuum channel gap C	1.0 μm = 0.5λ_p
Pillar height H	1.6 μm = 0.8λ_p
Pillar width A	1.4 μm = 0.7λ_p
Misalignment level Δ	0.0 m

3.5.2 Laser Parameters

In the simulation, a linearly polarized Gaussian laser plane wave, as shown in Figure 43, is launched to propagate along the *y*-axis to illuminate the optimum dual-grating structure:

$$E_z = E_p e^{-\left(\frac{z}{w_z}\right)^2 - 2\ln 2\left(\frac{t}{\tau_0}\right)^2} \cos(2\pi f t - k_0 y + \phi), \quad (48)$$

where E_p, w_z, τ_0, f, k_0 and ϕ represent the peak field, *z*-axis waist radius, FWHM duration, angular frequency, wave number, and phase term, respectively. All relevant parameters are described in Table 8. Such a laser pulse can be emitted from thulium-fiber laser system. The peak laser field E_p is set to 5.0 GV/m and the resulted maximum field in the structure E_m = 7.60 GV/m is still under the damage threshold, which yields an unloaded gradient G = 1.29 GV/m according to G/E_m = 0.170 from the geometry optimization studies. In its co-moving frame, the electrons experience a Gaussian-distributed temporal field $E_t = G_p e^{-\left(\frac{z}{w_{int}}\right)^2}$ with a characteristic interaction length $w_{int} = \left(\frac{1}{w_z^2} + \frac{2\ln 2}{(c\tau_0)^2}\right)^{-0.5}$ = 22.7 μm, as described in Ref. [92], [107], where c is the speed of light. Considering z = 0 to be the longitudinal centre of a multi-period dual-grating structure, an energy gain $\Delta E_m = \int_{-0.5LZ}^{0.5LZ} qG_p e^{-\left(\frac{z}{w_{int}}\right)^2} dz$ is obtained, where LZ is the longitudinal length of a multi-period dual-grating structure and q is the charge on a single electron. It can be easily seen that for $LZ \geq 200$ μm a peak gradient of G_p = 1.0 GV/m results in a energy gain of $\Delta E_m \approx \sqrt{\pi} w_{int}$ = 40 keV, which is used to calculate the loaded gradient for subsequent analysis.

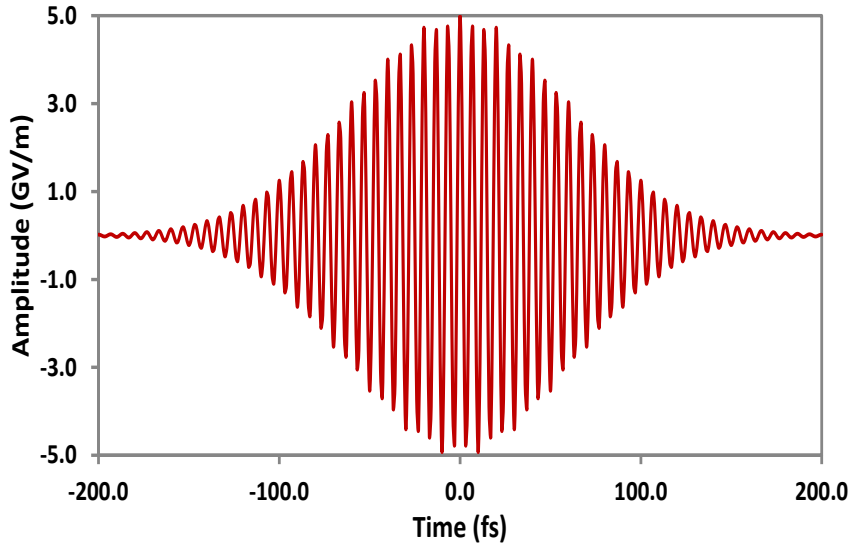

Figure 43. The electric field envelope of the laser plane wave.

Table 8. Parameters of the Gaussian laser plane wave used in the simulation.

Laser characteristics	
Propagation direction	$+y$
Wavelength λ	2.0 μm
Peak laser field E_p	5 GV/m
FWHM duration τ_0	100 fs
Waist radius w_z	50 μm
Frequency f	150 THz

3.5.3 Electron Bunch Parameters

CLARA is a normal-conducting linear electron accelerator capable of accelerating electrons to 250 MeV with bunch charge of up to 250 pC. Here we will use beam parameters from the CLARA front-end for our simulations. Table 9 shows the detailed CLARA bunch parameters reproduced from Ref. [119].

Table 9. CLARA bunch parameters used in our simulation.

Bunch parameters	CLARA	Simulation
Bunch energy [MeV]	50-250	50
Bunch charge [pC]	≤ 250	0.1
Bunch RMS length [μm]	9-300	9
Bunch RMS radius [μm]	10-100	10
Bunch density [m^{-3}]	10^{18}-10^{22}	4.4×10^{19}
Normalized emittance [mm·mrad]	≤ 1	0.2
Energy spread	(0.01-0.10)%	0.05%

When CLARA works in ultra-short pulse mode [119], a short electron bunch with a longitudinal RMS length of 9 μm can be generated. When such a bunch is transmitted through the energy collimators, a bunch with a charge of 0.1 pC, and energy spread of 0.05% is expected. It can then be focused by a permanent quadrupole magnet to give a transverse RMS radius of 10 μm, as presented in Table 8, before injection into the optimum dual-grating structure. Here, the transverse size is much bigger than the vacuum channel gap of 1 μm, so that only a small fraction of electrons traverses through the vacuum channel of the structure. Those electrons travelling through the quartz substrate and grating pillars suffer significant energy loss due to collisional straggling [90] in the dielectric material, so they are excluded in subsequent analysis. All of our simulations focus only on those electrons modulated by the laser field in the vacuum channel, for analysis in terms of emittance and energy spread, which can be seen in Figure 44. In addition, considering that the electron energy of 50 MeV is highly relativistic, space charge is not taken into account in our simulations.

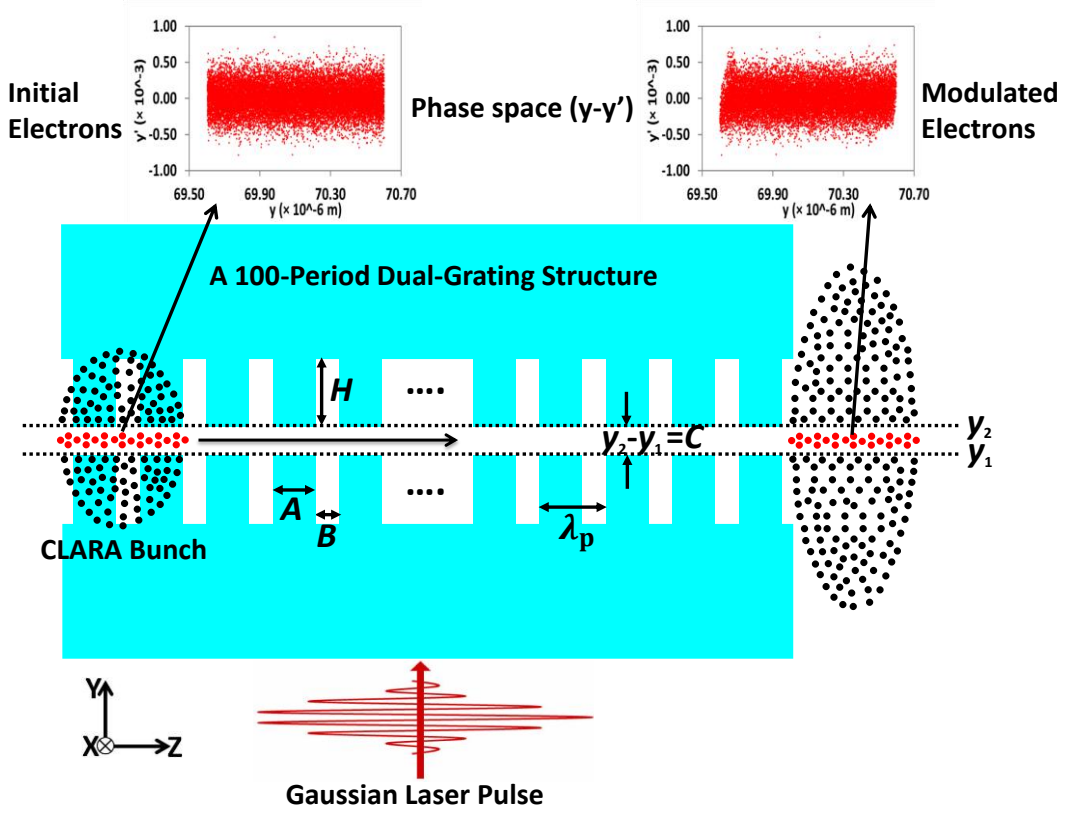

Figure 44. Schematic of a CLARA electron bunch travelling through the optimum structure to interact with a Gaussian laser pulse, where the phase spaces for initial and modulated electrons are shown in subplots.

3.5.4 The CLARA Bunch Travels Through The Structure When The Laser Is Off

In the first PIC simulation, the CLARA electron bunch travels through the optimum structure without interacting with the laser. The wakefield it excites is reflected back by dielectric gratings and interacts with the bunch itself, which may result in energy loss or deflection of those electrons in the bunch tails in terms of its final emittance and energy spread. The mesh size is set to 10 nm (z) × 10 nm (y) so that the results are convergent. 500,000 macro particles, which are close to the number of electrons for a bunch charge of 0.1 pC, are used for our particle tracking simulations. It is found that about 4% of the 50 MeV bunch is transmitted through the vacuum channel gap of 1.0 μm. When the bunch travels out of the optimum structure, the charge is 3.9 fC, transverse RMS normalized emittance is 5.5 nm and energy spread is 0.05% for those electrons between the y_1 and y_2 planes (see Figure 44). The final bunch energy spectrum as shown in Figure 45, which is calculated from the results of each individual particle trace, indicates that the longitudinal wakefield has a weak force on the bunch itself after comparison with the initial spectrum.

This agrees well with the simulated results from the longitudinal wakefield studies in section 3.4. This could also be used for comparison with the laser-on case which follows.

3.5.5 The CLARA Bunch Travels Through The Structure When The Laser Is On

In the second simulation scenario, the CLARA electron bunch is injected into the optimum structure to interact with the laser, as summarized in Table 7. From particle tracking simulations, it is found that the transverse RMS normalized emittance is 5.7 nm and the RMS energy spread is 0.103% for those modulated electrons when the bunch travels out of the structure (see Figure 44), corresponding to increases of 3.6% for emittance and 106% for energy spread compared to those of the laser-off case. With an RMS bunch length of 9 μm, the electrons are able to sample all phases of the laser field in the channel gap, causing some electrons to gain energy from acceleration while others are decelerated, which generates a big energy spread. The minor emittance difference may be explained by a weak deflecting force excited by the laser plane wave. It also indicates, however, that the laser field inside the structure does not have an obvious effect on the final bunch transverse emittance at such a short interaction length (w_{int} = 22.7 μm).

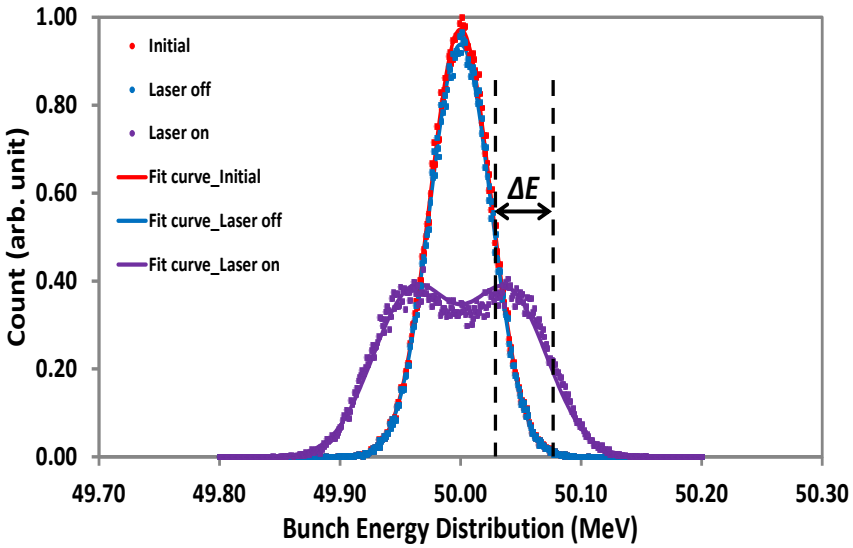

Figure 45. Bunch energy distribution for initial electrons and modulated electrons with the laser off and on. Electrons travelling through the quartz substrate and grating pillars are not shown in this figure.

The CLARA electron bunch can be partitioned into a series of short slices of length $\Delta t \ll \lambda_0/c$. After interacting with the sinusoidal electric field in the channel gap of the structure, each slice of the electron bunch experiences a net energy shift described by

$$g(\Delta t, \Delta E) = \Delta E \cos\left(\frac{2\pi c}{\lambda_0}\Delta t\right), \tag{49}$$

where ΔE is the maximum energy gain for the electrons. For a bunch with a Gaussian distributed energy spectrum, when all contributions from each slice are superimposed, it is easily predicted that the energy spectrum will be changed to a double-peaked profile [47], [48], [112], as shown in Figure 45. Using the Gaussian fits to these energy spectra, the maximum energy gain is calculated from the difference between the abscissa of the half-width at half-maximum (HWHM) point for a laser-on spectrum and a laser-off spectrum [47], [48]. Figure 45 demonstrates that the maximum energy gain is ΔE = 46 keV, corresponding to a maximum accelerating gradient of G = 1.15 GV/m. Given a maximum electric field generated in the structure E_m = 7.60 GV/m, the accelerating factor $AF = G/E_m$ = 0.151 can be compared with the unloaded AF = 0.170 from analytical simulations in subsection 3.3.3.

3.6 Beam Quality Optimizations

In this section, I study in detail some factors influencing the final beam quality in terms of emittance and energy spread. Figure 46 (a) and (b) illustrate that the emittance and energy spread rise with a larger peak laser field, which induces a stronger accelerating and deflecting field for electrons to experience. For a peak laser field of 1 GV/m, small increases of 0.4% for emittance and 6% for energy spread are expected, but at the cost of a reduced accelerating gradient. With a bigger laser waist radius and FWHM duration, the emittance and energy spread increase as shown in Figure 46 (c)-(f). This is expected, because the interaction length w_{int} is related to laser waist radius and FWHM duration. Figure 46 (g) and (h) show that the emittance and energy spread remain constant when the bunch charge Q is between 0.02 pC and 2.5 pC, and increase when Q > 2.5 pC, which corresponds to a bunch density of 1.1×10^{21} /m^3. This means that a bunch density higher than 1.1×10^{21} /m^3 can excite a stronger longitudinal and transverse wakefield, which results in larger emittance and energy spread. Based on these analyses, a high peak laser field with long waist radius and FWHM duration is preferred to achieve a considerable energy gain in long-range acceleration; however, the resulting emittance increase could be an issue. A low bunch density of $<1.1\times10^{21}$ /m^3 is desirable to load into such a dual-grating structure to interact with laser pulses, in which a small emittance increase of ~3.6% can be achieved. In addition, the deflecting force can be compensated for by symmetric illumination using two laser beams from opposite sides due to excitation of opposite deflecting fields.

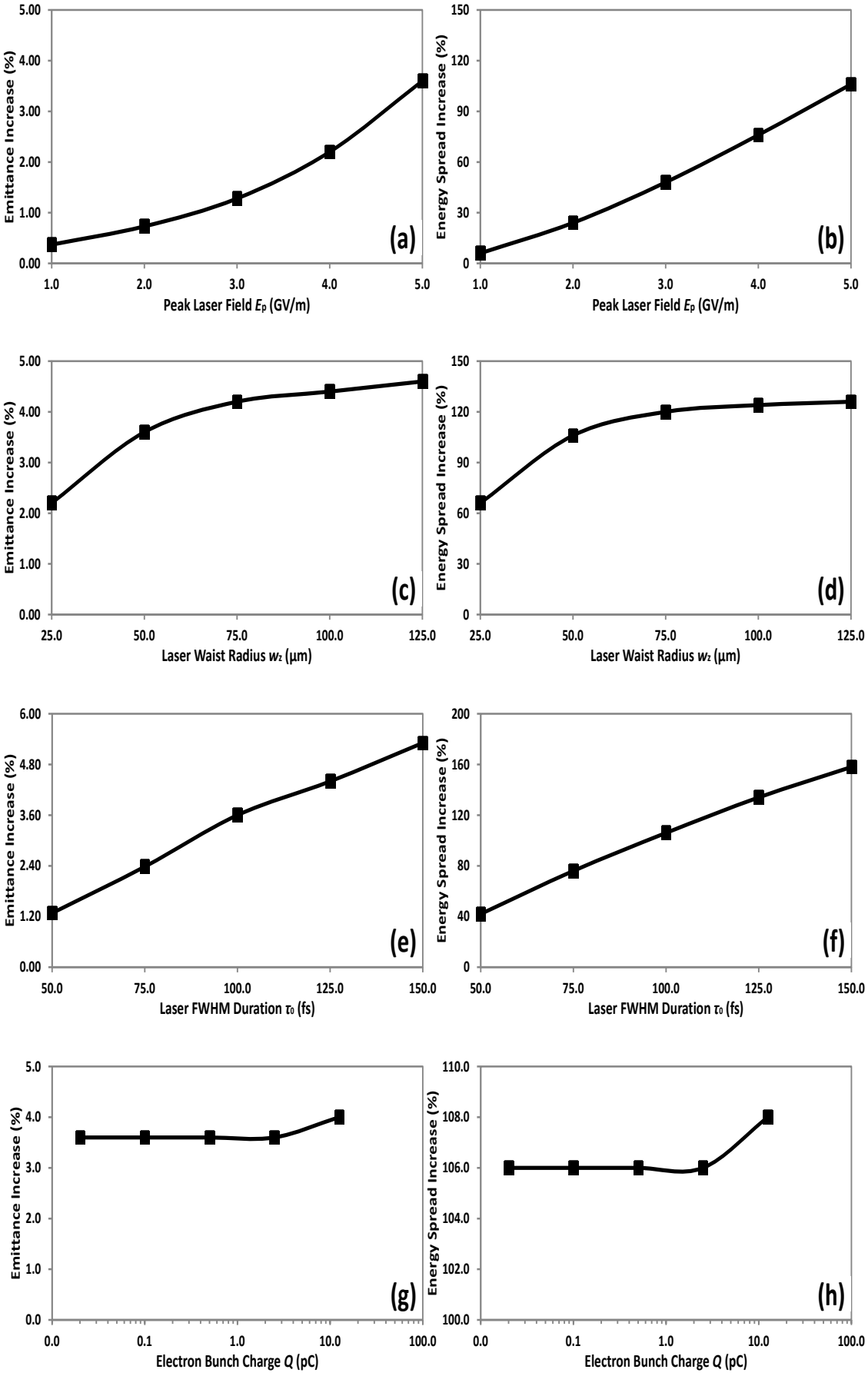
Emittance Increase (%)
Peak Laser Field E_P (GV/m)
(a)
Energy Spread Increase (%)
Peak Laser Field E_P (GV/m)
(b)
Emittance Increase (%)
Laser Waist Radius w_z (μm)
(c)
Energy Spread Increase (%)
Laser Waist Radius w_z (μm)
(d)
Emittance Increase (%)
Laser FWHM Duration τ_0 (fs)
(e)
Energy Spread Increase (%)
Laser FWHM Duration τ_0 (fs)
(f)
Emittance Increase (%)
Electron Bunch Charge Q (pC)
(g)
Energy Spread Increase (%)
Electron Bunch Charge Q (pC)
(h)

Figure 46. Emittance ((a), (c), (e), (g)) and energy spread ((b), (d), (f), (h)) for modulated electrons as functions of peak laser field E_p (w_z = 50 μm, τ_0 = 100 fs, Q = 0.1 pC), laser waist radius w_z (E_p = 5.0 GV/m, τ_0 = 100 fs, Q = 0.1 pC), laser FWHM duration τ_0 (E_p = 5.0 GV/m, w_z = 50 μm, Q = 0.1 pC) and electron bunch charge Q (E_p = 5.0 GV/m, w_z = 50 μm, τ_0 = 100 fs).

3.7 Chapter Summary

This chapter presents detailed geometry optimizations, wakefield and beam quality studies for dual-grating DLAs. In order to analyze the accelerating performance for dual-grating structures, two different codes (CST and VSim) are used to study the acceleration of relativistic and non-relativistic electrons, and comparisons of both codes are also described. It is found that the simulation results show very good agreement from both codes, giving confidence in the validity of the results. For acceleration of non-relativistic electrons, different spatial harmonics can be excited to interact with 25 keV electrons in dual-grating structures. It is found that the first spatial harmonics are the most efficient when compared to the second and third spatial harmonics. For acceleration of relativistic electrons, a maximum accelerating factor AF = 0.170 can be obtained for a channel gap of half the laser wavelength, corresponding to an unloaded gradient G = 1.70 GV/m for quartz structures.

This is followed by detailed wakefield and beam quality studies for an optimized 100-period dual-grating structure, in terms of the emittance, energy spread and loaded gradient. Using VSim, a realistic CLARA electron bunch with a longitudinal bunch length of 9 μm and a transverse RMS size of 10 μm is loaded into the optimum dual-grating structure to interact with a Gaussian laser pulse. Our simulations only focus on electrons travelling through the channel to interact with laser field. In this case, when the modulated electrons travel out of the structure, the transverse normalized emittance increases by 3.60% compared to that of laser-off case, the energy spread changes from 0.05% to 0.103%, and an accelerating gradient up to 1.15 GV/m is predicted by the particle tracking simulations. In addition, I also analyze in detail the effect of laser parameters and electron density on the beam quality. When electrons interact with a higher laser field with longer waist radius and FWHM duration, it leads to increased emittance and energy spread. However, a low electron bunch density of $<1.1\times10^{21}$ /m^3 is desirable to ensure a small emittance increase of ~3.6%.

These simulation results not only demonstrate theoretically the capabilities of a dual-grating DLA with good beam quality, but also predict numerically realistic DLA experiment results in terms of emittance, energy spread and loaded gradient. However, the energy gain in our simulations is limited by the laser-electron interaction length. Pulse-front-tilt operation for a laser beam is proposed to extend the interaction length, resulting in greater energy gain for a DLA. This will be studied in detail in Chapter 4.

4. Energy Efficiency Studies for Laser-driven Dual-grating Structures

Optimal studies of dual-grating structures have already been performed in Chapter 3 with the aim of maximizing the accelerating gradient and hence the electron energy gain. This chapter presents two kinds of scheme, the addition of a Bragg reflector and the use of PFT laser illumination, to improve the electron energy efficiency for dual-grating structures. It should be noted that the definition of energy efficiency has been described in Section 2.3. The detailed analytical calculations and PIC simulations for each scheme are investigated in this chapter.

Section 4.1 describes the first scheme, which is to introduce a Bragg reflector into a bare dual-grating structure to boost the accelerating field in the vacuum channel, increasing the accelerating gradient by more than 70% compared to bare dual-gratings, from analytical calculations. This prediction is also supported by 2D PIC simulations using VSim, where a 50 MeV electron bunch is loaded into an optimized 100-period structure to interact with a 100 fs pulsed laser.

Pulse-front-tilt operation for a laser beam is proposed in Section 4.2 as a second scheme to extend the interaction length, resulting in a greater energy gain by more than 100% for a dual-grating DLA. The optical system necessary to generate PFT laser beams with an ultrashort pulse duration of 100 fs is also studied in detail. The relevant 2D PIC simulations using VSim are also carried out to study the energy gain for such a PFT laser beam. This is followed by a detailed study of the dependences of the energy gain on the tilt angle, incident laser waist radius and the number of structures.

Section 4.3 studies a dual-grating DLA combining both schemes together to improve the energy efficiency. Through 2D PIC simulations in VSim, the energy efficiency is analysed in detail.

In addition, Section 4.4 investigates the potential diffraction effect which is caused when the fabricated vertical size is smaller than the transverse laser waist radius. This will be an important reference for the realistic fabrication of dual-grating structures with a Bragg reflector.

4.1 Dual-grating Structures with a Bragg Reflector

In this section, a Bragg reflector consisting of many layers of dielectric material is proposed as the first scheme to realise an efficient dielectric laser-driven accelerating structure, which is called 'dual-gratings with a Bragg reflector' [126], as shown in Figure 47. This design reflects back the laser power to enhance the accelerating field in the vacuum channel, thereby increasing the accelerating gradient for electrons. Compared to the dual-grating structures reported in Refs [47], [48], [51]–[53], [79]–[82], it has extra geometry at distance D between dual-gratings and Bragg reflector, as seen in Figure 47. It can be optimized to generate the maximum accelerating field by creating constructive interference in the channel centre. Moreover, mature lithographic techniques allow the dual-gratings to be integrated with a Bragg reflector into a single wafer, with nanometre precision and at low cost [127], [128].

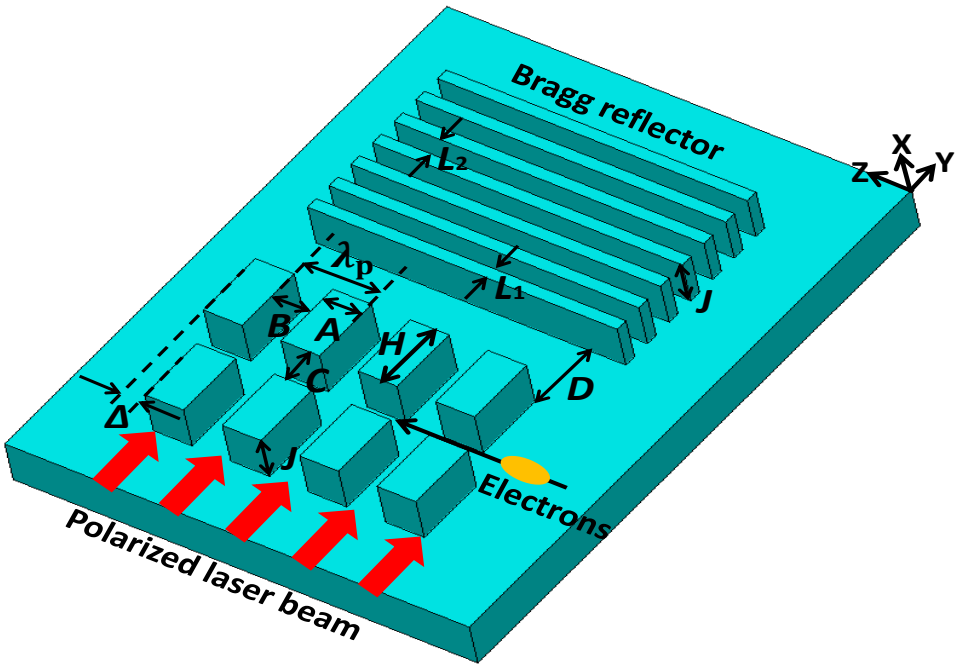

Figure 47. Schematic of a laser-driven dual-grating structure with a 7-layer Bragg reflector. λ_p, A, B, C, D, H, J, L_1, L_2 and Δ represent grating period, pillar width, pillar trench, vacuum channel gap, distance between dual-gratings and Bragg reflector, pillar height, vertical size, dielectric-layer thickness, vacuum-layer thickness and longitudinal shift, respectively. The condition $A + B = \lambda_p$ is selected for all simulations to ensure synchronicity.

4.1.1 Analytical Studies

Through numerical studies carried out in Chapter 3, the results from both codes (CST and VSim) are in very good agreement with each other, so either code can be used to simulate such a structure. Here, the code VSim, based on a FDTD method, is used to

compute the electric and magnetic fields generated in such a structure. It can also perform intensive PIC simulations to obtain all the relevant physical characteristics of the structures.

As a first step, a dual-grating structure is modelled without a Bragg reflector. As shown in Figure 49 (a), when a uniform plane wave travels through a single-period structure, the speed of the wave in vacuum is higher than that in the dielectric grating pillar. This creates a phase difference of π for the wave front in the vacuum channel where electrons are travelling and are periodically modulated along the longitudinal *z*-axis. To produce the desired phase difference of π, the grating pillar height *H* should be set to $H = \frac{\lambda_0}{2(n_r-1)} = \lambda_0$, where n_r = 1.5 is the refractive index of the quartz chosen as the grating material. The grating period λ_p equals the laser wavelength λ_0, so that relativistic electrons are synchronous with the first spatial harmonics [88], this being the most efficient compared to other spatial harmonics.

After setting the phase difference and synchronicity, we need to optimize the longitudinal electric field $E_z[z(t), t]$ in the channel centre to maximize the accelerating gradient *G*, which is defined by Equation (25). Here, $z(t)$ is the position of the electrons in the vacuum channel at time *t*. Like previous studies in Chapter 3, two important factors are used to evaluate the accelerating performance: accelerating efficiency $AE = G/E_0$ and accelerating factor $AF = G/E_m$, where E_m is the maximum field distributed in the structure for an input laser field of E_0. When E_m is lower than the material damage threshold, optimizations are carried out to maximize the accelerating efficiency. However, when E_m is close to the material damage threshold, it is necessary to restrict the maximum field in the gratings, which should not exceed this threshold.

To find the optimum designs for the dual-gratings without a Bragg reflector, *C*, *A*, and Δ are varied to maximize the accelerating factor or accelerating efficiency at a fixed pillar height $H = \lambda_p$. Reported studies [79]–[82] have shown that for such bare dual-gratings, the accelerating gradient usually decreases for a larger channel gap. A gap of $C = 0.5\lambda_p$ is therefore chosen to start our optimization due to the trade-off between the accelerating gradient and the available phase space in which high gradient occurs. The pillar width *A* is then swept from $0.10\lambda_p$ to $0.90\lambda_p$ combining with a variable longitudinal shift Δ from $-0.5\lambda_p$ to $0.5\lambda_p$ for optimizations. Figure 48 (a) shows that the maximum AF = 0.155 is obtained at $C = 0.5\lambda_p$, $H = \lambda_p$, $A = 0.6\lambda_p$, Δ = 0 m while the maximum AE = 0.440 occurs at $C = 0.5\lambda_p$, $H = \lambda_p$, $A = 0.5\lambda_p$, Δ = 0 nm, which can be seen in Figure 48 (b). It is found that such bare dual-gratings perform best when they are perfectly aligned (Δ = 0 m), which agrees well with the results from England *et al*. [79]–[82], [97].

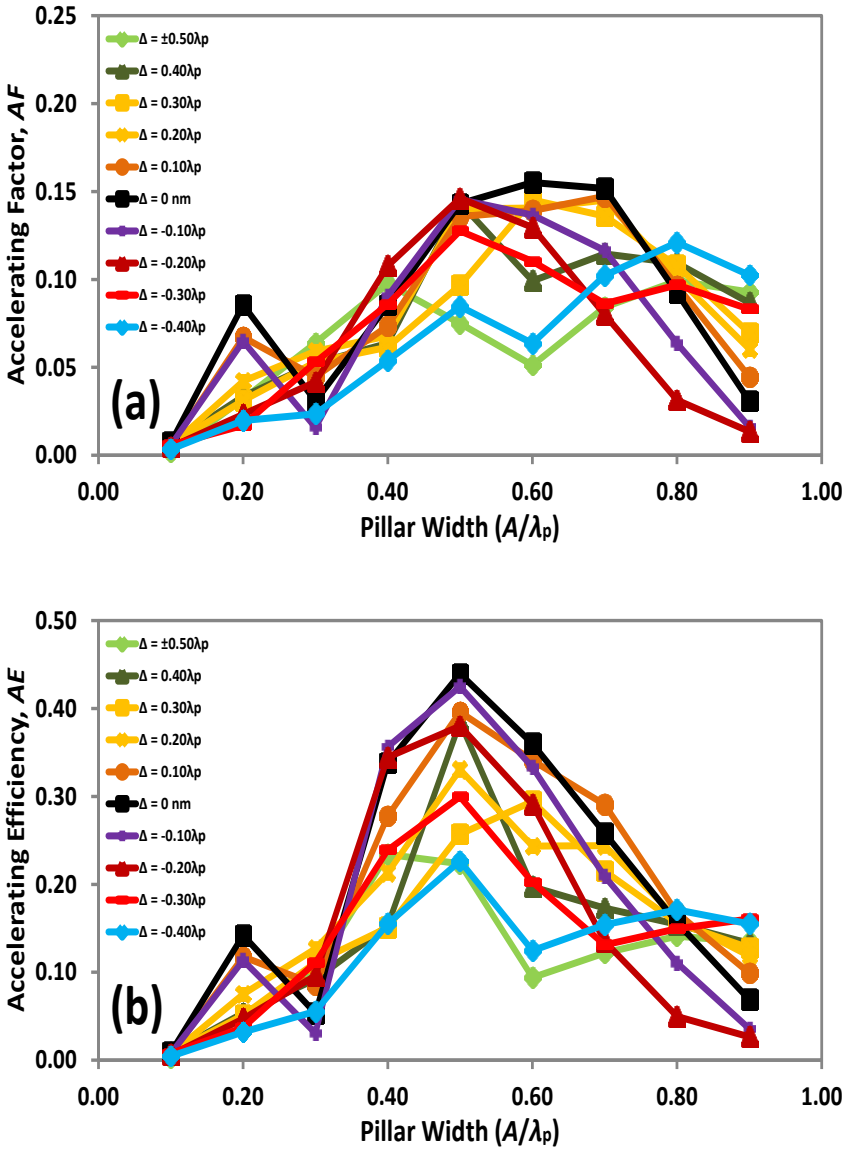

Figure 48. Optimized accelerating factor *AF* (a) and accelerating efficiency *AE* (b) as a function of pillar width *A* with variable longitudinal shift *Δ* for dual-gratings without a Bragg reflector: $C = 0.5\lambda_p$ and $H = \lambda_p$.

After optimization of a bare dual-grating structure, a Bragg reflector consisting of *N* layers of dielectric material and *N*-1 layers of vacuum is added into the simulation. The optical thicknesses in Figure 49 (b) are typically chosen to be a quarter-wavelength long, that is, $n_r L_1 = n_0 L_2 = \lambda_0/4$ at laser wavelength λ_0, where n_r and n_0 are the refractive indices for dielectric and vacuum layers in the Bragg reflector. Considering quartz ($n_r = 1.5$) as the dielectric material, power reflectances of 93%, 99% and 99.7% are calculated for a Bragg reflector with $N = 5$, 7, and 9 respectively. By adjusting the distance *D* from 0 to λ_p, the reflected field can constructively interfere with the subsequent input laser field. As illustrated in Figure 49 (c), the electric field along the vacuum channel centre is apparently enhanced when adding a Bragg reflector to a bare dual-grating structure, boosting the accelerating

gradient significantly. Figure 49 (c) also shows that the longitudinal electric field for 7- layer Bragg reflector is slightly higher than that for 5-layer reflector, but stays the same as that for 9-layer Bragg reflector. A 7-layer Bragg reflector is therefore chosen for our optimized structure. The maxima $AF = 0.173$ and $AE = 0.76$ are achieved at $C = 0.5\lambda_p$, $H = \lambda_p$, $A = 0.5\lambda_p$, $\Delta = 0$ m and $D = 0.8\lambda_p$. Considering that the damage threshold for quartz is 2 J/cm^2 for laser pulses of 100 fs [93]–[95], which is equivalent to an electric field of $E_{th} = 10$ GV/m, the maximum achievable gradient is $AF \times E_{th} = 1.73$ GV/m.

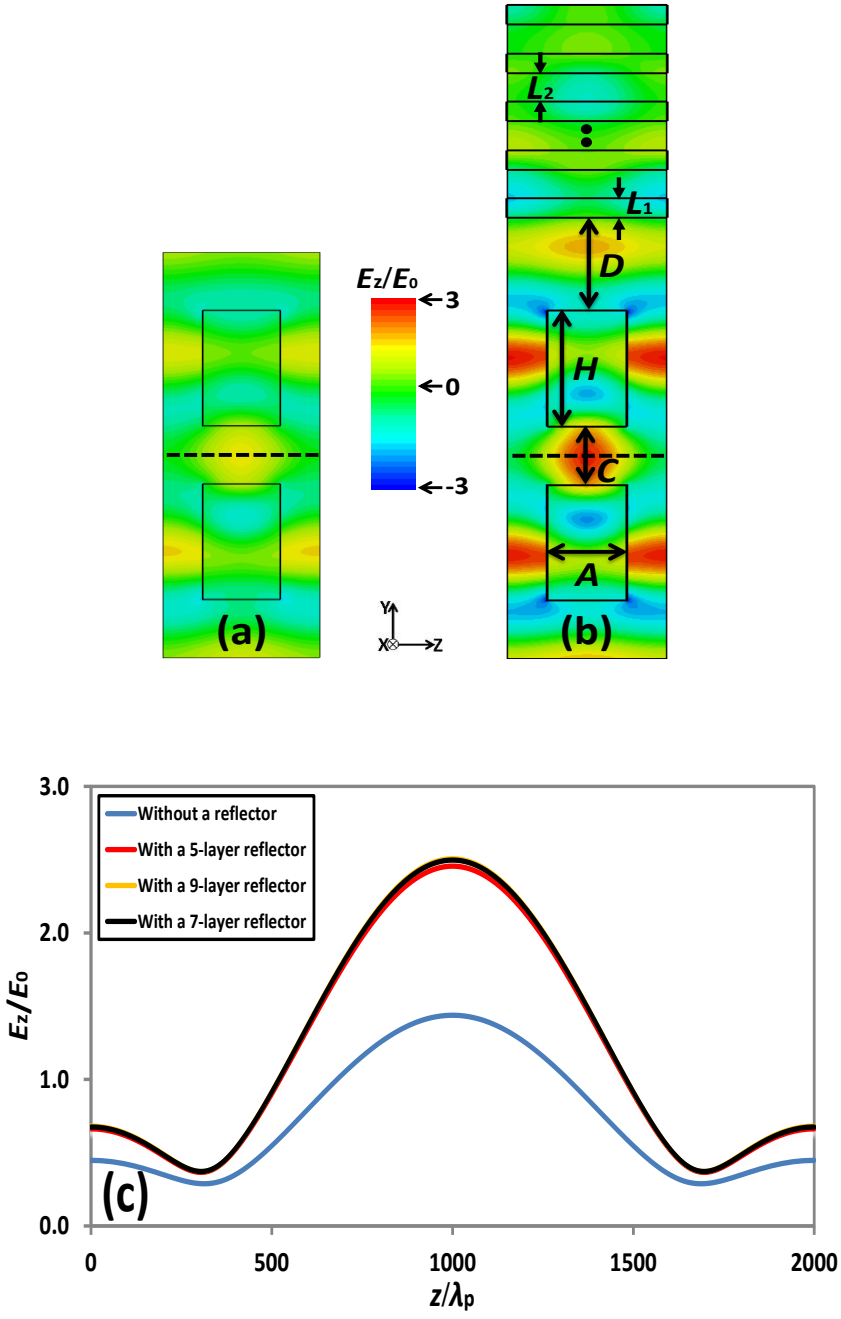

Figure 49. Longitudinal electric field E_z distribution for a single-period structure, (a) without a Bragg reflector, (b) with a Bragg reflector, and (c) a comparison of both cases where a uniform laser field E_0 is used: $C = 0.5\lambda_p$, $H = \lambda_p$, $A = 0.5\lambda_p$, $\Delta = 0$ m. Note that in (c) the black line overlaps with the yellow line.

The effect of rounded corners on the accelerating performance is also studied for such an optimized dual-grating structure with a Bragg reflector. In order to reduce the maximum field generated in the rectangular corners, rounded corners with a radius R are used as shown in the subplot of Figure 50. For dual-gratings with a Bragg reflector with $C = 0.5\lambda_p$, $H = \lambda_p$, $A = 0.5\lambda_p$, $\Delta = 0$ m and $D = 0.8\lambda_p$, the relationship between accelerating performance and radius R is studied. It can be seen in Figure 50 that accelerating factor AF initially increases but then starts to decrease with larger radius, whereas accelerating efficiency AE gradually decreases with increasing radius. The maximum $AF = 0.185$ is achieved at a radius $R = 0.05\lambda_p$, while AE peaks for rectangular pillars with $R = 0.0$ m. When a radius $R = 0.05\lambda_p$ is chosen for the rounded corners, we get a maximum $AF = 0.185$ which is a minor increase of 0.012 compared to the optimized rectangular dual-grating with a Bragg reflector, while AE decreases from $AE = 0.76$ to 0.75. This means that rounded corners do not significantly change the accelerating factor and the accelerating efficiency for such a dual-grating structure with a Bragg reflector. In this case, rectangular corners with $R = 0.0$ m are still chosen for our optimized structures.

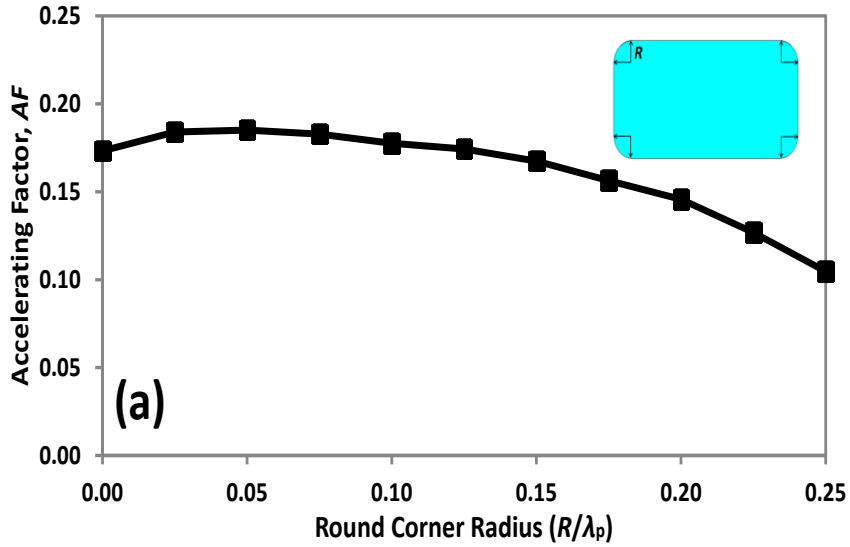

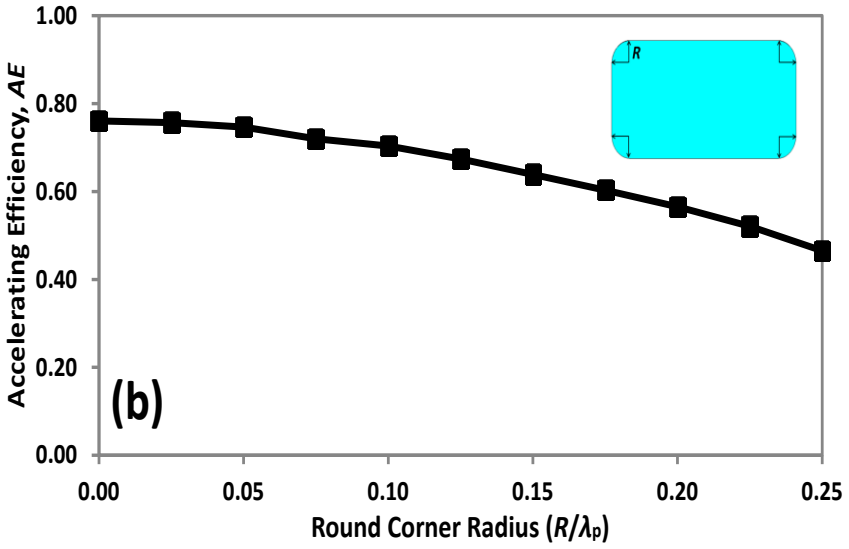

Figure 50. Optimized accelerating factor *AF* (a) and accelerating efficiency *AE* (b) as a function of rounded corner radius *R* for dual-gratings with a 7-layer Bragg reflector: $C = 0.5\lambda_p$, $H = \lambda_p$, $A = 0.5\lambda_p$, $\Delta = 0$ m, and $D = 0.8\lambda_p$.

Following the same procedure, structures with fixed $H = \lambda_p$, $A = 0.5\lambda_p$, $\Delta = 0$ nm, $R = 0$ nm and $D = 0.8\lambda_p$ but different vacuum channel gaps C between $0.2\lambda_p$ and λ_p are optimized, with the aim of maximizing the accelerating factor or the accelerating efficiency. It can be seen in Figure 51 that both the accelerating factor and accelerating efficiency gradually decrease with a larger vacuum channel gap *C*, which agrees well with previously reported studies in Ref. [79]–[82]. Figure 51 (a) shows that dual-gratings with a 7-layer Bragg reflector can generate a slightly larger accelerating factor than bare dual-gratings. The minor increments on the plot are in the range of 0.02 ~ 0.04, which indicates that a Bragg reflector can increase the maximum achievable gradient by 0.18 ~ 0.36 GV/m for the 100 fs-pulsed laser illumination. As shown in Figure 51 (a), the maximum increment of 0.04 occurs at a channel gap $C = 0.2\lambda_p$ while $C = 0.5\lambda_p$ and $C = 0.8\lambda_p$ generate a minimum increment of 0.02. It can be seen in Figure 51 (b) that the accelerating efficiency is significantly improved by more than 70%, when a Bragg reflector is added for dual-gratings. This indicates that dual-gratings with a Bragg reflector can be illuminated by a laser with 65% less power to generate the same accelerating gradient, compared to bare dual-grating structures. The maximum accelerating efficiency reaches as high as 0.92, which is 84% higher than previously-reported dual-grating structures, which have a maximum accelerating efficiency of 0.50 for single laser beam illumination [79], [80]. Such an accelerating efficiency is the same as that generated from symmetric laser illumination [79], [80]. For a channel gap $C = 0.50\lambda_p$ which is used for our optimized structures, the accelerating factor and the accelerating efficiency

are increased by 12% and 73% respectively, when a Bragg reflector is used. For a channel gap $C = \lambda_p$, the accelerating gradient can even be doubled when a Bragg reflector is added.

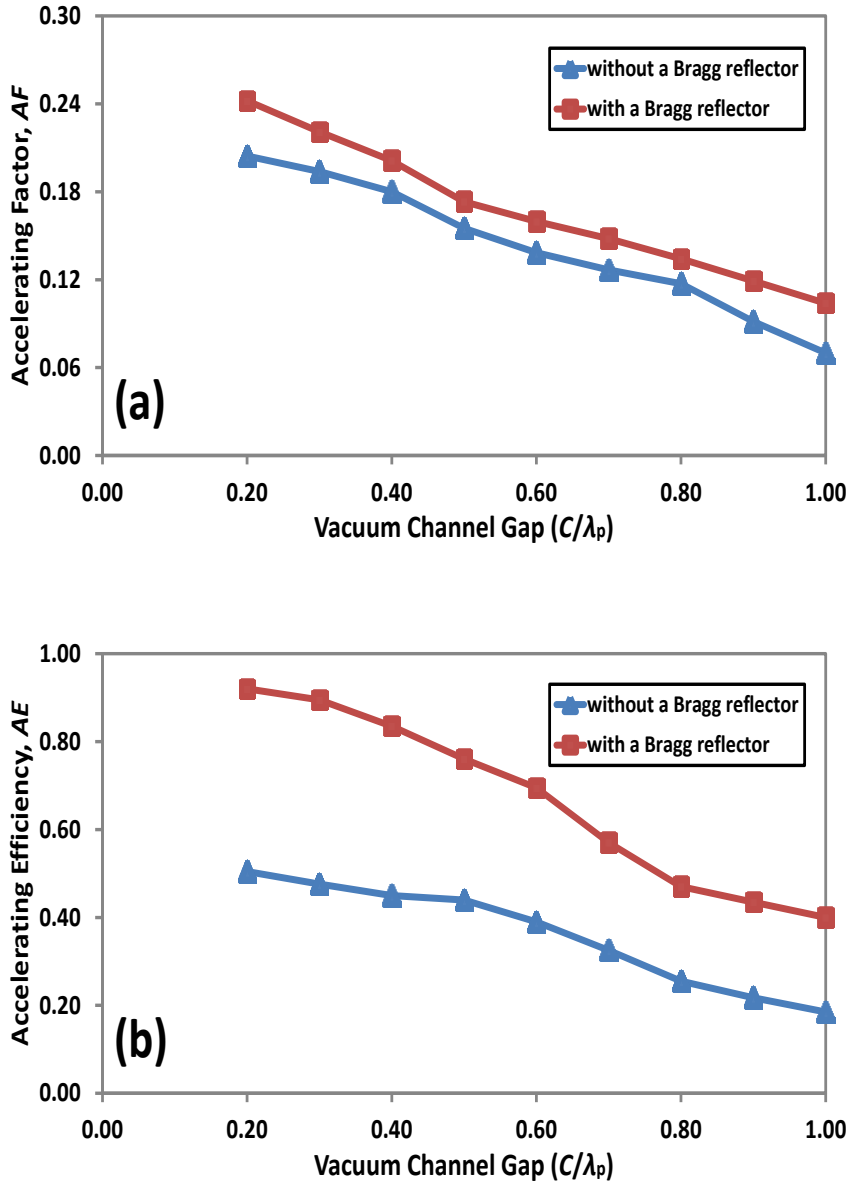

Figure 51. Optimized accelerating factor *AF* (a) and accelerating efficiency *AE* (b) as a function of vacuum channel gap *C* for dual-gratings with a 7-layer Bragg reflector: $H = \lambda_p$, $A = 0.5\lambda_p$, $\Delta = 0$ m, $R = 0.05\lambda_p$ and $D = 0.8\lambda_p$.

4.1.2 Particle-In-Cell Simulations

As a practical example, a dual-grating structure with a 7-layer Bragg reflector, with $C = 0.5\lambda_p$, $H = \lambda_p$, $A = 0.5\lambda_p$, $\Delta = 0$ m, $R = 0$ m, $D = 0.8\lambda_p$, $\lambda_p = 2.0$ μm, is chosen as the optimum for our 2D PIC simulations. The electron bunch employed in our simulations has a mean energy of 50 MeV, bunch charge of 0.1 pC, RMS length of 9 μm, RMS radius of 10 μm,

normalised emittance of 0.2 mm·mrad, and energy spread of 0.03%. Such an electron bunch can be produced by the future CLARA [119] or the Advanced Superconducting Test Accelerator (ASTA) at Fermilab [129]. It should be noted that an energy spread of 0.03% is used here, which is smaller than that used in PIC simulations of Chapter 3. This is because a laser pulse with a peak field of 2.0 GV/m is chosen for our PIC simulations here, which is smaller than the 5.0 GV/m used in PIC simulations of Chapter 3. In order to generate an obvious double-peaked profile for the bunch energy distribution, a small energy spread of 0.03% is employed here.

A uniform plane wave was used for our analytical studies in subsection 4.1.1; however, a linearly polatized Gaussian laser pulse, which can be represented as a superposition of plane waves with different *k*-vector magnitudes, is chosen for our 2D PIC simulations. In this case, the simulation results can be used to compare with future realistic demonstrations. Here, a laser pulse with wavelength λ_0 = 2.0 μm, pulse energy ΔP = 2.1 μJ, pulse duration τ_0= 100 fs, and waist radii $w_x = 50$ μm, $w_z = 50$ μm would generate an input field E_0 = 2.0 GV/m. The mathematical expression for such a Gaussian laser pulse is given in Equation (48). When such a Gaussian laser field is used for illumination, the maximum electric field is still below the damage threshold for quartz structures. However, the grating structures break down if a peak field of 5 GV/m is used instead. This is why a laser field of 5.0 GV/m is not chosen in my PIC simulation here. The Gaussian laser field is propagating through the optimized structure along the *y*-axis while the electron bunch travels along the *z*-axis, as shown in Figure 47. In a co-moving frame of the laser pulse, the electrons experience a temporal electric field $E_t = G_p e^{-\left(\frac{z}{w_{int}}\right)^2}$ with a characteristic interaction length $w_{int} = \left(\frac{1}{w_z^2} + \frac{2\ln 2}{(c\tau_0)^2}\right)^{-0.5}$ = 22.7 μm, as described in Ref. [92], [107], where *c* is the speed of light. Integration of this field E_t with a peak accelerating gradient of G_p = 1.0 GV/m results in a maximum energy gain of ΔE_m = 40 keV, which can be used to calculate the loaded accelerating gradient for subsequent simulations. Due to limitations in our computing hardware, a 100-period optimum structure with a length of *LZ* = 200 μm is chosen for our PIC simulations.

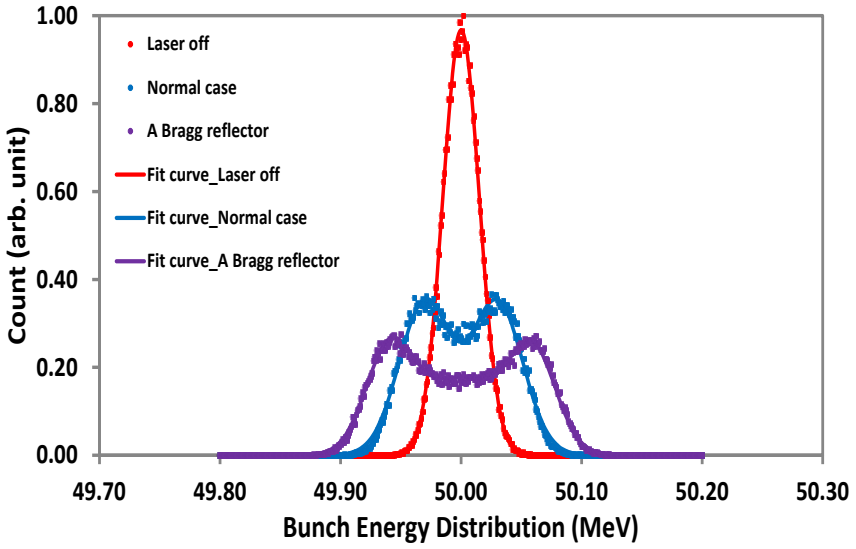

Figure 52. Bunch energy distribution for three cases: laser-off (red dots and fit curve); laser-on without a Bragg reflector (blue dots and fit curve); laser-on with a Bragg reflector (purple dots and fit curve).

In the PIC simulation, the mesh size is set to 10 nm (z) × 20 nm (y) so that the results are found to be convergent. We use 500,000 macro particles, close to the number of electrons for a bunch charge of 0.1 pC. These parameters are exactly the same as those used in PIC simulations in Chapter 3. Due to the bunch transverse size which is much bigger than the vacuum channel gap of 1 μm, only a small fraction of electrons traverses through the vacuum channel of the structure. It can be calculated that about 4% of the 50 MeV bunch is transmitted through the vacuum channel gap of 1.0 μm. Electrons travelling through the quartz structure suffer significant energy loss due to collisional straggling [90] in the dielectric material, so only the electrons modulated by the laser field in the vacuum channel are used for the analysis which follows.

Figure 52 shows the bunch energy distribution for the modulated electrons, with the laser off and on. It can be seen that the energy sprectrum has a double-peaked profile after laser-bunch interaction, due to the RMS bunch length of 9.0 μm being longer than the laser wavelength of 2.0 μm, which agrees well with the reported results [47], [48], [112]. Using the Gaussian fits to these energy spectra, the maximum energy gain is calculated from the difference between the abscissa of the half-width at half-maximum (HWHM) point for a laser-on spectrum and a laser-off spectrum [47], [48]. The maximum energy gain is $\Delta E_2 = 63$ keV for optimized dual-gratings with a Bragg reflector, while it is $\Delta E_1 = 37$ keV for bare dual-gratings. This corresponds to loaded peak gradients of 1.575 GV/m and 0.925 GV/m, respectively. The loaded acclerating gradient is therefore increased by 70% when a Bragg reflector is added, for optimized dual-gratings. This indicates that the energy efficiency is improved by 70% when a 7-layer Bragg reflector is used.

4.2 Dual-grating Structures Driven by a Pulse-Front-Tilted Laser

Many geometric optimizations [79]–[82], [112], [124], [126], including adding a Bragg reflector, have been carried out to maximize the accelerating gradient, resulting in the large electron energy gain for dual-grating DLAs. However, previous DLA studies were performed with a normally-incident laser beam. In this case, the increase in electron energy is limited by the short interaction length between the laser pulses and the electron bunch. In this section I explore dual-grating DLAs driven by a PFT laser [130], which is proposed as a second scheme to extend the interaction length, resulting in a larger energy gain for the DLAs. As shown in Figure 53, a PFT laser beam is introduced to interact with an electron bunch in a dual-grating structure. The tilt angle γ can be chosen to overlap an electron bunch synchronously with the laser pulse envelope so that the electrons gain the largest possible energy. Subsection 4.2.1 presents a theoretical analysis for laser-bunch interaction in dual-grating structures which are illuminated by a normal or by a pulse-front-tilted laser beam, respectively. A comparison of both illumination schemes is also discussed. In subsection 4.2.2 the detailed optical system to generate a PFT laser beam with an ultrashort pulse duration is described from mathematical calculations. Finally, in subsection 4.2.3 2D PIC simulations are carried out by introducing a PFT laser beam into a 100-period dual-grating structure to interact with a 50 MeV electron bunch.

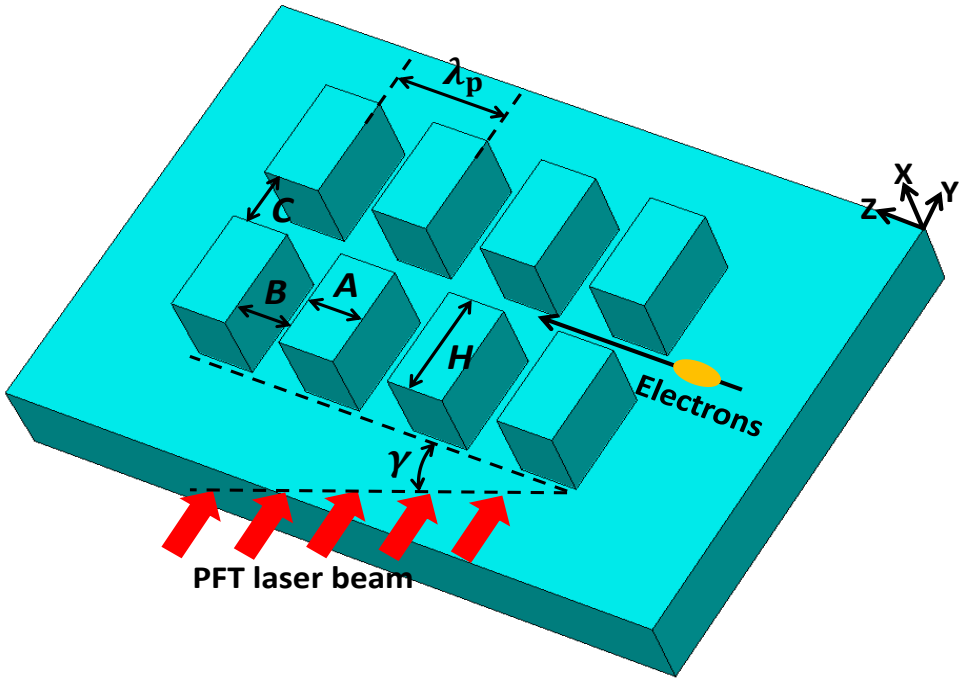

Figure 53. Schematic of a dual-grating structure illuminated by a PFT laser beam with a tilt angle of γ. λ_p, *A*, *B*, *C*, and *H* represent the same geometry as Figure 47.

4.2.1 Theory

Linearly-polarized Gaussian laser pulses are introduced along the *y*-axis to illuminate the dual-grating structure while the electrons are travelling in the channel centre along the *z*-axis, which is the normal scheme for DLAs, as shown in Figure 54 (a). Such a laser pulse exhibits a cycle-averaged electric field as follows:

$$E_{\mathrm{z}} = E_{\mathrm{p}} e^{-\left(\frac{z}{w_{\mathrm{z}}}\right)^2 - 2\ln 2\left(\frac{t}{\tau_0}\right)^2} \cos(\omega t - k_0 y + \phi_1), \tag{50}$$

where E_{p}, w_{z}, τ_0, ω, k_0 and ϕ_1 represent the peak field, *z*-axis waist radius, FWHM duration, angular frequency, wave number, and phase term, respectively. Actually this is exactly the same as Equation (48). In a co-moving frame, electrons move along the *z*-axis at a speed $v = \beta c$ and experience the optical phase periodically, $z = \beta c t$; the temporal electric field E_{t}, which electrons experience in the channel [92], [107], is therefore derived:

$$E_{\mathrm{t}} = G_{\mathrm{p}} e^{-\left(\frac{z}{w_{\mathrm{int}}}\right)^2} \cos(\omega t - k_{\mathrm{z}} z + \phi_2), \tag{51}$$

where $w_{\mathrm{int}} = \left(\frac{1}{w_{\mathrm{z}}^2} + \frac{2\ln 2}{(\beta c \tau_0)^2}\right)^{-0.5}$ is the characteristic interaction length, G_{p} is the peak accelerating gradient related to E_{p}, k_{z} is the longitudinal wave number, with $k_{\mathrm{z}} = k_0/\beta$, $\beta = v/c$ for electron velocity v, and ϕ is a phase term. If it is assumed that the electrons experience the optimum accelerating phase, the energy gain is obtained:

$$\Delta E = \int_{z_1}^{z_2} q G_{\mathrm{p}} e^{-\left(\frac{z}{w_{\mathrm{int}}}\right)^2} dz = \int_{-0.5LZ}^{0.5LZ} q G_{\mathrm{p}} e^{-\left(\frac{z}{w_{\mathrm{int}}}\right)^2} dz, \tag{52}$$

where q is the charge of a single electron, $z_1 = -0.5LZ$ and $z_2 = 0.5LZ$ are the positions along the *z*-axis, $z = 0$ is the longitudinal centre of the dual-grating structure, and LZ is the longitudinal length of a multi-period dual-grating structure. When $LZ \gg w_{\mathrm{int}}$, the energy gain is derived as:

$$\Delta E_{\mathrm{m}} = q G_{\mathrm{p}} \sqrt{\pi}\, w_{\mathrm{int}}. \tag{53}$$

It should be noted that the characteristic interaction length w_{int} is 'interaction length' which is used in the following analysis throughout the paper. Equation (52) indicates that a longer laser FWHM duration τ_0 and waist radius w_{z} increase the interaction length w_{int}, resulting in a larger energy gain for the normal scheme. The analytically-computed interaction lengths for relativistic electrons with $\beta \approx 1.0$ are illustrated in Figure 55. It can be seen that the interaction length gradually reaches saturation with increasing waist radius, for variable FWHM durations. In addition, the waist radius does not change the interaction

length significantly for a 100 fs pulsed laser. Using normally-incident laser illumination, SLAC has demonstrated a maximum energy gain of 24 keV over a short interaction length of 16.3 μm, for a <100 fs pulsed laser [30]. In this demonstration, the interaction length was limited mainly by the short laser FWHM duration.

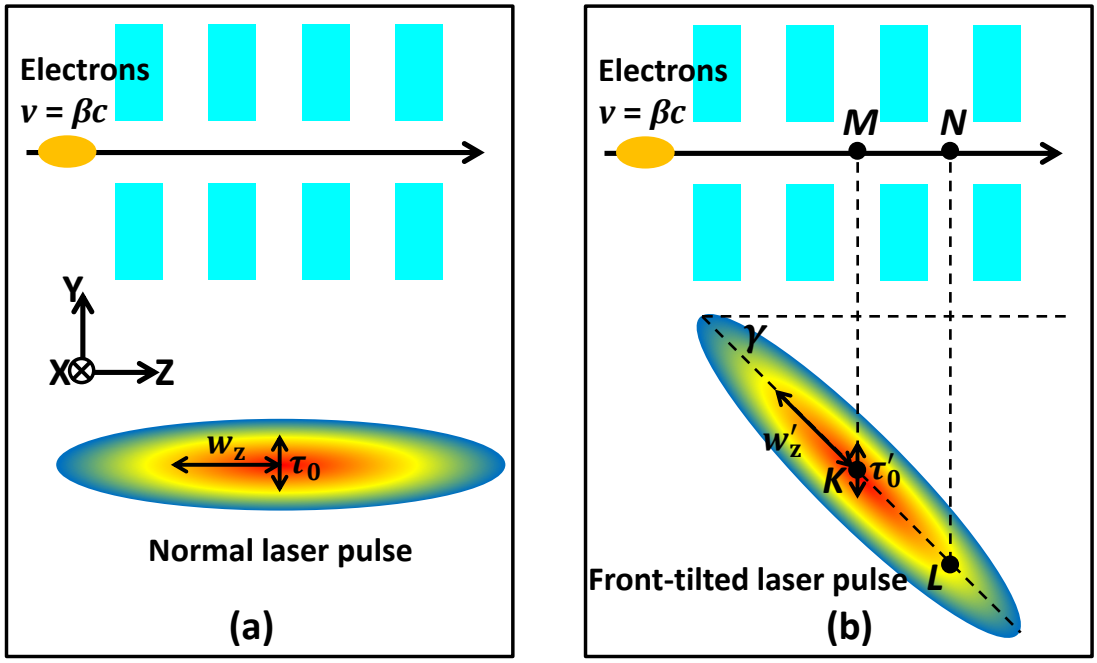

Figure 54. Dual-grating structures are illuminated by (a) a normally incident laser pulse and (b) a front-tilted laser pulse.

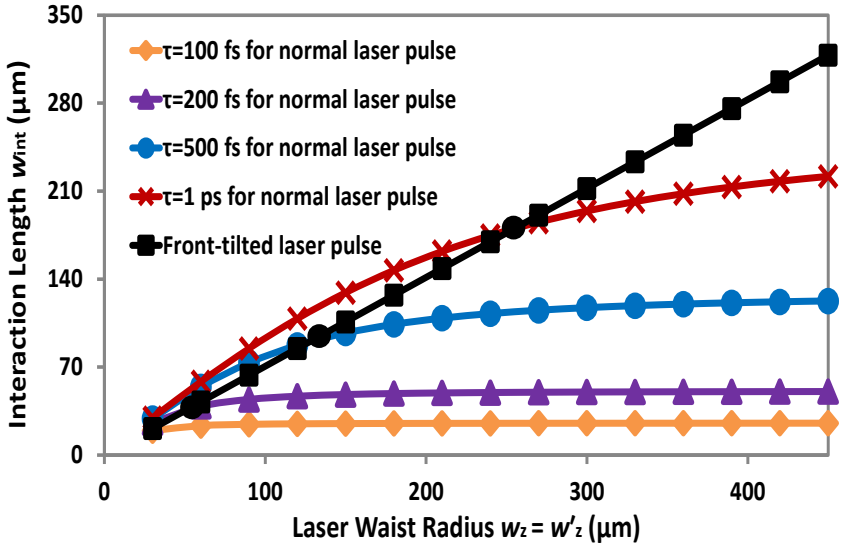

Figure 55. Relationship between interaction length w_{int} and laser waist radius w_z with variable laser FWHM duration τ, when the electrons are relativistic with $\beta \approx 1.0$. Note that the black circles are critical waist radii at which interaction lengths are the same for both schemes.

In the other case for DLAs studied here, a front-tilted laser pulse is used to illuminate the dual-grating structure, as shown in Figure 54 (b). Due to the phase-reset properties of the dual-grating structure, this front-tilted laser field overlaps efficiently with the electron beam to extend the interaction length, thereby boosting the energy gain for the same laser parameters and grating geometries. For a sufficiently short (in the range of several attoseconds) electron bunch with velocity $\beta = v/c$, travelling from point M to N in one grating period, as seen in Figure 54 (b), the velocity of the electrons can be assumed to stay constant, i.e. $\Delta\beta/\beta \sim 0$. This is true for relativistic electrons where $\beta \approx 1.0$, as the change in velocity is practically zero. It also holds in the non-relativistic case when the energy gain over one grating period λ_p is well below several keV, so that the velocity of the electrons can be assumed to be constant. Figure 54 (b) also shows that there is some time delay for the pulse front at points K and L to arrive at points M and N, respectively. The time delay between K and L is:

$$\Delta t = \lambda_p \tan\gamma / c. \tag{54}$$

In time Δt the electrons have travelled from M to N:

$$\lambda_p = v\Delta t. \tag{55}$$

Thus

$$\beta = v/c = 1/\tan\gamma. \tag{56}$$

Equation (56) shows that the tilt angle for the pulse front is in the range of $45^\circ \leq \gamma < 90^\circ$ and is determined by the electron injection velocity, to meet the synchronous condition.

Using the same laser frequency and wave number as for the normal DLA scheme, the electrons experience a Gaussian field along the channel centre:

$$E_z' = E_p e^{-\left(\frac{z}{w_z' \cos\gamma}\right)^2 - 2\ln 2\left(\frac{t-pz}{\tau_0'}\right)^2} \cos(\omega t - k_0 y + \phi_1). \tag{57}$$

where w_z' is the tilted waist radius, τ_0' is the local pulse duration and $p = \frac{dt}{dz}$ is the PFT factor which is defined by the derivative of the pulse-front arrival time with respect to z, and γ is the PFT angle, as shown in Figure 54 (b). The relationship between p and γ is then given in Ref. [131] by:

$$\tan\gamma = pc. \tag{58}$$

Using Equations (56) and (58), we find $t - pz = 0$ when the electrons move at a speed of $v = \beta c$, so that the electrons experience a Gaussian field along the channel centre of:

$$E'_{\mathrm{t}} = G_{\mathrm{p}} e^{-\left(\frac{z}{w'_{\mathrm{z}}\cos\gamma}\right)^2} \cos(\omega t - k_{\mathrm{z}} z + \phi_2). \tag{59}$$

It should be noted that here the distortion effect [132] is not taken into account for our analysis. When the electrons experience the optimum optical phase due to the phase-reset properties of the dual-grating structure, the electrons' energy gain is derived thus:

$$\Delta E' = \int_{z_1}^{z_2} q G_{\mathrm{p}} e^{-\left(\frac{z}{w'_{\mathrm{z}}\cos\gamma}\right)^2} dz = \int_{-0.5LZ}^{0.5LZ} q G_{\mathrm{p}} e^{-\left(\frac{z}{w'_{\mathrm{z}}\cos\gamma}\right)^2} dz. \tag{60}$$

We obtain the characteristic interaction length $w'_{\mathrm{int}} = w'_{\mathrm{z}}\cos\gamma$. When $LZ \gg w'_{\mathrm{z}}\cos\gamma$, the energy gain is

$$\Delta E'_{\mathrm{m}} = q G_{\mathrm{p}} \sqrt{\pi}\, w'_{\mathrm{z}} \cos\gamma. \tag{61}$$

Compared to Equation (53), Equation (61) shows that the energy gain is only related to waist radius w'_{z} and tilt angle γ. The interaction length is plotted as a function of waist radius in Figure 55, where $w'_{\mathrm{z}} = w_{\mathrm{z}}$ and $\beta \approx 1.0$ are assumed for our calculations. For a shorter FWHM duration of $\tau_0 \leq 100$ fs, a front-tilted laser pulse generates a larger interaction length than a normally-incident laser pulse. For a longer FWHM of $\tau_0 > 100$ fs, there is a critical waist radius w_{c} where both schemes have the same interaction length, but when $w_{\mathrm{z}} > w_{\mathrm{c}}$, a front-tilted laser pulse is more efficient than a normal one.

4.2.2 Optical System for Generating a PFT Laser

In this subsection, the optical system is discussed to generate the desired PFT laser. A PFT laser can be generated either by angular dispersion (AD), which causes different frequency components to propagate at different angles, or by simultaneous spatial and temporal focusing (SSTF) in the absence of AD. SSTF has been demonstrated in Ref. [133] to generate a PFT laser beam with an ultrashort pulse duration of ~100 fs at the focal region, but the waist radius is also focused to tens of μm, thereby limiting the energy gain for DLAs. Martinez *et al*. [132] have showed that the PFT laser achieved by AD gives rise to pulse broadening and changing of the tilt angle as it moves away from a diffractive grating or prism. However, these distortions can be compensated for by using an imaging system to transfer the image of a tilted pulse front on the diffraction grating into the dual-grating DLAs.

As shown in Figure 56, our optical setup consists of a diffraction grating and a 1:1 imaging system with a two-lens telescope. An incident laser beam experiences angular dispersion when it is propagating through a diffraction grating. This means that different spectral components of a laser pulse travel in different directions after passing the diffraction grating. As a consequence, the pulse front is tilted by an angle γ whereas the phase fronts of

the pulse are always perpendicular to the pulse propagation direction. In order to reduce the distortion, a 1:1 imaging system with a two-lens telescope is used to recreate the same pulse front tilt, which can be introduced to illuminate a dual-grating structure to interact with the electrons.

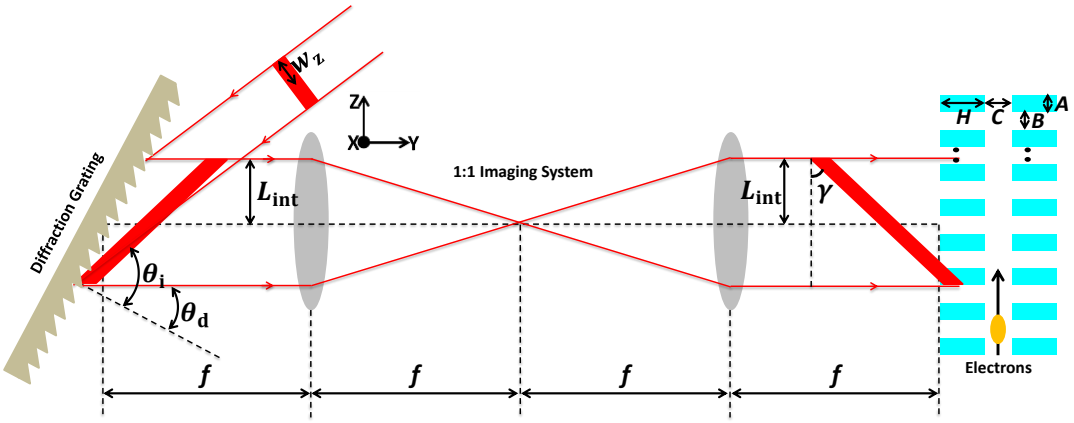

Figure 56. Diagram of a PFT laser generated by a dedicated optical system.

For the diffraction grating as shown in Figure 56, the grating equation is

$$\sin\theta_{\mathrm{i}} + \sin\theta_{\mathrm{d}} = \frac{\lambda_0}{g}. \tag{62}$$

where θ_{i} and θ_{d} are the incidence and diffraction angles respectively, λ_0 is the laser wavelength, g is the diffraction grating period. The tilt angle is also given by Ref. [134]:

$$\tan\gamma = \frac{\lambda_0}{g\cos\theta_{\mathrm{d}}}. \tag{63}$$

In order to overlap synchronously with relativistic electrons, the PFT angle γ equals 45^0, as described in Equation (56).

When the incidence angle θ_{i} is the same as the diffraction angle θ_{d}, the diffraction efficiency of a grating is usually maximal in Littrow configuration. Combined with Equations (62) and (63), we get $\theta_{\mathrm{i}} = \theta_{\mathrm{d}} = 26.6^0$. When a laser wavelength of $\lambda_0 = 2.0$ μm is chosen, the diffraction grating period is $g = 2.236$ μm, corresponding to a groove density of $n_{\mathrm{g}} = 447$ lines/mm for the diffraction grating. Since this is impractical, a groove density of $n_{\mathrm{g}} = 450$ lines/mm is chosen as an optimum for our optical system. In this case, we get $\theta_{\mathrm{i}} = 27.65^0$, $\theta_{\mathrm{d}} = 25.84^0$.

When an incident laser pulse travels through the diffraction grating, the upper side of the pulse is diffracted by the grating earlier than the lower side of the pulse, as can be seen in Figure 56. This generates an optical path difference, which contributes to a front-tilted pulse close to the grating. Such a front-tilted pulse has the same pulse duration as the incident laser

pulse. In this case, the pulse intensity and peak field remain constant. A 1:1 imaging system is then used to transfer this tilted pulse to the dual-grating structure. This imaging process does not generate any distortion for the front-tilted pulse. The imaged front-tilted pulse should be put close enough to the dual-grating structure to reduce the broadening effect [134]. Here, the pulse duration is assumed to remain constant when it is introduced into the dual-grating DLAs.

For an incident laser pulse with a waist radius w_z, the interaction length L_{int} as shown in Figure 56 can be mathematically calculated:

$$L_{\mathrm{int}} = \frac{\sqrt{2}\left(\left(\frac{2w_z}{\cos\theta_{\mathrm{i}}}\right)^2 + (2w_z\tan\theta_{\mathrm{i}})^2 - 2\frac{2w_z}{\cos\theta_{\mathrm{i}}}2w_z\tan\theta_{\mathrm{i}}\cos(90^0+\theta_{\mathrm{d}})\right)^{0.5}}{4}. \tag{64}$$

Equation (64) clearly shows that the interaction length L_{int} is dependent on the w_z, θ_{i} and θ_{d}. Using such an optical system, a PFT laser beam with a peak field of E_0, a waist radius of $\sqrt{2}L_{\mathrm{int}}$ and a local temporal duration of τ_0 can be generated. From Equation (57), I get the mathematical expression for the electric field of such a PFT beam:

$$E_{\mathrm{z}}' = E_0 e^{-\left(\frac{z}{L_{\mathrm{int}}}\right)^2 - 2\ln 2\left(\frac{t-pz}{\tau_0}\right)^2}\cos(\omega t - k_0 y + \phi_1). \tag{65}$$

4.2.3 Particle-In-Cell Simulations

In this subsection, the PIC code VSim is again used to investigate the interaction between a front-tilted laser pulse and a Gaussian electron bunch in a 100-period dual-grating structure with geometries: $C = 0.5\lambda_{\mathrm{p}}$, $H = \lambda_{\mathrm{p}}$, $A = 0.5\lambda_{\mathrm{p}}$, $\Delta = 0$ m, $\lambda_{\mathrm{p}} = 2.0$ μm, $LZ = 200.0$ μm. These parameters are the optimum geometries which are obtained from Section 4.1. The electron bunch employed in our simulations has a mean energy of 50 MeV, bunch charge of 0.1 pC, RMS length of 9 μm, RMS radius of 10 μm, normalised emittance of 0.2 mm·mrad, and energy spread of 0.03%. Such an electron bunch can be generated by the future CLARA [119] or the Advanced Superconducting Test Accelerator (ASTA) at Fermilab [129]. The electron bunch parameters are still the same as those used in Section 4.1.

An incident Gaussian laser pulse with $\lambda_0 = 2.0$ μm wavelength, $\Delta P = 2.1$ μJ pulse energy, $\tau_0 = 100$ fs pulse duration, and $w_{\mathrm{z}} = 50$ μm waist radius would generate a peak input field E_0 = 2.0 GV/m. When such a laser pulse is used for normal illumination, we find a maximum electric field of 6.10 GV/m generated in the structure area, which is still under the damage threshold for quartz structures. The calculated interaction length is $w_{\mathrm{int}} = \left(\frac{1}{w_{\mathrm{z}}^2} + \frac{2\ln 2}{(c\tau_0)^2}\right)^{-0.5}$ = 22.7 μm, which is much smaller than LZ = 200.0 μm. Using Equation (53) with a peak accelerating gradient of G_{p} = 1.0 GV/m results in a maximum energy gain of ΔE_{m} = 40 keV,

which is used to calculate the loaded accelerating gradient for subsequent analysis on normally-incident laser illumination.

The same laser parameters are used for the optical system shown in Figure 56 to generate a front-tilted pulse with an ultrashort pulse duration of τ_0 = 100 fs and a tilt angle of $\gamma = 45^0$. By substituting $w_z = 50$ μm, $\theta_i = 27.65^0$and $\theta_d = 25.84^0$ into Equation (64), an interaction length of $L_{int} = 51$ μm is obtained. Equation (65) is then used to mathematically model a front-tilted pulse for our 2D PIC simulation. When such a front-tilted pulse propagates through the dual-grating structure to interact with the electron bunch, according to Equation (61) the maximum energy gain is calculated to be $\Delta E'_m$ = 90 keV when G_p = 1.0 GV/m is assumed. Such an energy gain of $\Delta E'_m$ = 90 keV is used to calculate the loaded accelerating gradient for the following simulations of PFT laser illumination.

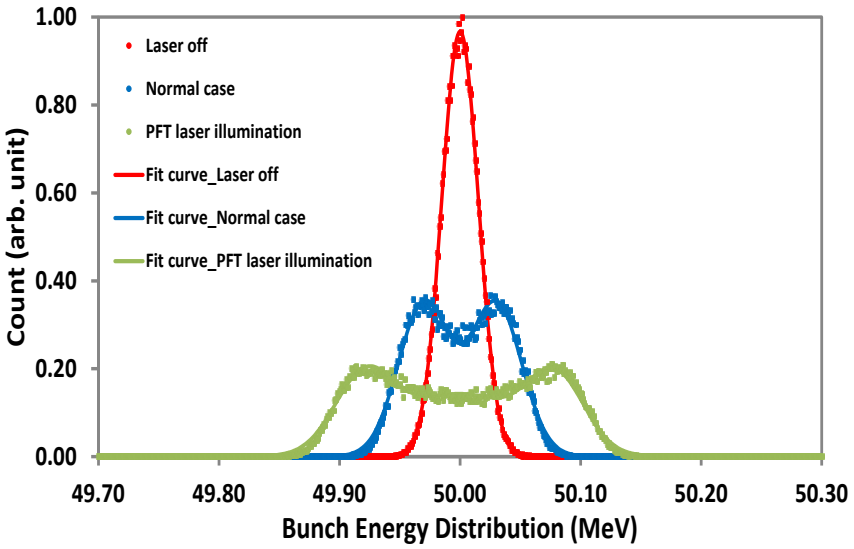

Figure 57. Bunch energy distribution for the cases of laser-off (red dots and fit curve), laser-on with a normal laser pulse (blue dots and fit curve), and laser-on with a front-tilted laser pulse (green dots and fit curve).

In our simulations, the electromagnetic fields are calculated based on the FDTD method. The dual-gratings are modelled as a 2D structure (y - z plane) because it is constant in the x direction. The mesh size is set to 10 nm (z) × 20 nm (y) so that the results are convergent. 500,000 macro particles are used for tracking, which is close to the number of electrons in the bunch. Those electrons travelling through the quartz structure suffer significant energy loss due to collisional straggling [90] in the dielectric material. Only the electrons modulated by the laser field in the vacuum channel are therefore used for our calculations. It is found that about 4% of the 50 MeV bunch is transmitted through the vacuum channel gap of 1.0 μm. Figure 57 compares the bunch energy distribution for modulated electrons, with the laser off and on. It is obvious that the energy spectrum has a double-peaked profile after

laser-bunch interaction, which agrees well with the reported results [47], [48], [112]. Gaussian fitting lines and HWHM methods [47], [48] are used to calculate the maximum energy gain. Figure 57 shows that the maximum energy gain is ΔE_1 = 37 keV for normal laser illumination, whereas it is ΔE_3 = 88 keV for PFT laser illumination. This corresponds to maximum loaded gradients of 0.925 GV/m and 0.978 GV/m, respectively. It is found that both illuminations have similar loaded gradients, but illumination by the PFT laser generates an energy gain which is larger than the normal laser by 138%. In addition, compared to PIC simulations in Section 4.1, the PFT laser illumination is more efficient than adding a Bragg reflector to improve the energy efficiency for dual-grating DLAs.

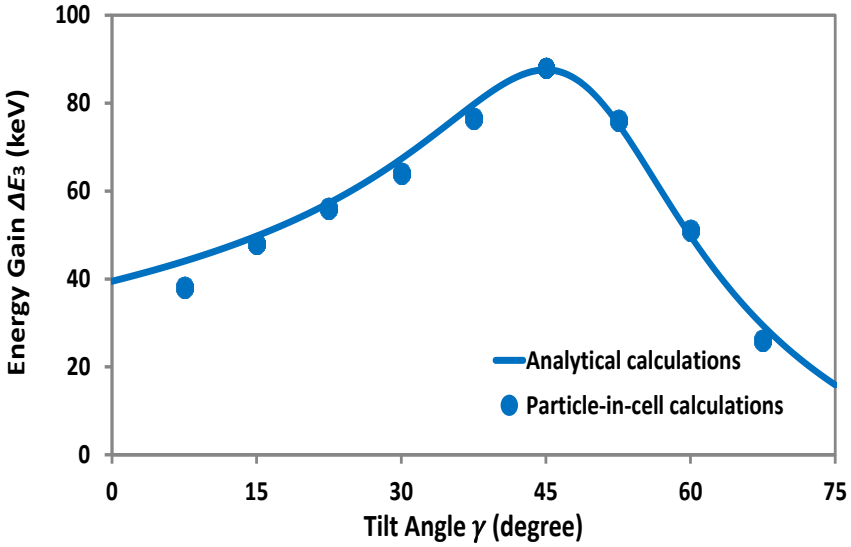

Figure 58. Energy gain from analytical (solid line) and PIC (dots) calculations with different tilt angles, for a 100-period dual-grating structure: $E_0 = 2$ GV/m, $\tau_0 = 100$ fs, and $L_{\text{int}} = 51$ μm.

The effect of the tilt angle on the energy gain ΔE_3 are also studied by running PIC simulations for the same electron bunch and structure. By substituting Equations (58) into Equation (65) and combining Equation (60) with a loaded gradient of $G_{\text{p}} = 0.978$ GV/m, the energy gain ΔE_3 with different tilt angles can be calculated analytically. Figure 58 shows the energy gain ΔE_3 from analytical and PIC calculations with different tilt angles, and good agreement between them is found. It can be seen from Figure 58 that the maximum energy gain ΔE_3 = 88 keV occurs at a tilt angle $\gamma = 45^0$. This strongly supports the synchronous acceleration of relativistic electrons through a PFT laser with a tilt angle of 45^0, which is in good agreement with Equation (56). In addition, a PFT laser with a tilt angle between 30^0 and 60^0 can still result in an energy gain larger than normal laser illumination, which provides some flexibility for the generated laser tilt angle in realistic DLA demonstrations.

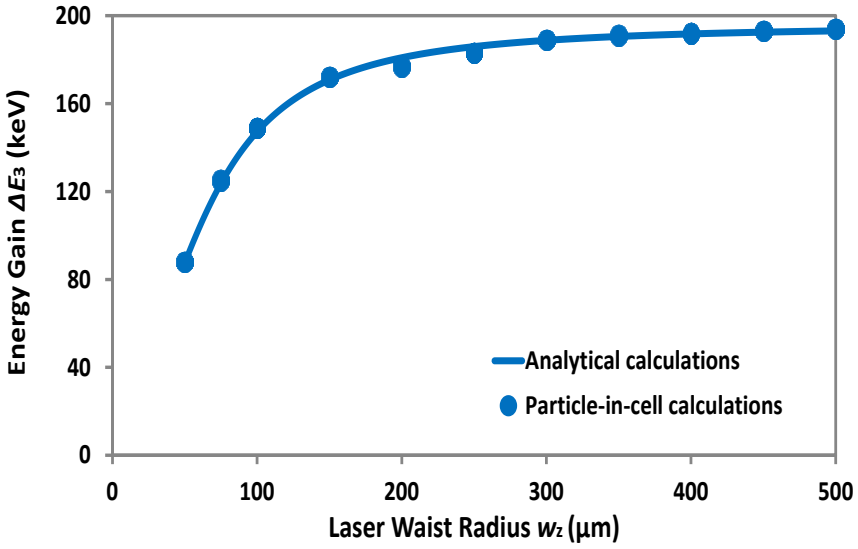

Figure 59. Energy gain from analytical (solid line) and PIC (dots) calculations with increasing laser waist radius, for a 100-period dual-grating structure: $E_0 = 2$ GV/m, $\tau_0 = 100$ fs, and $\gamma = 45^0$.

After this, the relationship between the energy gain ΔE_3 and the waist radius w_z of the incident laser beam is investigated. It can be seen in Equation (64) that the interaction length L_{int} increases linearly with the waist radius w_z of the incident laser beam. By substituting Equations (64) into Equation (65) and combining Equation (60) with a loaded gradient of $G_p = 0.978$ GV/m, I can calculate the energy gain ΔE_3 with the incident laser waist radius w_z analytically. In our PIC simulations, only the laser waist radius w_z is changed and other parameters are kept the same, including the electron bunch and structure. Figure 59 shows the energy gain from analytical and PIC calculations with variable laser waist radii w_z, and very good agreement between them is found. This strongly validates our mathematical calculations in Equations (50)-(65), and also shows clear evidence for our converged, realistic simulation methods. As shown in Figure 59, when the laser waist radius w_z increases from 50 μm to 500 μm, the energy gain ΔE_3 gradually saturates due to convergence of Equation (60). For a 100-period dual-grating structure, the maximum energy gain is calculated to be 194 keV when the laser waist radius $w_z \geq 400.0$ μm, which is 400% larger than for normal laser illumination.

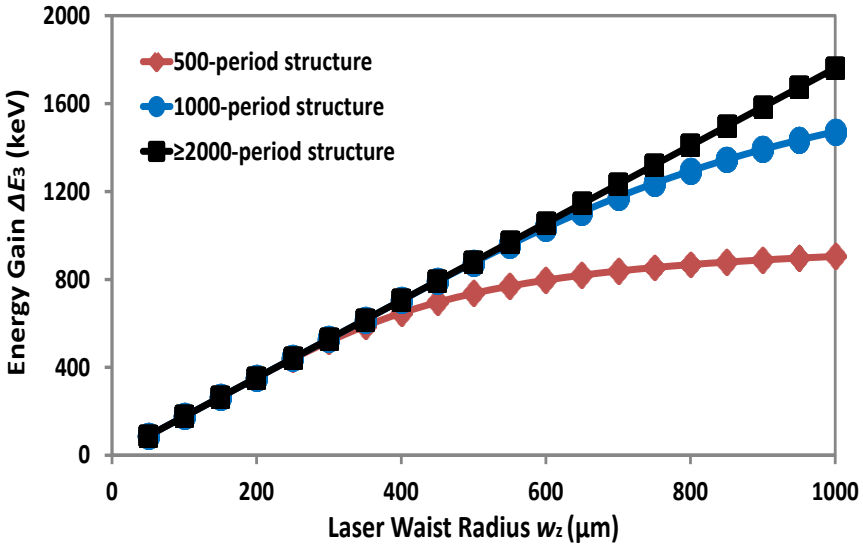

Figure 60. Analytically-calculated energy gain with increasing laser waist radius, for different periods of the dual-grating structure: $E_0 = 2$ GV/m, $\tau_0 = 100$ fs, $\gamma = 45^0$.

It should be noted that a 100-period structure with a length of $LZ = 200.0$ μm is used for our PIC simulations due to limitations in our computing hardware. Equation (60) indicates that a larger number of periods results in a higher energy gain for the same electron bunch and laser beam. Using the same mathematical Equations (60), (64), and (65) with the same loaded gradient of $G_{\mathrm{p}} = 0.978$ GV/m, the energy gain ΔE_3 with variable structure lengths LZ and laser waist radii w_{z} can be analytically calculated. Figure 60 shows that the analytically-calculated energy gain gradually saturates when the laser waist radius w_{z} increases from 50 μm to 1000 μm for the structures with 500 and 1000 periods. For a dual-grating structure with over 2000 periods, corresponding to a length of LZ = 4000 μm, the energy gain increases linearly with laser waist radius from 50 μm to 1000 μm due to the linearity of Equation (60). In this case, a laser waist radius of 1000 μm would generate an interaction length of L_{int} = 1020 μm from Equation (64) and hence a maximum energy gain of 1.7 MeV for a dual-grating structure with over 2000 periods, as shown in Figure 60.

Our analytical and PIC calculations in this section have therefore shown that the energy gain for bare dual-grating structures can be greatly enhanced by PFT laser illumination, and that it depends strongly on the tilt angle, incident laser waist radius, and the number of structure periods.

4.3 Dual-grating Structures with a Bragg Reflector Driven by a PFT Laser

In Sections 4.1 and 4.2, two kinds of schemes, the addition of a Bragg reflector and the use of PFT laser illumination, have been separately investigated in detail to improve the energy efficiency for dual-grating DLAs. Through PIC simulations, it was found that the PFT laser illumination could improve the energy efficiency by 138% while adding a Bragg reflector increased the energy efficiency by 70%. In this section, we set out to study the improvement of the energy efficiency for dual-grating DLAs through combining both schemes together. Here, a dual-grating structure with a 7-layer Bragg reflector has the same geometrical parameters as Section 4.1: $C = 0.5\lambda_p$, $H = \lambda_p$, $A = 0.5\lambda_p$, $\Delta = 0$ m, $D = 0.8\lambda_p$, λ_p = 2.0 μm. Such a quartz structure with 100 periods will be explored, driven by a PFT laser beam; hence, an energy efficiency larger than either of the two schemes can be expected. As shown in Figure 61, a 7-layer Bragg reflector is added into a dual-grating structure which is driven by a PFT laser beam with a tilt angle of γ. For relativistic electrons with $\beta = 1.0$ used in the following simulations, the tilt angle γ is chosen to be 45^0 to meet the synchronous condition.

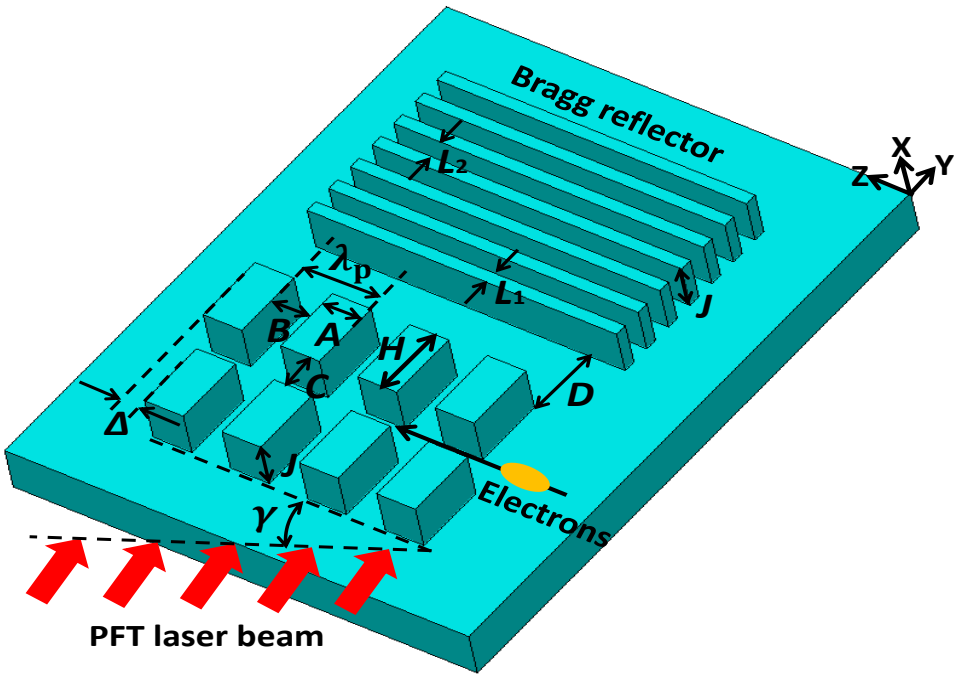

Figure 61. Schematic of the dual-gratings with a 7-layer Bragg reflector driven by a PFT laser beam with a tilt angle of γ. λ_p, A, B, C, D, H, J, L_1, L_2 and Δ represent the same geometry as Figure 47.

The same electron bunch as in Sections 4.1 and 4.2 is employed in the following simulations: mean energy of 50 MeV, bunch charge of 0.1 pC, RMS length of 9 μm, RMS radius of 10 μm, normalised emittance of 0.2 mm·mrad, and energy spread of 0.03%. The same assumptions as Sections 4.1 and 4.2 are also used here, that is: electrons travelling through the quartz structure suffer significant energy loss due to collisional straggling [90] in the dielectric material, so that only the electrons modulated by the laser field in the vacuum channel, calculated to be about 4% of the electrons at 50 MeV, are used for the following analysis.

An incident Gaussian laser pulse with the same parameters as in Sections 4.1 and 4.2 is used to generate a front-tilted laser pulse through the optical system as shown in Figure 56: wavelength of λ_0 = 2.0 μm, pulse energy of ΔP = 2.1 μJ, pulse duration of τ_0 = 100 fs, and waist radius of w_z = 50 μm. This would generate a peak laser field of E_0 = 2.0 GV/m, an ultrashort pulse duration of τ_0 = 100 fs and a tilt angle of $\gamma = 45^0$. When such a front-tilted laser pulse illuminates a dual-grating structure with a Bragg reflector, the maximum field generated in the structure area is still under the damage threshold for quartz structures. According to Equations (53) and (61), the maximum energy gain is calculated to be ΔE_m = 40 keV for normal laser illumination, and it is $\Delta E'_m$ = 90 keV for PFT laser illumination, when a peak accelerating gradient of G_p = 1.0 GV/m is assumed. These two values will be used to calculate the loaded accelerating gradients for subsequent analysis.

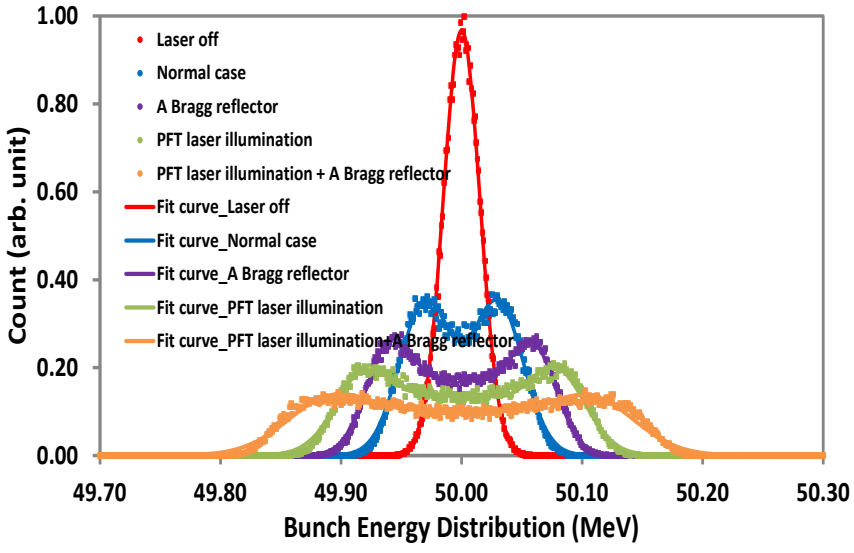

Figure 62. Bunch energy distribution for the cases of laser-off (red dots and fit curve), laser-on with a normal laser pulse for bare dual-gratings (blue dots and fit curve), laser-on with a normal laser pulse for dual-gratings with a Bragg reflector (purple dots and fit curve), laser-on with a front-tilted laser pulse for bare dual-gratings (green dots and fit curve), and laser-on with a front-tilted laser pulse for dual-gratings with a Bragg reflector (yellow dots and fit curve).

In the PIC simulations, the mesh size is set to 10 nm (z) × 20 nm (y) so that the results are convergent. The same 500,000 macro particles are used for particle tracking simulations. Figure 62 shows the results of the PIC simulations for the different configurations. Based on the Gaussian fits and HWHM methods, the maximum energy gain is ΔE_1 = 37 keV for normal laser illumination on bare dual-gratings, ΔE_2 = 63 keV for normal laser illumination on dual-gratings with a Bragg reflector, ΔE_3 = 88 keV for PFT laser illumination on bare dual-gratings, and ΔE_4 = 131 keV for PFT laser illumination on dual-gratings with a Bragg reflector. This corresponds to maximum loaded gradients of 0.925 GV/m, 1.575 GV/m, 0.978 GV/m, and 1.456 GV/m, respectively. As expected, while PFT laser illumination has a similar loaded gradient to the normal one, a Bragg reflector boosts the loaded gradient, and hence the energy efficiency, for dual-grating DLAs. The loaded accelerating gradients are increased by 70% and 49% for normal and PFT laser illumination respectively, when a Bragg reflector is added, for bare dual-grating structures. For dual-gratings with a Bragg reflector driven by a PFT laser beam, the energy gain is increased by 254% as compared to normally-incident laser illumination on bare dual-gratings

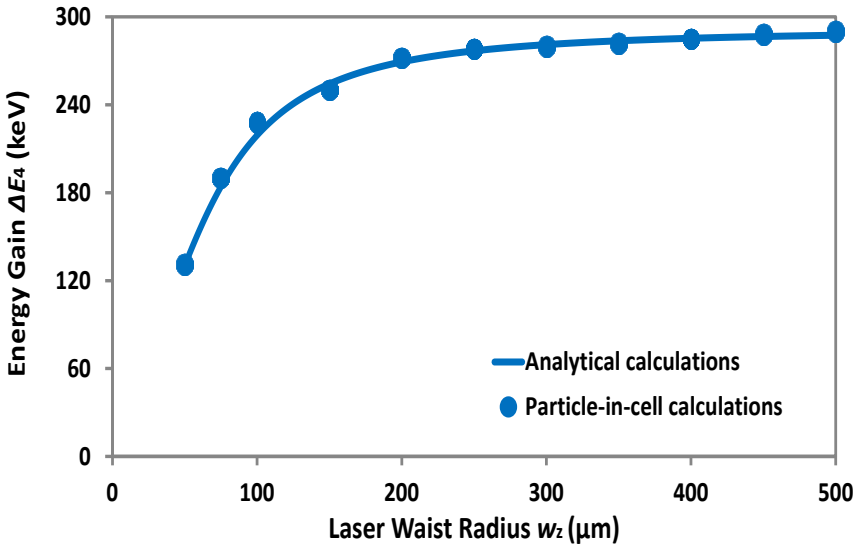

Figure 63. Energy gain from analytical (solid line) and PIC (dots) calculations as a function of the laser waist radius, for a 100-period dual-grating structure with a Bragg reflector driven by a PFT laser: $E_0 = 2$ GV/m, $\tau_0 =$ 100 fs, and $\gamma = 45^0$.

We then study further the relationship between the energy gain ΔE_4 when a PFT laser and a Bragg reflector are used and the waist radius w_z of the incident laser beam. It can be seen in Equation (64) that the interaction length L_{int} increases linearly with the waist radius w_z of the incident laser beam. By substituting Equations (64) into Equation (65) and combining Equation (60) with a loaded gradient of G_p= 1.456 GV/m, I can calculate the

energy gain ΔE_4 with the incident laser waist radius w_z analytically. Figure 63 shows the energy gain ΔE_4 from analytical and PIC calculations with variable laser waist radius w_z, and very good agreement between them is found. As shown in Figure 63, the energy gain gradually increases with a larger laser waist radius, and it reaches saturation when the laser waist radius is larger than 400 μm. For a 100-period dual-grating structure with a Bragg reflector driven by a PFT laser, the maximum energy gain is calculated to be 290 keV.

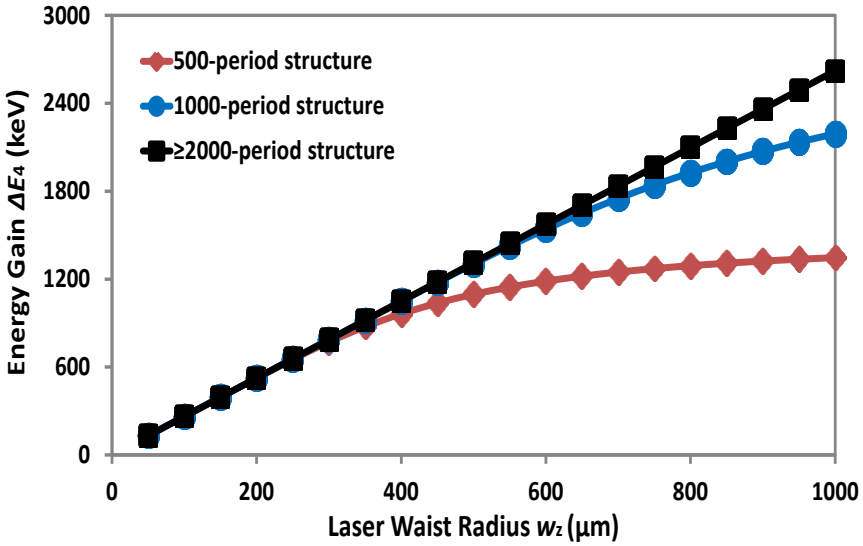

Figure 64. Analytically-calculated energy gain with increasing laser waist radius, for different periods of a dual-grating structure with a Bragg reflector driven by a PFT laser: $E_0 = 2$ GV/m, $\tau_0 = 100$ fs, and $\gamma = 45^0$.

As studied in subsection 4.2.3, a larger number of grating periods results in a higher energy gain for a bare dual-grating structure using the same electron bunch and PFT laser beam. This also applies to the dual-gratings with a Bragg reflector. Using the same mathematical Equations (60), (64), and (65) with a loaded gradient of G_p= 1.456 GV/m, the energy gain ΔE_4 with variable structure lengths LZ and laser waist radii w_z can be calculated analytically. Figure 64 shows the analytically-calculated energy gain which gradually increases to reach saturation with the laser waist radius w_z from 50 μm to 1000 μm for different periods of the structures. For a dual-grating structure with a Bragg reflector with over 2000 periods, corresponding to a length of LZ = 4000 μm, the energy gain increases linearly with laser waist radius from 50 μm to 1000 μm due to linearity of Equation (60). In this case, a laser waist radius of 1000 μm would generate an interaction length of L_{int} = 1020 μm from Equation (64) and hence a maximum energy gain of 2.6 MeV for a dual-grating structure with a Bragg reflector with over 2000 periods, as shown in Figure 64. Therefore, the energy gain for dual-gratings with a Bragg reflector which is driven by a PFT laser depends strongly on the incident laser waist radius and the number of structure periods.

4.4 Diffraction Effect

Our 2D analytical optimizations and PIC simulations in Sections 4.1, 4.2 and 4.3 are based on the assumption that the electromagnetic field is invariant along the *x*-direction and hence that the field has a 2D solution. In reality, the fabricated vertical size *J* as shown in Figure 65 plays an important role in the accelerating performance for optimized dual-gratings with a Bragg reflector. For an incident laser with a transverse waist radius $w_x = 10$ μm, the fabricated vertical size *J* should ideally be more than 20 μm so that the laser fields can be fully reflected back to enhance the accelerating fields in the vacuum channel of the structures. It would however be quite challenging to fabricate a Bragg reflector with such a high aspect ratio as $J/L_1 = 60$ based on existing quartz etching technology, although etching to a depth of over 100 μm with vertical sidewalls has been demonstrated in Ref. [135]–[137]. In this case, diffraction effects may alter the distribution of a reflected laser beam when the fabricated vertical size *J* is smaller than the transverse laser waist radius w_x. As illustrated in Figure 65, the longitudinal electric field in the channel centre is not evenly distributed along the *x*-direction, thereby reducing the accelerating performance when electrons are travelling along the channel centre of the structures in terms of the accelerating factor and the accelerating efficiency.

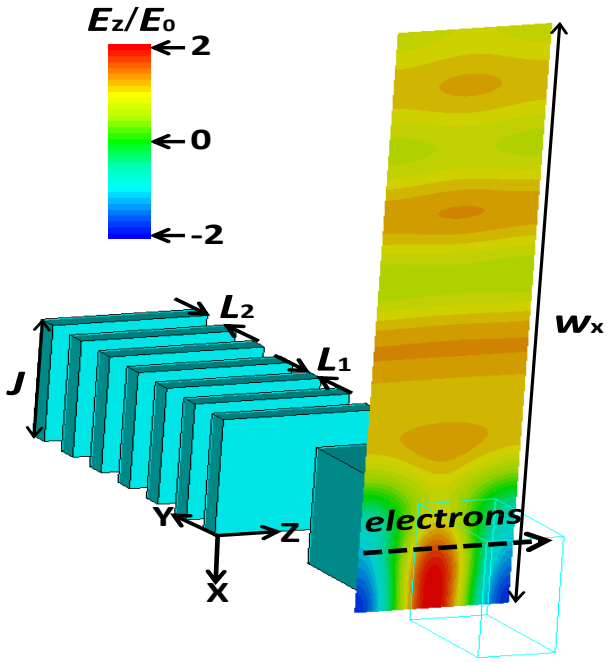

Figure 65. Transverse profile of the longitudinal electric field at the channel centre for the optimized structures of a vertical size $J/w_x = 0.2$. The green wireframe is the outline of the other grating, which is hidden in order to show the field distribution clearly.

The relationships between the fabricated vertical size J/w_x, the accelerating factor *AF*, and the accelerating efficiency *AE* are then studied in detail for normal laser illumination, which are shown in Figure 66. It is found that the maximum $AF = 0.173$ can be achieved at $J/w_x = 1.0$, while *AE* peaks at $J/w_x = 0.4$. When J/w_x equals 0.10, we get $AF = 0.09$ and $AE = 0.52$, which are comparable with the values for simulated 2D dual-gratings without a Bragg reflector. In this situation a Bragg reflector does not work at all. However, when J/w_x equals 0.20, the Bragg reflector starts to work and we find $AF = 0.10$ and $AE = 0.70$, as shown in Figure 66. The fabricated vertical size *J* should therefore be at least $0.20w_x$ if an acceptable accelerating performance is to be expected.

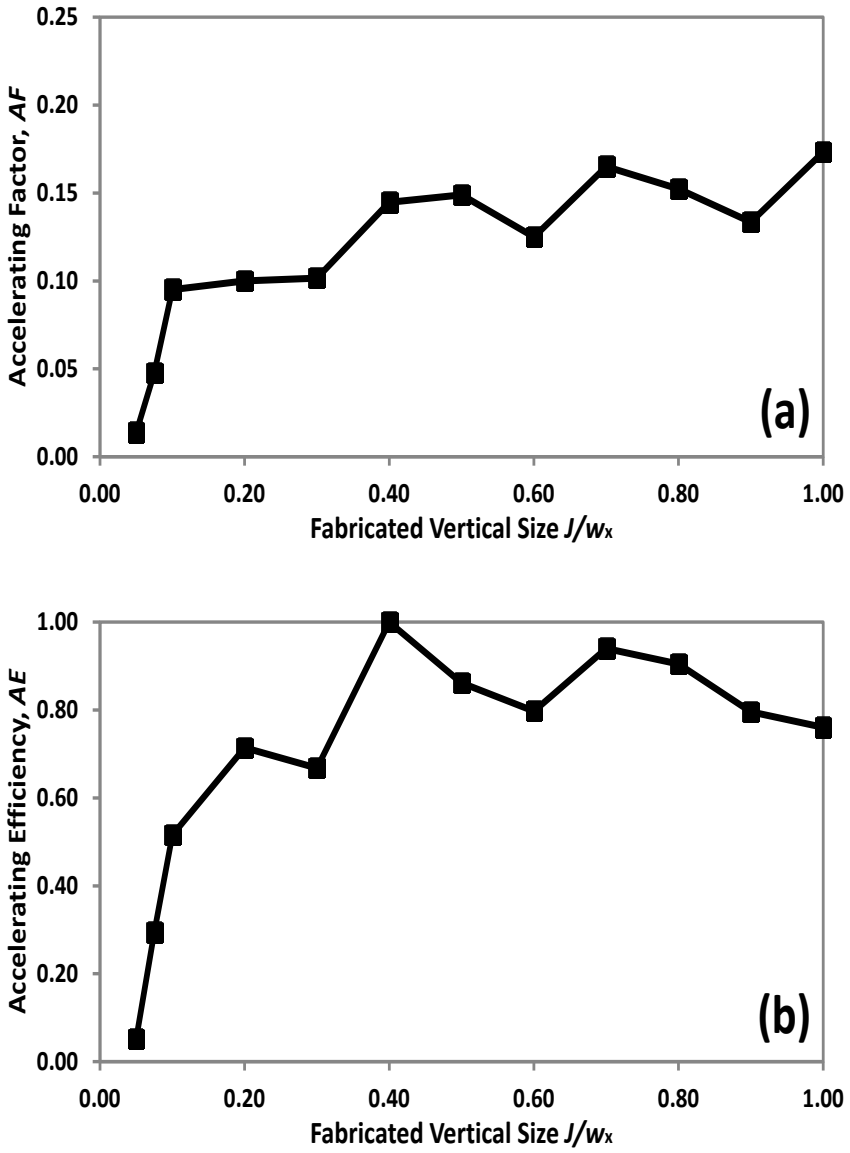

Figure 66. Optimized accelerating factor *AF* (a) and accelerating efficiency *AE* (b) as a function of fabricated vertical size of *J* which is normalized to the transverse laser waist radius w_x, for dual-gratings with a 7-layer Bragg reflector: $C = 0.5\lambda_p$, $H = \lambda_p$, $A = 0.5\lambda_p$, $\Delta = 0$ m, $R = 0.05\lambda_p$, and $D = 0.8\lambda_p$.

For example, for a normally-incident laser waist radius of $w_x = 10$ μm, an optimized structure can be fabricated with a vertical size $J \geq 2$ μm so that an aspect ratio of $J/L_1 \geq 6$ can be obtained for such a Bragg reflector. Considering that deep etching into quartz of over 100 μm with an aspect ratio of over 10 to 1 has been demonstrated in Ref. [137], a Bragg reflector with an aspect ratio of $J/L_1 \geq 6$ can be achieved using existing quartz etching technology. For a vertical size $J = 2$ μm, the analytically-calculated gradient is $0.70E_0$, which is a reduction of 8% from the value of $0.76E_0$ for 2D optimized structures. The resulting loaded gradient can in principle be decreased from 1.575 GV/m to 1.449 GV/m, based on the same PIC simulation as in Section 4.1. However, due to the small accelerating factor $AF = 0.10$, the maximum achievable gradient is limited to 1.0 GV/m. This corresponds to an incident laser with an input field of 1.43 GV/m, which generates a maximum field close to the damage threshold in the quartz structure.

In addition, through PIC simulations in Section 4.3, it is found that the PFT laser illumination generates a similar accelerating gradient to the normal one for dual-gratings with a Bragg reflector. Therefore, a vertical size $J/w_x \geq 0.20$ should also be used for fabricating such an optimized structure which is driven by a PFT laser, in order to generate an acceptable accelerating performance. For an optimized structure with a fabricated vertical size $J = 2$ μm driven by a PFT laser, the resulting loaded gradient should also have a similar reduction of 8 % from 1.456 GV/m for 2D PIC simulation.

4.5 Chapter Summary

In conclusion, this chapter has presented results from numerical studies into two schemes to improve the electron energy efficiency for dual-grating structures: adding a Bragg reflector and using PFT laser illumination.

When a 7-layer Bragg reflector is added into the bare dual-gratings, the analytical results show that this structure can generate a 70% higher accelerating gradient for the same input laser fluence, and an accelerating factor slightly larger by 0.02 ~ 0.04, than bare dual-gratings. Despite the small improvement in accelerating factor, this design could yield the same accelerating gradient when operated at a 65% less laser power, compared to that reported for bare dual-gratings. Moreover, 2D PIC simulations have been run in which a 50 MeV electron bunch is loaded into an optimized 100-period structure to interact with a laser pulse. A loaded accelerating gradient of 1.575 GV/m can be achieved, which is 70% higher than that of bare dual-gratings.

When the bare dual-gratings are driven by a PFT laser, it has been shown that this setup can extend the interaction length between laser and beam, thereby boosting the energy gain as compared to conventionally-driven DLAs. Analytical studies to calculate the energy gain for normally-incident and PFT lasers are also presented in this chapter. For DLAs driven by a laser with a FWHM duration $\tau_0 \leq 100$ fs, PFT laser illumination generates a greater interaction length than a normal one. For longer FWHMs of $\tau_0 > 100$ fs, there is a critical waist radius w_c at which both schemes have the same interaction length, but when $w_z > w_c$, a PFT laser is more efficient than a normal one. I have also studied a dedicated optical system to generate our desired PFT laser beam with an ultrashort pulse duration of 100 fs, based on mathematical calculations. In order to have the maximum diffraction efficiency, a groove density of $n_g = 450$ lines/mm is chosen as the optimum for the grating of our optical system. In this case, detailed investigations into electron beam acceleration and transmission for a laser waist radius of w_z = 50 μm are also presented. It has been found that the maximum gradient remains unchanged, but that the energy gain is increased by 138% for PFT laser illumination as compared to normal illumination. Moreover, it is found that the energy gain is strongly dependent on the tilt angle, incident laser waist radius and the number of structure periods. The maximum energy gain occurs at a tilt angle of 45^0 for relativistic electrons. For a 100-period dual-grating structure, when the incident laser waist radius w_z increases from 50 μm to 500 μm, the energy gain gradually saturates to 194 keV. For an incident laser with a waist radius of 1000 μm, a PFT laser beam with an interaction length of L_{int} = 1020 μm can be generated using our optical system. When such a PFT laser beam is introduced to illuminate a dual-grating structure with over 2000 periods, a maximum energy gain of 1.7 MeV can be expected.

When the dual-gratings with a Bragg reflector are driven by a PFT laser, the generated energy gain is increased by 254% as compared to normal laser illumination on the bare dual-gratings. For a 100-period dual-grating structure with a Bragg reflector driven by a PFT laser, the maximum energy gain is calculated to be 290 keV. For a dual-grating structure with a Bragg reflector with over 2000 periods driven by a PFT laser, the energy gain increases linearly with laser waist radius from 50 μm to 1000 μm. A maximum energy gain of 2.6 MeV can be obtained for an incident laser with a waist radius of 1000 μm. In this case, a PFT laser beam with an interaction length of L_{int} = 1020 μm can be generated using our optical system.

Finally, studies of the diffraction effect due to a fabricated vertical size *J* smaller than the laser waist radius have also been presented. It is found that the optimized structure should be

fabricated with a vertical size $J/w_x \geq 0.20$, to generate an acceptable accelerating performance.

By extension, a Bragg reflector and PFT laser illumination can be used to improve the energy efficiency for any DLA structure. A Bragg reflector can be integrated with any DLA structure into a single wafer, using existing nanofabrication technology. This eliminates the complicated alignment process involved when a mirror is used externally to reflect the laser power back into any structure. Such an integrated structure can be illuminated by a PFT laser beam generated through our optical system, which can extend the interaction length and boost the energy gain. However, realistic fabrication and experimental studies are still required to pave the way for implementing the proposed concept for such an integrated nano-structure driven by a PFT laser beam.

5. THz-driven Dual-grating Structures

Dual-grating structures driven by laser pulses have been studied in Chapter 3 and Chapter 4. In this chapter a quartz dual-grating structure is investigated for accelerating electrons at THz frequencies. In this case, the geometry dimensions for dual-gratings are much larger than those driven by laser pulses so that they can be fabricated with conventional machining techniques. In Section 5.2, geometry studies are performed in order to find the optimum dual-grating structure for the acceleration of relativistic electrons. It is then followed in Section 5.3 by a detailed wakefield study in which an electron bunch is loaded into an optimized 100-period dual-grating structure. Such an electron bunch can be obtained from the future CLARA [119]. In Section 5.4, a linearly-polarized THz pulse is introduced to interact with the electron bunch in the optimized structure. The beam quality achievable is analyzed in terms of emittance, energy spread and loaded accelerating gradient.

5.1 Motivation

Dielectric structures have been found to withstand electric fields one to two orders of magnitude larger than metals at optical frequencies, thereby sustaining high accelerating gradients in the range of GV/m. These dielectric structures can be driven either by infrared optical or by THz pulses, enabling dielectric laser-driven accelerators (DLAs) and dielectric THz-driven accelerators (DTAs). Empirically, it is found that the RF-induced breakdown threshold E_s scales with frequency as $f^{1/2}$and with pulse duration as $\tau^{-1/4}$, as described in $E_s \propto f^{1/2}\tau^{-1/4}$ [138], [139]. This indicates that in principle, DLAs can generate accelerating gradients higher than DTAs. DLAs have successfully demonstrated accelerating gradients of 300 MV/m [47] and 690 MV/m [48] for relativistic electron acceleration, and gradients of 25 MV/m [51], 220 MV/m [52] and 370 MV/m [53] for non-relativistic electron acceleration. However, DLAs suffer from low bunch charge and sub-femtosecond timing requirements due to the short wavelength of operation. In a DLA, a laser beam is used to accelerate particles through a microscopic channel in an artfully-crafted glass chip. Such a channel gap can be no wider than a few μm [47], [48], [79]–[82], [112], [126], [130] in order to generate a high gradient of GV/m, which limits the transverse size and hence the bunch charge. Furthermore, for a laser wavelength of 2 μm, the particle bunch has to occupy only a small fraction of the optical cycle in order to maintain good beam quality in terms of emittance and energy spread. If 1^0 of optical cycle is used, the total bunch length is only 5.6 nm, which also limits the particle bunch charge. In addition, the timing precision between the

optical cycle and the arrival of the particle bunch is a practical concern. Using a laser wavelength of 2 μm, a 1^0 phase jitter requires a timing jitter of < 20 attoseconds between the optical pulse and the particle bunch, which is challenging to maintain over long distances.

THz frequencies provide wavelengths two orders of magnitude longer than optical sources. In this situation, DTAs can be fabricated with conventional machining techniques due to the relatively long wavelength of operation. This accommodates particle bunches with larger sizes and charges, which is more beneficial for bending and focusing [140] compared to DLAs. DTAs also provide a more accurate timing jitter than DLAs. For a THz wavelength of 600 μm, 1^0 of optical cycle corresponds to a 1.7 μm bunch length, while 1^0 of phase jitter requires a 5.6 fs timing jitter, which is readily achievable [141]. With recent advances in sources for the generation of THz, pulse energies in mJ and extremely high electric fields in the GV/m have been achieved [142]–[144], which can boost the accelerating gradient up to GV/m for a DTA. Experiments have already demonstrated the acceleration of electrons in THz-driven dielectric structures [145]–[147]. Therefore, DTAs hold great potential for reducing the size and cost of future particle accelerators.

This chapter investigates numerically a quartz dual-grating structure which is driven by THz-pulses to accelerate electrons [148]. As shown schematically in Figure 67, a short, intense THz pulse is used to illuminate a dual-grating structure, creating a standing-wave-like electric field in the structure's channel gap where the electrons travel and are accelerated. Such a dual-grating structure has the same geometry, but different dimensions, as compared to one driven by laser pulses.

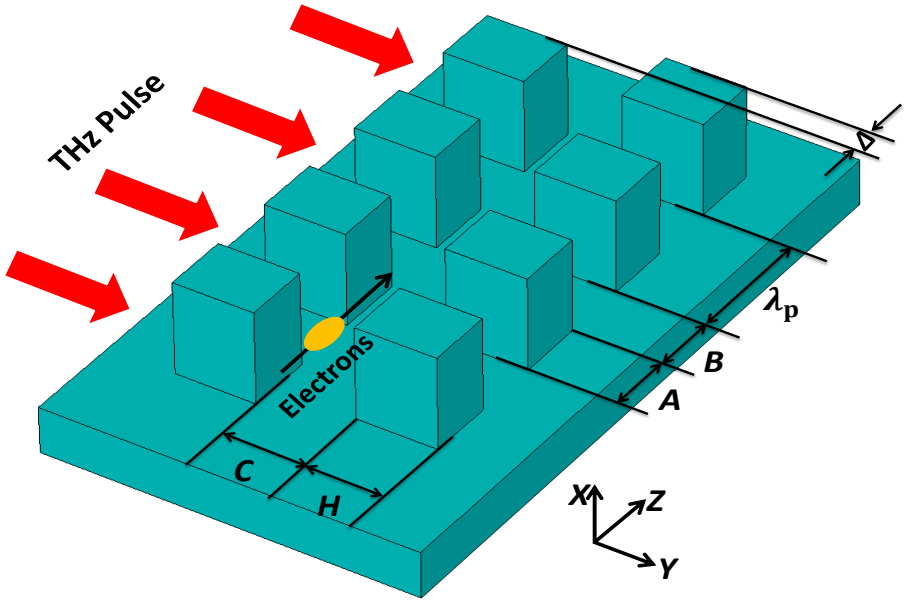

Figure 67. Schematic of a THz-driven dual-grating structure. λ_p, *A*, *B*, *C*, *H*, and *Δ* represent the same geometry as Figure 47.

5.2 Geometry Optimizations

When a linearly-polarized THz pulse travels through the structure, the speed of the wave in vacuum is higher than that in the dielectric grating pillar. This produces the desired π phase difference in the vacuum channel for the wave front, resulting in periodic energy modulation for electrons travelling along the longitudinal *z*-axis. In order to optimize such a dual-grating structure, the code VSim, based on a FDTD method, is used to compute the electric and magnetic fields generated in the structure. The gratings are modelled as a 2-dimensional (*y*-*z* plane) structure to simplify our computations for the electric and magnetic fields. Periodic boundary conditions are applied along the electron channel in the z direction. Perfectly matched layers (PMLs) are used along the THz propagation direction (*y*-axis) to absorb the transmitted wave. The mesh sizes are set to $\lambda_p/200$ and $\lambda_p/100$ so that the simulation results converge to increase accuracy.

A uniform plane wave with a wavelength of λ_0 = 150 μm and a field amplitude E_0 propagates in +*y* and illuminates a single-period dual-grating structure, as illustrated in Figure 68. A grating period of λ_p = 150 μm is chosen so that the first spatial harmonic and relativistic electrons are synchronized [88]. The desired π phase difference for the wave front can be achieved by setting pillar height $H = \frac{\lambda_0}{2(n_r-1)} = 0.5\lambda_0$, here quartz [149] with a refractive index of $n_r = 2$ is chosen due to its high damage threshold [87], [145]–[147], [150], [151] and thermal conductivity.

We then need to optimize the longitudinal electric field $E_z[z(t), t]$ in the channel centre of the structure, as shown in Figure 68, to maximize the accelerating gradient G_0, which is defined as Equation (25). To find the maximum accelerating gradient, we need to maximize the electric field distributed in the structure, which should not exceed the material damage field. Therefore, the accelerating factor, which is defined by the ratio of the accelerating gradient G_0 to the maximum electric field E_m in the structure, needs to be maximized for geometry optimization.

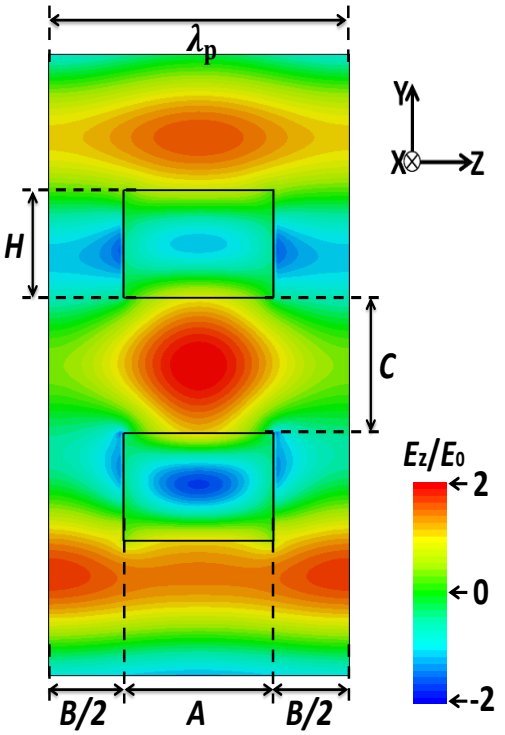

Figure 68. Longitudinal electric field E_z distribution in a single-period dual-grating structure illuminated by a uniform plane wave with a field E_0 along y-axis.

As shown in Figure 69 (a), for an initial pillar height $H = 0.50\lambda_0$, a maximum accelerating factor $AF = 0.18$ can be achieved when the vacuum channel gap $C = 0.2\lambda_0$. When C increases above $0.20\lambda_0$, the accelerating factor AF gradually decreases, which can be also seen in Figure 69 (a). This means that the achievable gradient gradually drops with $C > 0.2\lambda_0$, and a channel gap of $C = 0.5\lambda_p$ is chosen as an acceptable parameter in a trade-off between the accelerating gradient and the available phase space in which high accelerating gradient occurs. As shown in Figure 69 (b), a maximum accelerating factor ($AF = 0.141$) occurs at a pillar height of $H = 0.80\lambda_p$ for the structure with an optimum channel gap, $C = 0.5\lambda_p$. Fixing the grating structure with $C = 0.5\lambda_p$ and $H = 0.8\lambda_p$, we then set out to find the optimal pillar width A. Figure 69 (c) shows that $AF = 0.141$ can be obtained for a pillar width $A = 0.5\lambda_p$. The effect of a longitudinal shift Δ between the gratings is also investigated. It can be seen from Figure 69 (d) that the maximum $AF = 0.141$ occurs when they are perfectly aligned ($\Delta = 0$ m). However, the worst shift can reduce the accelerating factor by a factor of 54% to $AF = 0.065$. The damage threshold for quartz at THz frequencies has been found experimentally to be ~13.8 GV/m [150]. A maximum accelerating factor of $AF = 0.141$ therefore corresponds to a maximum achievable gradient of $0.141 \times 13.8 = 1.95$ GV/m for a quartz dual-grating structure.

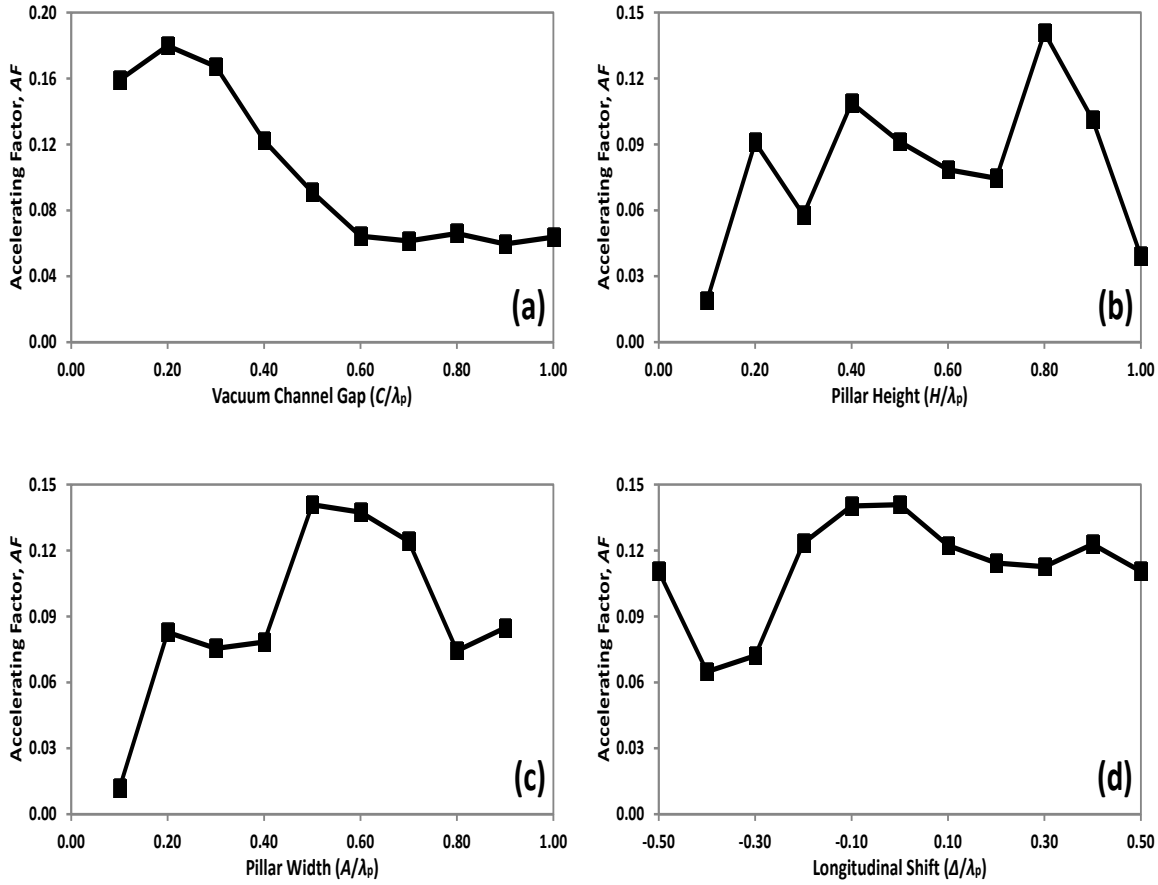

Figure 69. FDTD optimization of accelerating factor *AF* as a function of (a) vacuum channel gap *C* with a fixed pillar height $H = 0.5\lambda_p$, (b) *H* with a fixed $C = 0.5\lambda_p$, (c) pillar width *A* with a fixed $C = 0.5\lambda_p$ and $H = 0.8\lambda_p$, and (d) longitudinal shift Δ with a fixed $C = 0.5\lambda_p$, $H = 0.8\lambda_p$ and $A = 0.5\lambda_p$.

5.3 Wakefield Study

After geometry optimization, a dual-grating structure with a channel gap of $C = 0.5\lambda_p$, pillar height of $H = 0.8\lambda_p$, pillar width of $A = 0.5\lambda_p$, longitudinal shift of $\Delta = 0$ m and grating period of $\lambda_p = 150$ μm is chosen as the optimum for the studies which follow. In this section, detailed wakefield studies are carried out by loading an electron bunch into this optimized 100-period dual-grating structure, initially without any THz illumination.

The electron bunch employed in our simulations has a mean energy of 50 MeV, bunch charge of 0.3 pC, RMS length of 90 μm, RMS radius of 5 μm, normalised emittance of 0.15 mm·mrad, and energy spread of 0.05%. Such an electron bunch can be generated in the future CLARA [119]. It should be noted that the bunch parameters are different from those used in Chapter 3 and Chapter 4 due to the different wavelength of operation. Such an electron bunch suffers no electron loss when it travels through a 100-period structure. In this case, the following simulation results can be precisely used for prediction of experimental demonstrations in the absence of electron-dielectric collision [90].

When such an electron bunch with Gaussian profiles is injected to travel along the channel centre of the optimized structure, without any offset in the y direction, it generates electromagnetic fields which propagate in the vacuum channel. The wakefields are reflected back by dielectric gratings and interact with the bunch itself, resulting in energy loss or deflection for electrons in the bunch. Here, the Wakefield Solver of CST is used to calculate the wakefield generated in the optimized structure. It is then followed by a VSim PIC simulation which is performed to analyze the effect of the wakefield on the bunch in terms of emittance and energy spread. The longitudinal (*z*-component) and transverse (y-component) wakefield distribution on the *z*-axis in the structure are illustrated in Figure 70. Figure 70 (a) gives a maximum longitudinal decelerating wakefield of 2.00 MV/m for the bunch. It agrees well with the final bunch energy distribution as given in Figure 71, which shows an energy spread of 0.068% and average energy loss of ΔE_a = 25 keV for the whole bunch, corresponding to a decelerating field of 1.67 MV/m. In addition, the transverse wakefield, which deflects electrons, is negligible as given in Figure 70 (b) due to the small transverse size and symmetrical Gaussian profile in the *y* direction. This is in accordance with results from particle tracking simulations showing that when the bunch travels out of the structure, the normalized RMS emittance is still 0.15 μm, remaining the same as it was initially.

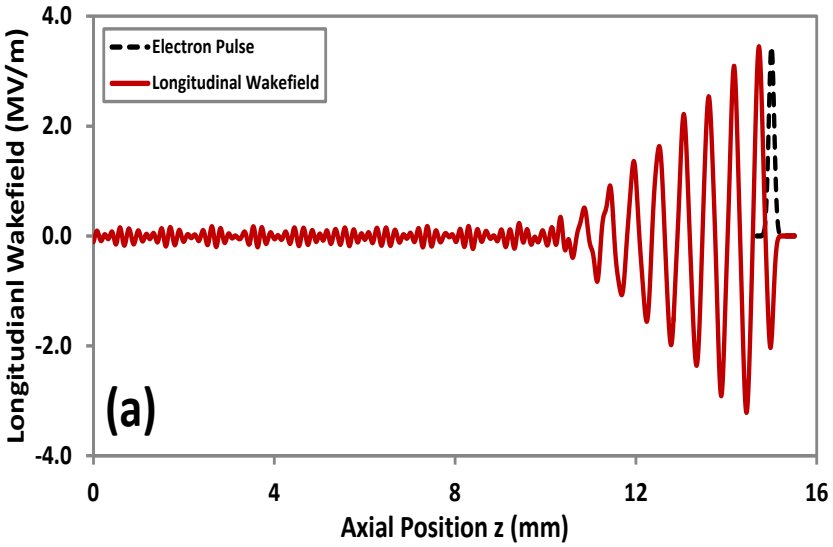

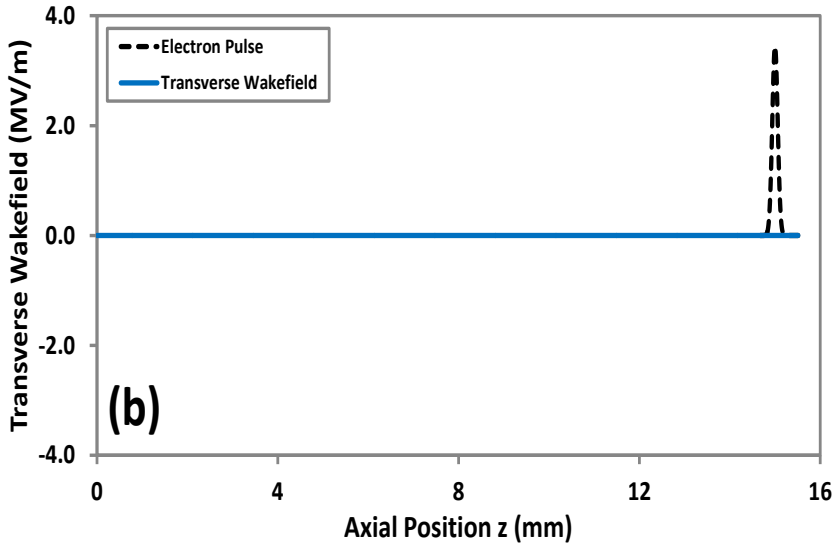

Figure 70. Simulated longitudinal (a) and transverse (b) wakefield distribution on *z*-axis. The electron bunch travels along the *z*-axis.

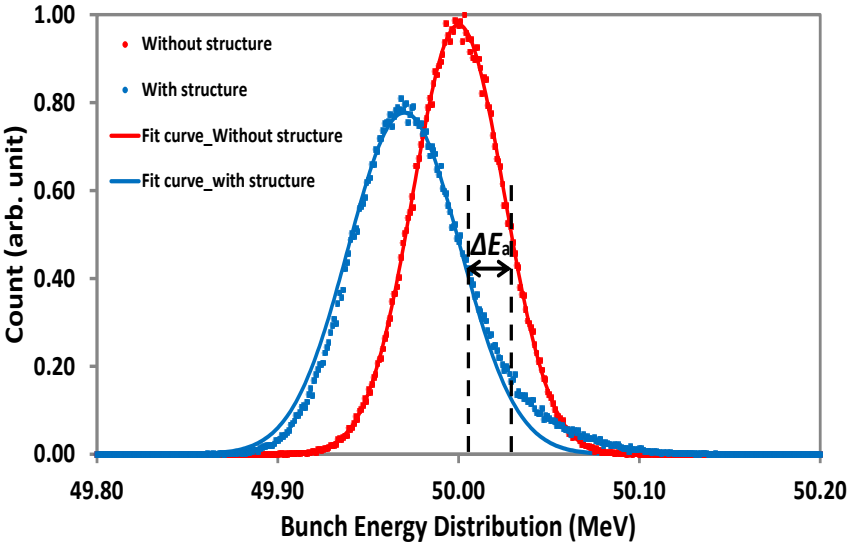

Figure 71. The bunch energy distribution without structure (red dots and fit curve) shows an energy spread ~25 keV (0.05%) whereas the bunch going through the structure (blue dots and fit curve) shows an energy spread ~34 keV (0.068%).

5.4 THz-bunch Interaction

In this section, a linearly polarized Gaussian THz pulse, as shown in Figure 72, is launched to propagate along the *y*-axis to interact with the electron bunch in the vacuum channel of the optimized structure. All relevant parameters are described in Table 10. Here, the peak field of the THz pulse is set to 1.0 GV/m, which can be obtained from a multi-cycle

THz pulse with mJ energy proposed by K. Ravi *et al.* [152]. This field is far below the quartz damage threshold. In its co-moving frame, the bunch experiences the strongest field in the channel centre, through precise timing calculation. The calculated interaction length is $w_{\mathrm{int}} = \left(\frac{1}{w_z^2} + \frac{2\ln 2}{(c\tau_p)^2}\right)^{-0.5}$ = 454 μm, as described in Ref. [92], [107], where c is the speed of light. Using Equation (53) with a peak accelerating gradient of G_p = 1.0 GV/m results in a maximum energy gain of $\Delta E_{mT} \approx 805$ keV is generated, which can be used to calculate the loaded accelerating gradient for the PIC simulations to follow.

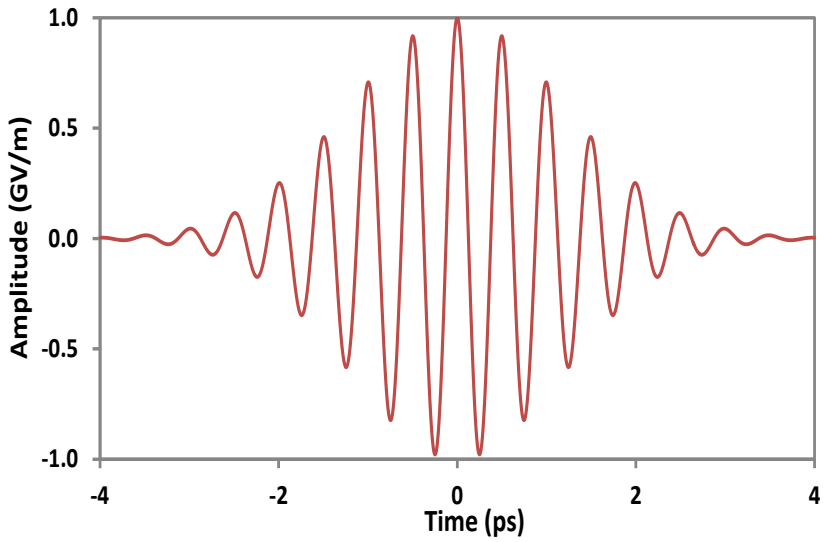

Figure 72. The electric field envelope of the THz pulse.

Table 10. Parameters of the THz pulse used in the simulation.

THz pulse characteristics	
Propagation direction	$+y$
Wavelength λ	150 μm
Peak field E_p	1.0 GV/m
FWHM duration τ_p	2.0 ps
Waist radius w_z	1.0 mm

A second PIC simulation is then carried out using the same bunch parameters, in which the electrons experience a field superposition of the particles' wakefields and the driving

field produced from the THz pulse. From PIC results, it is found that the transverse RMS emittance is 0.155 μm when the bunch travels out of the structure, corresponding to an increase of 3.0% compared to the THz-off case. This minor increment can be explained by the weak deflecting force excited by the THz pulse. However, this deflecting force does not change the bunch transverse emittance significantly for such a short interaction distance. It can also be compensated by symmetric illumination using two THz pulses from opposite sides.

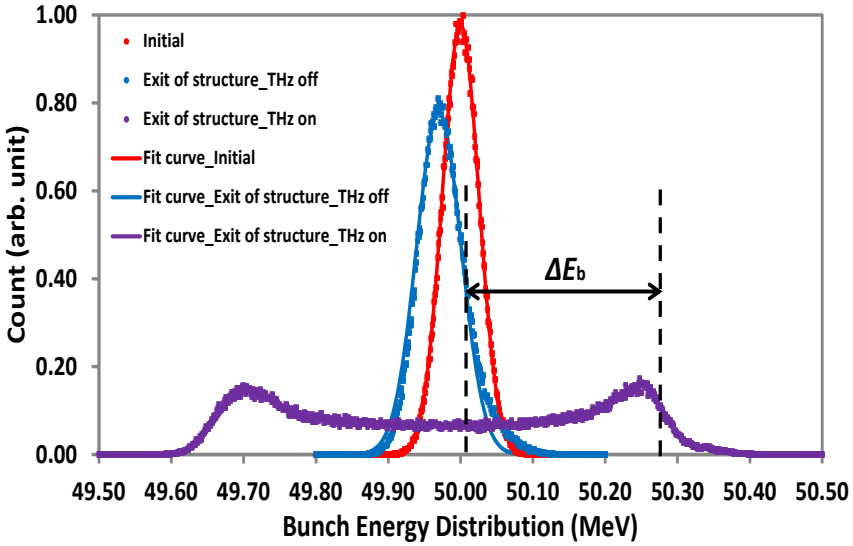

Figure 73. The energy distribution for the initial bunch (red dots and fit curve), and the bunch exiting the optimized structure when THz is off (blue dots and fit curve) and on (purple dots and fit curve).

The electron bunch has an RMS length of σ_z = 90 μm, so that most electrons in the range of ± σ_z are able to sample all phases of the THz field. Each slice of electrons ($\Delta t \ll \lambda_0/c$) samples a different phase of the sinusoidal electric field in the vacuum channel, which results in some electrons gaining energy from acceleration while others are decelerated. This generates a double-peaked profile [148] for the final bunch energy distribution, as shown in Figure 73. The final bunch has an energy spread of 0.42% when calculated with particle tracking simulations. It is also found that the maximum energy gain is ΔE_b = 281 keV, corresponding to a maximum accelerating gradient of G_m = 349 MV/m. It should be noted here that such a calculated gradient is different from that published in Ref. [148] due to different calculation methods for energy gain. When the peak field of a THz pulse is increased to E_p = 3.0 GV/m, an accelerating gradient greater than 1.0 GV/m will be expected for such a structure. It is seen from the simulation that this THz field of 3.0 GV/m leads to a maximum field of 9.37 GV/m, which is still below the damage threshold for quartz structures.

5.5 Chapter Summary

This chapter presents numerical simulations for a THz-driven dual-grating structure to accelerate electrons, including detailed studies of geometry optimizations, wakefield and THz-bunch interaction. Geometry studies have been carried out to maximize the accelerating factor with the widest channel gap C. For an optimized structure with a channel gap of $C = 0.5\lambda_p$, pillar height of $H = 0.8\lambda_p$, pillar width of $A = 0.5\lambda_p$ and longitudinal shift of $\Delta = 0$ m, a maximum accelerating factor $AF = 0.141$ can be obtained, corresponding to a maximum unloaded gradient of $G = 1.95$ GV/m. Using CST and VSim, a Gaussian electron bunch from the future CLARA is loaded into an optimized 100-period structure for a detailed wakefield study. When the bunch travels out of the optimized structure, the average energy is reduced by 25 keV due to its interaction with the longitudinal decelerating wakefield. The transverse wakefield will be negligible so that it does not have any effect on the bunch emittance. An intense THz pulse is then added to the simulation to interact with the CLARA bunch in the optimized structure. When the bunch propagates out of the structure, the transverse RMS emittance is increased by 3.0% compared to the THz-off case, the energy spread changes from 0.05% to 0.42%, and an accelerating gradient of 349 MV/m is expected, from the particle tracking simulations.

These simulations have demonstrated numerically the high gradient acceleration of electrons in a dual-grating structure driven by THz pulses, with a small emittance increase. However, there are still some technical challenges to implementing it in reality. Firstly, despite some experiments which have generated multi-cycle THz pulses with nJ [153] and μJ energies [154], further development is needed to obtain THz pulses with mJ energies, to generate the peak field of 1 GV/m which is assumed for our simulations. The second challenge is to improve the electrons' energy gain, which is limited by the short THz-bunch interaction length caused by the short THz pulse duration. A principal option for DLAs is to tilt the front of the laser pulses by diffraction gratings to extend the interaction length, thereby increasing the electrons' energy gain. However, THz pulses cannot be operated in the same way due to their wide bandwidth [155]. For DTAs a multilayer dielectric Bragg reflector [126] could instead be incorporated into the structure to boost the accelerating field in the channel, which has the potential to increase the energy gain. Further research efforts on fabrication and experiment are still required to pave the way for a realistic high-energy DTA concept.

6. Preliminary Fabrication and Preparation for Experiments with Dual-grating Structures

In Chapter 3 the optimized geometry for dual-grating structures was obtained. In this chapter we investigate the techniques used to fabricate such optimized dual-grating structures. Laser damage threshold experiments have shown that Sapphire (Al_2O_3) can withstand a laser influence of 4.9 J/cm^2, the highest for all the dielectrics tested [93]–[95]. However, fabrication techniques for Sapphire are not as well developed as for Silicon, which forms the basis of the current semiconductor industry. Unfortunately, Silicon has a much lower damage threshold of only 0.18 J/cm^2. As a compromise, quartz (SiO_2) with a promising damage threshold of 2 J/cm^2 has been chosen for our structures. Having already decided on quartz as the substrate material, the next step is to develop a process for fabrication. With the help of researchers from PSI, a monolithic method was developed to fabricate the desired dual-grating structures. This method eliminates the complicated bonding process and generates a good alignment of the two gratings, as compared to structures developed at SLAC [47]. In addition, some experimental preparations using the SwissFEL [156]–[158] are also presented in this chapter, which paves the way for future demonstrations using our fabricated structures.

6.1 Fabrication Studies

There are many methods of fabricating dual-grating structures. A fabrication process has been successfully developed by researchers from SLAC including lithography, etching, alignment and bonding [47]. The bonding process requires a micrometre-controlled stage and a microscope for manual alignment, yielding an alignment accuracy of ~3.0 μm. To eliminate such a bonding process and improve the alignment accuracy, a monolithic method has been developed to fabricate the desired dual-grating structures. In this method, electron-beam lithography is used to pattern the structure onto the surface of the quartz wafer. A trench of area $J \times C$ defining the vacuum channel is then etched onto the quartz substrate by a gaseous plasma, as shown in Figure 74. In this configuration, accurate alignment between two gratings can be achieved. Figure 74 shows the 3D geometry for a dual-grating structure with a grating period of 2.0 μm on a wafer. However, the etching technology for quartz material is not as well developed as for silicon. Although etching into quartz to a depth of over 100 μm, with an aspect ratio of over 10 to 1, has been demonstrated in Ref. [137], the

issue still arises that the channel depth J can only be fabricated to a few micro-meters for a channel gap of 1.0 μm. In this case, the potential diffraction effect caused by a channel fabricated to a depth smaller than the transverse laser waist radius will affect the accelerating performance for our structures. In addition, a small channel depth J also limits the transverse size of the electron bunch injected into the vacuum channel gap, and brings challenges for laser focusing.

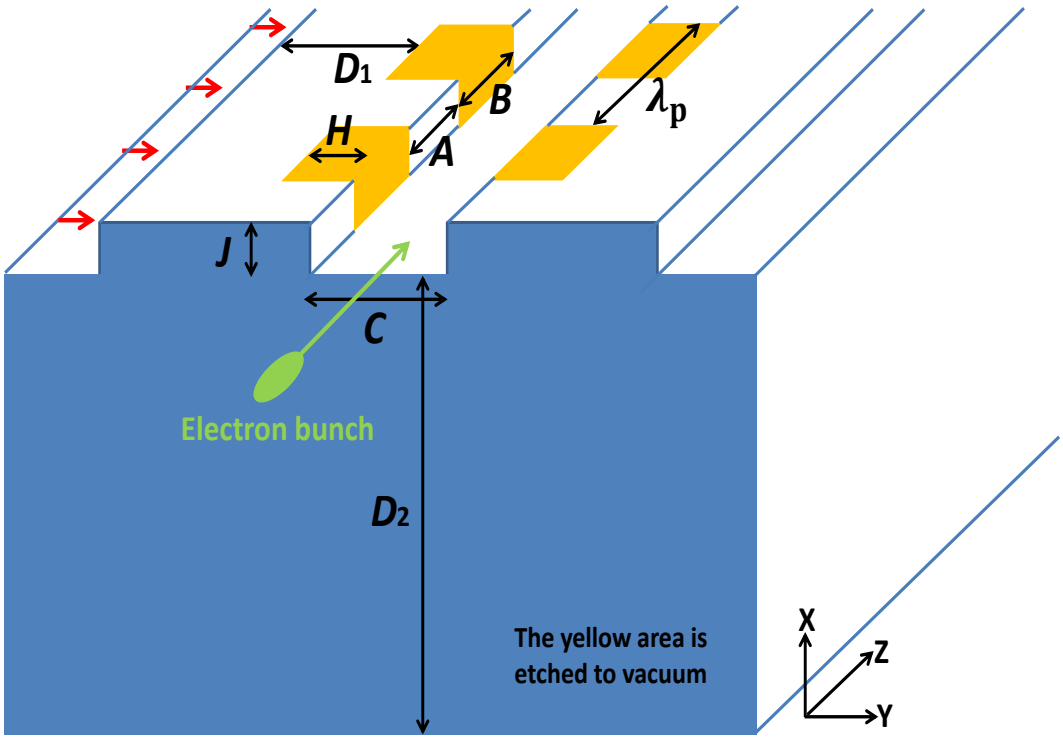

Figure 74. 3D geometry for a dual-grating structure on a wafer: λ_p, A, B, C, H, D_1, D_2, and J represent grating period, pillar width, pillar trench, vacuum channel gap, pillar height, grating thickness, wafer height, and vacuum channel depth, respectively.

Table 11 shows the fabricated geometry for a dual-grating structure which is the same as the optimum one mentioned in Chapter 3. Four kinds of dual-grating structures with 100, 200, 500, and 1000 periods will be fabricated. This allows us to have more flexibility in our experimental setup. As we described in Chapter 4, a larger number of periods results in a higher energy gain for the same electron bunch and laser beam. Different energy gains for different structures can therefore be expected in realistic demonstrations. It should be noted here that the channel depth J is a key parameter for accelerating performance, and it is still to be determined for the following fabrication process. In addition, the grating thickness D_1 is chosen to be 10 μm in order to avoid guided-mode resonance [159] which may increase the field inside the structure and hence cause it to break down.

Table 11. Geometry parameters for the fabricated dual-grating structures.

Geometries	
Number of periods	100, 200, 500, 1000
Grating period λ_p	2.0 μm
Vacuum channel gap C	1.0 μm = 0.50λ_p
Pillar height H	1.6 μm = 0.80λ_p
Pillar width A	1.4 μm = 0.70λ_p
Trench width B	0.6 μm = 0.30λ_p
Longitudinal shift Δ	0.0 nm
Grating thickness D_1	10.0 μm
Wafer height D_2	500.0 μm
Vacuum channel depth J	To be determined

6.1.1 Diffraction Effect

For an incident laser with a transverse waist radius $w_x = 10$ μm, the fabricated channel depth J should ideally be more than 20 μm, so that the laser fields can propagate through the structure to generate the accelerating fields in the vacuum channel, as shown in Figure 74. It would however be quite challenging to fabricate a channel with such a high aspect ratio as $J/C = 20$ based on existing quartz etching technology, although deep etching into quartz of over 100 μm with an aspect ratio of over 10 to 1 has been demonstrated in Ref. [137]. In this case, diffraction effects may alter the distribution of accelerating fields in the channel when the fabricated channel depth J is smaller than the transverse laser waist radius w_x.

The relationship between the fabricated channel depth J/w_x, the accelerating factor AF, and accelerating efficiency AE are then studied in detail for normal laser illumination, and are shown in Figure 75. It is found that the maximum $AF = 0.170$ can be achieved at $J/w_x = 1.0$, while AE peaks at $J/w_x = 0.5$. When J/w_x equals 0.30, we get $AF = 0.115$ which is reduced by 32% from AF at $J/w_x = 1.0$, and $AE = 0.33$ which is comparable with AE at $J/w_x = 1.0$. In this situation the fabricated channel depth J should therefore be at least $0.30w_x$ if an

acceptable accelerating performance is to be expected. For example, if an incident laser with a transverse waist radius $w_x = 20$ μm is used in the experiment to illuminate our structures, the fabricated channel depth J should be at least 6 μm, which is the target for the fabrication process to be followed.

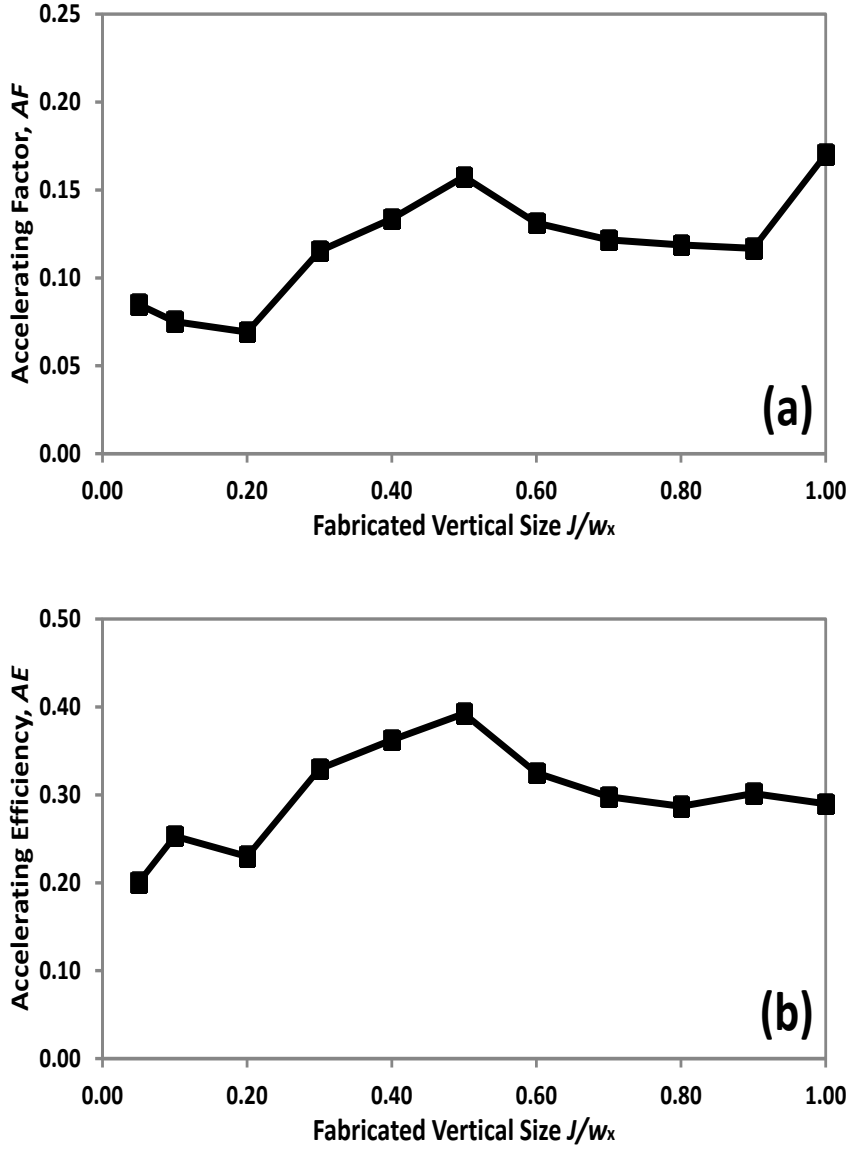

Figure 75. Acelerating factor *AF* (a) and accelerating efficiency *AE* (b) as a function of fabricated channel depth J which is normalized to the transverse laser waist radius w_x, for dual-gratings with geometry as given in Table 11.

6.1.2 Fabrication Process

Figure 76 shows the fabrication process for our dual-grating structures. At step 1, methyl methacrylate (MMA): poly methyl methacrylate (PMMA) bilayers are deposited onto the quartz substrate for positive electron-beam resist. These materials consist of long polymer chains of carbon atoms which come in various molecular weights. The MMA: PMMA bilayers are useful for processes that require lift-off of metallic structures. For good lift-off an undercut resist profile is needed to avoid coating the sidewall of the resist when the metal is evaporated. This is particularly true for obtaining an extremely vertical sidewall profile. The MMA/PMMA bilayer gives a good undercut profile. It should be noted that as a good rule of thumb, the lower layer of resist should be twice as thick as the metal lifted off. A first layer of MMA 8.5 (9% in ethyl lactate) is spin-coated onto a quartz substrate using a spin coater and is oven baked at 140 °*C* for 2 minutes in order to evaporate any excess solvent in the resist. A second layer of PMMA 950 (2% in anisole) is then spun on top of that layer and soft-baked at 170 °*C* for 2 minutes. The thickness was usually set to 400 nm for the MMA layer and 125 nm for the PMMA, but different thicknesses could be used depending on the thickness and the resolution desired for the final structure.

At step 2, the wafer is placed into a high vacuum chamber inside an Edwards electron beam evaporator, where a thin chromium (Cr) layer is deposited on top of the pattern in order to prevent surface charging during the electron-beam lithography.

At step 3, the wafer is then exposed to an electron-beam for lithography. Exposure causes scission of the long polymer chains. This means that areas exposed by the electron-beam have lighter molecular weight (blue part) for PMMA and MMA, while other parts not exposed by e-beam have heavier molecular weight. The Cr layer and exposed (lighter molecular weight) bilayer are then removed in a solvent developer.

At step 4, a layer of Cr with a thickness of 200 nm and a layer of Nickel (Ni) with a thickness of 50 nm are deposited onto the sample surface. This is followed by step 5, where the sample is immersed into acetone for lift-off. After this, only the Cr and Ni layer covering the structure pattern are left on the sample surface.

Finally, at step 6, the wafer is diced to create 12 samples, and each sample is put into a Reactive Ion Etching (RIE) 100 machine for etching by plasma gases. A trench of area $J \times C$ defining the vacuum channel is etched onto the quartz substrate. More details can be found in the following subsection 6.1.4.

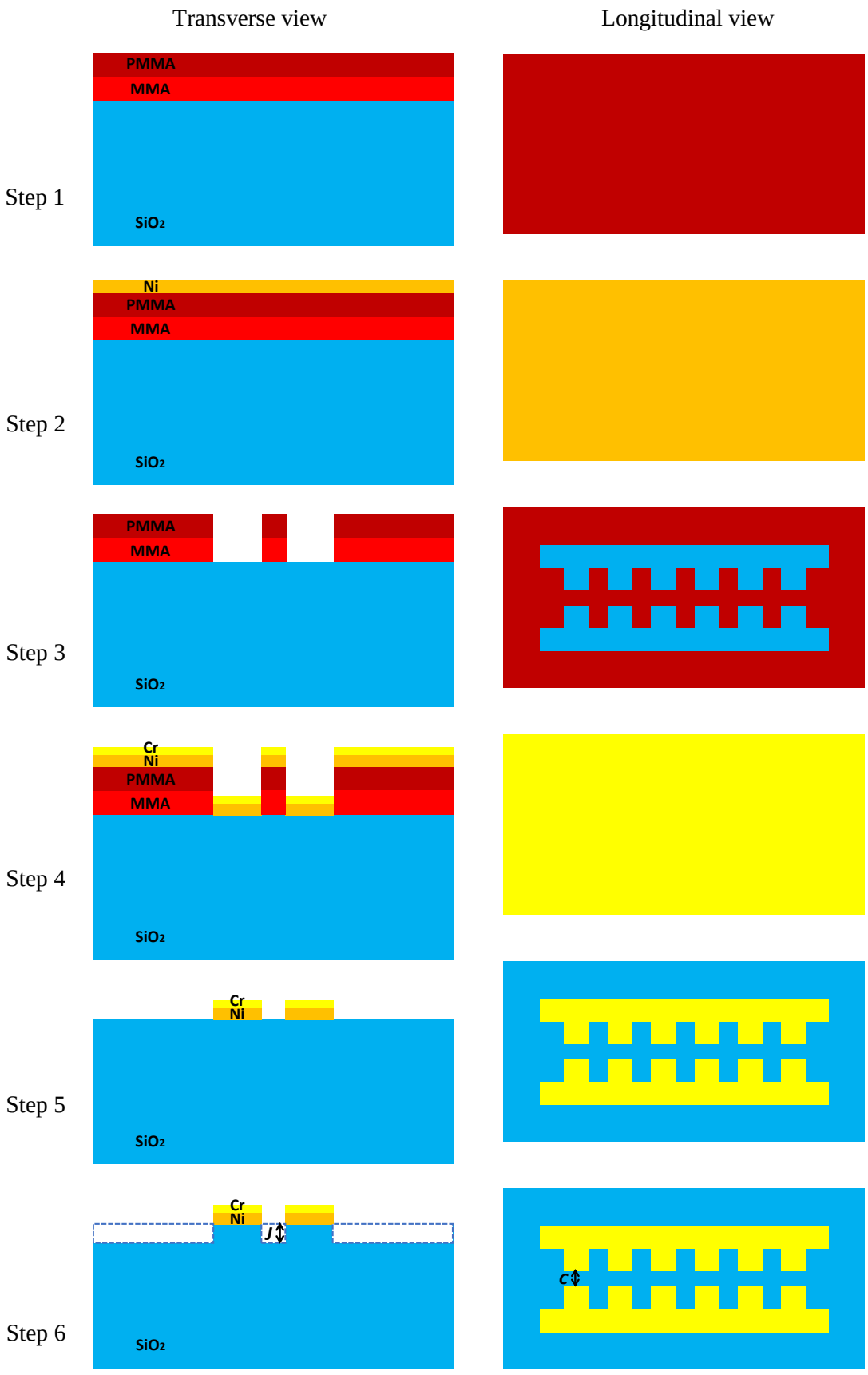

Figure 76. The fabrication process from step (1) to step (6) in the transverse and longitudinal view, respectively.

6.1.3 Structure Pattern on a Wafer

As illustrated in Figure 77 (a), a quartz wafer can be diced into 12 samples. Each sample has an area of 22 mm × 22 mm, and it consists of 8 dual-grating structures on the surface: 2 identical structures with periods of 100, 200, 500, and 1000, respectively. One sample can be diced into 4 chips, each of which occupies an identical area of 11 mm × 11 mm, as can be seen in Figure 77 (c). There are some special labels along the purple lines, as shown in Figure 77 (b), which can be used for more accurate dicing alignment. On a single chip, the dual-grating structures are put close to the chip edges in order to mitigate the diffraction effect which is caused by the small depth *J*. In addition, the chip edges can be used for alignment of the electron beam injected into the dual-grating structures.

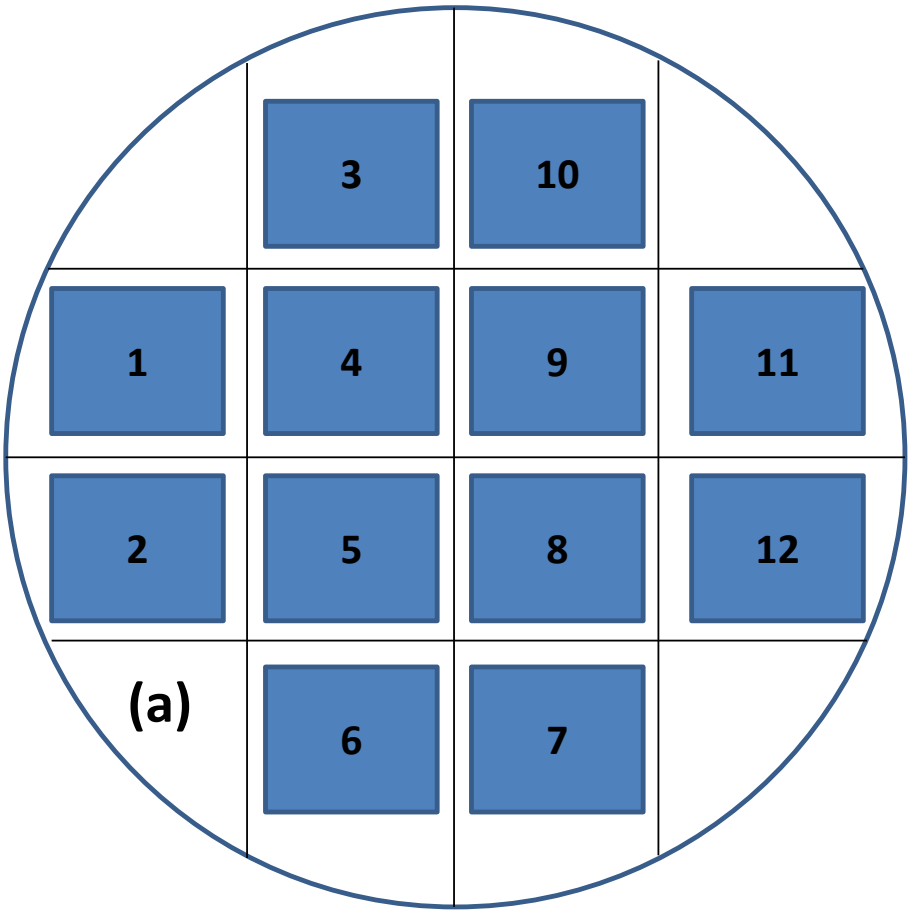

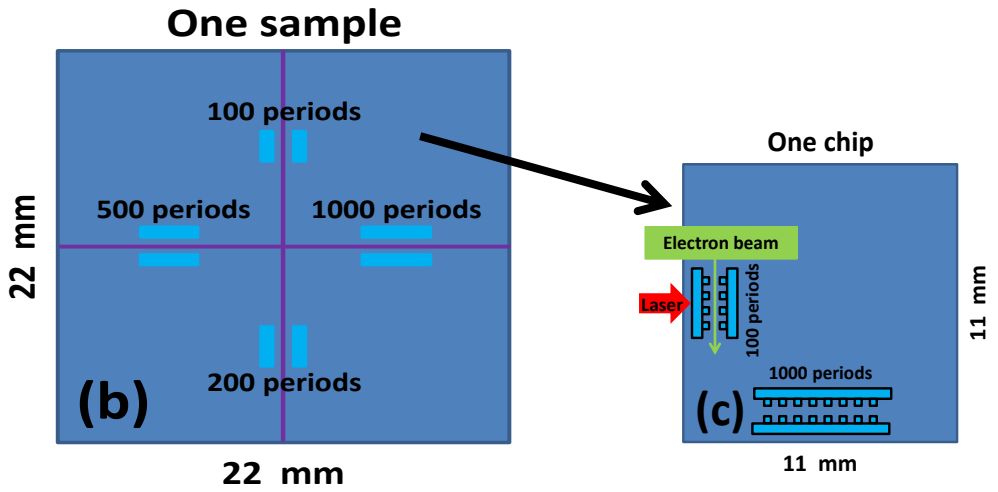

Figure 77. Layout of the samples and chips on a quartz wafer. There are 12 identical samples on a single wafer (a), 8 dual-grating structures on each sample (b), and 2 dual-grating structures on each chip (c).

6.1.4 Reactive Ion Etching

Many methods have been studied for directional microfabrication of quartz wafers: drilling, powder blasting [160], [161], laser ablation [162], [163], ion beam etching [164], plasma etching [165]–[169], and plasma jet etching [170]. Among these methods, fluorine-based inductively-coupled plasma reactive ion etching (ICP RIE) is a technique widely used for microfabrication of quartz. Plasma etching has mainly two advantages over the other methods: (1) a whole wafer may be processed at the same time, and (2) the verticality of side walls as well as the flat surface and etched bottom can be tuned to a certain extent.

Here, our samples are put into an RIE 100 machine for plasma etching. This determines the achievable channel depth J, which plays a significant role for our structures. The mechanisms of plasma etching of quartz have been previously reported in the literature [137], [171]–[174]. It may be summarized as follows: the etch process employs a continuous polymerization-dissolution process based on the ionization of CxFy fluorocarbons; the dissolution of the quartz occurs due to a complex interaction between ions in the plasma and the solid quartz, resulting in the removal of quartz and fluorocarbon polymer formation on the substrate. Due to the directionality of the incoming ions there is a preferential removal direction of the polymer, which leads to anisotropy in the etched feature shape [171].

With the help of researchers in PSI, Switzerland, a C_3F_8 (20 sccm) / O_2(10 sccm) recipe has been used initially for plasma etching of our samples. RF bias power is first set to 200 watts, and the substrate temperature is 0° Celsius. Oxygen (O_2) is used to improve stability, etch rate, mask selectivity, and anisotropy (sidewall shape). The etching time is set to 30

minutes, with an O_2 clean time of 30 seconds performed to improve the roughness of the etched surface. An etch rate of 400 nm/min and etched featured sidewalls having an angle of 90° can be expected from the recommended recipe. After each plasma etching, scanning probe microscopes are used to observe the trench depth until it becomes larger than 6 μm. As shown in Figure 78, the pillar width in the structure is also etched to some extent by plasma gases.

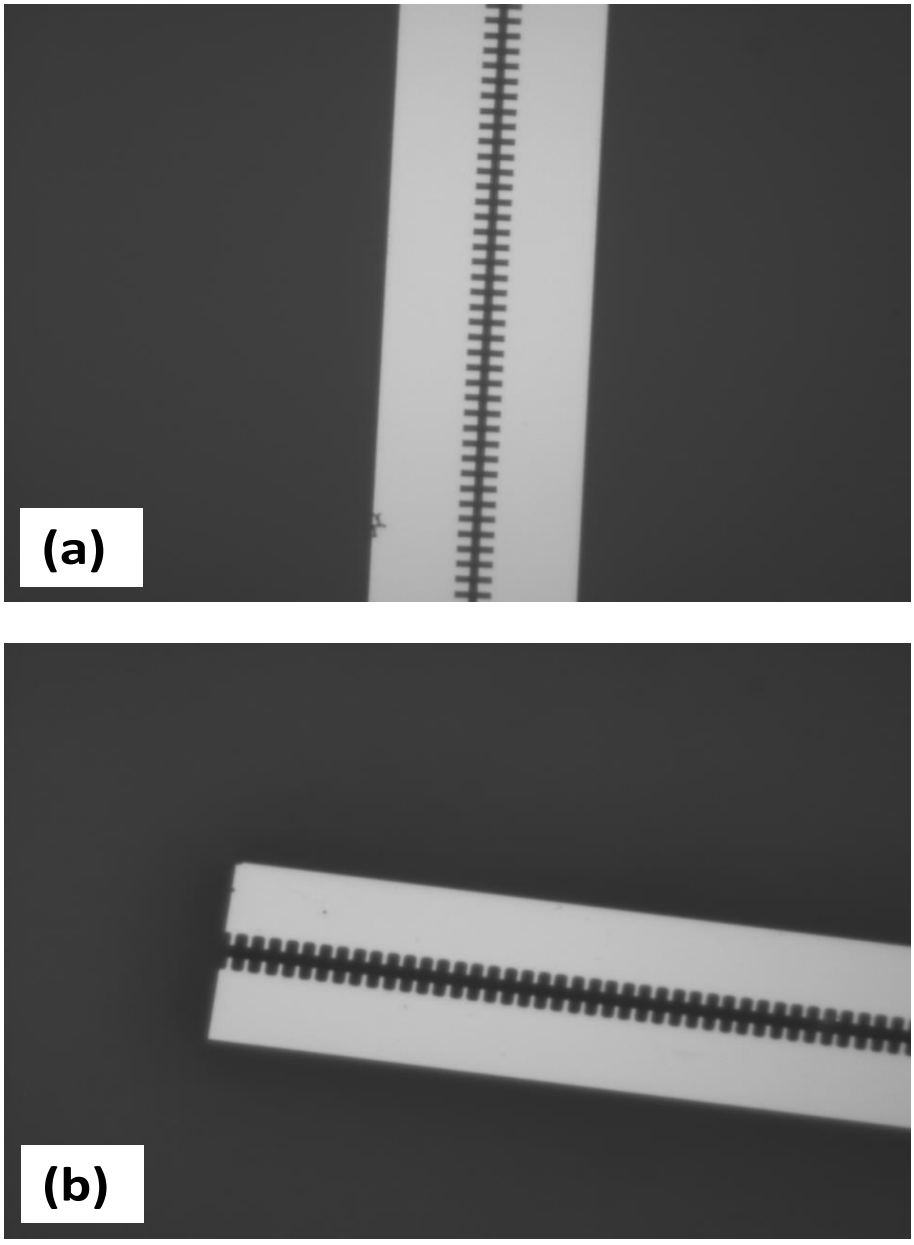

Figure 78. Optical microscope images of the dual-grating structures before plasma etching (a), and after plasma etching(b).

Finally, after tuning the etching recipe many times, a channel depth of J = 7.6 μm was obtained under an optimum recipe of C_3F_8 (30 sccm) / O_2(10 sccm) with 1000-watt RF bias power. It was found that the roughness and wall skew could be improved by lowering the

etching temperature. As shown in Figure 79 (a), the surface roughness is rather poor at a temperature of 0° Celsius, because many polymers are left during the plasma etching. However, as shown in Figure 79 (b), a lower temeprature results in less polymer deposition and hence a smoother surface during the etching process [175].

In conclusion, a channel depth of J = 7.6 μm has been achieved, which meets the requirements of the design target. However, these structures are still waiting for further testing when the laser system arrives in 2018. In addition, our fabrication process still needs further optimization to deliver a more uniform channel and a smoother surface.

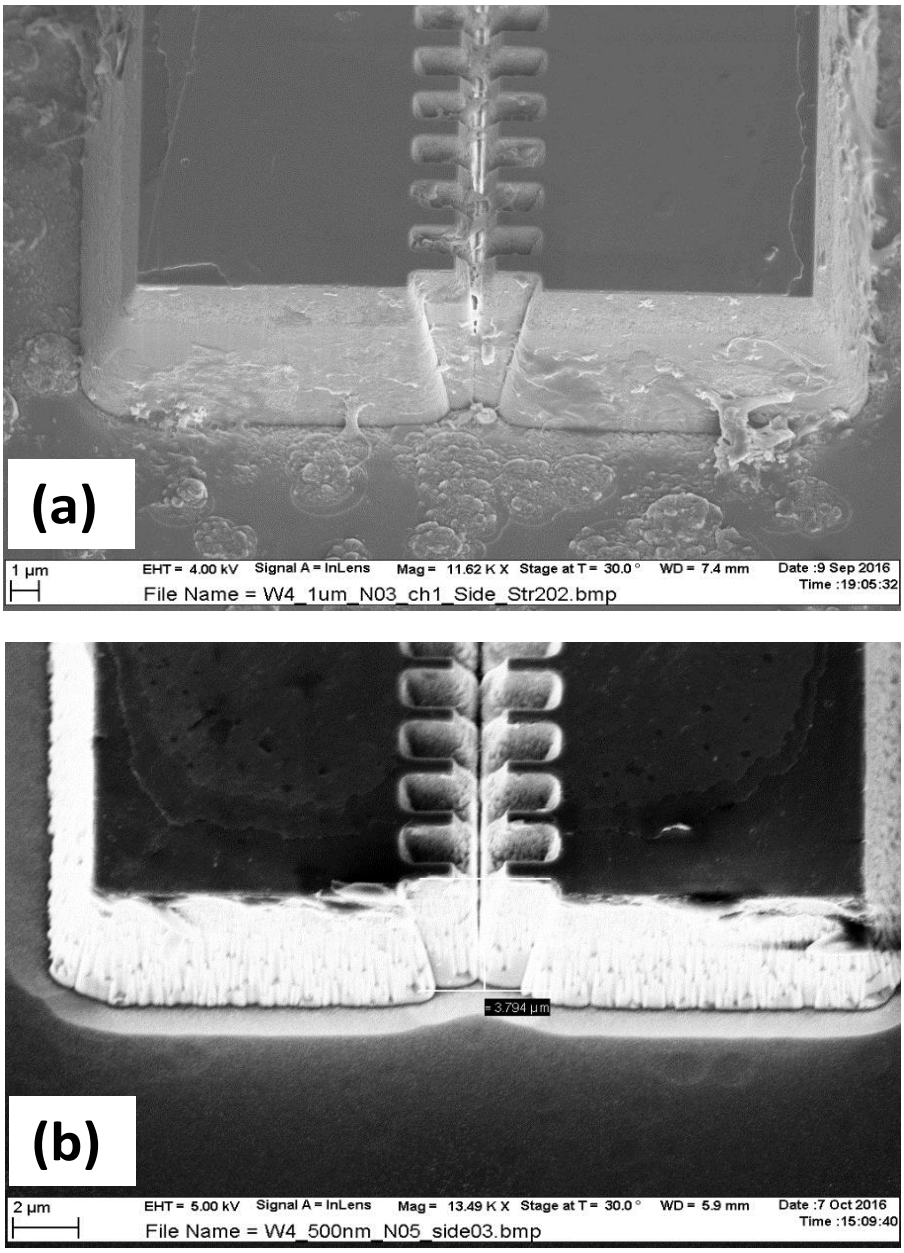

Figure 79. Scanning Electron Microscope (SEM) images of dual-grating structures etched by plasma at temperatures of 0° Celsius (a), -10° Celsius (b).

6.2 Experimental Preparations

After the fabrication studies, the experimental platform is prepared to be set up in collaboration with researchers from PSI using the SwissFEL [156]–[158], a facility presently under construction at PSI that will serve two beamlines: Aramis, a hard X-ray beamline that produces FEL radiation in 2017, and Athos, a soft X-ray beamline expected to lase by 2021. Figure 80 shows a schematic overview of the SwissFEL facility. The electrons are generated in an RF photoinjector. The electron beam is then accelerated with S-band technology ($f \approx 3$ GHz) to an energy of 330 MeV and compressed in the first bunch compressor (BC1). Our experiment chamber is located after BC1 (see Figure 80), so an electron beam with an energy of 330 MeV will be used for our experimental studies.

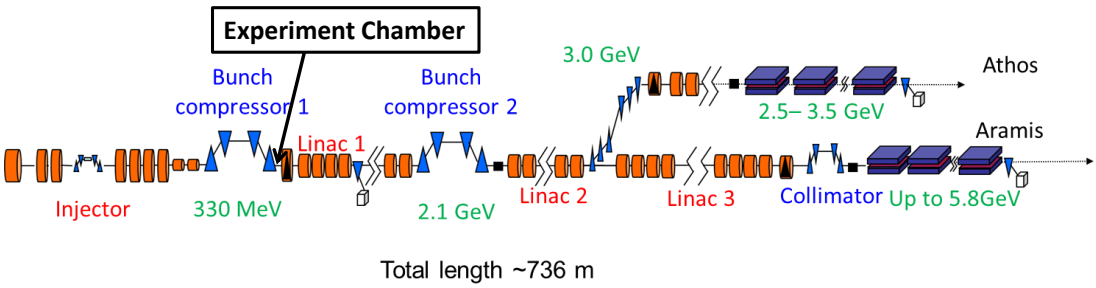

Figure 80. Schematic overview of the SwissFEL facility.

As we do not have an ultrafast laser system to test the fabricated laser-driven dual-grating structures, the first experiment is to study the bunch wakefield effect inside a dielectric THz-driven structure, as shown in Figure 81. Compared to the structures studied in Chapter 5, this THz-driven structure consists of 100-period double-rows of cylindrical pillars integrated with a 5-layer Bragg reflector. Silicon is the material chosen for this structure, to enhance the wakefield effect. Such a structure is originally from Ref. [157] and has a grating period of 150 μm and a channel gap of 100 μm, which has been studied and fabricated by researchers in PSI.

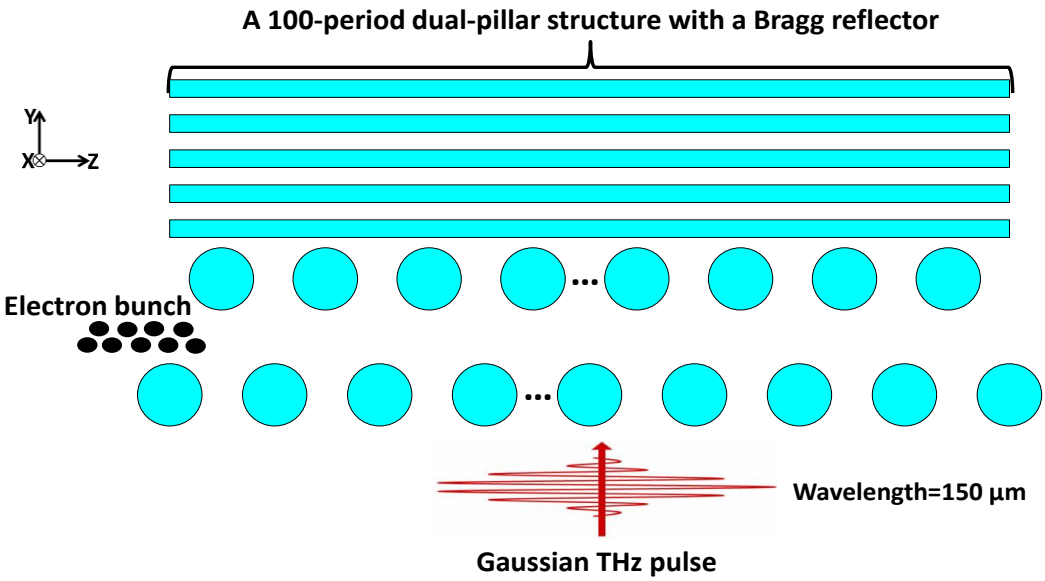

Figure 81. Schematic of a THz-driven dual-pillar structure with a Bragg reflector in PSI.

In the wakefield experiment, an electron bunch with a mean energy of 330 MeV, bunch charge of 3.0 pC, RMS length of 90 μm, RMS radius of 5 μm, normalised emittance of 0.15 mm·mrad, and energy spread of 0.05% can be employed in the chamber. When such an electron bunch is loaded into the dual-pillar structure as shown in Figure 81 in the absence of THz pulses, the wakefield interacts with the electron itself, resulting in energy loss or deflection of electrons in the bunch. As shown in Figure 82 (a), the electron bunch experiences a decelerating gradient of 18.7 MV/m when it travels out of the structure. This means that an energy loss of 300 keV can be expected in our measurements. Furthermore, when the electron bunch travels exactly along the channel centre, the transverse wakefield is negligible for the bunch, as can be seen in Figure 82 (b). However, when the electron bunch travels at an offset to the channel centre, the transverse wakefield is expected to deflect the bunch and increase the bunch emittance.

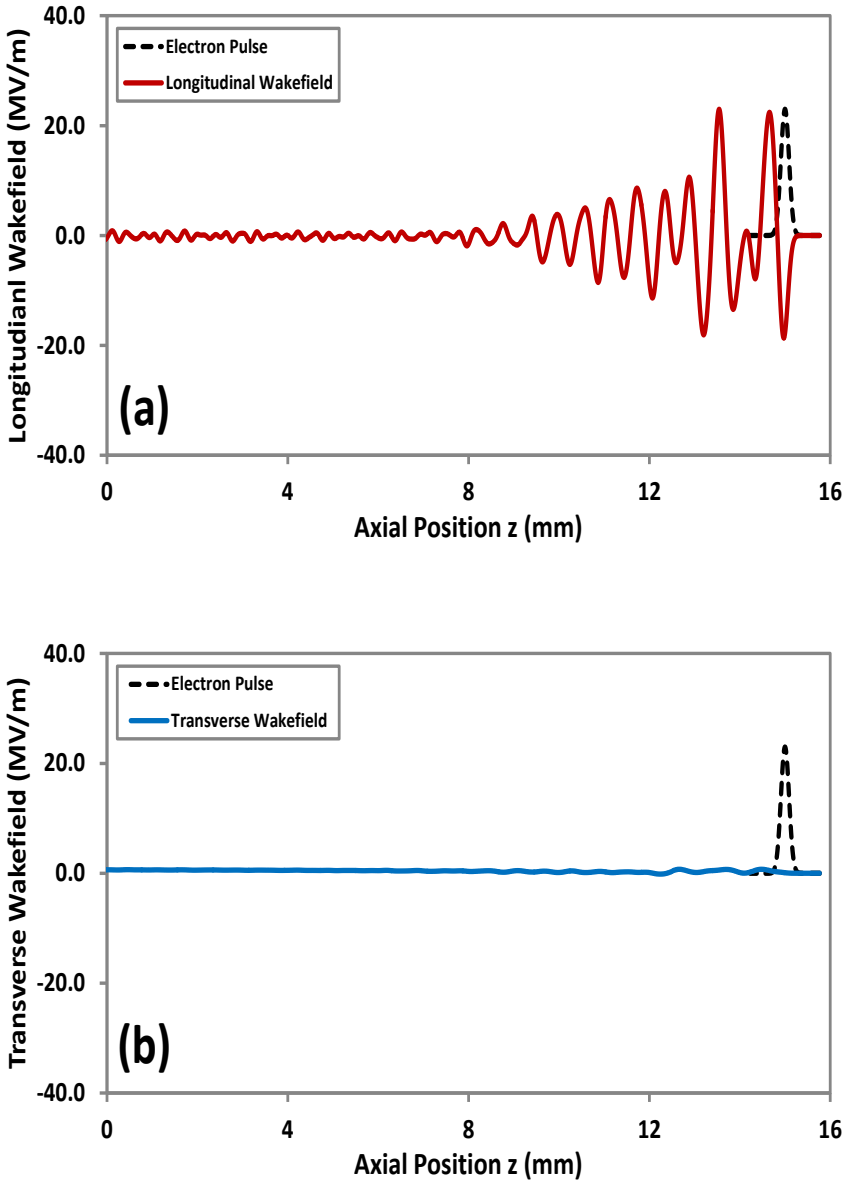

Figure 82. Simulated longitudinal (a) and transverse (b) wakefield distribution on the *z*-axis. The electron bunch travels along the *z*-axis.

This THz-driven structure is fixed onto the surface of metal holders, sitting on a custom mounting plate on top of a motorized stage, as shown in Figure 83. Such a stage can move up and down only, to adjust the structure location. The alignment between the electron beam and vacuum channel gap plays a vital role for the wakefield experiment. We can gradually adjust the structure location to see the bunch energy modulation at each stage step. However, it will take a very long beam time, and several cameras can be installed in the chamber to image the bunch and structure; this is still underway as the next step in the work.

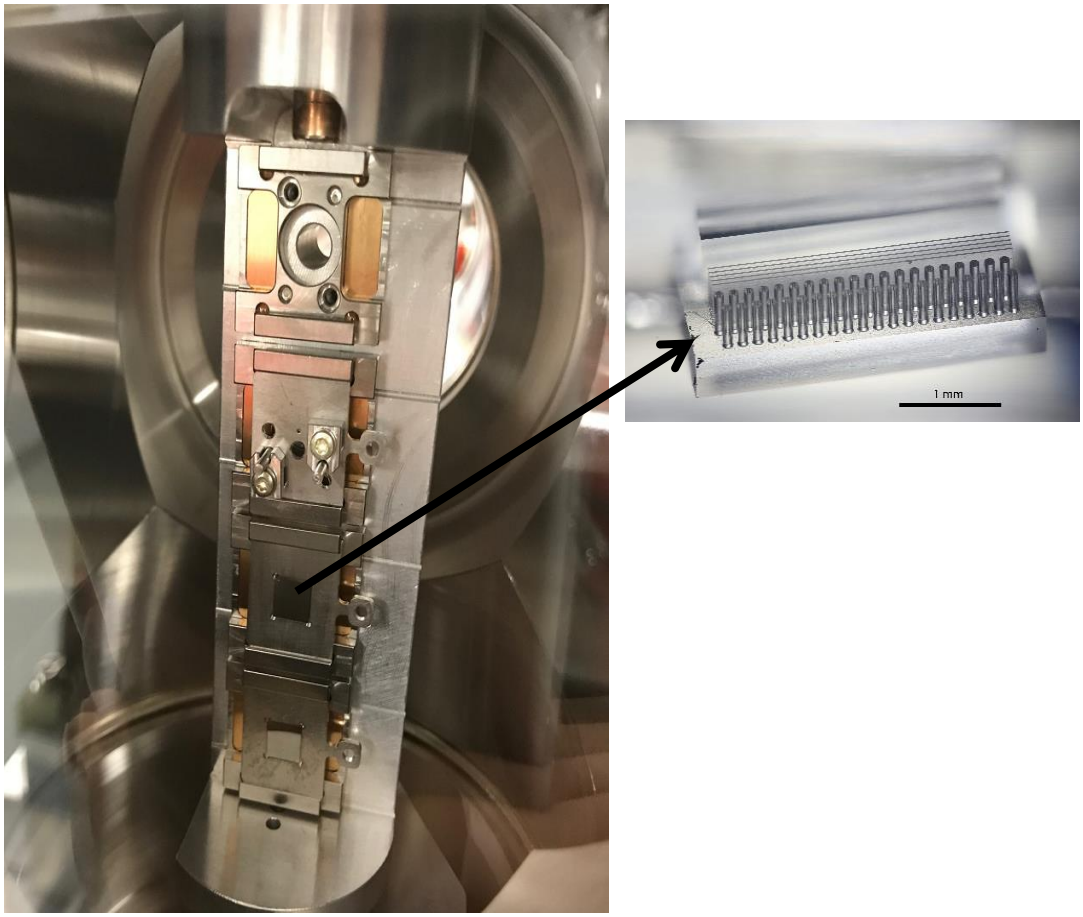

Figure 83. THz-driven structure (see subplot) on the holder inside the SwissFEL chamber

Using Swiss FEL standard optics, we can focus an electron beam with transverse sizes (Gaussian fits) of 30 μm × 80 μm and bunch charge of 260 fC on the YAG screen, as shown in Figure 84. This YAG screen, located in front of the structure in our vacuum chamber, is used to characterize the beam size injected into the structure. This transverse size is still much larger desired, and so is not suitable for injecting into the THz-driven structure.

We then set out to tune the beam optics parameters to find the smallest beam size. After a series of optimization tuning, beta functions of $\beta_{\mathrm{x}} = 16$ cm, $\beta_{\mathrm{y}} = 16$ cm result in the smallest beam size of 12 μm × 13 μm for a bunch charge of $q = 200$ fC, as shown in Figure 85. These sizes are still larger than we require. When the beta functions are decreased, the beam sizes always remain constant. This is probably due to the limited YAG screen resolution. A sub-μm wirescanner is therefore needed to test the beam size in the range of μm. This wirescanner is still under development at PSI.

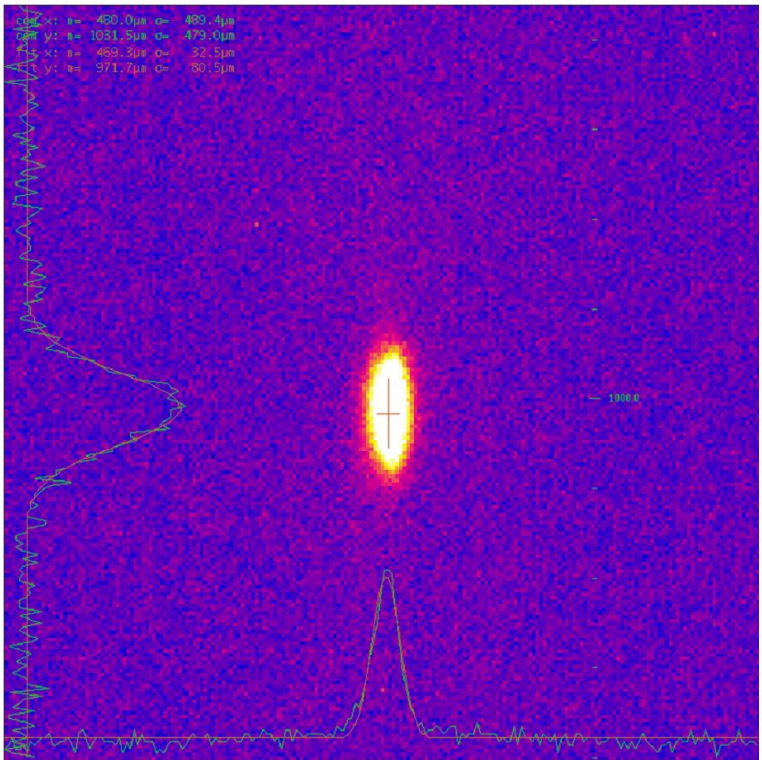

Figure 84. The minimum achievable beam size: 30 μm × 80 μm in our chamber using standard Swiss FEL optics, with a bunch charge of 260 fC.

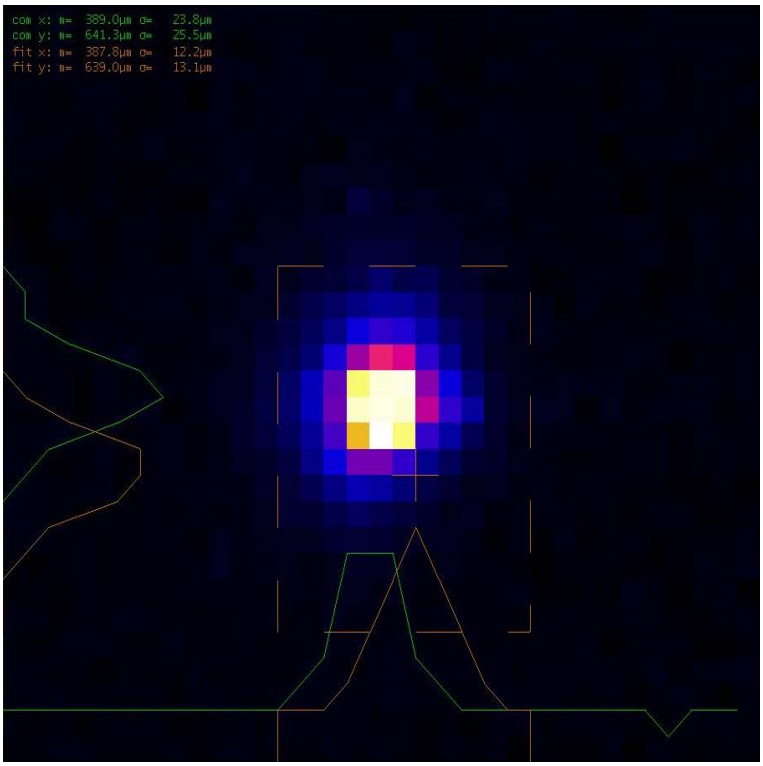

Figure 85. The minimum achievable beam size: 12 μm × 13 μm in our chamber using special optics with $\beta_x = 16$ cm, $\beta_y = 16$ cm, with a bunch charge of 200 fC.

7. Conclusion and Outlook

7.1 Conclusion

This thesis has presented detailed numerical investigations, preliminary fabrication and experimental studies for dual-grating DLAs. These studies pave the way for implementing a new generation of particle accelerators 'on a chip' in the future.

Specifically, Chapter 1 has reviewed the background and motivation for dual-grating DLAs. Chapter 2 has discussed the theory of particle acceleration in grating-based structures including single-gratings and dual-gratings. Some basic definitions have also been presented.

Chapter 3 has described the geometry optimizations and beam quality studies for dual-grating structures in terms of the emittance, energy spread, and loaded accelerating gradient. In order to optimize these dual-grating structures, two different simulation codes (CST and VSim) are used to study the acceleration of relativistic and non-relativistic electrons and comparisons from both codes are also described. It is found that the simulation results show very good agreement for both codes, giving confidence in the validity of the results. After the optimization studies, a realistic electron bunch from the future CLARA accelerator is modelled, loaded into an optimized 100-period structure to interact with a Gaussian laser pulse. Our numerical simulations focus only on electrons travelling through the vacuum channel to interact with laser field. In this case, when the modulated electrons travel out of the structure, the transverse normalized emittance increases by 3.60% compared to that of the laser-off case, the energy spread changes from 0.05% to 0.103%, and an accelerating gradient up to 1.15 GV/m can be expected, based on the particle tracking simulations. I also analyzed in detail the effect of laser parameters and electron density on the beam quality. When electrons interact with a higher peak laser field with longer waist radius and FWHM duration, it leads to an increase in emittance and energy spread. However, keeping the electron bunch density below 1.1×10^{21} /m^3 is desirable to limit the emittance increase to ~3.6%.

In Chapter 4, two kinds of scheme, to add a Bragg reflector and to use PFT laser illumination, have been studied to improve the energy efficiency for dual-grating DLAs. For a Gaussian laser pulse with λ_0 = 2.0 μm wavelength, E_0 = 2.0 GV/m peak field, τ_0 = 100 fs pulse duration, and w_z = 50 μm waist radius, normally incident, illuminating a 100-period bare dual-grating structure, the energy gain is increased by 70% when a Bragg reflector is added. Such a laser pulse can be used with the optical system shown in Figure 56 to generate

a front-tilted pulse with an ultrashort pulse duration of τ_0 = 100 fs and a tilt angle of $\gamma = 45^0$. It is found that this PFT laser generates an energy gain larger than that of a normal laser by 138% for bare dual-gratings. When dual-gratings with a Bragg reflector are driven by a PFT laser in a combination of both schemes, the energy gain is boosted by 254% as compared to normal laser illumination on bare dual-gratings. An energy gain of as much as 2.6 MeV can be expected for a PFT laser beam with an interaction length L_{int} = 1020 μm, illuminating a 2000-period dual-grating structure with a Bragg reflector. The diffraction effect due to a fabricated vertical channel depth size *J* being smaller than the laser waist radius has also been presented. It is found that the optimized structure should be fabricated with a vertical size $J/w_{\mathrm{x}} \geq 0.20$, to generate an acceptable accelerating performance.

Chapter 5 has investigated a dual-grating structure driven by THz pulses to accelerate electrons, including geometry optimizations and wakefield and THz-bunch interaction studies. These studies could be extended for dual-grating structures on THz acceleration.

Chapter 6 has presented the preliminary fabrication and experimental studies for dual-grating structures. A monolithic method has been developed to fabricate the quartz structure using electron-beam lithography and plasma etching. This method eliminated the complicated bonding process of other methods, and obtained a better alignment of the two gratings as compared to SLAC structures. Some experimental preparations using the SwissFEL were also presented in this chapter, opening the way for future demonstrations with our fabricated structures.

7.2 Outlook

As a next step, a sub-μm wirescanner will be installed around the YAG screen at SwissFEL, to test the focused beam size. This will provide us with an accurate beam size in the range of sub-μm. Such a focused beam can be injected into our THz-driven structure for wakefield studies. In the absence of access to THz sources, we can study the bunch wakefield interacting with the bunch itself, in terms of the energy modulation and emittace increment. Two bunches can then be loaded into the same structure, allowing the effect of the wakefield of a driver bunch on the witness bunch to be investigated. These experimental measurements can be directly compared to our simulation results.

After experimental wakefield studies, we must also prepare to test fabricated dual-grating structures with a grating period of 2.0 μm. The laser pulses that drive the structures are produced by a Ti: Sapphire mode-locked system with a central wavelength of 2.0 μm.

Such a laser system will be introduced and installed at the end of 2018. The optics system will be set up for a series of measurements, described as follows:

- Damage threshold measurements will be carried out for our bulk quartz material and fabricated structures. For quartz material, Breuer *et al.* [92] have demonstrated a damage threshold of 0.5 J/cm^2 for 70 fs pulsed laser illumination while Soong *et al*. [93], [94] have demonstrated a damage threshold of 4 J/cm^2 for 1 ps pulsed laser illumination. Lenzner *et al*. [95] measured about twice as large a damage threshold for 1ps pulses, as compared with 100 fs pulses. Based on these measurements, a damage threshold of 2 J/cm^2 is assumed for quartz material illuminated by a 100 fs pulsed laser, which has been used in Chapters 3, 4 and 5. However, it is still necessary to measure the damage threshold for our quartz structures, as this directly affects the accelerating performance for our structures. In addition, we must also measure the damage threshold for other optical materials such as Sapphire, which could be an alternative for future DLA structures.
- A laser beam will be focused onto the side of the fabricated structure with surface area $J \times L$, to generate the maximum accelerating field in the channel gap. As already stated, the fabricated channel depth J is only about 7.6 μm and L represents the structure length. It would therefore be quite challenging to focus a laser beam onto such a side surface area. An optical microscope may be needed to achieve accurate focusing.
- We will then investigate the laser-bunch interaction in a fabricated dual-grating structure with a grating period of 2.0 μm, as show in Figure 86. In this experiment, alignment including temporal and spatial overlap will play a crucial role. We must ensure that the electron beam interacts with the laser beam at an interaction point located in the middle of structure's vacuum channel, so that the accelerating fields are strongest. Moreover, these two beams must also be temporally aligned so that they arrive at the interaction point at the same time. To perform the spatial alignment, Peralta *et al.* [47] used a miniature aluminium pellicle mirror and a long working distance Cassegrain telescope to image the optical transition radiation (OTR) signal and scattered laser signal to within ~10 μm. For the temporal overlap, Peralta *et al.* [47] provided a method which is summarised as follows: a fast photodiode (of 25 GHz bandwidth) was used to detect the OTR signal which the electron beam generated at an aluminium pellicle located downstream of the sample. The transmitted laser pulse was also measured simultaneously, on the same detector and oscilloscope. They measured the arrival time of the two signals by adjusting a motorized optical delay line and scanning a voice-coil-actuated retroreflector to achieve picosecond-scale overlap.

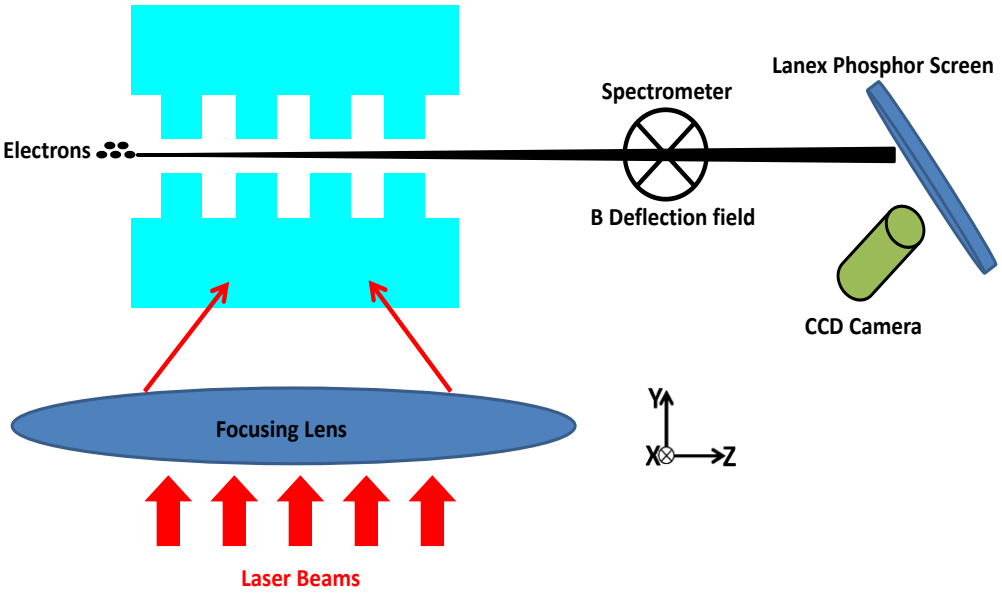

Figure 86. Schematic of the experimental setup for DLAs. Electrons interact with focused laser pulses in the vacuum channel of the dual-grating structure, pass through the spectrometer and are measured by a lanex phosphor screen and CCD camera.

Further research efforts will focus on the combination of the DLA structures with a laser-triggered high-brightness electron source that is synchronized with the driving laser. Such a pulsed electron source with 3 ampere peak current has been demonstrated [176]. This peak current would allow a study of the acceleration process, space-charge effect or microbunching in a more detailed manner. Moreover, the simulation and experimental demonstration of mm-long dual-grating structures that accelerate non-relativistic electrons up to relativistic energies must be undertaken as a next step in the research work. It should be noted here that the difficulty lies in the compensation of dephasing and beam expansion due to space charge. Focusing structures driven by laser pulses still need to be explored.

Finally, due to their high accelerating gradients of up to several GV/m, the main application of DLAs lies in providing compact sources of coherent X-ray radiation. These lab-scale x-ray light sources may lead to a revolution in experiments probing the structure of matter by making available to many laboratories around the world techniques that are currently limited to large-scale research facilities. Moreover, a DLA system on a millimetre to centimetre scale would enable a DLA-based fibre endoscope [97] which could generate a multi-MeV electron beam for the purpose of tumour irradiation. DLA structures may also be used for acceleration of protons and ions with applications in compact sources for cancer therapy.

Publications

(1) **Y. Wei**, M. Ibison, J. Resta-Lopez, C. P. Welsch, R. Ischebeck, S. Jamison, G. Xia, M. Dehler, E. Prat, J. D. A. Smith, Energy efficiency studies for dual-grating dielectric laser-driven accelerators, **Nuclear Instruments & Methods in Physics Research Section A**, available at https://doi.org/10.1016/j.nima.2017.12.049, in press (2018);

(2) **Y. Wei**, R. Ischebeck, M. Dehler, E. Ferrari, N. Hiller, S. Jamison, G. Xia, K. Hanahoe, Y. Li, J. D. A. Smith, and C. P. Welsch, Investigations into dual-grating THz-driven accelerators, **Nuclear Instruments & Methods in Physics Research Section A** 877, 173-177 (2018);

(3) **Y. Wei**, M. Ibison, G. Xia, J. D. A. Smith, and C. P. Welsch, Dual-grating dielectric accelerators driven by a pulse-front-tilted laser, **Applied Optics** 56, 8201-8206 (2017);

(4) **Y. Wei**, G. Xia, J. D. A. Smith, and C. P. Welsch, Dual-gratings with a Bragg reflector for dielectric laser-driven accelerators, **Physics of Plasmas** 24, 073115 (2017);

(5) **Y. Wei**, S. Jamison, G. Xia, K. Hanahoe, Y. Li, J. D. A. Smith, and C. P. Welsch, Beam quality study for a grating-based dielectric laser-driven accelerator, **Physics of Plasmas** 24, 023102 (2017);

(6) **Y. Wei**, C.P. Welsch, G. Xia, M. Dehler, E. Ferrari, N. Hiller, R. Ischebeck, J.D.A. Smith, Dual-grating dielectric accelerators driven by a pulse-front-tilted laser, Proceedings of IPAC2017, Copenhagen, Denmark; available at http://accelconf.web.cern.ch/AccelConf/ipac2017/papers/wepva020.pdf (2017);

(7) **Y. Wei**, C. P. Welsch, S. Jamison, G. X. Xia, K. Hanahoe, Y. Li, J. D. A. Smith, Beam dynamics studies into grating-based dielectric laser-driven accelerators, Proceedings of IPAC2016, Busan, Korea; available at http://accelconf.web.cern.ch/accelconf/ipac2016/papers/tupoy027.pdf (2016);

(8) **Yelong Wei**, Guoxing Xia, Jonathan. D. A. Smith, Kieran Hanahoe, Oznur Mete, Steve P. Jamison, Carsten P. Welsch, Numerical study of a multi-stage dielectric laser-driven accelerator, Physics Procedia 77, 50-57 (2015);

(9) **Y. Wei**, C. P. Welsch, G. X. Xia, O. Mete, K. Hanahoe, J. D. A. Smith, Investigations into dielectric laser-driven accelerators using the CST and VSim simulation codes, Proceedings of IPAC2015, Richmond, VA, USA; available at http://accelconf.web.cern.ch/AccelConf/IPAC2015/papers/wepwa051.pdf (2015);

(10) G. Xia, Y. Nie, O. Mete, K. Hanahoe, M. Dover, M. Wigram, J. Wright, J. Zhang, J. Smith, T. Pacey, Y. Li, **Y. Wei**, C. Welsch, Plasma wakefield acceleration at CLARA facility in Daresbury Laboratory, **Nuclear Instruments & Methods in Physics Research Section A** 829, 43-49 (2016);

(11) E. Gschwendtner, E. Adli, L. Amorim, R. Apsimon, R. Assmann, … **Y. Wei**, C. P. Welsch, et al., AWAKE, The Advanced Proton Driven Plasma Wakefield Acceleration Experiment at CERN, **Nuclear Instruments & Methods in Physics Research Section A** 829, 76-82 (2016);

(12) A. Caldwell, E. Adli, L. Amorim, R. Apsimon, T. Argyropoulos, … **Y. Wei**, C. P. Welsch, et al., Path to AWAKE: Evolution of the concept, **Nuclear Instruments & Methods in Physics Research Section A** 829, 3-16 (2016).

References

[1] J. D. Cockcroft and E. T. S. Walton, "Disintegration of lithium by swift protons," *Nature*, vol. 129, no. 3261, p. 649, 1932.

[2] R. J. Van de Graaff, K. T. Compton, and L. C. Van Atta, "The electrostatic generation of high voltages for nuclear investigations," *Phys. Rev.*, vol. 43, no. 3, pp. 149–157, 1933.

[3] R. J. van de Graaff, "Tandem electrostatic accelerators," *Nuclear Instruments and Methods*, vol. 8, no. 2. pp. 195–202, 1959.

[4] J. D. Jackson, "Classical Electrodynamics Third Edition," *John Wiley & Sons, INC.* pp. 75–79, 1999.

[5] J. Schwinger, "On the classical radiation of accelerated electrons," *Phys. Rev.*, vol. 75, no. 12, pp. 1912–1925, 1949.

[6] J. T. Seeman, "The stanford linear collider," *SLAC-PUB-5607*, pp. 389–428, 1991.

[7] T. Higo, "Progress of X-Band Accelerating Structures," *Proc. Linear Accel. Conf. LINAC2010, Tsukuba, Japan*, pp. 1038–1042, 2010.

[8] T. Higo *et al.*, "Advances in X-band TW accelerator structures operating in the 100MV/m regime," in *Proceedings of IPAC'10, Kyoto, Japan*, 2010, pp. 3702–3704.

[9] V. Yakovlev, P. Avrakhov, A. Kanareykin, S. Kazakov, and N. Solyak, "Progress towards development of a superconducting traveling wave accelerating structure," in *Proceedings of the IEEE Particle Accelerator Conference*, 2007, pp. 2182–2184.

[10] J. Norem *et al.*, "Dark current, breakdown, and magnetic field effects in a multicell, 805 MHz cavity," *Phys. Rev. Spec. Top. - Accel. Beams*, vol. 6, no. 7, p. 072001, 2003.

[11] A. Moretti, Z. Qian, J. Norem, Y. Torun, D. Li, and M. Zisman, "Effects of high solenoidal magnetic fields on rf accelerating cavities," *Phys. Rev. Spec. Top. - Accel. Beams*, vol. 8, no. 7, p. 072001, 2005.

[12] M. R. Jana *et al.*, "Investigation of breakdown induced surface damage on 805 MHz pill box cavity interior surfaces," in *Proceedings of PAC2013, Pasadena, CA USA*, 2013, pp. 1007–1009.

[13] T. Wangler, *RF Linear Accelerators*. 2008.

[14] R. J. England *et al.*, "Conceptual layout for a wafer-scale dielectric laser accelerator," in *AIP Conference Proceedings*, 2016, vol. 1777, p. 060002.

[15] B. Aune *et al.*, "Superconducting TESLA cavities," *Phys. Rev. Spec. Top. - Accel. Beams*, vol. 3, no. 9, p. 092001, 2000.

[16] E. Esarey, C. B. Schroeder, and W. P. Leemans, "Physics of laser-driven plasma-based electron accelerators," *Rev. Mod. Phys.*, vol. 81, no. 3, pp. 1229–1285, 2009.

[17] T. Tajima and J. M. Dawson, "Laser electron accelerator," *Phys. Rev. Lett.*, vol. 43, no. 4, pp. 267–270, 1979.

[18] A. I. Akhiezer and R. V. Polovin, "Theory of wave motion of an electron plasma," *JETP Lett.*, vol. 3, no. 5, pp. 696–705, 1956.

[19] A. Modena *et al.*, "Electron acceleration from the breaking of relativistic plasma waves," *Nature*, vol. 377, no. 6550. pp. 606–608, 1995.

[20] E. Esarey, S. P., J. Krall, and A. Ting, “Overview of plasma-bsed accelerator concepts,” *IEEE Trans. Plasma Sci.*, vol. 24, no. 2, pp. 252–288, 1996.

[21] D. Strickland and G. Mourou, “Compression of amplified chirped optical pulses,” *Opt. Commun.*, vol. 56, no. 3, pp. 219–221, 1985.

[22] V. Malka, “Laser plasma accelerators,” *Phys. Plasmas*, vol. 19, no. 5, p. 055501, 2012.

[23] V. Malka, J. Faure, Y. A. Gauduel, E. Lefebvre, A. Rousse, and K. T. Phuoc, “Principles and applications of compact laser-plasma accelerators,” *Nat. Phys.*, vol. 4, no. 6, pp. 447–453, 2008.

[24] K. Nakajima *et al.*, “Observation of ultrahigh gradient electron acceleration by a self-modulated intense short laser pulse,” *Phys. Rev. Lett.*, vol. 74, no. 22, pp. 4428–4431, 1995.

[25] A. Ting *et al.*, “Plasma wakefield generation and electron acceleration in a self-modulated laser wakefield accelerator experiment,” *Phys. Plasmas*, vol. 4, no. 5 /2, pp. 1889–1899, 1997.

[26] C. Gahn *et al.*, “Multi-MeV electron beam generation by direct laser acceleration in high-density plasma channels,” *Phys. Rev. Lett.*, vol. 83, no. 23, pp. 4772–4775, 1999.

[27] V. Malka, “Electron acceleration by a wake field forced by an intense ultrashort laser pulse,” *Science (80-.).*, vol. 298, no. 5598, pp. 1596–1600, 2002.

[28] S. P. D. Mangles *et al.*, “Monoenergetic beams of relativistic electrons from intense laser–plasma interactions,” *Nature*, vol. 431, no. 7008, pp. 535–538, 2004.

[29] C. G. R. Geddes *et al.*, “High-quality electron beams from a laser wakefield accelerator using plasma-channel guiding,” *Nature*, vol. 431, no. 7008, pp. 538–541, 2004.

[30] J. Faure *et al.*, “A laser-plasma accelerator producing monoenergetic electron beams,” *Nature*, vol. 431, no. 7008, pp. 541–544, 2004.

[31] W. P. Leemans *et al.*, “GeV electron beams from a centimetre-scale accelerator,” *Nat. Phys.*, vol. 2, no. 10, pp. 696–699, 2006.

[32] X. Wang *et al.*, “Quasi-monoenergetic laser-plasma acceleration of electrons to 2 GeV,” *Nat. Commun.*, vol. 4, p. 2988, 2013.

[33] W. Leemans and E. Esarey, “Laser-driven plasma-wave electron accelerators,” *Phys. Today*, vol. 62, no. 3, pp. 44–49, 2009.

[34] E. Esarey, P. Sprangle, and J. Krall, “Laser acceleration of electrons in vacuum,” *Phys. Rev. E*, vol. 52, no. 5, pp. 5443–5453, 1995.

[35] P. Woodward, “A method of calculating the field over a plane aperture required to produce a given polar diagram,” *J. Inst. Electr. Eng. - Part IIIA Radiolocation*, vol. 93, no. 10, pp. 1554–1558, 1946.

[36] J. D. Lawson, “Lasers and accelerators,” *IEEE Trans. Nucl. Sci.*, vol. 26, no. 3, pp. 4217–4219, 1979.

[37] F. O. Kirchner, A. Gliserin, F. Krausz, and P. Baum, “Laser streaking of free electrons at 25 keV,” *Nat. Photonics*, vol. 8, pp. 52–57, 2014.

[38] A. Gliserin, M. Walbran, and P. Baum, “A high-resolution time-of-flight energy analyzer for femtosecond electron pulses at 30 keV,” *Rev. Sci. Instrum.*, vol. 87, no. 3, p. 033302, 2016.

[39] C. Kealhofer, W. Schneider, D. Ehberger, A. Ryabov, F. Krausz, and P. Baum, “All-

optical control and metrology of electron pulses," *Science (80-.).*, vol. 352, no. 6284, pp. 429–433, 2016.

[40] R. B. Palmer, "Acceleration theorems," in *AIP Conference Proceedings*, 1995, pp. 90–100.

[41] Y. Takeda and I. Matsui, "Laser linac with grating," *Nucl. Instruments Methods*, vol. 62, no. 3, pp. 306–310, 1968.

[42] K. Mizuno, S. Ono, and O. Shimoe, "Interaction between coherent light waves and free electrons with a reflection grating," *Nature*, vol. 253, pp. 184–185, 1975.

[43] K. Mizuno, J. Pae, T. Nozokido, and K. Furuya, "Experimental evidence of the inverse Smith–Purcell effect," *Nature*, vol. 328, pp. 45–47, 1987.

[44] F. Loehl, I. Bazarov, and S. Belomestnykh, "High current and high brightness electron sources," in *Proceedings of the 2010 Particle Accelerator Conference, Kyoto, Japan*, 2010, pp. 45–49.

[45] B. Spataro *et al.*, "Technological issues and high gradient test results on X-band molybdenum accelerating structures," *Nucl. Instruments Methods Phys. Res. Sect. A Accel. Spectrometers, Detect. Assoc. Equip.*, vol. 657, no. 1, pp. 114–121, 2011.

[46] E. Colby, R. J. England, and R. J. Noble., "A laser-driven linear collider: Sample machine parameters and configuration," in *Proceedings of the 2011 Particle Accelerator Conference,New York, NY, USA*, 2011, pp. 262–264.

[47] E. A. Peralta *et al.*, "Demonstration of electron acceleration in a laser-driven dielectric microstructure," *Nature*, vol. 503, no. 7474, pp. 91–94, 2013.

[48] K. P. Wootton *et al.*, "Demonstration of acceleration of relativistic electrons at a dielectric microstructure using femtosecond laser pulses," *Opt. Lett.*, vol. 41, no. 12, pp. 2696–2699, 2016.

[49] J. Maxson, D. Cesar, G. Calmasini, A. Ody, P. Musumeci, and D. Alesini, "Direct measurement of sub-10 fs relativistic electron beams with ultralow emittance," *Phys. Rev. Lett.*, vol. 118, no. 15, p. 154802, 2017.

[50] R. K. Li, K. G. Roberts, C. M. Scoby, H. To, and P. Musumeci, "Nanometer emittance ultralow charge beams from rf photoinjectors," *Phys. Rev. Spec. Top. - Accel. Beams*, vol. 15, no. 9, p. 090702, 2012.

[51] J. Breuer and P. Hommelhoff, "Laser-based acceleration of nonrelativistic electrons at a dielectric structure," *Phys. Rev. Lett.*, vol. 111, no. 13, p. 134803, 2013.

[52] K. J. Leedle, R. Fabian Pease, R. L. Byer, and J. S. Harris, "Laser acceleration and deflection of 96.3 keV electrons with a silicon dielectric structure," *Optica*, vol. 2, no. 2, pp. 158–161, 2015.

[53] K. J. Leedle *et al.*, "Dielectric laser acceleration of sub-100 keV electrons with silicon dual-pillar grating structures," *Opt. Lett.*, vol. 40, no. 18, pp. 4344–4347, 2015.

[54] M. Krüger, M. Schenk, P. Hommelhoff, and M. Kruger, "Attosecond control of electrons emitted from a nanoscale metal tip.," *Nature*, vol. 475, no. 7354, pp. 78–81, 2011.

[55] J. Hoffrogge *et al.*, "Tip-based source of femtosecond electron pulses at 30 keV," *J. Appl. Phys.*, vol. 115, no. 9, p. 094506, 2014.

[56] D. Ehberger *et al.*, "Highly coherent electron beam from a laser-triggered tungsten needle tip," *Phys. Rev. Lett.*, vol. 114, no. 22, p. 227601, 2015.

[57] M. Forster *et al.*, "Two-color coherent control of femtosecond above-threshold

photoemission from a Tungsten nanotip," *Phys. Rev. Lett.*, vol. 117, no. 21, p. 217601, 2016.

[58] J. McNeur *et al.*, "A miniaturized electron source based on dielectric laser accelerator operation at higher spatial harmonics and a nanotip photoemitter," *J. Phys. B At. Mol. Opt. Phys.*, vol. 49, no. 3, p. 034006, 2016.

[59] E. I. Simakov, H. L. Andrews, M. J. Herman, K. M. Hubbard, and E. Weis, "Diamond field emitter array cathodes and possibilities of employing additive manufacturing for dielectric laser accelerating structures," in *AIP Conference Proceedings*, 2017, vol. 1812, p. 060010.

[60] M. E. Swanwick *et al.*, "Nanostructured ultrafast silicon-tip optical field-emitter arrays," *Nano Lett.*, vol. 14, no. 9, pp. 5035–5043, 2014.

[61] H. Ye *et al.*, "Velocity map imaging of electrons strong-field photoemitted from Si-nanotip arrays," in *Springer Proceedings in Physics*, 2015, vol. 162, pp. 663–666.

[62] S. Y. Lin *et al.*, "A three-dimensional photonic crystal operating at infrared wavelengths," *Nature*, vol. 394, no. 6690, pp. 251–253, 1998.

[63] B. M. Cowan, "Three-dimensional dielectric photonic crystal structures for laser-driven acceleration," *Phys. Rev. Spec. Top. - Accel. Beams*, vol. 11, no. 1, p. 011301, 2008.

[64] C. McGuinness, "Particle accelerator on a chip: fabrication and characterization of woodpile accelerator structure, Ph.D. thesis, Stanford University," 2012.

[65] Z. Wu *et al.*, "Coupling power into accelerating mode of a three-dimensional silicon woodpile photonic band-gap waveguide," *Phys. Rev. Spec. Top. - Accel. Beams*, vol. 17, no. 8, p. 081301, 2014.

[66] Z. Wu, C. Lee, K. P. Wootton, C. K. Ng, M. Qi, and R. J. England, "A traveling-wave forward coupler design for a new accelerating mode in a silicon woodpile accelerator," *IEEE J. Sel. Top. Quantum Electron.*, vol. 22, no. 2, p. 4400909, 2016.

[67] R. J. England, "Review of laser-driven photonic structure-based particle acceleration," *IEEE J. Sel. Top. Quantum Electron.*, vol. 22, no. 2, p. 4401007, 2016.

[68] X. E. Lin, "Photonic band gap fiber accelerator," *Phys. Rev. Spec. Top. - Accel. Beams*, vol. 4, no. 5, p. 051301, 2001.

[69] B. M. Cowan, "Two-dimensional photonic crystal accelerator structures," *Phys. Rev. Spec. Top. - Accel. Beams*, vol. 6, no. 10, p. 101301, 2003.

[70] R. J. Noble, J. E. Spencer, and B. T. Kuhlmey, "Hollow-core photonic band gap fibers for particle acceleration," *Phys. Rev. Spec. Top. - Accel. Beams*, vol. 14, no. 12, p. 121303, 2011.

[71] V. Reboud *et al.*, "Lasing in nanoimprinted two-dimensional photonic crystal band-edge lasers," *Appl. Phys. Lett.*, vol. 102, no. 7, p. 073101, 2013.

[72] A. Mizrahi and L. Schächter, "Bragg acceleration structures," in *Proceedings of APAC 2004, Gyeongju, Korea*, 2004, pp. 452–454.

[73] A. Mizrahi, "Analysis and design of optical Bragg acceleration structures," in *AIP Conference Proceedings*, 2004, vol. 737, pp. 804–810.

[74] A. Mizrahi and L. Schächter, "Optical Bragg accelerators," *Phys. Rev. E - Stat. Nonlinear, Soft Matter Phys.*, vol. 70, no. 1, p. 016505, 2004.

[75] J. McNeur, J. B. Rosenzweig, G. Travish, J. Zhou, and R. Yoder, "An examination of resonance, acceleration, and particle dynamics in the micro-accelerator platform," in

AIP Conference Proceedings, 2010, vol. 1299, pp. 427–432.

[76] J. McNeur, K. S. Hazra, G. Liu, E. B. Sozer, G. Travish, and R. B. Yoder, "Resonance, particle dynamics, and particle transmission in the micro-accelerator platform," in *AIP Conference Proceedings*, 2012, vol. 1507, pp. 470–475.

[77] J. McNeur *et al.*, "Experimental search for acceleration in the micro-accelerator platform," in *Proceedings of IPAC2013, Shanghai, China*, 2013, pp. 1307–1309.

[78] J. McNeur *et al.*, "Experimental results from the micro-accelerator platform, a resonant slab-symmetric dielectric laser accelerator," in *AIP Conference Proceedings*, 2016, vol. 1777, p. 060014.

[79] T. Plettner, P. P. Lu, and R. L. Byer, "Proposed few-optical cycle laser-driven particle accelerator structure," *Phys. Rev. Spec. Top. - Accel. Beams*, vol. 9, no. 11, p. 111301, 2006.

[80] A. Aimidula *et al.*, "Numerically optimized structures for dielectric asymmetric dual-grating laser accelerators," *Phys. Plasmas*, vol. 21, no. 2, p. 023110, 2014.

[81] A. Aimidula *et al.*, "Numerical investigations into a fiber laser based dielectric reverse dual-grating accelerator," *Nucl. Instruments Methods Phys. Res. Sect. A Accel. Spectrometers, Detect. Assoc. Equip.*, vol. 740, pp. 108–113, 2014.

[82] C. M. Chang and O. Solgaard, "Silicon buried gratings for dielectric laser electron accelerators," *Appl. Phys. Lett.*, vol. 104, no. 18, p. 184102, 2014.

[83] R. J. England *et al.*, "Experiment to detect accelerating modes in a photonic bandgap fiber," in *AIP Conference Proceedings*, 2009, vol. 1086, pp. 550–555.

[84] P. Yeh and A. Yariv, "Bragg reflection waveguides," *Opt. Commun.*, vol. 19, no. 3, pp. 427–430, 1976.

[85] P. Yeh, A. Yariv, and E. Marom, "Theory of Bragg fiber," *J. Opt. Soc. Am.*, vol. 68, no. 9, p. 1196, 1978.

[86] K. P. Wootton, J. McNeur, and K. J. Leedle, "Dielectric laser accelerators: designs, experiments, and applications," *Rev. Accel. Sci. Technol.*, vol. 09, pp. 105–126, 2016.

[87] G. Andonian *et al.*, "Planar-dielectric-wakefield accelerator structure using Bragg-reflector boundaries," *Phys. Rev. Lett.*, vol. 113, no. 26, p. 264801, 2014.

[88] T. Plettner, R. L. Byer, and B. Montazeri, "Electromagnetic forces in the vacuum region of laser-driven layered grating structures," *J. Mod. Opt.*, vol. 58, no. 17, pp. 1518–1528, 2011.

[89] Y. Wei *et al.*, "Numerical Study of a Multi-stage Dielectric Laser-driven Accelerator," in *Physics Procedia*, 2015, vol. 77, pp. 50–57.

[90] C. Warner and F. Rohrlich, "Energy loss and straggling of electrons," *Phys. Rev.*, vol. 93, no. 3, pp. 406–407, 1954.

[91] J. Breuer and P. Hommelhoff, "Dielectric laser acceleration of 28keV electrons with the inverse Smith–Purcell effect," *Nucl. Instruments Methods Phys. Res. Sect. A Accel. Spectrometers, Detect. Assoc. Equip.*, vol. 740, pp. 114–116, 2014.

[92] J. Breuer, R. Graf, A. Apolonski, and P. Hommelhoff, "Dielectric laser acceleration of nonrelativistic electrons at a single fused silica grating structure: experimental part," *Phys. Rev. Spec. Top. - Accel. Beams*, vol. 17, no. 2, p. 021301, 2014.

[93] K. Soong, R. Byer, C. McGuinness, E. a. Peralta, and E. Colby, "Experimental determination of damage threshold characteristics of IR compatible optical materials," in *Proceedings of the 2011 Particle Accelerator Conference, New York, NY, USA*,

2011, pp. 277–279.

[94] K. Soong, R. L. Byer, E. R. Colby, R. J. England, and E. A. Peralta, “Laser damage threshold measurements of optical materials for direct laser accelerators,” in *AIP Conference Proceedings*, 2012, vol. 1507, pp. 511–515.

[95] M. Lenzner *et al.*, “Femtosecond optical breakdown in dielectrics,” *Phys. Rev. Lett.*, vol. 80, no. 18, pp. 4076–4079, 1998.

[96] D. Verellen, M. De Ridder, and G. Storme, “A (short) history of image-guided radiotherapy,” *Radiother. Oncol.*, vol. 86, no. 1, pp. 4–13, 2008.

[97] R. J. England, R. J. Noble, Z. Wu, and M. Qi, “Dielectric Laser Acceleration,” *Rev. Mod. Phys.*, vol. 86, no. 4, pp. 1337–1389, 2014.

[98] T. Plettner and R. L. Byer, “Microstructure-based laser-driven free-electron laser,” *Nucl. Instruments Methods Phys. Res. Sect. A Accel. Spectrometers, Detect. Assoc. Equip.*, vol. 593, no. 1–2, pp. 63–66, 2008.

[99] T. Plettner and R. L. Byer, “Proposed dielectric-based microstructure laser-driven undulator,” *Phys. Rev. Spec. Top. - Accel. Beams*, vol. 11, no. 3, p. 030704, 2008.

[100] T. Plettner, R. L. Byer, C. McGuinness, and P. Hommelhoff, “Photonic-based laser driven electron beam deflection and focusing structures,” *Phys. Rev. Spec. Top. - Accel. Beams*, vol. 12, no. 10, p. 101302, 2009.

[101] K. Soong, R. L. Byer, E. R. Colby, R. J. England, and E. A. Peralta, “Grating-based deflecting, focusing, and diagnostic dielectric laser accelerator structures,” in *AIP Conference Proceedings*, 2012, vol. 1507, pp. 516–520.

[102] E. A. P. K. P. Wootton, R. J. England, I. V. Makasyuk, Z. Wu, A. Tafel, R. L. Byer, “Design and optimisation of dielectric laser deflecting structures,” in *Proceedings of IPAC2015*, 2015, pp. 2698–2701.

[103] R. H. Siemann, “Energy efficiency of laser driven, structure based accelerators,” *Phys. Rev. Spec. Top. - Accel. Beams*, vol. 7, no. 6, p. 061303, 2004.

[104] Y. C. Neil Na, R. H. Siemann, and R. L. Byer, “Energy efficiency of an intracavity coupled, laser-driven linear accelerator pumped by an external laser,” *Phys. Rev. Spec. Top. - Accel. Beams*, vol. 8, no. 3, p. 031301, 2005.

[105] R. B. Palmer, “A laser-driven grating LINAC,” *Part. Accel.*, vol. 11, pp. 81–90, 1980.

[106] D. M. Pai and K. A. Awada, “Analysis of dielectric gratings of arbitrary profiles and thicknesses,” *J. Opt. Soc. Am. A*, vol. 8, no. 5, pp. 755–762, 1991.

[107] J. Breuer, J. McNeur, and P. Hommelhoff, “Dielectric laser acceleration of electrons in the vicinity of single and double grating structures - theory and simulations,” *J. Phys. B At. Mol. Opt. Phys.*, vol. 47, no. 23, p. 234004, 2014.

[108] M. L. Good, “Phase-reversal focusing in linear accelerators,” *Phys. Rev.*, vol. 92, p. 538, 1953.

[109] D. A. Swensont, “Alternating phase focused linacs,” *Part. Accel.*, vol. 7, pp. 61–67, 1976.

[110] R. H. Miller, H. Deruyter, W. R. Fowkes, J. M. Potter, R. G. Schonberg, and J. N. Weaver, “RF phase focusing in portable X-band accelerators,” *IEEE Trans. Nucl. Sci.*, vol. 32, no. 5, pp. 3231–3233, 1985.

[111] B. Naranjo, A. Valloni, S. Putterman, and J. B. Rosenzweig, “Stable charged-particle acceleration and focusing in a laser accelerator using spatial harmonics,” *Phys. Rev. Lett.*, vol. 109, no. 16, p. 164803, 2012.

[112] Y. Wei *et al.*, "Beam quality study for a grating-based dielectric laser-driven accelerator," *Phys. Plasmas*, vol. 24, no. 2, p. 023102, 2017.

[113] K. S. Kunz and R. J. Luebbers, *The Finite Difference Time Domain Method for Electromagnetics*. CRC Press, Boca Raton, 1993.

[114] A. Wolski, "Linear beam dynamics for accelerators," *https://www.cockcroft.ac.uk/archives/course/linear-beam-dynamics-for-accelerators*, 2012. .

[115] S. Y. Lee, *Accelerator physics*. 2004.

[116] H. Wiedemann, *Particle accelerator physics*. 2007.

[117] C. Agritellis, R. Chasman, and T. J. M. Sluyters, "Design of the low-energy beam transport system of the Brookhaven 200-MeV injector linac," *IEEE Trans. Nucl. Sci.*, vol. 16, no. 3, pp. 221–226, 1969.

[118] P. Lapostolle, "Quelques Proprietes Essentielles Des Effets De La Charge D'Espace Dans Des Faisceaux Continus," 1970.

[119] J. A. Clarke *et al.*, "CLARA conceptual design report," *J. Instrum.*, vol. 9, no. 05, p. T05001, 2014.

[120] R. Kitamura, L. Pilon, and M. Jonasz, "Optical constants of silica glass from extreme ultraviolet to far infrared at near room temperature," *Appl. Opt.*, vol. 46, no. 33, pp. 8118–8133, 2007.

[121] "CST software." https://www.cst.com/, 2017.

[122] T. Weiland, "A discretization model for the solution of Maxwell's equations for six-component fields," *Arch. Elektron. und Uebertragungstechnik*, vol. 31, pp. 116–120, 1977.

[123] "VSim code." https://www.txcorp.com/vsim, 2017.

[124] Y. Wei *et al.*, "Investigations into dielectric laser-driven accelerators using the CST and VSim simulation codes," in *Proceedings of IPAC2015*, 2015, pp. 2618–2620.

[125] B. W. Zotter and S. Kheifets, *Impedances and Wakes in High-energy Particle Accelerators*. 1998.

[126] Y. Wei, G. Xia, J. D. A. Smith, and C. P. Welsch, "Dual-gratings with a Bragg reflector for dielectric laser-driven accelerators," *Phys. Plasmas*, vol. 24, no. 7, p. 073115, 2017.

[127] B. Cui, Z. Yu, H. Ge, and S. Y. Chou, "Large area 50 nm period grating by multiple nanoimprint lithography and spatial frequency doubling," *Appl. Phys. Lett.*, vol. 90, no. 4, p. 043118, 2007.

[128] R. Ghodssi and P. Lin, *MEMS Materials and Processes Handbook*, vol. 1. Springer US, 2011.

[129] P. Piot *et al.*, "The Advanced Superconducting Test Accelerator (ASTA) at Fermilab: A User-Driven Facility Dedicated to Accelerator Science & Technology," *arXiv:1304.0311*, pp. 1–3, 2013.

[130] Y. Wei, M. Ibison, G. Xia, J. D. A. Smith, and C. P. Welsch, "Dual-grating dielectric accelerators driven by a pulse-front-tilted laser," *Appl. Opt.*, vol. 56, no. 29, pp. 8201–8206, 2017.

[131] S. Akturk, X. Gu, E. Zeek, and R. Trebino, "Pulse-front tilt caused by spatial and temporal chirp," *Opt. Express*, vol. 12, no. 19, pp. 4399–4410, 2004.

[132] O. E. Martinez, “Pulse distortions in tilted pulse schemes for ultrashort pulses,” *Opt. Commun.*, vol. 59, no. 3, pp. 229–232, 1986.

[133] M. E. Durst, G. Zhu, and C. Xu, “Simultaneous spatial and temporal focusing in nonlinear microscopy,” *Opt. Commun.*, vol. 281, no. 7, pp. 1796–1805, 2008.

[134] J. A. Fülöp, L. Pálfalvi, G. Almási, and J. Hebling, “Design of high-energy terahertz sources based on optical rectification.,” *Opt. Express*, vol. 18, no. 12, pp. 12311–12327, 2010.

[135] Y. Morikawa, T. Koidesawa, T. Hayashi, and K. Suu, “A novel deep etching technology for Si and quartz materials,” *Thin Solid Films*, vol. 515, no. 12, pp. 4918–4922, 2007.

[136] Y. H. Tang, Y. H. Lin, T. T. Huang, J. S. Wang, M. H. Shiao, and C. S. Yu, “Investigation of fabricated through glass via (TGV) process by inductively coupled plasma reactive ion etching of quartz glass,” *2015 IEEE 10th Int. Conf. Nano/Micro Eng. Mol. Syst. NEMS 2015*, pp. 401–404, 2015.

[137] M. Ozgur and M. Huff, “Plasma etching of deep high-aspect ratio features into fused silica,” *J. Microelectromechanical Syst.*, vol. 26, no. 2, pp. 448–455, 2017.

[138] W. D. Kilpatrick, “Criterion for vacuum sparking designed to include both rf and dc,” *Rev. Sci. Instrum.*, vol. 28, no. 10, pp. 824–826, 1957.

[139] J. W. Wang and G. A. Loew, “Field Emission and RF Breakdown in High-Gradient Room-Temperature Linac Structures,” *SLAC-PUB*, vol. 7684, pp. 1–27, 1997.

[140] J. Hebling, J. A. Fülöp, M. I. Mechler, L. Pálfalvi, C. Tőke, and G. Almási, “Optical manipulation of relativistic electron beams using THz pulses,” *arXiv:1109.6852*, pp. 1–4, 2011.

[141] T. R. Schibli *et al.*, “Attosecond active synchronization of passively mode-locked lasers by balanced cross correlation,” *Opt. Lett.*, vol. 28, no. 11, pp. 947–949, 2003.

[142] Z. Wu *et al.*, “Intense terahertz pulses from SLAC electron beams using coherent transition radiation,” *Rev. Sci. Instrum.*, vol. 84, no. 2, p. 022701, 2013.

[143] J. A. Fülöp *et al.*, “Efficient generation of THz pulses with 04 mJ energy,” *Opt. Express*, vol. 22, no. 17, pp. 20155–20163, 2014.

[144] C. Vicario, A. V Ovchinnikov, S. I. Ashitkov, M. B. Agranat, V. E. Fortov, and C. P. Hauri, “Generation of 0.9-mJ THz pulses in DSTMS pumped by a Cr:Mg2SiO4 laser,” *Opt. Lett.*, vol. 39, no. 23, pp. 6632–6635, 2014.

[145] G. Andonian *et al.*, “Dielectric wakefield acceleration of a relativistic electron beam in a slab-symmetric dielectric lined waveguide,” *Phys. Rev. Lett.*, vol. 108, no. 24, p. 244801, 2012.

[146] E. A. Nanni *et al.*, “Terahertz-driven linear electron acceleration,” *Nat. Commun.*, vol. 6, p. 8486, 2015.

[147] B. D. O’Shea *et al.*, “Observation of acceleration and deceleration in gigaelectron-volt-per-metre gradient dielectric wakefield accelerators,” *Nat. Commun.*, vol. 7, p. 12763, 2016.

[148] Y. Wei *et al.*, “Investigations into dual-grating THz-driven accelerators,” *Nucl. Instruments Methods Phys. Res. Sect. A Accel. Spectrometers, Detect. Assoc. Equip.*, vol. 877, pp. 173–177, 2018.

[149] J. O. Tocho and F. Sanjuan, “Optical properties of silicon, sapphire, silica and glass in the Terahertz range,” in *Latin America Optics and Photonics Conference, OSA Technical Digest (Online), Paper LT4C.1, Optical Society of America*, 2012.

[150] M. C. Thompson *et al.*, "Breakdown limits on gigavolt-per-meter electron-beam-driven wakefields in dielectric structures," *Phys. Rev. Lett.*, vol. 100, no. 21, p. 214801, 2008.

[151] A. M. Cook, R. Tikhoplav, S. Y. Tochitsky, G. Travish, O. B. Williams, and J. B. Rosenzweig, "Observation of narrow-band terahertz coherent cherenkov radiation from a cylindrical dielectric-lined waveguide," *Phys. Rev. Lett.*, vol. 103, no. 9, p. 095003, 2009.

[152] K. Ravi, D. Schimpf, and F. Kärtner, "Pulse sequences for efficient multi-cycle terahertz generation in periodically poled lithium niobate," *Opt. Express*, vol. 24, no. 22, pp. 25582–25607, 2016.

[153] J. Lu, H. Y. Hwang, X. Li, S.-H. Lee, O.-P. Kwon, and K. A. Nelson, "Tunable multi-cycle THz generation in organic crystal HMQ-TMS," *Opt. Express*, vol. 23, no. 17, pp. 22723–22729, 2015.

[154] Y. Shen *et al.*, "Generation of tunable narrowband terahertz pulses from coherent transition radiation," in *Conference on Lasers and Electro-Optics, OSA Technical Digest (online), Paper CTu1B.1, Optical Society of America*, 2012.

[155] G. Pretzler, A. Kasper, and K. J. Witte, "Angular chirp and tilted light pulses in CPA lasers," *Appl. Phys. B*, vol. 70, no. 1, pp. 1–9, 2000.

[156] T. Schietinger *et al.*, "Commissioning experience and beam physics measurements at the SwissFEL Injector Test Facility," *Phys. Rev. Accel. Beams*, vol. 19, no. 10, p. 100702, 2016.

[157] E. Prat *et al.*, "Outline of a dielectric laser acceleration experiment at SwissFEL," *Nucl. Instruments Methods Phys. Res. Sect. A Accel. Spectrometers, Detect. Assoc. Equip.*, vol. 865, pp. 87–90, 2017.

[158] C. Milne *et al.*, "SwissFEL: The Swiss X-ray Free Electron Laser," *Appl. Sci.*, vol. 7, no. 7, p. 720, 2017.

[159] A. Szczepkowicz, "Guided-mode resonance, resonant grating thickness, and finite-size effects in dielectric laser acceleration structures," *Appl. Opt.*, vol. 55, no. 10, pp. 2634–2638, 2016.

[160] E. Belloy, A. Sayah, and M. A. M. Gijs, "Powder blasting for three-dimensional microstructuring of glass," *Sensors Actuators A Phys.*, vol. 86, no. 3, pp. 231–237, 2000.

[161] D. S. Park, M. W. Cho, H. Lee, and W. S. Cho, "Micro-grooving of glass using micro-abrasive jet machining," *J. Mater. Process. Technol.*, vol. 146, no. 2, pp. 234–240, 2004.

[162] X. Zeng, X. Mao, S.-B. Wen, R. Greif, and R. E. Russo, "Energy deposition and shock wave propagation during pulsed laser ablation in fused silica cavities," *J. Phys. D. Appl. Phys.*, vol. 37, no. 7, pp. 1132–1136, 2004.

[163] H. Niino, Y. Kawaguchi, T. Sato, A. Narazaki, T. Gumpenberger, and R. Kurosaki, "Laser ablation of toluene liquid for surface micro-structuring of silica glass," *Appl. Surf. Sci.*, vol. 252, no. 13, pp. 4387–4391, 2006.

[164] P. J. Revell and G. F. Goldspink, "A review of reactive production ion beam etching for production," *Vacuum*, vol. 34, no. 3–4, pp. 455–462, 1984.

[165] P. Leech, "Reactive ion etching of quartz and silica-based glasses in CF4/CHF3 plasmas," *Vacuum*, vol. 55, no. 3–4, pp. 191–196, 1999.

[166] X. Li, T. Abe, Y. Liu, and M. Esashi, "Fabrication of high-density electrical feed-

throughs by deep-reactive-ion etching of Pyrex glass," *J. Microelectromechanical Syst.*, vol. 11, no. 6, pp. 625–630, 2002.

[167] X. Li *et al.*, "Effects of Ar and O2 additives on SiO2 etching in C4F8-based plasmas," *J. Vac. Sci. Technol. A Vacuum, Surfaces, Film.*, vol. 21, no. 1, pp. 284–293, 2003.

[168] J. H. Park, N. E. Lee, J. Lee, J. S. Park, and H. D. Park, "Deep dry etching of borosilicate glass using SF6 and SF 6/Ar inductively coupled plasmas," *Microelectron. Eng.*, vol. 82, no. 2, pp. 119–128, 2005.

[169] T. Akashi and Y. Yoshimura, "Deep reactive ion etching of borosilicate glass using an anodically bonded silicon wafer as an etching mask," *J. Micromechanics Microengineering*, vol. 16, no. 5, pp. 1051–1056, 2006.

[170] T. Ichiki, Y. Sugiyama, R. Taura, T. Koidesawa, and Y. Horiike, "Plasma applications for biochip technology," *Thin Solid Films*, vol. 435, no. 1–2, pp. 62–68, 2003.

[171] D. Zhang and M. J. Kushner, "Investigations of surface reactions during C2F6 plasma etching of SiO2 with equipment and feature scale models," *J. Vac. Sci. Technol. A Vacuum, Surfaces, Film.*, vol. 19, no. 2, pp. 524–538, 2001.

[172] T. Fukasawa, T. Hayashi, and Y. Horiike, "Conelike Defect in Deep Quartz Etching Employing Neutral Loop Discharge," *Jpn. J. Appl. Phys.*, vol. 42, no. 10, pp. 6691–6697, 2003.

[173] A. Sankaran and M. J. Kushner, "Etching of porous and solid SiO2 in Ar/c-C4F8, O2/c-C4F8 and Ar/O2/c-C4F8 plasmas," *J. Appl. Phys.*, vol. 97, no. 2, p. 023307, 2005.

[174] K. Kolari, V. Saarela, and S. Franssila, "Deep plasma etching of glass for fluidic devices with different mask materials," *J. Micromechanics Microengineering*, vol. 18, no. 6, p. 064010, 2008.

[175] G. Craciun, M. Blauw, E. van der Drift, P. Sarro, and P. French, "Temperature influence on etching deep holes with SF6/O2 cryogenic plasma," *J. Micromechanics Microengineering*, vol. 12, no. 4, pp. 390–394, 2002.

[176] R. Ganter *et al.*, "Laser-photofield emission from needle cathodes for low-emittance electron beams," *Phys. Rev. Lett.*, vol. 100, no. 6, p. 064801, 2008.